

Fundamental Limits of Electromagnetic Axion and Hidden-Photon Dark Matter Searches: Part I - The Quantum Limit

Saptarshi Chaudhuri,¹ Kent Irwin,^{1,2,3} Peter W. Graham,^{1,2,4} and Jeremy Mardon^{1,4}

¹*Department of Physics, Stanford University, Stanford, CA 94305*

²*Kavli Institute for Particle Astrophysics and Cosmology,
Stanford University, Stanford, CA 94305*

³*SLAC National Accelerator Laboratory, Menlo Park, CA 94025*

⁴*Stanford Institute for Theoretical Physics,
Department of Physics, Stanford University, Stanford, CA 94305*

(Dated: December 3, 2024)

Abstract

We discuss fundamental limits of electromagnetic searches for axion- and hidden-photon dark matter. We begin by showing the signal-to-noise advantage of scanned resonant detectors over purely resistive broadband detectors. Building on this calculation, we discuss why the optimal detector circuit must be driven by the dark-matter signal through a reactance (an equivalent inductance or capacitance); examples of such detectors include single-pole resonators, which are used broadly in axion and hidden-photon detection. Focusing thereafter on reactively coupled detectors, we develop a framework to optimize dark matter searches using prior information about the dark matter signal. Priors can arise, for example, from cosmological or astrophysical constraints, constraints from previous direct-detection searches, or preferred search ranges associated with the QCD axion. We define integrated sensitivity as a figure of merit in comparing searches over a wide frequency range and show that the Bode-Fano criterion sets a limit on integrated sensitivity. We show that when resonator thermal noise dominates amplifier noise, substantial sensitivity is available away from the resonator bandwidth. The optimization of this sensitivity is found to be closely related to noise mismatch with the amplifier and the concept of measurement back-action. Additionally, we show that the optimized one-pole resonator is close to the Bode-Fano limit. *The Bode-Fano constraint establishes the single-pole resonator as a near-ideal method for single-moded dark-matter detection.* We optimize the integrated sensitivity in a scanned tunable resonator search by optimizing time allocation using priors. We derive quantum limits on resonant search sensitivity. We show that, in contrast to some previous work, resonant searches benefit from quality factors above one million, which corresponds to the characteristic quality factor (inverse of fractional bandwidth) of the dark-matter signal. We also show that the optimized resonator is superior, in signal-to-noise ratio, to the optimized reactive broadband detector at all frequencies at which a resonator may practically be made. At low frequencies, the application of our optimization may enhance scan rates by a few orders of magnitude. Finally, we discuss prospects for evading the quantum limits using backaction evasion, photon counting, squeezing and other nonclassical approaches, as a prelude to Part II.

CONTENTS

I. Introduction	5
II. A Comparison of Reactive Resonant and Resistive Broadband Coupling Schemes	15
III. Coupling to the Dark-Matter Signal	27
A. Optimizing the Coupling Element	27
B. Single-Pole Resonant Receiver Circuits for Axion and Hidden-Photon Detection	31
IV. Sensitivity Calculation of a Search for Light-Field Dark Matter	35
A. Scattering Representation of Resonant Detection Circuit	36
B. Scattering Representation of A Single-Moded Reactive Detector	42
C. Signal-to-Noise Ratio of Search	44
1. SNR for single circuit configuration	45
2. SNR for multiple circuit configurations: combining data	50
3. SNR of search with a quantum-limited amplifier	52
V. Search Optimization	57
A. Optimization of Matching Network	58
1. Value functional for matching network optimization in a log-uniform search	61
2. Matching network optimization for log-uniform search: the Bode-Fano constraint	64
3. Matching network optimization for log-uniform search with single-pole resonator	67
4. Discussion of single-pole resonator matching optimization for log-uniform search	72
5. Evading the Bode-Fano Constraint	78
6. Optimization of matching network for candidate signal	81
7. Comparison to other calculations	82
B. Optimization of Time Distribution	83
1. Aspects of a Practical Scan Strategy	89

VI. Fundamental Limit: Resonant Detector Read Out by a Quantum-Limited Amplifier	91
VII. Conclusions	98
A. The Electromagnetic Properties of the Axion and Hidden-Photon Dark-Matter Signal	101
1. Coherence Properties of the Dark-Matter Field	101
2. Signal Size	103
B. Amplitude, Direction, and Distribution Variation in the Dark-Matter Field	107
1. Amplitude Variation	107
2. Direction Variation	109
3. Distribution Variation	109
C. The Standard Halo Model	111
D. Noise Correlations for Quantum-Limited, Phase-Insensitive Amplifiers in the Scattering Mode Representation	112
E. Flux-to-Voltage Amplifiers	114
1. Classical Description of Noise in Flux-to-Voltage Amplifiers	115
2. Standard Quantum Limit on Noise in a Flux-to-Voltage Amplifier	118
F. Scan Optimization for Tunable Resonator Searches with Flux-to-Voltage Amplifiers	122
1. Signal-To-Noise Ratio of Search With Flux-To-Voltage Amplifier	123
2. Bode-Fano constraint on integrated sensitivity	125
3. Quantum-Limited Flux-to-Voltage Amplifiers with Uncorrelated Imprecision and Backaction Noise	129
4. Optimization for Imperfect Flux-to-Voltage Amplifiers	135
G. Comparison of Resonant and Broadband Searches with Flux-to-Voltage Amplifiers	141
References	154

I. INTRODUCTION

A significant body of astrophysical and cosmological evidence points to the existence of dark matter, which comprises 27% of the mass-energy in the universe [1]. Dark matter is a direct window to physics beyond the Standard Model. The vast majority of experimental efforts to directly detect cold dark matter have focused on weakly interacting massive particles (WIMPs) [2–4]. These searches, conducted over the past few decades, have so far yielded no detections and have placed strong constraints on the existence of WIMP dark matter. The lack of a detection of weak-scale dark matter motivates a search for other dark-matter candidates.

Another possibility for cold dark matter is an ultralight boson with mass below ~ 0.1 eV (in contrast to the $\sim \text{GeV}$ mass scale of WIMPs). The extremely low mass of an ultralight boson implies a large number density because the local dark-matter density is $\rho_{\text{DM}} \sim 0.3 \text{ GeV}/\text{cm}^3$. As a result, these bosons are best described as classical fields oscillating at a frequency slightly greater than their rest frequency, $\nu_{\text{DM}}^0 = m_{\text{DM}}c^2/h$ (m_{DM} is the rest mass of the dark matter, c is the speed of light, and h is Planck’s constant); the actual oscillation frequency is slightly higher than ν_{DM}^0 as a result of the small kinetic energy. Two prominent candidates in the class of ultralight bosons are axions and hidden photons. The “QCD axion” is a spin-0 pseudoscalar originally motivated as a solution to the strong CP problem [5, 6] that can also be dark matter. However, spin-0 pseudoscalar dark matter may exist even with parameters that do not solve the strong CP problem. Such particles are sometimes referred to as “axion-like particles.” In this work, we refer to both QCD axions and axion-like particles as “axions.”

Axions may be produced nonthermally (as would be required for a sub-eV particle to be cold, nonrelativistic dark matter) through the misalignment mechanism [7, 8]. One may search for axions via their coupling to the strong force [9] or their coupling to electromagnetism [10, 11]. The latter interaction, described by the Lagrangian

$$\mathcal{L}_{\text{int},a} = g_{a\gamma\gamma} a F \tilde{F}, \tag{1}$$

will be discussed further in this paper. In particular, in the presence of a DC magnetic field, the axion is converted to a photon. We will focus on this detection technique, a decision that may be motivated by the above Lagrangian. In the limit of a stiff axion field—the relevant practical limit—equation (1) demonstrates that the amplitude of the photon signal

grows with the amplitude of the background electromagnetic field. We would thus like the background field to be as large as possible. In laboratory searches, DC fields can be orders of magnitude larger than AC fields. As shown in Appendix A 2, the effect of DC electric fields is suppressed, relative to their magnetic counterparts, by the virial velocity of the dark matter $v/c \sim 10^{-3}$, so a background DC magnetic field is optimal.

The hidden photon is a spin-1 vector. Such particles emerge generically from models for physics beyond the Standard Model, often from theories with new U(1) symmetries and light hidden sectors [12]. The hidden photon was initially described as a dark-matter candidate in [13] and is further investigated in [14]. Like axions, hidden photons may be produced through the misalignment mechanism. They may also be produced during cosmic inflation. In fact, a vector particle in the 10 μeV - 10 meV mass range produced from quantum fluctuations during inflation would naturally have the proper abundance to be a dominant component of the dark matter [15]. One may search for hidden-photon dark matter via its coupling to electromagnetism [16], which arises from kinetic mixing:

$$\mathcal{L}_{\text{int},\gamma'} = \varepsilon FF'. \quad (2)$$

A traditional WIMP detector registers energy deposition from the scattering of a single dark-matter particle with a nucleus or electron. For an ultralight boson, such a measurement scheme is not appropriate. The energy deposition would be too small to be measured. Instead, it is possible to search for the weak collective interactions of the dark-matter field. For example, as a result of their coupling to electromagnetism, the effect of the hidden-photon or axion field may be modeled as an effective electromagnetic current density. (See Appendix A 2 for more details.) For the hidden photon, the direction of this current density is set by the vector direction, whereas for the axion, it is set by the direction of the applied magnetic field required for axion-to-photon conversion. These current densities produce observable electromagnetic fields oscillating at frequency slightly greater than ν_{DM}^0 , which couple to a receiver circuit and may be read out with a sensitive magnetometer, amplifier, or photon detector.

In ADMX [10, 11, 17], HAYSTAC [18], Axion LC search [19], and DM Radio [16, 20], the receiver takes the form of a tunable high-Q resonant circuit. If dark matter exists at a frequency near the resonance frequency, the electromagnetic fields induced by the dark matter ring up the resonator. The signal in the resonator is read out by a Superconduct-

ing Quantum Interference Device (SQUID) amplifier or a near-quantum-limited parametric amplifier. By tuning the resonator across a wide frequency range, one may obtain strong limits on light-field dark matter. In this manner, a search for axion- or hidden-photon dark matter operates much like an AM radio.

The amplifiers in these searches couple to a single mode of the resonator. This is clearly not always the optimal receiver circuit. For instance, if the circuit has multiple resonant modes (at different frequencies) that do not interact parasitically with each other, and each couple to the electromagnetic fields from the dark matter, one may increase the scan rate, relative to a single-moded resonator. The principal purpose of this work is to determine the properties of the optimal receiver to search for the electromagnetic coupling of axion- and hidden-photon dark matter.

We start by asking: What are the characteristics of the optimal receiver? To answer this question, we must first understand the basic structure of a receiver, irreducible noise sources in such receivers, and the role of impedance matching and amplifier noise matching.

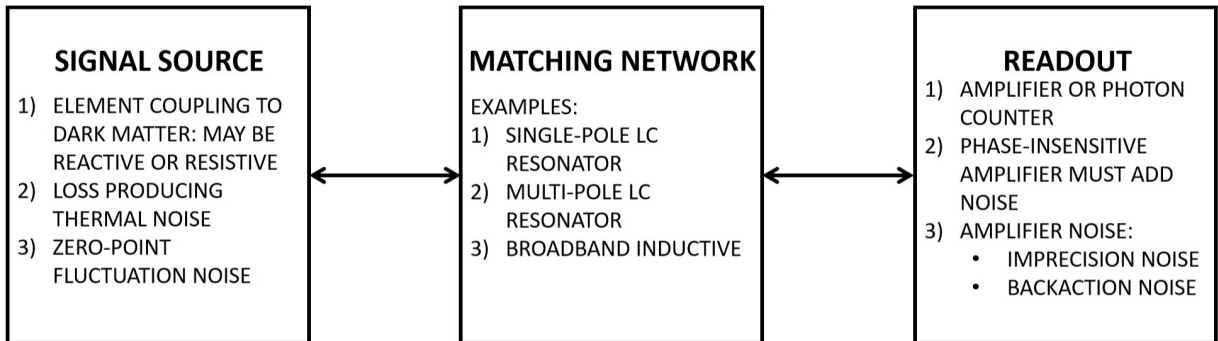


FIG. 1. Diagram showing the elements of a dark-matter receiver: the signal source (including loss in the coupling element), the matching circuit, and the readout element, which may be an amplifier or photon counter. The amplifier noise has two parts, the imprecision noise and the backaction noise. The double-arrows signify that signals can travel in both directions through the receiver. For instance, the dark-matter signal propagates to the readout, but the backaction noise propagates to the dark-matter-coupling element in the signal source.

The elements of a dark-matter receiver circuit are shown as a schematic block diagram in Fig. 1.¹ This paper is organized around optimizing each of these blocks, and globally

¹One may note that the readout of a receiver signal with phase-insensitive amplifier constitutes coherent

optimizing the blocks and their interactions across a full scan.

Central to every detection circuit is an element that couples to the dark-matter field. The element may be reactive, e.g. an inductive pickup coil that couples to the magnetic field produced by the dark matter or a capacitance that couples to the electric field. We may alternatively use a purely resistive detector. The resistive detector may be a phased antenna array presenting a real impedance to the electromagnetic field, or a simple resistive sheet. Electric fields induced by dark matter would drive current flow in a resistive sheet, resulting in a dissipated power.² Over the next two sections, we will explain why a single-pole resonator is superior (in terms of signal-to-noise ratio (SNR)) to a broadband resistive sheet. (Similarly, we also show that a single-pole resonator is superior to a broadband reactive detector, such as that presently used in ABRACADABRA [22]. See Appendix G.) We will in fact make the more general statement that the optimal detector has the property that it is driven by the dark-matter-induced electromagnetic fields through a reactance. The explanation relies on understanding the requirements, formulated in ref. [23], for coupling efficiently—or “impedance matching”—to power available in the dark-matter field. Thereafter, since a single-pole resonator is a prime example of a reactive detector, we will focus solely on reactive coupling. Every detection circuit has some loss (i.e. some resistance), which produces thermal noise. If the circuit is cold and $h\nu_{\text{DM}}^0 \gg kT$, where k is Boltzmann’s constant and T is the physical temperature, one will observe the effects of the zero-point fluctuations in the detector. We refer to these three components (dark-matter signal, thermal noise from loss, and zero-point fluctuation noise) collectively as the “Signal Source” in Fig. 1. This is the first element in the receiver model.

The second element of every receiver is an impedance-matching network. The impedance matching network is used to provide a better match between the complex reactive impedance of the pickup element and the input impedance of an amplifier, which typically possesses a real part or is purely real. A single-pole LC resonator is an example of a matching network. It uses a capacitor or network of capacitors to transform the inductive pickup coil to a real impedance on resonance, as seen by the readout. In the high-frequency cavity limit (e.g. ADMX), each mode can be modeled as an equivalent RLC circuit serving as a matching network, which has been studied extensively in the context of radio astronomy for the past several decades [21]. In fact, one way to model the detection circuit is as an astronomical receiver coupled very weakly to a photon source, i.e. the dark-matter field.

²Whether it is better to couple to the electric field or the magnetic field is a subject of Section III. An important role is played by electromagnetic shielding.

work. Another matching network is a multi-pole resonator, which, for instance, could have many LC poles at the same frequency. One may also use broadband inductive coupling, where a pickup coil is wired directly to the input of a SQUID (e.g. ABRACADABRA). The signal source and matching network may contain mechanical elements, such as piezoelectrics and crystal oscillators which behave electrically as RLC circuits. We will restrict our attention to linear, passive circuits.

The third and final element is an amplifier or photon counter to read out the signal passed through the impedance matching network. Photon-counting and quantum-squeezing techniques are being developed for light field dark-matter detection [24], but we will focus here on readout with phase-insensitive amplifiers, which coherently amplify both quadratures of an incoming signal with the same gain [25]. The application of photon counting and quantum squeezing in the context of this comprehensive consideration of axion- and hidden-photon detection through electromagnetic coupling will be left to future work. We will also assume that the output of the amplifier is not fed back to the detection circuit in an active feedback or feedback damping scheme, which can effectively improve the impedance matching between signal source and amplifier [26, 27]. Feedback will also be addressed in future work.

In a readout with a phase-insensitive amplifier, both quadratures of the signal are amplified equally and analyzed for a signal. As dictated by the Heisenberg uncertainty principle, the experimental sensitivity is subject to a second source of effective noise, which is noise added by the amplifier. The limitation set by Heisenberg for phase-insensitive measurement is sometimes referred to as the Standard Quantum Limit (SQL). In the high-gain limit, the quantum limit on added noise corresponds to a minimum noise temperature of one-half photon, $kT_N(\nu) = h\nu/2$ [25].³

In particular, every amplifier has two effective noise sources: imprecision noise and backaction noise. The imprecision noise simply acts to add some uncertainty to the output of the amplifier, independent of the input load. The backaction noise injects noise into the input circuit. This noise, having been filtered according to the impedance of the input

³The noise temperature of the amplifier $T_N(\nu)$ is defined as follows. The resistor at temperature T produces a thermal noise spectral density proportional to the Bose-Einstein thermal occupation number $n(\nu) = (\exp(h\nu/kT) - 1)^{-1}$; see equations (59), (60), and (F2). We may define an added noise number $N_A(\nu)$ as the increase in thermal occupation number such that the increase in thermal noise equals the amplifier noise. The noise temperature is then given by $T_N(\nu) \equiv N_A(\nu)h\nu/k$. This definition is equivalent to that used in Ref. [28], but differs from that in Ref. [25]. We stress that this difference is simply one of convention, rather than one originating in physical principles.

circuit, is added to the amplifier input and appears as additional noise on the output. In contrast to imprecision noise, backaction noise (referred to the amplifier input) is inherently dependent on the source impedance. The spectral densities of both noise contributions can be frequency-dependent. Consider the simple case where the matching network possesses negligible loss, so that the only loss is that in the signal source (and the coupling to the input impedance of the amplifier). When the noise temperature is minimized with respect to the source impedance, it is said that the input circuit is *noise matched* to the amplifier. [28, 29] If, in addition to noise matching, the imprecision and backaction noise modes obey certain relations [28] (see Appendices D and E 2 for more information), then the quantum limit on noise temperature of $kT_N(\nu) = h\nu/2$ can be achieved.

The optimal receiver circuit therefore has the following characteristics:

1. The detection circuit should be reactively coupled and should present an impedance match to the electromagnetic signal from the dark matter. In other words, it should couple as efficiently as possible to the power available in the local dark-matter "source."
2. The energy coupled into the detector from the dark-matter signal increases with the detector volume, so the reactive detection element should possess as much coupled volume as is practical.
3. The loss in the detection circuit should be as low as possible and as cold as possible. Larger receivers may have more loss and be more difficult to get cold than smaller receivers, so this third characteristic must be optimized in combination with the second. Furthermore, some sources of loss are reduced at low temperatures (e.g. loss from electrons in superconductors), and some are increased (e.g. saturable two-level systems in a dielectric), so a practical optimization may be complicated.
4. The characteristics of the impedance-matching network (second block in Fig. 1) and the amplifier should permit the noise temperature (with respect to input load) to be minimized, subject to the quantum limit. This minimization should be achieved at as large a range of frequencies as possible to reduce scan time of the full search.

The first criterion is discussed in depth in [23], which presents a modified circuit model for understanding the dark-matter electromagnetic interaction. There, it is shown that a single-pole resonator, in principle, possesses the key attributes required for an efficient impedance

match to the dark matter. Nevertheless, the intrinsic loss needed (in a resonant detector or otherwise) to optimally match to, or backact on, the dark-matter signal is far too low to be achieved in any practical experiment. The electromagnetic signal induced by dark matter can be assumed to be a stiff signal, thereby motivating the second and third criteria.

The second and third criteria are constrained by familiar experimental limitations. The detector volume will be limited by constraints on the fabrication of detector materials and the maximum possible size of the shield, which surrounds the detector and is required in order to block external electromagnetic interference. The loss in the circuit can be optimized by using superconductors, although their use can be precluded in axion searches if the detector and the applied DC magnetic field are not spatially separated [17, 18]. The temperature is usually limited by the performance of the cryogenic refrigeration scheme; the use of a dilution refrigerator enables ~ 10 mK operating temperatures.

The last criterion, and more generally, the concepts of amplifier impedance matching and noise matching as they apply to dark-matter detection, will be the primary focus of the paper. Ideally, one would possess an amplifier that is quantum-limited (capable of reaching the half-photon noise temperature with appropriate noise match) and noise-matched to the input circuit at all frequencies. However, such a device has not been experimentally demonstrated. In fact, as we will show, if the input impedance of the quantum-limited amplifier is real-valued (which is the circumstance for practical quantum-limited microwave amplifiers, such as Josephson parametric amplifiers [30]), then the Bode-Fano criterion [31, 32] places a powerful constraint on the sensitivity of a single-moded detection circuit integrated across the search band. A single-pole resonator is approximately 75% of the Bode-Fano fundamental limit. Together with the circuit model framework of [23], the Bode-Fano limit motivates the single-pole resonator as a near-ideal technique to detect the dark-matter field.

Having produced this general framework for understanding circuits to detect electromagnetic coupling to ultralight dark-matter fields, we now return to single-pole resonant detectors. The thermal noise and the dark-matter signal are both filtered by the impedance-matching network. Therefore, if the filtered thermal noise from the loss in the signal source dominates the amplifier noise (i.e. the physical temperature of the resistor is larger than the minimum amplifier noise temperature), then the sensitivity is independent of the detuning from resonance. It is to our advantage to maximize the bandwidth over which thermal noise dominates amplifier noise, while maintaining high sensitivity. This bandwidth may be con-

siderably larger than the resonator bandwidth. *A unique aspect of light-field dark-matter searches is that a quantum-limited amplifier is desirable even when the frequency being probed satisfies $h\nu \ll kT$.* Some previous work only accounted for the information available within the resonator bandwidth and therefore underestimates the sensitivity of resonant searches. [10, 11, 16, 22]

As stated before, a fundamental feature of a resonant search is that one must scan the resonance frequency over a broad range. In this work, we discuss the optimization of scan strategies. We show that this optimization is closely related to the optimization of noise matching. When combined with the aforementioned constraints on impedance matching to the dark-matter signal and amplifier, this optimization results in a fundamental limit on the sensitivity of axion and hidden-photon searches read out with a phase-insensitive amplifier coupled to an induced electromagnetic signal.

The outline of this paper is as follows. In Section II, we focus on two simple examples of light-field dark-matter detectors: a resistive sheet and a tunable cavity resonator. In an apples-to-apples comparison, the cavity is found to be superior to the resistive broadband detector. We contrast this behavior with the absorption of vacuum electromagnetic waves that satisfy (unmodified) Maxwell’s equations. A similar result is found in comparison of a resonator and a reactive broadband search, such as ABRACADABRA [22]; details are left for Appendix G. This appendix should be read after the full quantitative machinery for analyzing signal-to-noise ratio has been introduced; the SNR framework is constructed in Section IV. The comparison in Section II allows us to introduce many of the concepts which are mentioned in Fig. 1, and which will be of primary concern in this paper.

In Section III, we further examine and categorize the schemes for coupling to the dark-matter signal. Using the results from [23], we explain why the optimal detector must be driven by the electromagnetic fields induced by dark matter through an equivalent-circuit reactance, i.e. an inductor or capacitor. The advantage of resonators over broadband resistive sheets is explained in terms of the “drag” on electrons due to visible-photon radiation. We also elucidate the role played by electromagnetic shielding, which is a practical requirement in any dark-matter search. In the limit that the characteristic size of the shield is much smaller than the Compton wavelength $\lambda_{\text{DM}}^0 \equiv c/\nu_{\text{DM}}^0$, the dominant observable is a dark-matter-induced magnetic field. One should then couple to the signal using an inductor. In the limit that the shield size and Compton wavelength are comparable, the induced

electric and magnetic fields are comparable. There is no advantage to a capacitive coupling over an inductive coupling. As such, for the remainder of the main text, we consider solely inductively-coupled detectors, while pointing out in various sections similar results for capacitively-coupled detectors. To provide a practical perspective for the analysis that follows, we discuss a variety of single-pole resonant detection schemes proposed or in use for ultralight field dark-matter detection. We discuss more specifically how such detectors are excited by electromagnetic fields induced by dark matter, and consider how such detectors are read out. Subsequent to this section, we will focus on a simple example, where the detector is coupled to a transmission line and read out by an amplifier operated in the scattering mode. [28] This is representative of the type of receiver used in ADMX and HAYSTAC. In Appendices E-G, we will consider a different example, directly related to DM Radio and the Axion LC search, where the resonator is read out with a flux-to-voltage amplifier (see Appendix E for a definition and description), such as a dc SQUID or dissipationless rf SQUID. The description is somewhat more complicated in this latter example, but the primary conclusions regarding resonator optimization and fundamental limits are the same as those found in the main text for the scattering-mode case.

In Section IV, we derive the signal-to-noise ratio (SNR) for a scanning search using a scattering matrix representation of the coupling (e.g. resonator) and amplification circuits. The analysis will apply not only to resonators, but to any single-moded reactive coupling scheme. This level of generality is critical in enabling us to set a limit on detection sensitivity with the Bode-Fano criterion. We give a brief quantitative discussion of the dark-matter signal as it relates to the scattering representation, leaving a more detailed treatment, including considerations of temporal and spatial coherence, for Appendix A. As will be discussed, the detection scheme is equivalent to a Dicke radiometer [33] used in radio astronomy. We discuss the signal processing steps of a Dicke radiometer as they relate to the detection circuit. The SNR is calculated in two parts. First, given a fixed dark-matter search frequency, we calculate the SNR from a single instance of the scan, e.g. a single resonance frequency. In doing so, we derive an optimal filter for the signal processing which maximizes SNR [34]. Second, using the results for the single instance, we calculate the SNR for a scan, which is comprised of many resonant frequencies. We determine the weighting of the data from the various scan steps that yields the highest possible SNR. As an example, we then provide an explicit calculation of SNR (for both the single scan step and whole scan) for

a quantum-limited scattering-mode amplifier with uncorrelated backaction and imprecision noise modes, for which the noise impedance and input impedance are real-valued and equal. This amplifier and its noise properties are discussed further in Appendix D. The results on SNR for a quantum-limited phase-insensitive amplifier sets a fundamental limit on the detection sensitivity of a search for electromagnetic coupling to ultralight dark matter. The optimization of a search using a quantum-limited phase-insensitive amplifier is the basis for the remainder of the main text. A similar SNR calculation for flux-to-voltage amplifiers is carried out in Appendix F.

In Section V, we discuss the optimization of the search. The optimization is carried out in two steps. In the first part, for a fixed scan step, we optimize the impedance-matching network. This network need not be resonant. We determine a value function for evaluating the merits of a matching network and optimize two types of searches. The first type is a “log uniform” search, to be defined in Section V, which makes the natural assumption of a logarithmically uniform probability for the mass and coupling of dark matter within the search band. It is here that we establish a limit on detection sensitivity with the Bode-Fano criterion, which constrains broadband matching between a complex impedance (the signal source) and a real impedance (the amplifier input). The second type is a candidate-signal search, where a signal has already been found in a previous search and one wishes to probe the signal as well as possible. In each of the two cases, we link our result to the concepts of noise matching, amplifier backaction, and sensitivity outside of the resonator bandwidth. We show that the optimized resonator is approximately 75% of the Bode-Fano limit, thereby motivating the single-pole tunable resonator as a near-ideal single-moded detector for probing ultralight-field dark matter. Hereafter, we will only discuss resonators in the main text. We discuss the impact of these results on scan time. In the second step, given a fixed total search time, we determine the optimal allocation of time across resonant scan steps for the log-uniform search. We introduce the notion of a dense scan, where each search frequency is probed by multiple resonant frequencies. We also briefly consider other possible value functions for time allocation based on prior assumptions about the probability distribution of dark matter.

Similar optimizations are carried out in the appendix. In Appendix F2, we derive a Bode-Fano constraint for an inductively-coupled detector read out with a quantum-limited flux-to-voltage amplifier possessing real-valued noise impedance. In Appendix F3, we con-

sider resonator optimization with a quantum-limited flux-to-voltage amplifier possessing uncorrelated imprecision and backaction noise (real noise impedance). The result is the same as that derived for the quantum-limited scattering mode amplifier. We again find that the optimized single-pole resonator is approximately 75% of the Bode-Fano limit. In Appendix F 4, we carry out the optimization for the log-uniform search after relaxing the assumptions of uncorrelated imprecision and backaction noise and minimum noise temperature equal to one-half photon.

The optimization of the resonant scan in Section V, in combination with the Bode-Fano criterion and the circuit model insights, yields a fundamental limit on the performance of axion and hidden-photon dark-matter searches read out by a phase-insensitive amplifier. We calculate this limit in Section VI. Owing to the identical results provided in the scan optimization, the limit is the same for scattering-mode and flux-to-voltage readouts. We analyze various features of this limit. In particular, we discuss the parametric dependence of the fundamental limit on quality factor and contrast it with previous works. [10, 11, 16] We show that use of the optimized scan strategy can increase the sensitivity to dark-matter coupling strength by as much as 1.25 orders of magnitude at low frequencies. This corresponds to an increase in scan rate of five orders of magnitude.

We conclude in Section VII. We provide directions for further investigation, with attention paid to topics that will be covered in Part II of this work. In particular, we discuss prospects for evading the Standard Quantum Limit of the dark-matter measurement using backaction evasion, squeezing, entanglement, and photon counting in the context of this comprehensive optimization framework.

II. A COMPARISON OF REACTIVE RESONANT AND RESISTIVE BROAD-BAND COUPLING SCHEMES

As shown in Fig. 1, one may couple to an electromagnetic signal induced by the dark-matter field using a reactive element or a purely resistive element. A purely resistive search can be modeled as a sheet of finite conductivity σ_r in free space. The resistive sheet is a model for a physical resistor or an array of antennas presenting a real impedance. An incident electromagnetic field induced by a dark-matter field drives currents in the sheet. Ohm's Law dictates that these currents must dissipate power, which may be detected, for

instance, with bolometric photon counting, or by antenna-coupled amplifiers.

Consider initially an electromagnetic plane wave governed by unmodified Maxwell’s equations, normally incident on a resistive sheet with vacuum on both sides. The absorption is maximized when the sheet impedance $Z_{sh} = 1/(\sigma_r h)$ is set to $Z_{fs}/2 = \mu_0 c/2 \approx 188 \, \Omega$. (Here, h is the thickness of the sheet. For simplicity of analysis, h is set to be much less than the skin depth at the frequency being absorbed. μ_0 is the vacuum permeability.) This setup absorbs 50% of the power available in the field. With the addition of a quarter-wave backshort and a sheet impedance of $Z_{sh} = Z_{fs}$, one may absorb 100% of the power. However, the addition of the backshort introduces an effective reactance in the problem, and limits the bandwidth over which the coupling is efficient.

In light of the fact that a purely resistive sheet is a relatively efficient detector of “normal” electromagnetic fields over wide bandwidth, one might ask why they are not used commonly to detect fields induced by dark-matter axions or hidden photons. Why does one choose a resonator over a broadband resistive absorber? After all, resistive absorbers are a critical piece of many millimeter-wave astronomy instruments [35], which also seek to detect small photon signals from cosmic sources.

To answer this question, we perform an apples-to-apples comparison of the sensitivity of a broadband resistive sheet and a tunable cavity. We first describe the experimental setup and then calculate the signal size in terms of power dissipation. This is followed by a brief SNR analysis (a more rigorous version of which will appear in Section IV C). We compare the SNRs at each dark-matter rest-mass frequency in our search band and show that the SNR for the cavity is always larger. In fact, we show that the advantage in SNR scales as the square root of the quality factor, a result that will be explored in far greater depth in Section VI.

See Fig. 2. In the introduction, we stated that the hidden-photon and axion fields can be modeled as effective current densities that produce electromagnetic fields. They may also be modeled more directly as electromagnetic fields themselves. For the hidden photon, representation as an effective current is known as the interaction basis, while representation as an effective electromagnetic field is known as the mass basis [36]. Relative to the electric field, the free-space magnetic field induced by dark matter is suppressed by the velocity of the dark matter $v/c \sim 10^{-3}$. This velocity arises from the $\sim 10^{-3}c$ virial velocity, in combination with the $\sim 10^{-3}c$ detector velocity (Earth velocity) in the galactic rest frame

(the frame in which the bulk motion of the dark matter is zero). As such, the dominant observable is an effective electric field. We denote this effective electric field by \vec{E}_{DM} in the figure and assume that this field is stiff. We will revisit this assumption below.

Owing to the nonzero velocity from virialization and Earth's motion, the electric field induced by dark matter is not monochromatic, but rather, possesses a nonzero bandwidth. The $\sim 10^{-3}c$ dark-matter velocity gives a $\sim 10^{-6}$ dispersion in kinetic energy and therefore, a bandwidth

$$\Delta\nu_{\text{DM}}(\nu_{\text{DM}}^0) \sim 10^{-6}\nu_{\text{DM}}^0. \quad (3)$$

The dark-matter signal thus spans the frequency range $\nu_{\text{DM}}^0 \leq \nu \lesssim \nu_{\text{DM}}^0 + \Delta\nu_{\text{DM}}(\nu_{\text{DM}}^0)$. We have made explicit here the dependence of the dark-matter bandwidth on search frequency to indicate that bandwidth is not constant across the search range, but is expected to grow linearly. Nevertheless, in the preliminary calculation in this section, we assume that the cavity linewidth is larger than this bandwidth, so that for the purpose of calculating experimental sensitivity, we may treat the dark-matter signal as monochromatic.

We assume that the cavity separation L is smaller than the de Broglie wavelength of the dark matter, which sets the coherence length of \vec{E}_{DM} . This is an appropriate assumption, given that for dark-matter signals near the fundamental resonance frequency, where the response is strongest, the length satisfies $L \sim \lambda_{\text{DM}}^0$, the Compton wavelength of the dark-matter signal, and is thus much less than the de Broglie coherence length $\sim 1000\lambda_{\text{DM}}^0$. We also assume that the lateral extent of the cavity is much smaller than the de Broglie wavelength, so that we may treat \vec{E}_{DM} as spatially uniform. Furthermore, we assume that the lateral extent of the cavity is much larger than λ_{DM}^0 , so that we may ignore fringe-field effects and effectively reduce the three-dimensional problem to a one-dimensional problem.

In Fig. 2a, we show a sheet of conductivity σ_r . For simplicity, we assume that the conductivity is frequency-independent. Frequency-dependence has no significant bearing on our conclusion that a tunable cavity is fundamentally superior to a broadband resistive sheet. The sheet lies in the x-z plane. Electric fields tangent to the surface dissipate power in the sheet.

In Fig. 2b, we show two sheets separated by length L : one of frequency-independent conductivity σ_c and the other possessing perfect conductivity. These two sheets form a resonant cavity. If the frequency ν of the electric field satisfies (or nearly satisfies) the

resonance condition

$$\exp(2\pi i\nu L/c) = -1, \quad \exp(4\pi i\nu L/c) = 1, \quad (4)$$

then the dark-matter fields ring up the cavity. The rung-up fields dissipate power in the left-side sheet. We assume that only a single detector mode is used: the fundamental resonance at $\nu_r = c/2L$. Although one might use multiple resonance modes or wider band information across the search range (the latter of which will be discussed in detail later in this paper), in this section we only consider signal sensitivity within the resonator bandwidth of this single mode. The cavity resonance frequency may be tuned by changing length L .

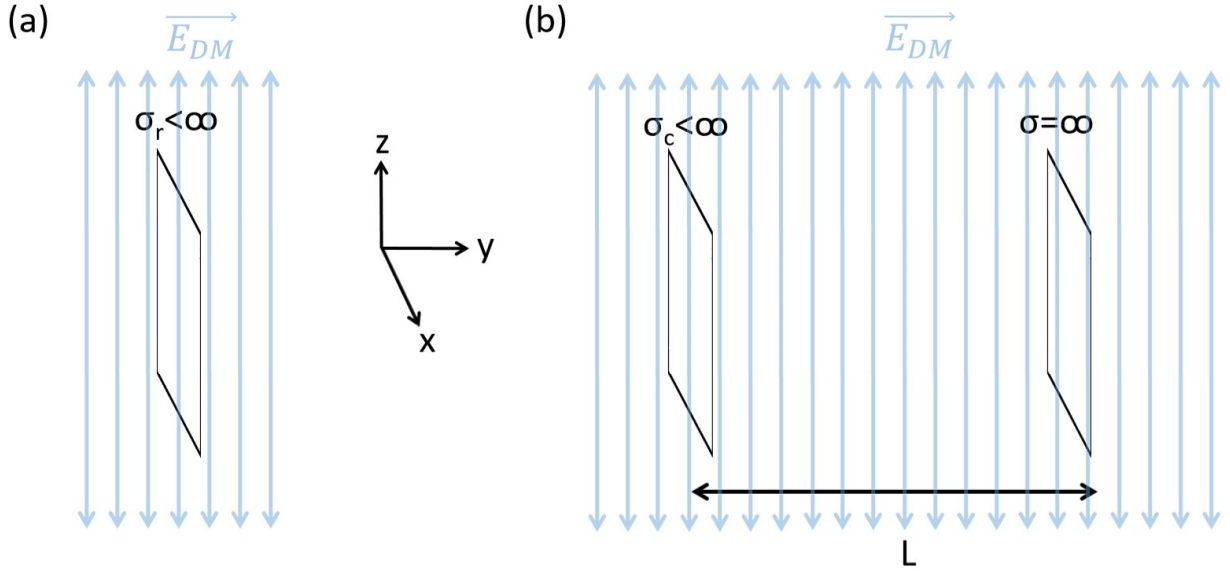


FIG. 2. Setup for comparison of resistive sheet and tunable cavity as dark-matter detectors. (a) Resistive sheet. (b) Half-wave cavity bounded by a sheet of finite conductivity and a sheet of perfect conductivity. The cavity may be tuned by changing the separation between the sheets. The dark matter produces a free-space electric field, which we assume is tangent to the surface of the sheets.

We assume that the dark-matter electric field lies in the \hat{z} direction. For the axion, this may be arranged by applying a DC magnetic field in the \hat{z} direction. We assume that the magnetic field is uniform. For the hidden photon, the experimentalist does not control the direction of the electric field. However, this is not of consequence for the sensitivity comparison. Misalignment with the detector will result in the same multiplicative reduction

in sensitivity for both the sheet and the cavity.

Under these assumptions, the dark-matter electric field can be approximated as

$$\vec{E}_{\text{DM}}(t) = \text{Re}(\tilde{E}_{\text{DM}} \exp(2\pi i \nu_{\text{DM}}^0 t)) \hat{z}. \quad (5)$$

We may relate the complex amplitude of this electric field to the complex amplitude of the z-component of the mass-basis hidden-photon vector potential, denoted \tilde{A}'_m [23]. The relation is

$$\tilde{E}_{\text{DM}} = -i(2\pi\nu)\epsilon\tilde{A}'_m \quad (6)$$

One may write a similar relationship for the axion pseudoscalar potential, whose complex amplitude is \tilde{a} :

$$\tilde{E}_{\text{DM}} = \kappa_a c B_0 \tilde{a} \quad (7)$$

where κ_a is related to the more traditional axion-photon coupling $g_{a\gamma\gamma}$ by

$$\kappa_a = g_{a\gamma\gamma} \sqrt{\hbar c \epsilon_0} \quad (8)$$

(ϵ_0 is the vacuum permittivity.), and B_0 is the magnitude of the applied magnetic field.

We calculate the steady-state power dissipated in the finite conductivity sheet in each of the two experiments. This will be the signal size that we use to compare experimental sensitivities. Note that, in the case of antenna-coupled amplifier readout, as compared to bolometric readout, we typically discuss signals in terms of power received rather than power dissipated. However, if the bolometer (sheet) and the antenna/amplifier setup present the same real impedance and possess the same receiving area, then the signal size is the same. Ohm's Law at each sheet dictates that the volumetric current density in each sheet is related to the electric field by

$$\vec{J}_{r,c}(\vec{x}, t) = \sigma_{r,c} \vec{E}_{r,c}^{\text{tot}}(\vec{x}, t), \quad (9)$$

where the subscript indicates whether the resistive sheet belongs to the broadband detector (“r”) or the cavity (“c”) and $\vec{E}_{r,c}^{\text{tot}}(\vec{x}, t)$ is the total electric field in the sheet. There is also a current in the perfect conductor—the right-hand sheet in the cavity—to screen electric fields from its interior and maintain the boundary condition that the electric field parallel to the surface vanish. We denote this current density as $\vec{J}_\infty(\vec{x}, t)$. The current in each of the three sheets arises both from the “incident” dark-matter electric field and the electric field radiated in response to this drive.

In general, the current density and the electric field will be position-dependent in the sheets. However, because we are ignoring fringing effects and because the thickness of each sheet is set to be much less than the skin depth at frequency ν_{DM}^0 , the current density and the electric field are considered to be uniform in each sheet. We may then turn the volumetric current density into an effective surface current density $\vec{K}_{r,c}(t)$. Setting all sheets to have a common thickness h , we find

$$\vec{K}_{r,c}(t) = \sigma_{r,c} h \vec{E}_{r,c}^{\text{tot}}(t), \quad (10)$$

where $\vec{E}_{r,c}^{\text{tot}}(t)$ is now most readily interpreted as the surface field. We may similarly define an effective surface current density for the perfect conductor, $\vec{K}_{\infty}(t)$, that keeps the surface field zero. We define the sheet impedances as

$$Z_r \equiv 1/(\sigma_r h), \quad Z_c \equiv 1/(\sigma_c h). \quad (11)$$

We also set the sheets to have a common surface area A .

Maxwell's equations yield a relationship between the electric field and the volume current density at any point in space:

$$(\partial_t^2 - c^2 \vec{\nabla}^2) \vec{E}(\vec{x}, t) = -\mu_0 c^2 \partial_t \vec{J}(\vec{x}, t). \quad (12)$$

For the broadband detector, $\vec{J}(\vec{x}, t)$ reflects the current density for the sheet, while for the cavity, $\vec{J}(\vec{x}, t)$ includes both the current densities on the finite conductivity and the perfect conductivity sheets: $\vec{J}(\vec{x}, t) = \vec{J}_c(\vec{x}, t) + \vec{J}_{\infty}(\vec{x}, t)$. We may solve for the current in each sheet, and consequently, the power dissipation using superposition. Because we ignore fringe-field effects, the electric field is only a function of y , the coordinate normal to the sheets.

a. Power Dissipation in Resistive Broadband Detector

We find the steady-state solution for the current and fields. All quantities oscillate at frequency ν_{DM}^0 and the fields and currents point in the \hat{z} direction, so we may write

$$\vec{K}_r(t) = \text{Re}(\tilde{K}_r \exp(2\pi i \nu_{\text{DM}}^0 t)) \hat{z}. \quad (13)$$

Setting the position of the sheet to be $y = 0$, the current density in eq. (12) is $\vec{J}_r(\vec{x}, t) = \vec{K}_r(t) \delta(y)$ where $\delta(y)$ is a Dirac delta function. The electric field produced by the sheet is then the plane wave

$$\vec{E}_r(y, t) = \text{Re}(\tilde{E}_r \exp(2\pi i \nu_{\text{DM}}^0 (t - |y|/c))), \quad (14)$$

where

$$\tilde{E}_r = -Z_{fs}\tilde{K}_r/2. \quad (15)$$

Equation (10) gives

$$\tilde{K}_r = \frac{1}{Z_r}(\tilde{E}_r + \tilde{E}_{DM}) = \frac{1}{Z_r} \left(\tilde{E}_{DM} - \frac{Z_{fs}}{2}\tilde{K}_r \right), \quad (16)$$

or, rearranging,

$$\tilde{K}_r = \frac{2\tilde{E}_{DM}}{2Z_r + Z_{fs}}. \quad (17)$$

The power dissipated by per unit area is then

$$\frac{P_r}{A} = \frac{Z_r}{2}|\tilde{K}_r|^2 = \frac{|\tilde{E}_{DM}|^2}{Z_{fs}} \frac{Z_{fs}/2Z_r}{(1 + Z_{fs}/2Z_r)^2}. \quad (18)$$

The power dissipation is maximized for sheet impedance $Z_r = Z_{fs}/2$. At this sheet impedance, the power dissipation is

$$\left. \frac{P_r}{A} \right|_{\max} = \frac{1}{4} \frac{|\tilde{E}_{DM}|^2}{Z_{fs}}. \quad (19)$$

Interestingly, though the dark-matter electric field is not a wave solution to Maxwell's equations in vacuum, the sheet impedance at maximum power dissipation is the same as the usual vacuum electromagnetic wave. We will explain this result further in terms of the dark-matter circuit model described in the next section.

b. Power Dissipation in Cavity Detector

Similar to equations (13) and (14), we may write the electric field produced by the sheet of impedance Z_c as

$$\vec{E}_c(y, t) = Re(\tilde{E}_c \exp(2\pi i \nu_{DM}^0(t - |y|/c)), \quad (20)$$

where

$$\tilde{E}_c = -Z_{fs}\tilde{K}_c/2. \quad (21)$$

Again, we have set the position of this sheet to $y = 0$. We may write the electric field produced by the perfectly conducting sheet as

$$\vec{E}_\infty(y, t) = Re(\tilde{E}_\infty \exp(2\pi i \nu_{DM}^0(t - |y - L|/c)), \quad (22)$$

where

$$\tilde{E}_\infty = -Z_{fs}\tilde{K}_\infty/2. \quad (23)$$

Since the electric field must vanish at the conductor, we have

$$\tilde{E}_\infty + \tilde{E}_{\text{DM}} + \tilde{E}_c \exp(-2\pi i \nu_{\text{DM}}^0 L/c) = 0. \quad (24)$$

Ohm's Law gives

$$\tilde{K}_c = \frac{1}{Z_c} \left(\tilde{E}_c + \tilde{E}_\infty \exp(-2\pi i \nu_{\text{DM}}^0 L/c) + \tilde{E}_{\text{DM}} \right). \quad (25)$$

We have four equations (21), (23), (24)-(25), and four unknowns, \tilde{E}_c , \tilde{E}_∞ , \tilde{K}_c , and \tilde{K}_∞ . The condition that the electric field must be continuous at each sheet, and zero at the perfect conductor, along with Ohm's Law (10) yields four equations. Solving the system gives the complex current amplitude on the sheet at $y = 0$,

$$\vec{K}_c = \frac{2(1 - \exp(-2\pi i \nu_{\text{DM}}^0 L/c)) \tilde{E}_{\text{DM}}}{2Z_c + Z_{fs}(1 - \exp(-4\pi i \nu_{\text{DM}}^0 L/c))}, \quad (26)$$

and a power dissipation per unit area of

$$\frac{P_c}{A} = \frac{|\tilde{E}_{\text{DM}}|^2}{Z_{fs}} \frac{(Z_{fs}/2Z_c) |1 - \exp(-2\pi i \nu_{\text{DM}}^0 L/c)|^2}{|1 + (Z_{fs}/2Z_c)(1 - \exp(-4\pi i \nu_{\text{DM}}^0 L/c))|^2}. \quad (27)$$

For dark-matter resonance frequencies close to resonance, $\nu_{\text{DM}}^0 \approx \nu_r = c/2L$, this equation may be expanded as

$$\frac{P_c}{A} \approx \frac{|\tilde{E}_{\text{DM}}|^2}{Z_{fs}} \frac{4(Z_{fs}/2Z_c)}{|1 + 2\pi i (Z_{fs}/2Z_c)(\nu_{\text{DM}}^0 - \nu_r)/\nu_r|^2} = \frac{4}{\pi} \frac{|\tilde{E}_{\text{DM}}|^2}{Z_{fs}} \frac{Q}{|1 + 2iQ(\nu_{\text{DM}}^0 - \nu_r)/\nu_r|^2}. \quad (28)$$

The response is a Lorentzian, as would be expected, and the quality factor of the cavity, as determined by the full width at half maximum, is $Q = \pi Z_{fs}/2Z_c$. For an on-resonance dark-matter signal, the power dissipation increases linearly linearly in Q . Taking the limit $Q \rightarrow \infty$ (sheet impedance to zero), it seems that arbitrarily large amounts of power can be dissipated. Of course, this is unphysical. Two assumptions that we have made break down. First, for high quality factors giving cavity linewidths narrower than the dark-matter linewidth ($Q \gtrsim 10^6$), not all parts of the dark-matter spectrum are fully rung up. A more complicated calculation, in which the shape of the dark-matter spectrum is convolved with the resonator response, is needed to calculate the power dissipation. Such a calculation is carried out in Sec. IV. Second, power conservation dictates that at some quality factor, we must begin to backact on the dark-matter electric field, producing enough dark matter through the electromagnetic interaction to locally change the value of the dark-matter density and effectively modify the value of \tilde{E}_{DM} . Understanding the conditions for backaction

requires us to understand the impedance properties of the dark-matter electromagnetic interaction. This topic is treated in ref. [23]. There, it is proved rigorously that, for transverse dark-matter modes (hidden photons propagating in a direction transverse to their polarization, or axions propagating transverse to the applied field), that backaction can be neglected for typical resonator quality factors $Q \lesssim 10^6$. The loss required to backact on the dark-matter drive field is far too low to be achieved in practice.

To perform the sensitivity comparison between the resistive broadband and cavity detectors, we assume that the rest-mass frequency is unknown. We set a search band between frequencies ν_l and ν_h and calculate the SNR from a dark-matter electric field \tilde{E}_{DM} causing power dissipation in the detector. (\tilde{E}_{DM} may be dependent on the frequency of the dark matter. However, for the purpose of sensitivity comparison, this will not be relevant, so we do not explicitly include it.) While the broadband detector will not change during the search, always being set to the optimal sheet impedance $Z_r = Z_{fs}/2$, the cavity resonance frequency will be stepped between ν_l and ν_h .

We can set the total system noise power P_n to be the same in the broadband search and on-resonance in the cavity for an apples-to-apples comparison of scan sensitivity. The impedance of the cavity in Fig. 2b is real on resonance, and the impedance of the resistance in Fig. 2a is real at all frequencies. We assume that the temperature of the resistance in both cases is the same. We further assume that the added noise power from the device reading out the power dissipation – that is by the bolometer or amplifier – is the same in both cases. In particular, for amplifier readout, we assume that the minimum noise temperature is the same and that the amplifier is noise-matched and impedance-matched (so as to prevent unwanted reflections) to the detector. The total system noise in both experiments, P_n , is dominated by the sum of the thermal Johnson-Nyquist noise power and the noise power added by the device reading out the power dissipation, allowing us to set P_n to be the same.

Additionally, we set the total experiment time, for each experiment, at T_{tot} . We assume that the total experiment time is large enough such that the cavity can ring up at every tuning step and so that the dark-matter signal can be resolved in a Fourier spectrum; the former requires time $\sim Q/\nu_r$ while the latter requires time $\sim 10^6/\nu_{\text{DM}}^0$. We also assume that the tuning time is negligible compared to the integration time at each step.

The Dicke radiometer equation [21, 33] gives the SNR in power (as opposed to amplitude)

for each experiment

$$SNR(\nu_{\text{DM}}^0) \approx \frac{P_{\text{diss}}}{P_n} \sqrt{\Delta\nu_{\text{DM}}(\nu_{\text{DM}}^0)T(\nu_{\text{DM}}^0)}, \quad (29)$$

where P_{diss} ($= P_r$ or P_c) is the power dissipated in the experiment and $T(\nu_{\text{DM}}^0)$ is the integration time at dark-matter frequency ν_{DM}^0 . For the broadband search, this integration time is simply the total experiment time T_{tot} , while for the cavity detector, it can be taken as the amount of time during which the dark-matter frequency ν_{DM}^0 is within the bandwidth of the resonator, Δt_0 . By using signal information only within the bandwidth of the resonator, we discard valuable information outside of the resonator bandwidth. We will make optimal use of information at all frequencies in later sections, but not in this preliminary calculation. The ratio of the SNRs for the cavity and resistive broadband detectors is then

$$\frac{SNR_c(\nu_{\text{DM}}^0)}{SNR_r(\nu_{\text{DM}}^0)} \approx \frac{P_c}{P_r} \sqrt{\frac{\Delta t_0}{T_{\text{tot}}}} = \frac{16Q}{\pi} \sqrt{\frac{\Delta t_0}{T_{\text{tot}}}}, \quad (30)$$

where, in the second equality, we have used eqs. (19) and (27).

If, in the cavity search, we spend an equal time Δt_0 at each frequency and step at one part in Q , the total integration time can be taken as the Δt_0 times the number of frequency steps between ν_l and ν_h . For broad scans ($\nu_h \gtrsim 2\nu_l$), the number of frequency steps can be approximated as an integral, so

$$\frac{T_{\text{tot}}}{\Delta t_0} \approx \int_{\nu_l}^{\nu_h} \frac{Q}{\nu} d\nu = Q \ln \frac{\nu_h}{\nu_l} \sim Q. \quad (31)$$

The SNR ratio in (30) then varies with Q as

$$\frac{SNR_c(\nu_{\text{DM}}^0)}{SNR_r(\nu_{\text{DM}}^0)} \sim \sqrt{Q}. \quad (32)$$

This demonstrates that high- Q cavities are superior to resistive broadband searches for dark matter, even if information outside of the resonator bandwidth is not used. The advantage of high- Q searches will be even larger if information outside of the bandwidth is used, as will be shown later. The SNR in power varies as square root of quality factor. This, in turn, implies that the minimum dark-matter coupling ($g_{a\gamma\gamma}$ for the axion and ε for the hidden photon) to which the cavity is sensitive scales as $Q^{-1/4}$. The result may have been intuited from the form of the Dicke radiometer equation: an experiment gains sensitivity much faster with higher signal power (linear relationship) than with longer integration time (square root relationship). Interestingly, as we will show in Sec. VI, the scaling even applies when the

quality factor is larger than the characteristic 10^6 quality factor of the dark-matter signal, for which resonator response and dark-matter spectrum must be convolved.

Our calculation of the cavity response makes clear the following: the dark-matter electric field and the electric fields that are produced in response act on both the sheet of finite conductivity and the sheet of infinite conductivity. That is, they act on both the power detector and the “reflector.” In this sense, we can apply the insights made here to the dish antenna experiment in [37]. In that work, the authors propose to use a spherical reflecting dish to focus the electric field signal induced by dark matter onto a power detector. The authors consider reflection at the dish; radiation and absorption at the feed (the detector) is ignored. However, as we have shown, such a consideration can be critical to calculating accurate response. We must carefully consider the impedance properties of the feed and the feed’s direct interaction with the dark-matter electric field \vec{E}_{DM} , in addition to the analogous characteristics of the dish. There are two electrical boundary conditions, one at the mirror and one at the feed, which sets intrinsic length and frequency scales for the experiment. Thus, the frequency response of a dish antenna experiment is not a broadband flat spectrum, but has significant frequency-dependence.

High-Q resonators are also superior to reactive broadband searches at all frequencies at which a resonator can practically be made. We show this explicitly in Appendix G where we compare a series RLC circuit read out by a flux-to-voltage amplifier (e.g. a SQUID) to a broadband LR circuit. We leave the quantitative details for later in the paper, after we have introduced the machinery needed to understand the comparison more completely. This will give greater depth to our result, allowing us to rigorously consider the effects of thermal noise, and also illustrate the full power of sensitivity outside of the resonator bandwidth. The result is in direct contrast to that in [22], which claims a frequency range in which a broadband search has superior sensitivity.

The comparison of resonant and broadband detection illustrates important differences between absorption of vacuum electric fields governed by the unmodified Maxwell’s equations and absorption of electric fields sourced by dark matter. One cause of this difference is that the electric field induced by dark matter is spatially uniform (and has a single phase) as long as the experimental dimensions are small as compared to the de Broglie wavelength. In contrast, consider a transverse vacuum electromagnetic wave of frequency ν (solving Maxwell’s equations) propagating in the \hat{y} direction linearly polarized in the \hat{z} direction.

Suppose that at the sheet at $z = 0$, the complex electric field amplitude for the incident wave is \tilde{E}_I . Then, the power dissipated in the cavity will be

$$\frac{P_c}{A} = \frac{|\tilde{E}_I|^2}{Z_{fs}} \frac{(Z_{fs}/2Z_c)|1 - \exp(-4\pi i\nu L/c)|^2}{|1 + (Z_{fs}/2Z_c)(1 - \exp(-4\pi i\nu L/c))|^2}. \quad (33)$$

The difference in the numerator of the right-hand side of (33), relative to (27), ($4\pi i\nu$ vs. $2\pi i\nu$) arises from the $2\pi\nu L/c$ phase shift of the incident visible electromagnetic field between the two sheets. When the cavity is a half-wavelength at frequency ν , the power dissipation vanishes. The phase shift results in destructive interference of the electromagnetic waves radiated by the sheets with the incident drive field, and consequently, no signal. The visible signal absorption is minimized at precisely the spacing that maximizes the dark-matter signal absorption. Furthermore, one can easily show that the absorption of a visible signal is maximized when the separation of the sheets is a quarter-wavelength at frequency ν and $Z_c = Z_{fs}$. The quarter-wavelength transforms the short (the perfect conductor) into an open, so that all power available in the wave will be absorbed in the sheet if impedance-matched to free space. However, this power per unit area is $|\tilde{E}_I|^2/2Z_{fs}$, which is only a factor of two larger than that absorbed by the purely resistive broadband detector (see eq. (19)). There is no large parametric improvement in the absorption of a visible signal due to the quarter-wave spacing, e.g. no dependence on a small value of Z_c as in (27), over the purely resistive broadband detector. This extra factor of two occurs only within a narrow bandwidth. While a quarter-wave transformer may seem like a natural choice for boosting sensitivity to dark matter, given the match to Maxwellian electromagnetic waves, that is not the case; the half-wave cavity is parametrically enhanced for the absorption of dark-matter signals.

A second disinction in the absorption comes from the assumption that the dark-matter electric field can be treated as stiff. This begs the question: what is required to optimally couple power from the dark-matter signal? How do we impedance match to it and how should this inform detection schemes? We now investigate more closely the optimal scheme for coupling to the dark matter—that is, the optimal coupling element in the Signal Source of Fig. 1.

III. COUPLING TO THE DARK-MATTER SIGNAL

In Sec. III A, we show, based on the concept of impedance matching, that inductively-coupled detectors (or more generally, detectors that can be modeled as coupling to dark matter through an inductance) are optimal. We explain why single-pole resonators are a relatively efficient impedance match to the dark-matter source. In Sec. III B, we provide examples of single-pole resonators being used for dark-matter searches. The presentation of these examples naturally leads to the scattering matrix formalism of Section IV, which is used to analyze SNR in inductively coupled detectors.

A. Optimizing the Coupling Element

As discussed in the introduction, we may couple to the electric field induced by dark matter via a resistance or capacitance, or couple to the magnetic field induced by dark matter via an inductance. Here, we investigate which of these three couplings is fundamentally best for an experimental search.

A critical measure of a detector's suitability for a sensitive search is its ability to extract power from the dark-matter field. Ideally, the detector would be able to absorb all of the available power. In traditional forms of electromagnetic detection, designing a detector to absorb maximal power is known as impedance matching, and the optimal impedance match is achieved by setting the detector impedance equal to the complex conjugate of the source impedance. To optimize a light-field dark-matter detector, one must then understand the source impedance properties of the dark-matter field.

Such an exploration is carried out in ref. [23]. We refer the reader there for a detailed discussion of the dark-matter source. Here, we apply the results of that paper to the present work. Signals described by Maxwell's equations are often characterized by developing circuit models for the detection process. However, by virtue of the interaction terms (1) and (2), dark-matter electrodynamics is governed by *modifications* to Maxwell's equations and cannot be represented with traditional circuit models. In ref. [23], extended circuit models are developed that take into account these modifications to Maxwell's equations. It is demonstrated that the effective source impedance of dark matter is far lower than the free-space impedance $Z_{fs} \approx 377 \Omega$. Dark matter can be treated as a spectrum of dispersive waves

(see Appendix A 1, as well as [16]), following dispersion relation (A3). For a hidden photon with transverse polarization, whose mixing angle is ε and whose frequency and wavenumber are $\nu(k)$ and k , respectively, ref. [23] shows that the effective source impedance is

$$Z_{DM}^s(k, \nu(k)) = \varepsilon^2 Z_{fs} \frac{2\pi\nu(k)}{kc} \approx \varepsilon^2 Z_{fs} \frac{c}{v}, \quad (34)$$

where the approximation holds in the non-relativistic limit, and $v = \hbar k / m_{DM}$ is the hidden photon velocity. The equivalent expression for the axion is given by replacing the hidden-photon mixing angle with an analogous “axion mixing angle”, quantifying axion-to-photon conversion in a background magnetic field of magnitude B_0 ⁴. The axion mixing angle is defined as

$$\varepsilon_a \equiv \frac{\kappa_a c B_0}{m_{DM} c / \hbar}, \quad (35)$$

where κ_a is as defined in eq. (8). For a virialized QCD axion in a $B_0 = 10$ T magnetic field, $\varepsilon_a \sim 10^{-16}$, so the axion source impedance is ~ 29 orders of magnitude lower than the free-space impedance! Such a low source impedance may have been expected from the weak coupling of dark matter to photons and in turn, to electronic charges and currents.

The low source impedance has important consequences for the sensitivity comparison in Section II. A broadband resistive sheet, like that shown in Fig. 2a, is an efficient radiator of visible photons, which possess wave impedance Z_{fs} . We term these waves “visible waves” to distinguish them from the dark-matter waves. Because the visible waves possess much higher impedance than the dark-matter electromagnetic signal, they exert an enormous “drag” on the electrons in the sheet. This limits power absorption from the dark matter, and consequently, the experimental sensitivity. A similar argument may be used if the resistive sheet is coupled to an arbitrary network of lumped elements (assuming that none of these elements are also driven by the dark-matter field); the resistive sheet, driven by the dark matter, radiates visible waves, which prevents power absorption.

In a resistive coupling, one must thus decouple radiated visible waves from the detector using multiple sheet resistors. This is precisely what the half-wave cavity of Fig. 2b does. The π phase shift that a visible wave radiated from one sheet accrues in propagating to the other sheet causes destructive interference of the two sheets’ radiated visible waves. The

⁴For an axion, an effective transverse mode is defined by the relative orientations of the uniform applied magnetic field and the direction of propagation. The “transverse” axion possesses a direction of propagation orthogonal to the applied field, while a “longitudinal” axion possesses a direction of propagation that is parallel.

dark-matter signal then provides the only force on the electrons, and efficient power absorption can be obtained. Consequently, the half-wave resonator is superior to a broadband resistive sheet or any resistive sheet coupled to a network of lumped elements. Ref. [23] shows that the half-wave resonator can, in principle, couple to as much as 1/2 of the power in a monochromatic, transverse dark-matter wave.

We conclude that we require a distributed structure of multiple resistive sheets in order to achieve efficient matching, which introduces a large reactance into the equivalent circuit model.

One may alternatively couple to the dark-matter source using a lumped inductive or capacitive coupling. Unlike sheet resistors, ideal lumped elements do not radiate and therefore, radiated visible waves do not present a challenge to detection. However, the dark-matter source impedance, when referred as an equivalent resistor (with real-valued impedance) in series with the pickup inductor/capacitor, is very low; it is much lower than the self-impedance of the coupling element. The self-impedance of the inductor or capacitor acts as a similar drag on electrons, limiting power absorption. One must therefore null the self-impedance, which means that the net reactance of the detector must be zero. On resonance, lumped LC resonators possess zero reactance. Like the half-wave resonator, they can also couple to as much as 1/2 of the power in a monochromatic, transverse dark-matter wave. *Resonators can thus be an efficient impedance match to the dark-matter signal*, whether they are free-space resonators formed by multiple conductors, or lumped-element resonators.

Nevertheless, because of the extremely low dark-matter source impedance, the intrinsic detector loss required for any detector (resonant or otherwise) to match to, and thus backact on, the dark matter is far lower than may be practically achieved. For instance, a cavity resonator requires a quality factor of $\sim 10^{29}$ to achieve optimal match to the QCD axion in a 10 T magnetic field. We may thus treat the dark-matter source as stiff. Having justified the stiff-source approximation, it is useful to think of the dark-matter source as stiff electromagnetic charge and current densities (the interaction basis for the hidden photon), as mentioned in Section I. These charge and current densities source stiff electric and magnetic fields. The charge/current representation differs from the direct electromagnetic field representation used in Section II, but we stress that the two are physically equivalent. The effects of the charge density are suppressed by the $\sim 10^{-3}$ virial velocity, so we focus only on the current density. See Appendix A 2 and refs. [16, 38] for a discussion of the current

density.

The resistively coupled distributed cavity structures and the lumped-element detectors discussed above are related in that they may be modeled as coupling to the dark-matter effective current through an equivalent circuit reactance (an inductance or capacitance). This is apparent for the inductively and capacitively coupled lumped-element detector, as well as any distributed-element counterpart.

The half-wave, resistively coupled cavity resonator may be modeled as an equivalent lumped RLC circuit. The electric and magnetic field energies contained in the cavity can be mapped onto electric and magnetic fields stored in capacitors and inductors. One may treat the effective current density as driving the capacitance, inductance, or both, as long as the excitation is treated appropriately [39]. More generally, for a resistive coupling with a distributed structure, one may treat the dark-matter effective current as driving the LC cavity modes of the structure. It is critical to note that the detector is not simply the resistive sheet, but the *entire* structure. Consider, for instance, a resistive sheet placed within an electromagnetic shield, where the signal read out by the observer is the power dissipation in the sheet. The shield acts as a cavity, and therefore, its internal electromagnetic fields can be decomposed into an orthonormal basis of modes. Each cavity mode can be treated as an equivalent RLC circuit, and the dark-matter effective current, on- or off-resonance, may be chosen to drive either the inductance or capacitance of each of these circuits. [36, 40] The resistive sheet inside the cavity acts as the dissipation mechanism (the "R" of the RLC) for each of these modes. For each mode, the excitation from dark matter results in some complex-valued electric field amplitude at the surface of the broadband sheet. The total electric field at the sheet surface is a coherent sum, over all modes, of these electric field amplitudes. In other words, the total electric field—and thus, the power dissipation signal—is determined by filtered summation of all LC cavity excitations. Thus, the detector may again be treated as being driven by dark matter through equivalent reactances.

We conclude that the optimal coupling element is thus inductive or capacitive. The same conclusion is reached more rigorously and quantitatively in ref. [23]. Should we choose inductive or capacitive coupling? An important role is played by electromagnetic shielding, which is necessary to avoid unwanted interference and dissipation.

In the limit where the size of the detector and shield are much smaller than the Compton wavelength (the lumped-element limit), the current may be treated quasi-statically. The

size of the magnetic field produced by the current is then much larger than the electric field (in terms of energy). Thus, the optimal detector in the lumped-element limit couples to dark matter via an inductance rather than a capacitance. The excitation of the capacitor is negligible.

In the limit where the size of the detector and shield are comparable to the Compton wavelength (the cavity limit), the magnetic field and electric field are comparable in size. If using lumped-element detectors, one could couple to either a capacitance or an inductance. There is no advantage either way. However, due to the challenge of significant stray impedances in this limit, it is common not to use lumped-element couplings, but rather mode couplings, e.g. a resonant free-space cavity. As discussed above, we can model its equivalent RLC circuit as being excited either electrically or magnetically (or both). Thus, without loss of generality, we can choose to model a cavity-limit circuit as coupling to an inductance, as in the case of the lumped-element limit.

For the remainder of the paper, we will focus on inductively coupled detectors, since they are appropriate for modeling both the lumped-element and cavity limit. Where useful, we will also point out equivalent results for capacitively coupled detectors.

We will now develop the SNR framework to optimize the impedance-matching network and readout, represented by the second and third boxes of Fig. 1. The analysis will culminate in a limit on detection sensitivity set by the Bode-Fano criterion. The limit will demonstrate the relatively high efficiency of searches with single-pole resonators. In other words, we will show that these resonators are near ideal for single-moded detection.

First, to enable a practical understanding of the broadly applicable SNR framework, we give some concrete examples of single-pole resonators that may be analyzed with the described framework. Our examples will span Sections III B and IV A. Section IV B lays the foundations for the more general treatment of any inductively coupled detector.

B. Single-Pole Resonant Receiver Circuits for Axion and Hidden-Photon Detection

Two implementations of resonant receiver circuits are shown in Fig. 3. For frequencies below ~ 1 GHz, the signal may be amplified with a Superconducting Quantum Interference Device (SQUID). [16] This detection scheme is displayed in the left panel of the figure. The

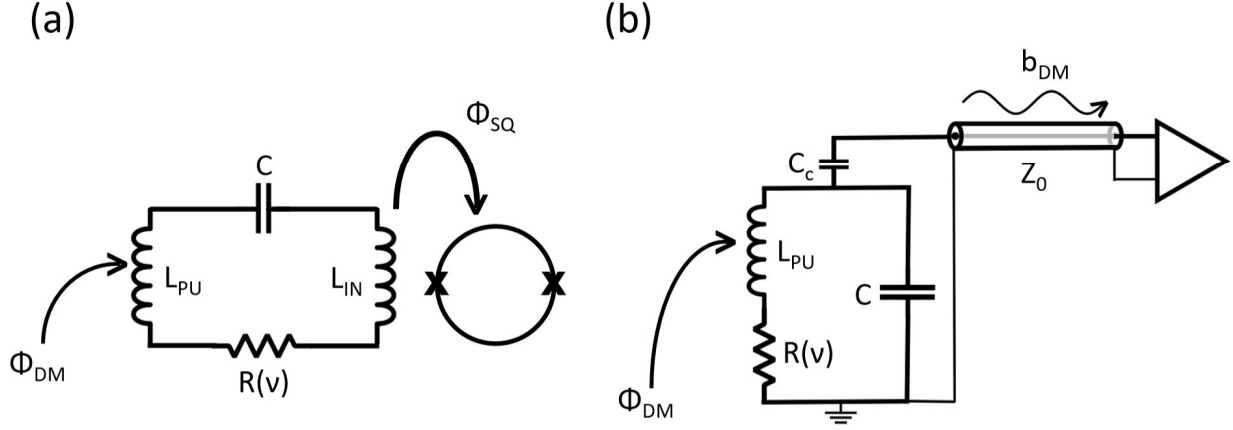


FIG. 3. Two implementations of a single-pole resonator for dark-matter detection. (a) A low-frequency detection circuit using a SQUID magnetometer. Dark matter induces a flux Φ_{DM} through the pickup inductor L_{PU} , which drives a current in the resonant circuit. The current is read out as a flux signal Φ_{SQ} in a magnetometer, coupled through the input coil L_{IN} . The flux to the magnetometer is usually coupled through a flux transformer (not shown). The magnetometer may be a dc SQUID (shown) or a single-junction dissipationless rf SQUID without resistive shunts, which can enable larger circuit Q . (b) Microwave/RF detection scheme with controlled impedances. Dark matter induces a magnetic flux through the equivalent circuit pickup inductor L_{PU} , which drives an equivalent series voltage in the resonant circuit. Power from this voltage signal propagates through a transmission line of impedance Z_0 , as represented by the wave b_{DM} , and is amplified with a microwave amplifier.

dark-matter effective current, through its induced magnetic field, feeds a flux Φ_{DM} through the pickup inductor L_{PU} . Since the effective current densities in practical circuits are stiff, this flux can be treated as stiff. The flux produces a resonantly enhanced current in the input coil L_{IN} and a flux in the SQUID. The SQUID provides high gain with near-quantum-limited noise performance, which allows this flux signal to be read out at high signal-to-noise. [41] The SQUID may be a dc SQUID, or if a larger circuit Q is desired, a single junction dissipationless rf SQUID [42]. This detection scheme is used in DM Radio and ADMX LC. [16, 19, 20] One could also remove the capacitor and do a broadband search [22].

For frequencies above ~ 1 GHz, a system with controlled impedances must be used; otherwise, reflections in wires create challenges toward efficient dark-matter detection. In this

case, the resonant RLC circuit, which may be a free-space cavity ⁵, is coupled (represented in the right panel with a coupling capacitance C_c) to a transmission line of characteristic impedance Z_0 (typically 50 ohms). A voltage signal generated in the resonator from the external, dark-matter-induced flux propagates to the input of an RF amplifier, as represented by the wave b_{DM} . This wave is amplified and read out with further electronics. Such a scheme is presently utilized by ADMX and HAYSTAC, which use near-quantum-limited microstrip SQUID amplifiers [43] and Josephson parametric amplifiers [30] to achieve exquisite sensitivity in the search for dark-matter axions. [17, 18] The resonant circuit is also a suitable description of a dielectric resonator, such as that in the MADMAX experiment, or a resonator with a mechanical element, such as a piezoelectric.

In both circuit models, the resonance frequency may be tuned by changing the capacitance C . One may then search over large range of dark-matter mass by scanning the resonance frequency.

Here, we analyze the second circuit in detail. The case of a search using a generic quantum-limited flux-to-voltage amplifier is covered in the appendix; the key results are the same as for the near-quantum-limited, scattering-mode amplification scheme.

The detector, as drawn, has resonance frequency $\nu_r = 1/(2\pi\sqrt{L_{\text{PU}}(C + C_c)})$. The quality factor Q of the resonator is determined by two sources of loss. First, resonator energy is lost by dissipation in the resistance $R(\nu)$. This frequency-dependent resistance represents internal losses of the resonator due to loss in metals or loss in the quasiparticle system (if superconductors are used), loss in wire insulation (in the case of lumped-element inductor coils), loss by coupling to parasitic electromagnetic modes, and loss in dielectrics. Second, resonator energy is lost by power flow into the transmission line. The resonator quality factor is thus

$$Q = (Q_{\text{int}}^{-1} + Q_{\text{cpl}}^{-1})^{-1}, \quad (36)$$

where the internal quality factor is

$$Q_{\text{int}} = 2\pi\nu_r L_{\text{PU}}/R(\nu_r), \quad (37)$$

and the coupled quality factor, representing losses to the transmission line, is

$$Q_{\text{cpl}} = \frac{1}{(2\pi\nu_r C_c)^2 Z_0 (2\pi\nu_r L_{\text{PU}})}. \quad (38)$$

⁵In terms of impedance, one mode of a free-space cavity can be represented as an equivalent lumped-LC circuit.

The resonator is driven by three voltage sources: a thermal noise voltage, a zero-point effective-fluctuation-noise voltage, and a dark-matter signal voltage. The two noise voltages, sourced by the resistor in the equivalent circuit model of Fig. 3, are lumped together in the calculations that follow. The dark-matter signal voltage may be represented by a voltage in series with the inductor. Dark matter of mass m_{DM} couples into the pickup loop L_{PU} through its induced magnetic field. The magnetic field, oscillating at frequency ν_{DM}^0 , produces a circuit voltage via Faraday’s Law $V = d\Phi/dt$. This stiff voltage can be treated classically, owing to the high number density of the light-field dark matter. Additionally, due to virialization, the dark-matter voltage signal possesses a nonzero bandwidth. This bandwidth was introduced in equation (3) and is $\Delta\nu_{\text{DM}}(\nu_{\text{DM}}^0) \sim 10^{-6}\nu_{\text{DM}}^0$. In Section IV, we discuss how the voltage spectrum scales with the dark-matter coupling to electromagnetism (quantified by $g_{a\gamma\gamma}$ in the case of the axion and ε in the case of the hidden photon); we also show how it is related to the dark-matter energy density distribution over frequency, which in turn, can be calculated from the more familiar dark-matter energy density distribution over velocity. (See Appendix D.) For the more quantitative treatments and in particular, the integral approximations, that follow in Sections IV and V, we will also need to define a “cutoff” bandwidth $\Delta\nu_{\text{DM}}^c(\nu_{\text{DM}}^0)$. We define this cutoff bandwidth such that, outside of the frequency band $\nu_{\text{DM}}^0 \leq \nu \leq \nu_{\text{DM}}^0 + \Delta\nu_{\text{DM}}^c(\nu_{\text{DM}}^0)$, the dark-matter signal power is small enough to be neglected. Because we are searching for nonrelativistic dark matter, we take this bandwidth to satisfy

$$\Delta\nu_{\text{DM}}(\nu_{\text{DM}}^0) \ll \Delta\nu_{\text{DM}}^c(\nu_{\text{DM}}^0) \ll \nu_{\text{DM}}^0. \quad (39)$$

As we will see, this cutoff bandwidth is needed to facilitate the calculations, but its exact value is unimportant, as long as this inequality is satisfied. For more information regarding dark-matter bandwidths and their relation to velocity, see Appendices A and C. Where convenient, we will suppress the bandwidth’s dependence on search frequency, with it implicitly understood.

The dark-matter signal at the amplifier input will be strongest when the transmission is largest: when ν_{DM}^0 lies within the resonator bandwidth. This observation suggests that a search should be conducted over a wide range of frequencies by scanning the resonance frequency ν_r (performed, e.g., via tuning of the capacitance) and amplifying the signal.

IV. SENSITIVITY CALCULATION OF A SEARCH FOR LIGHT-FIELD DARK MATTER

Before performing detailed calculations for the SNR of this detector, we qualitatively discuss the processing of the signal. This discussion applies not just to resonators, but to any detector; as such, our SNR treatment in this section will apply broadly. The dark-matter signal has a finite coherence time, set by the inverse of the dark-matter bandwidth, (see Appendix A 1)

$$\tau_{\text{coh}} \sim (\Delta\nu_{\text{DM}})^{-1} \sim 10^6/\nu_{\text{DM}}^0. \quad (40)$$

On timescales much shorter than the dark-matter coherence time, the dark-matter signal behaves as a monochromatic wave with frequency ν_{DM}^0 . In such a situation, one may determine if a timestream contains a signal by using a time-domain Wiener optimal filter [34]. This filter gives an estimate for the amplitude of the dark-matter signal if one exists in the timestream. If this amplitude is much greater than the uncertainty, set by the noise, then a candidate signal has been detected.

However, stronger constraints on coupling parameter space will require integration longer than this time. We assume here integration longer than the coherence time. Once the integration time has exceeded the dark-matter coherence time, the dark matter no longer behaves as a coherent amplitude signal, but rather, an incoherent power signal. Conceptually, an incoherent power signal can be processed using a Dicke radiometer, first described in [33]. A schematic diagram of a Dicke radiometer, as it pertains to our dark-matter receiver circuit, is shown in Fig. 4.

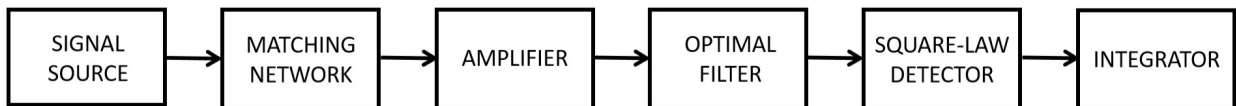


FIG. 4. Diagram showing the components of a Dicke radiometer.

As indicated in Fig. 1, the signals from the source, which, in this case are the dark-matter signal, thermal noise, and zero-point fluctuation noise, are fed into a matching network and read out with an amplifier. The output signal of the amplifier is sent to an optimal filter to maximize SNR and then to a square-law detector, whose output voltage is proportional to the

input power. This voltage is sent to an integrator. The square-law detector and integrator average down fluctuations in the noise power (i.e. thermal, zero-point fluctuation, and amplifier noise power), which sets the variance (uncertainty) in the measurement scheme. When power is observed in excess of the mean noise power, then a candidate dark-matter signal has been detected, and follow-up is required to validate or reject this signal. In a typical experiment, the output of the amplifier is fed into a computer, and the optimal filtering, square-law detection, and integration steps are executed in software.

The well known expression for the SNR of a Dicke radiometer is given by

$$SNR \approx \frac{P_{sig}}{P_n} \sqrt{\Delta\nu \cdot t}, \quad (41)$$

where $\Delta\nu$ is the signal bandwidth, t is the integration time, P_{sig} and P_n are, respectively the signal and mean noise power within that bandwidth.

Our analysis of optimal signal processing does not directly use this formula. However, it uses signal manipulation parallel to that implemented in a Dicke radiometer (amplification, square-law detection, integration) in order to provide a rigorous framework for understanding sensitivity in these receiver circuits. In particular, this framework will allow us to derive the optimal filter. It will enable us to consider the effects on SNR from scanning the resonance frequency or more generally, using information from multiple detection circuits. The method is easily extended to nonclassical detection schemes (e.g. squeezing and photon counting) that will be considered in Part II. Nevertheless, we will use (41) to build intuition about our results.

We begin by producing a scattering-matrix representation of the resonant circuit in the right panel of Fig. 3 (Sec. IV A). We then generalize this representation to any detection circuit with inductive coupling to the dark matter (Sec. IV B).

A. Scattering Representation of Resonant Detection Circuit

Expressing the resonant detection scheme in a scattering matrix representation gives rise to a simple method for analyzing the sensitivity. The detection schematic may be represented as a cascade of two separate two-port circuits, as shown in Fig. 5.

In the first of these two circuits (at the left), the resistance $R(\nu)$ is replaced by a semi-infinite, lossless transmission line of characteristic impedance $R(\nu)$; on this line, thermal

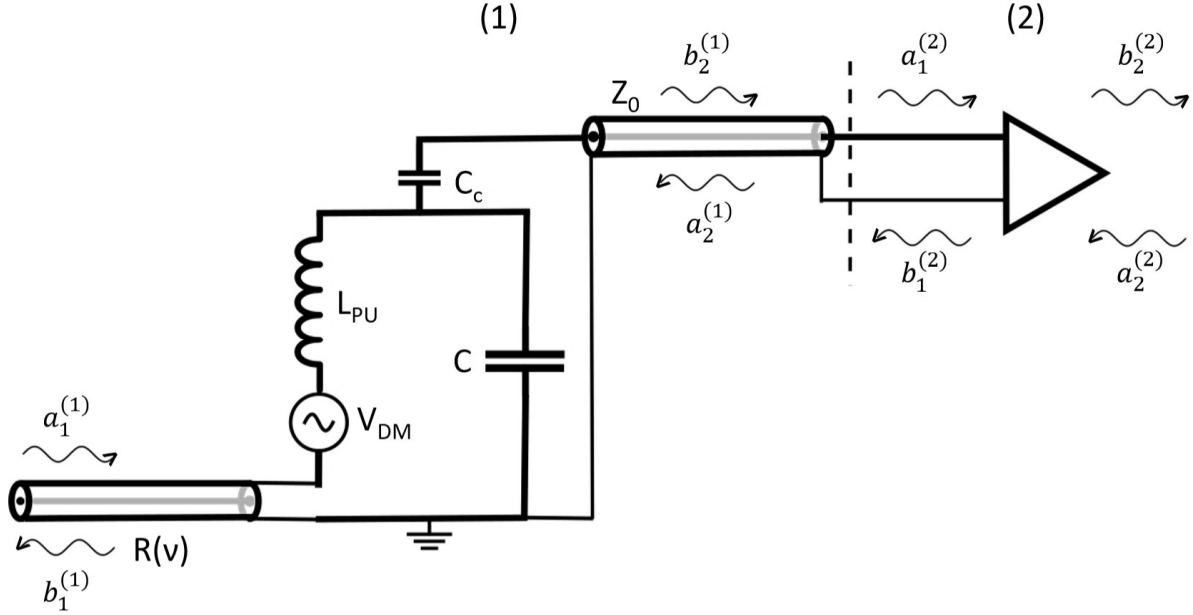


FIG. 5. Representation of detection circuit in Fig. 3 as a cascade of two-port circuits. The internal resistance R has been replaced with a semi-infinite transmission line, on which thermal noise is injected into the system and on which power is carried away from the resonator (equivalent to dissipation). The dark-matter signal, which is a magnetic flux through the inductor, is represented as a voltage in series with the inductor. Circuit (1) represents the resonator, while circuit (2) represents the amplifier. Because the amplifier does not perform a unitary transformation on the incoming waves, the outgoing waves must consist of noise waves generated by the amplifier.

noise and zero-point fluctuations are injected into the system. This is a typical representation in the quantum optics literature [44]. The dark-matter signal voltage V_{DM} in our model is in series with the inductor. The incoming and outgoing waves at each port in Fig. 5 are defined in the frequency domain by the complex phasors (in units $\sqrt{\text{Watts/Hz}}$)

$$a_1^{(1)}(\nu) = \frac{V_1(\nu) + I_1(\nu)R(\nu)}{2\sqrt{R(\nu)}} \quad (42)$$

$$a_2^{(1)}(\nu) = \frac{V_2(\nu) + I_2(\nu)Z_0}{2\sqrt{Z_0}} \quad (43)$$

$$b_1^{(1)}(\nu) = \frac{V_1(\nu) - I_1(\nu)R(\nu)}{2\sqrt{R(\nu)}} \quad (44)$$

$$b_2^{(1)}(\nu) = \frac{V_2(\nu) - I_2(\nu)Z_0}{2\sqrt{Z_0}} \quad (45)$$

where $V_{1,2}(\nu)$ and $I_{1,2}(\nu)$ are, respectively, input and output voltages and currents at the far ends of the two transmission lines. (Subscript 1 corresponds to the transmission line of impedance $R(\nu)$, and subscript 2 corresponds to the transmission line of impedance Z_0 .)

These wave amplitudes are related by

$$\begin{bmatrix} b_1^{(1)}(\nu) \\ b_2^{(1)}(\nu) \end{bmatrix} = \begin{bmatrix} S_{11}^{(1)}(\nu, \nu_r) & S_{12}^{(1)}(\nu, \nu_r) \\ S_{21}^{(1)}(\nu, \nu_r) & S_{22}^{(1)}(\nu, \nu_r) \end{bmatrix} \begin{bmatrix} a_1^{(1)}(\nu) \\ a_2^{(1)}(\nu) \end{bmatrix} + \begin{bmatrix} -\frac{S_{12}^{(1)}(\nu, \nu_r)}{2\sqrt{R(\nu)}} V_{\text{DM}}(\nu, g_{\text{DM}}, \frac{d\rho_{\text{DM}}}{d\nu}(\nu, \nu_{\text{DM}}^0)) \sqrt{\frac{Q_{\text{cpl}}}{Q_{\text{int}}}} \exp(+i\frac{2\pi\nu}{\bar{c}}l) \\ \frac{S_{21}^{(1)}(\nu, \nu_r)}{2\sqrt{R(\nu)}} V_{\text{DM}}(\nu, g_{\text{DM}}, \frac{d\rho_{\text{DM}}}{d\nu}(\nu, \nu_{\text{DM}}^0)) \end{bmatrix} \quad (46)$$

where

$$S_{11}^{(1)}(\nu, \nu_r) = \frac{Q_{\text{int}} - Q_{\text{cpl}} + 2iQ_{\text{int}}Q_{\text{cpl}}\left(\frac{\nu}{\nu_r} - 1\right)}{Q_{\text{int}} + Q_{\text{cpl}} + 2iQ_{\text{int}}Q_{\text{cpl}}\left(\frac{\nu}{\nu_r} - 1\right)} \quad (47)$$

$$S_{21}^{(1)}(\nu, \nu_r) = S_{12}^{(1)}(\nu, \nu_r) = \frac{2\sqrt{Q_{\text{int}}Q_{\text{cpl}}}}{Q_{\text{int}} + Q_{\text{cpl}} + 2iQ_{\text{int}}Q_{\text{cpl}}\left(\frac{\nu}{\nu_r} - 1\right)} \exp\left(-i\frac{2\pi\nu}{\bar{c}}l\right) \quad (48)$$

$$S_{22}^{(1)}(\nu, \nu_r) = \frac{Q_{\text{cpl}} - Q_{\text{int}} + 2iQ_{\text{int}}Q_{\text{cpl}}\left(\frac{\nu}{\nu_r} - 1\right)}{Q_{\text{int}} + Q_{\text{cpl}} + 2iQ_{\text{int}}Q_{\text{cpl}}\left(\frac{\nu}{\nu_r} - 1\right)} \exp\left(-i\frac{4\pi\nu}{\bar{c}}l\right) \quad (49)$$

are the scattering parameters for the circuit. l and \bar{c} are the length and phase velocity of the Z_0 transmission line. In deriving eqs. (47)-(49), we assume $|\nu - \nu_r| \ll \nu_r$; we also assume $Q, Q_{\text{int}} \gg 1$, and $2\pi\nu_r Z_0 C_c \gg 1$, which are typical design parameters for resonant circuits. In equation (46), $V_{\text{DM}}(\nu, g_{\text{DM}}, \frac{d\rho_{\text{DM}}}{d\nu}(\nu, \nu_{\text{DM}}^0))$ represents the frequency component of the dark-matter voltage signal at frequency ν . The voltage spectrum depends on the distribution of dark-matter energy density over frequency, denoted by $\frac{d\rho_{\text{DM}}}{d\nu}(\nu, \nu_{\text{DM}}^0)$, which in turn, depends on the rest mass $m_{\text{DM}} = \frac{h\nu_{\text{DM}}^0}{c^2}$. The factor g_{DM} is related to the dark-matter coupling to electromagnetism. We now define this factor and show how V_{DM} can be related to the coupling and the distribution.

We will assume that, while the resonator is scanned near the dark-matter frequency, the amplitude of the dark-matter field (proportional to the local density) does not change. In the case of a hidden photon (vector) field, we also assume that its direction also does not change during this period of time. In Appendix B, we discuss deviations from this behavior, and its implications for scan strategy. There we will also discuss strategies to mitigate inevitable detector misalignment with a vector dark-matter field. We will further assume that the

distribution stays fixed during the scan. We discuss deviations from this assumption in the context of annual modulation in Appendix B. We also assume that the size of the resonant detector is much less than the coherence length $\sim 1000\lambda_{\text{DM}}^0$, so that spatial variations of the dark-matter field are inconsequential.

Under these assumptions, we may relate the spectral density of the voltage signal to the energy coupled into the dark-matter circuit by

$$\left| V_{\text{DM}} \left(\nu, g_{\text{DM}}, \frac{d\rho_{\text{DM}}}{d\nu}(\nu, \nu_{\text{DM}}^0) \right) \right|^2 = 2(2\pi\nu)^2 L_{\text{PU}} E_{\text{DM}} \left(\nu, g_{\text{DM}}, \frac{d\rho_{\text{DM}}}{d\nu}(\nu, \nu_{\text{DM}}^0) \right), \quad (50)$$

where $E_{\text{DM}}(\nu, \nu_{\text{DM}}^0)$ is an energy spectral density (in units of energy per unit bandwidth). $E_{\text{DM}}(\nu, \nu_{\text{DM}}^0)$ may be parametrized as

$$E_{\text{DM}} \left(\nu, g_{\text{DM}}, \frac{d\rho_{\text{DM}}}{d\nu}(\nu, \nu_{\text{DM}}^0) \right) = g_{\text{DM}}^2 V_{\text{PU}} \frac{d\rho_{\text{DM}}}{d\nu}(\nu, \nu_{\text{DM}}^0), \quad (51)$$

where V_{PU} is the volume of the pickup inductor⁶, and g_{DM} is the effective dimensionless coupling of the DM field to the detector.

Equation (51) is derived in Appendix A 2. The value of $g_{\text{DM}} = g_{\text{DM}}(\nu_{\text{DM}}^0)$ is

$$g_{\text{DM}} = \begin{cases} \kappa_a c B_0 c_{\text{PU}} V_{\text{PU}}^{1/3}, & \text{axions} \\ \varepsilon c_{\text{PU}} V_{\text{PU}}^{1/3} / \lambda_{\text{DM}}^0, & \text{hidden photons} \end{cases} \quad (52)$$

at frequencies for which the Compton wavelength λ_{DM}^0 is much longer than the characteristic size of the detector. For frequencies where the wavelength is comparable to the size of the detector,

$$g_{\text{DM}} = \begin{cases} \kappa_a c B_0 c_{\text{PU}} \lambda_{\text{DM}}^0, & \text{axions} \\ \varepsilon c_{\text{PU}}, & \text{hidden photons.} \end{cases} \quad (53)$$

We omit the explicit dependence of g_{DM} on dark-matter rest-mass frequency where convenient. c_{PU} is a geometrical factor relating to the pickup pattern and aspect ratio of the inductor and the shape of the drive field. In practice, it is determined by calibration and modeling of the detector geometry.

The energy-density distribution $d\rho_{\text{DM}}/d\nu$ has units of energy per-unit-volume per-unit-bandwidth and must satisfy

$$\int d\nu \frac{d\rho_{\text{DM}}}{d\nu}(\nu, \nu_{\text{DM}}^0) = \rho_{\text{DM}}, \quad (54)$$

⁶When a free-space cavity, rather than a lumped-element inductor, is used to couple to the signal, L_{PU} represents the equivalent inductance and V_{PU} represents the coupled volume for the mode under consideration.

where $\rho_{\text{DM}} \sim 0.3 \text{ GeV/cm}^3$ is the total local energy density. $d\rho_{\text{DM}}/d\nu$ can be calculated from the density distribution across velocity. As an example, in Appendix C, we calculate $d\rho_{\text{DM}}/d\nu$ explicitly for the standard halo model. For more details on the determination of the signal strength, see references [11, 16, 19].

It is shown in [23] that, at small velocities $\frac{v}{c} \ll \varepsilon^2$ (or equivalently for the axion, $\frac{v}{c} \ll \frac{\kappa_a c B_0}{m_{\text{DM}} c / \hbar}$), backaction is significant at any quality factor. It may thus seem that our equations (50) and (51) are inaccurate. However, given that the dark-matter virial velocity $v_{\text{virial}} \sim 10^{-3}c$ is much greater than ε^2 over all open parameter spaces, it is appropriate to assume that dark matter at these extremely small velocities makes up a very small component of the total dark-matter distribution. See, for instance, the standard halo model in Appendix C. Therefore, assuming the validity of (50) and (51) over all velocities, instead of only for those which satisfy $v/c \gtrsim \varepsilon^2$, will result in a negligible change in calculated SNR.

From equations (50) and (51), the voltage signal may be fully parametrized as

$$V_{\text{DM}} = V_{\text{DM}} \left(\nu, g_{\text{DM}}, \frac{d\rho_{\text{DM}}}{d\nu}(\nu, \nu_{\text{DM}}^0), L_{\text{PU}}, V_{\text{PU}} \right). \quad (55)$$

However, for brevity, we will truncate the dependence to

$$V_{\text{DM}} = V_{\text{DM}} \left(\nu, g_{\text{DM}}, \frac{d\rho_{\text{DM}}}{d\nu}(\nu, \nu_{\text{DM}}^0) \right). \quad (56)$$

Unlike L_{PU} and V_{PU} , which are parameters of the detection system, g_{DM} and $d\rho_{\text{DM}}/d\nu$ are model-dependent parameters.

An amplifier is represented in the second of the two two-port circuits. We will assume that the amplifier has perfect input and output match to the transmission line, i.e. its input impedance is Z_0 . Input and output match prevent the emergence of cavity modes on the transmission line, which complicate readout of the dark-matter signal. We will also assume that it possesses reverse isolation, so that waves incoming on the right port do not transmit to the resonant detector. Reverse isolation is an experimentally desired attribute for amplifiers, as it prevents heating of the resonator and interference due to spurious signals on the feedline. The amplifier is described by the following scattering relation for a signal at frequency ν :

$$\begin{bmatrix} b_1^{(2)}(\nu) \\ b_2^{(2)}(\nu) \end{bmatrix} = \begin{bmatrix} 0 & 0 \\ \sqrt{G(\nu)} & 0 \end{bmatrix} \begin{bmatrix} a_1^{(2)}(\nu) \\ a_2^{(2)}(\nu) \end{bmatrix} + \begin{bmatrix} c_1^{(2)}(\nu) \\ c_2^{(2)}(\nu) \end{bmatrix}, \quad (57)$$

where $|G(\nu)|$ is the power gain of the amplifier. $c_1^{(2)}(\nu)$ and $c_2^{(2)}(\nu)$ are, respectively, the backward and forward-traveling noise waves generated by the amplifier. A phase-insensitive amplifier must necessarily add such noise to the detection scheme [25]. The backward-traveling noise wave may be thought of as the backaction noise of the amplifier, while the forward-traveling noise wave is the intrinsic added noise, or in the language used in Section I, the imprecision noise. We will assume that the amplifier has high power gain $|G(\nu)| \gg 1$ over the entire search band such that we may ignore the noise introduced by follow-on electronics (e.g. further analog amplification and filtering, digitization). This condition may be realized by using different high power gain amplifiers in the different frequency regimes. A possible implementation of this is discussed in [16].

Combining equations (46) and (57) with the connection relations $a_1^{(2)}(\nu) = b_2^{(1)}(\nu)$ and $a_2^{(1)}(\nu) = b_1^{(2)}(\nu)$, we obtain the scattering relations for the cascaded circuit:

$$\begin{aligned} \begin{bmatrix} b_1^{(1)}(\nu) \\ b_2^{(2)}(\nu) \end{bmatrix} = & \begin{bmatrix} S_{11}^{(1)}(\nu, \nu_r) & 0 \\ \sqrt{G(\nu)} S_{21}^{(1)}(\nu, \nu_r) & 0 \end{bmatrix} \begin{bmatrix} a_1^{(1)}(\nu) \\ a_2^{(2)}(\nu) \end{bmatrix} \\ & + \begin{bmatrix} S_{12}^{(1)}(\nu, \nu_r) c_1^{(2)}(\nu) \\ \sqrt{G(\nu)} S_{22}^{(1)}(\nu, \nu_r) c_1^{(2)}(\nu) + c_2^{(2)}(\nu) \end{bmatrix} \\ & + \begin{bmatrix} -\frac{S_{12}^{(1)}(\nu, \nu_r)}{2\sqrt{R(\nu)}} V_{\text{DM}}(\nu, g_{\text{DM}}, \frac{d\rho_{\text{DM}}}{d\nu}(\nu, \nu_{\text{DM}}^0)) \sqrt{\frac{Q_{\text{cpl}}}{Q_{\text{int}}}} \exp(+i\frac{2\pi\nu}{c}l) \\ \sqrt{G(\nu)} \frac{S_{21}^{(1)}(\nu, \nu_r)}{2\sqrt{R(\nu)}} V_{\text{DM}}(\nu, g_{\text{DM}}, \frac{d\rho_{\text{DM}}}{d\nu}(\nu, \nu_{\text{DM}}^0)) \end{bmatrix}. \end{aligned} \quad (58)$$

The left-hand side of equation (58) is a single vector. The top term of this vector $b_1^{(1)}(\nu)$ represents the wave that is dissipated in the resonator. The bottom term $b_2^{(2)}(\nu)$ represents the wave that is amplified and read out with further electronics. The signal and noise content of $b_2^{(2)}(\nu)$ determines the sensitivity of the detector.

On the right-hand side of equation (58), there are three terms. The first term represents the response of the cascaded circuit to waves injected at the ports. Note that the response is independent of the incoming wave at port 2 of circuit (2); this is a result of reverse isolation. As stated before, $a_1^{(1)}(\nu)$ represents the thermal- and zero-point-fluctuation noise waves injected into the system. Assuming that the detector system is at temperature T , the noise correlation for this wave is

$$\langle a_1^{(1)}(\nu)(a_1^{(1)}(\nu'))^* \rangle = h\nu(n(\nu, T) + 1/2)\delta(\nu - \nu'), \quad (59)$$

where

$$n(\nu, T) = \frac{1}{\exp(h\nu/k_B T) - 1} \quad (60)$$

is the thermal occupation number of the resonator. We will suppress the dependence on temperature T where convenient. As stated before, we have lumped together the thermal and zero-point noise; in (59), the “ $n(\nu, T)$ ” term represents the thermal noise, while the “ $1/2$ ” term represents the zero-point fluctuations.

The second vector in equation represents the response of the circuit to amplifier noise. The top term is the backaction noise that is dissipated in the resonator. The bottom term is the sum of the intrinsic added noise and the backaction noise which is reflected at the resonator and transmitted through the amplifier. The amplifier noise is typically quantified by use of a 2×2 noise correlation matrix $C(\nu)$ with values given by

$$\langle c_i^{(2)}(\nu) c_j^{(2)}(\nu')^* \rangle = C_{ij}(\nu) \delta(\nu - \nu'), \quad (61)$$

where the values i and j are either 1 or 2. Note that $C_{12}(\nu) = C_{21}(\nu)^*$.

The third vector is the response of the circuit to the dark-matter signal. The top term is the portion of the signal that is dissipated in the resonator. The bottom term is the portion of the signal that is transmitted and amplified.

B. Scattering Representation of A Single-Moded Reactive Detector

As yet, we have not determined whether a single-pole resonator is an optimal detection circuit. We may generalize our treatment for the resonator to a single-moded, inductively coupled detector read out by a scattering-mode amplifier. The prescription for doing so is displayed in Fig. 6.

As in the case of the single-pole resonator, the dark-matter signal presents as a voltage in series with the pickup inductor L_{PU} , with spectrum described by (50) and (51). As before, we assume that the amplitude, frequency distribution, and direction of the dark-matter field are constant during the scan, and that the pickup inductor’s linear dimensions are much smaller than the coherence length. The inductor is inevitably accompanied by some loss, denoted as the frequency-dependent quantity $R(\nu)$. The resistance is replaced by a transmission line on which thermal noise and zero-point-fluctuation noise enter the system,

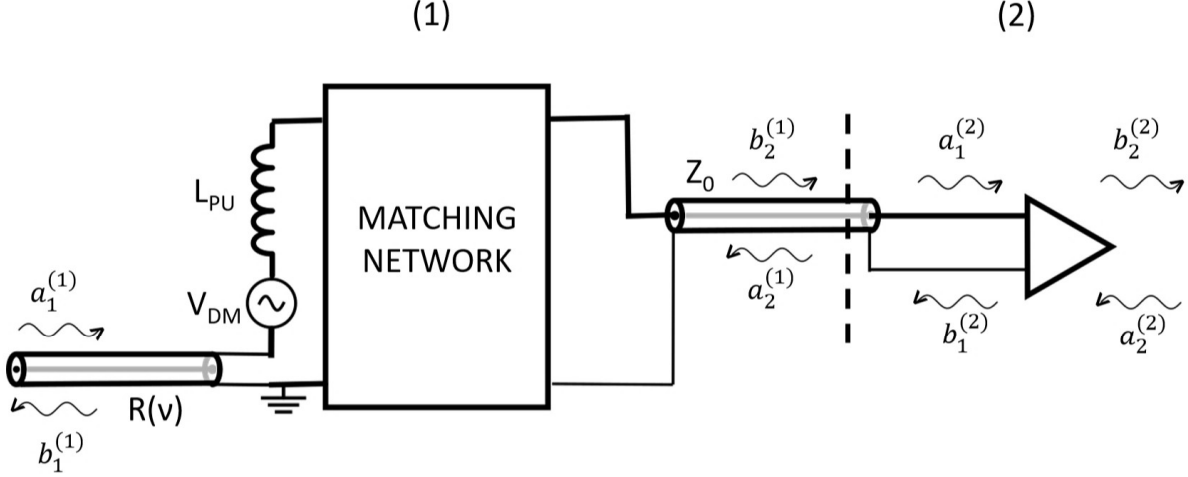


FIG. 6. Scattering representation of a generic inductively coupled detector as a cascade of two-port circuits. The signal source consists of a pickup inductor L_{PU} in series with a frequency-dependent resistance $R(\nu)$ representing loss in the circuit. The resistance has been replaced with a semi-infinite transmission line, on which thermal noise is injected into the system and on which power is carried away from the detector (equivalent to dissipation). The dark-matter signal, which is a magnetic flux through the inductor, is represented as a voltage in series with the inductor. These signals are fed into the amplifier through an impedance-matching network. Circuit (1) (to the left of the dashed line) represents the signal source and matching network, while circuit (2) represents the amplifier.

and on which power is carried away as dissipation. The signals are fed through the matching network to an amplifier.

The signal source and matching network are represented by one 2×2 scattering matrix, denoted here as $S^{(1)}(\nu)$:

$$S^{(1)}(\nu) = \begin{bmatrix} S_{11}^{(1)}(\nu) & S_{12}^{(1)}(\nu) \\ S_{21}^{(1)}(\nu) & S_{22}^{(1)}(\nu) \end{bmatrix}. \quad (62)$$

Recall that for a resonator, the values of this scattering matrix are given by (47), (48) and (49). We assume that all loss is contained within $R(\nu)$, so that the matching network itself is lossless. We further assume that the matching network is linear and contains only passive components. Then, $S^{(1)}(\nu)$ is unitary at each frequency ν :

$$S^{(1)}(\nu)[S^{(1)}(\nu)]^\dagger = I, \quad (63)$$

where I is the 2×2 identity matrix.

The amplifier is described by (57) and produces outgoing noise waves at both its input and output. In analogy with (58), it is straightforward to write an expression for the wave amplitude at the output of the amplifier:

$$b_2^{(2)}(\nu) = \sqrt{G(\nu)}S_{21}^{(1)}(\nu)a_1^{(1)}(\nu) + \sqrt{G(\nu)}S_{22}^{(1)}(\nu)c_1^{(2)}(\nu) + c_2^{(2)}(\nu) + \sqrt{G(\nu)}\frac{S_{21}^{(1)}(\nu)}{2\sqrt{R(\nu)}}V_{\text{DM}}\left(\nu, g_{\text{DM}}, \frac{d\rho_{\text{DM}}}{d\nu}(\nu, \nu_{\text{DM}}^0)\right), \quad (64)$$

where $a_1^{(1)}(\nu)$ obeys (59) and the amplifier noise waves obey (61).

We are now ready to develop the framework to determine the signal-to-noise ratio (SNR) for detectors with reactive coupling to the dark-matter signal. Our treatment will focus on statistical moments of the frequency components $b_2^{(2)}(\nu)$ at the output of the amplifier. See refs. [21] and [45] for a related analysis of thermal noise, photon noise and amplifier noise in astronomical receivers. This particular framework can be generalized to understand the performance using quantum measurement techniques, as will be done in Part II.

C. Signal-to-Noise Ratio of Search

We will calculate the SNR at a single dark-matter search frequency in two steps. In the first step, we calculate the SNR from a single circuit or a single instance of a tunable circuit. For example, for a tunable single-pole resonator, one instance consists of a single resonance frequency, which may or may not align with the dark-matter search frequency. In the second step, we discuss how information from multiple circuits or multiple circuit instances (e.g. many steps in resonance frequency in a tunable resonator) may be combined. We answer the question of how to calculate SNR from the combined datastream of multiple resonance frequencies or even two entirely different detection setups. The third and final part of this section is dedicated to specific results for quantum-limited amplifiers, which will be used extensively in the search optimization in Section V. We conclude with some implications for a scan, which will naturally introduce the value functions for the optimization.

1. SNR for single circuit configuration

Suppose we have a single circuit configuration (e.g. a single step in a tunable circuit) and we wish to test whether there is dark matter at frequency ν_{DM}^0 . At the output of the amplifier (including further electronics, e.g. room-temperature amplification and mixing), we receive a timestream of values $b(t)$, which is related to the frequency-domain function $b_2^{(2)}(\nu)$ by

$$b(t) = \int_0^\infty d\nu b_2^{(2)}(\nu) \exp(+i2\pi\nu t). \quad (65)$$

In the remainder of this section, we drop the subscript and superscript in $b_2^{(2)}(\nu)$, and simply write $b(\nu)$, unless otherwise stated (since the wave $b_1^{(1)}(\nu)$ does not affect the SNR, and will not be frequently considered). We write $b^n(\nu)$ to indicate solely the noise terms in $b(\nu)$ (in the absence of axion- or hidden-photon signal). We also drop the limits on the frequency integrals; $(0, +\infty)$ is implied.

The length τ of this timestream is assumed to be much longer than the dark-matter coherence time $t_{\text{coh}} \sim 10^6/\nu_{\text{DM}}^0$, as well as any characteristic time associated with the slowest pole in the circuit. We denote this characteristic time as t_{pole} ; it sets the time required for the circuit to reach steady state given a voltage excitation in the pickup inductor. For a resonator, the characteristic time is the resonator ring-up time $\sim Q/\nu_r$. The assumption on the integration time implies that the dark matter has reached steady state, so that Fourier transforms are appropriate mathematical tools. In addition, by the end of the timestream, we assume that we have integrated long enough that phase decoherence of the dark-matter signal has occurred. This last observation will become important when we combine data from multiple circuit configurations/ different resonant frequencies. We will be using this assumption frequently, so we define a timescale

$$t_{\text{circ}}^*(\nu_{\text{DM}}^0) \equiv \max(10^6/\nu_{\text{DM}}^0, t_{\text{pole}}). \quad (66)$$

We emphasize that the timescale is inherently dependent on both the dark-matter rest mass and the circuit parameters.

We now describe how the software implementation of the Dicke radiometer of Fig. 4 is performed. This timestream from the output of the amplifier is fed through a software convolution filter described by the function $f(t)$, resulting in an output $(f * b)(t)$. The SNR can be maximized by deriving an optimal convolution filter [34]. In the frequency-domain,

this convolution filter implements a multiplicative weighting on $b(\nu)$ and their complex conjugates $b^*(\nu)$.

$$b(\nu) \rightarrow f(\nu)b(\nu) \quad (67)$$

$$b^*(\nu) \rightarrow f^*(\nu)b^*(\nu) \quad (68)$$

Here, $f(\nu)$ are the Fourier components of $f(t)$ and $f^*(\nu)$ their complex conjugates. The filtered timestream is then fed through the square-law detector and integrator. The output of the integrator is the time-averaged power at the output of the convolution filter, quantified by

$$d = \frac{1}{\tau} \int_0^\tau dt |(f * b)(t)|^2. \quad (69)$$

The statistics of d give the SNR. The dark-matter power in d is the signal, while the standard deviation of d , as produced by thermal, zero-point fluctuation, and amplifier noise, sets the noise. If, in an experiment, the total power in d is in excess of the mean noise power in d by many standard deviations, then a candidate signal has been detected, and follow-up and characterization is required.

In our measurement of d , we have assumed that we are simultaneously measuring both quadratures of the signal, and thus that the amplifier must add noise [25], an assumption that will be relaxed in Part II. This noise is represented by the presence of amplifier noise waves in the output timestream, as can be observed in equation (64). We will optimize SNR with respect to the filter f . As this filter is executed in software, the filter is allowed to vary with the scanned characteristics of the circuit (e.g. the resonance frequency) and the assumed properties of candidate dark-matter signals at the search frequency. We will show that the optimum filter depends on the shape of the dark-matter spectrum, but not on the coupling of dark matter to electromagnetism, quantified by g_{DM} . We may therefore write

$$f(\nu) = f_{\text{circ}} \left(\nu, \nu_{\text{DM}}^0, \frac{d\rho_{\text{DM}}}{d\nu}(\nu, \nu_{\text{DM}}^0) \right). \quad (70)$$

For brevity, where convenient, we skip the full parametrization and write $f(\nu)$ with the other dependencies implicitly understood.

We stress that the optimal filter is dependent on the circuit parameters, e.g. S-parameters. Indeed, we will find that this is the case for all of the quantities calculated in this section. We will omit explicit dependence on these parameters (e.g. with a subscript *circ*), unless beneficial.

We examine the noise first. A useful quantity will be total noise correlator for the output Fourier components $b(\nu)$. The noise in the frequency domain is

$$b^n(\nu) = \sqrt{G(\nu)}S_{21}^{(1)}(\nu)a_1^{(1)}(\nu) + \sqrt{G(\nu)}S_{22}^{(1)}(\nu)c_1^{(2)}(\nu) + c_2^{(2)}(\nu). \quad (71)$$

The correlator is defined by

$$\langle b^n(\nu)b^n(\nu')^* \rangle \equiv B(\nu)\delta(\nu - \nu'). \quad (72)$$

Plugging (59), (61), (71) into (72) yields

$$\begin{aligned} B(\nu) = & |G(\nu)||S_{21}^{(1)}(\nu)|^2 h\nu(n(\nu) + 1/2) \\ & + |G(\nu)||S_{22}^{(1)}(\nu)|^2 C_{11}(\nu) + C_{22}(\nu) + 2\text{Re}(\sqrt{G(\nu)}S_{22}(\nu)C_{12}(\nu)). \end{aligned} \quad (73)$$

The noise correlator is dependent not only on the noise covariance matrix and the temperature T of the detector, but on the S-parameters of circuit (1) in Fig. 6.

The mean noise power (the mean of d resulting from noise) is

$$\begin{aligned} \langle d^n \rangle = & \frac{1}{\tau} \int_0^\tau dt \int_0^\infty d\nu \int_0^\infty d\nu' f(\nu)f(\nu')^* \langle b^n(\nu)b^n(\nu')^* \rangle e^{+i2\pi(\nu-\nu')t} \\ = & \frac{1}{\tau} \int_0^\tau dt \int d\nu \int d\nu' f(\nu)f(\nu')^* B(\nu)\delta(\nu - \nu')e^{+i2\pi(\nu-\nu')t} \\ = & \int_0^\infty d\nu |f(\nu)|^2 B(\nu). \end{aligned} \quad (74)$$

The second moment of d due to noise is

$$\begin{aligned} \langle (d^n)^2 \rangle = & \frac{1}{\tau^2} \int_0^\tau dt \int_0^\tau dt' \int d\nu_1 \int d\nu_2 \int d\nu_3 \int d\nu_4 f(\nu_1)f^*(\nu_2)f(\nu_3)f^*(\nu_4) \\ & \langle b^n(\nu_1)(b^n(\nu_2))^*b^n(\nu_3)(b^n(\nu_4))^* \rangle e^{+i2\pi(\nu_1-\nu_2)t}e^{+i2\pi(\nu_3-\nu_4)t'}. \end{aligned} \quad (75)$$

Assuming that the noise modes are Gaussian (as one would have with a quantum-limited amplifier and thermal noise in the signal source), the four-point correlation may be evaluated by decomposing it into sums of products of two-point correlations. In particular,

$$\begin{aligned} \langle b^n(\nu_1)(b^n(\nu_2))^*b^n(\nu_3)(b^n(\nu_4))^* \rangle = & \langle b^n(\nu_1)(b^n(\nu_2))^* \rangle \langle b^n(\nu_3)(b^n(\nu_4))^* \rangle \\ & \langle b^n(\nu_1)(b^n(\nu_4))^* \rangle \langle b^n(\nu_2)(b^n(\nu_3))^* \rangle. \end{aligned} \quad (76)$$

Using equations (72) and (74) gives

$$\begin{aligned} \langle (d^n)^2 \rangle = & \langle d^n \rangle^2 \\ & + \frac{1}{\tau^2} \int_0^\tau dt \int_0^\tau dt' \int d\nu_1 \int d\nu_3 |f(\nu_1)|^2 |f(\nu_3)|^2 B(\nu_1)B(\nu_3)e^{+i2\pi(\nu_1-\nu_3)(t-t')}. \end{aligned} \quad (77)$$

When $|\nu_1 - \nu_3|\tau \gg 1$,

$$\frac{1}{\tau^2} \int_0^\tau dt \int_0^\tau dt' e^{+i2\pi(\nu_1 - \nu_3)(t-t')} \approx \frac{1}{\tau} \delta(\nu_1 - \nu_3). \quad (78)$$

We may use this approximation because the integration time is much longer than $t_{\text{circ}}^*(\nu_{\text{DM}}^0)$, set by the two characteristic times in the detection system (the dark-matter coherence time and the longest timescale associated with circuit poles). The variance in d^n is thus

$$\begin{aligned} \sigma_d \left(\tau, f_{\text{circ}} \left(\nu, \nu_{\text{DM}}^0, \frac{d\rho_{\text{DM}}}{d\nu}(\nu, \nu_{\text{DM}}^0) \right) \right)^2 &= \langle (d^n)^2 \rangle - \langle d^n \rangle^2 \\ &= \frac{1}{\tau} \int d\nu \left| f_{\text{circ}} \left(\nu, \nu_{\text{DM}}^0, \frac{d\rho_{\text{DM}}}{d\nu}(\nu, \nu_{\text{DM}}^0) \right) \right|^4 B(\nu)^2. \end{aligned} \quad (79)$$

The variance sets the uncertainty in power at the output of the integrator.

Using equations (50), (51), (64), and (69), we may write down the contribution of the dark-matter signal to the integrated power d :

$$\begin{aligned} d_{\text{DM}} \left(\nu_{\text{DM}}^0, g_{\text{DM}}, \frac{d\rho_{\text{DM}}}{d\nu}(\nu, \nu_{\text{DM}}^0), f_{\text{circ}} \left(\nu, \nu_{\text{DM}}^0, \frac{d\rho_{\text{DM}}}{d\nu}(\nu, \nu_{\text{DM}}^0) \right) \right) \\ = \frac{1}{\tau} \int_0^\tau dt \int d\nu \int d\nu' f(\nu) f^*(\nu') e^{+i2\pi(\nu - \nu')t} \\ \sqrt{G(\nu)G(\nu')^*} S_{21}^{(1)}(\nu, \nu_r) S_{21}^{(1)*}(\nu', \nu_r) \frac{V_{\text{DM}}(\nu, g_{\text{DM}}, \frac{d\rho_{\text{DM}}}{d\nu}(\nu, \nu_{\text{DM}}^0)) V_{\text{DM}}^*(\nu', g_{\text{DM}}, \frac{d\rho_{\text{DM}}}{d\nu'}(\nu', \nu_{\text{DM}}^0))}{4\sqrt{R(\nu)}\sqrt{R(\nu')}} \\ \approx \int d\nu \int d\nu' f(\nu) f^*(\nu') \delta(\nu - \nu') \\ \sqrt{G(\nu)G(\nu')^*} S_{21}^{(1)}(\nu) S_{21}^{(1)*}(\nu') \frac{V_{\text{DM}}(\nu, g_{\text{DM}}, \frac{d\rho_{\text{DM}}}{d\nu}(\nu, \nu_{\text{DM}}^0)) V_{\text{DM}}^*(\nu', g_{\text{DM}}, \frac{d\rho_{\text{DM}}}{d\nu'}(\nu', \nu_{\text{DM}}^0))}{4\sqrt{R(\nu)}\sqrt{R(\nu')}} \\ = \int d\nu \left| f_{\text{circ}} \left(\nu, \nu_{\text{DM}}^0, \frac{d\rho_{\text{DM}}}{d\nu}(\nu, \nu_{\text{DM}}^0) \right) \right|^2 P_{\text{DM}} \left(\nu, g_{\text{DM}}, \frac{d\rho_{\text{DM}}}{d\nu}(\nu, \nu_{\text{DM}}^0) \right), \end{aligned} \quad (80)$$

where the approximation in the second line holds because the integration time is much longer than $t_{\text{circ}}^*(\nu_{\text{DM}}^0)$. $P_{\text{DM}}(\nu, g_{\text{DM}}, \frac{d\rho_{\text{DM}}}{d\nu}(\nu, \nu_{\text{DM}}^0))$ is the power density of the signal at the output of the amplifier, given from (50) and (51) by

$$P_{\text{DM}} \left(\nu, g_{\text{DM}}, \frac{d\rho_{\text{DM}}}{d\nu}(\nu, \nu_{\text{DM}}^0) \right) = |G(\nu)| |S_{21}^{(1)}(\nu)|^2 \frac{2(\pi\nu)^2 L_{\text{PU}}}{R(\nu)} E_{\text{DM}} \left(\nu, g_{\text{DM}}, \frac{d\rho_{\text{DM}}}{d\nu}(\nu, \nu_{\text{DM}}^0) \right). \quad (81)$$

The SNR for this single measurement of length τ is given by the dark-matter power (the

power in excess of the mean noise power) divided by the standard deviation in noise power:

$$\begin{aligned}
SNR & \left[\nu_{\text{DM}}^0, g_{\text{DM}}, \frac{d\rho_{\text{DM}}}{d\nu}(\nu, \nu_{\text{DM}}^0), \tau, f_{\text{circ}} \left(\nu, \nu_{\text{DM}}^0, \frac{d\rho_{\text{DM}}}{d\nu}(\nu, \nu_{\text{DM}}^0) \right) \right] \\
&= \frac{d_{\text{DM}}(\nu_{\text{DM}}^0, g_{\text{DM}}, \frac{d\rho_{\text{DM}}}{d\nu}(\nu, \nu_{\text{DM}}^0), f_{\text{circ}}(\nu, \nu_{\text{DM}}^0, \frac{d\rho_{\text{DM}}}{d\nu}(\nu, \nu_{\text{DM}}^0)))}{\sigma_d(\tau, f_{\text{circ}}(\nu, \nu_{\text{DM}}^0, \frac{d\rho_{\text{DM}}}{d\nu}(\nu, \nu_{\text{DM}}^0)))} \\
&= \frac{\int d\nu |f_{\text{circ}}(\nu, \nu_{\text{DM}}^0, \frac{d\rho_{\text{DM}}}{d\nu}(\nu, \nu_{\text{DM}}^0))|^2 P_{\text{DM}}(\nu, g_{\text{DM}}, \frac{d\rho_{\text{DM}}}{d\nu}(\nu, \nu_{\text{DM}}^0))}{(\tau^{-1} \int d\nu |f_{\text{circ}}(\nu, \nu_{\text{DM}}^0, \frac{d\rho_{\text{DM}}}{d\nu}(\nu, \nu_{\text{DM}}^0))|^4 B(\nu)^2)^{1/2}}. \tag{82}
\end{aligned}$$

The optimal filter, which maximizes SNR, is given by

$$\left| f_{\text{circ}}^{\text{opt}} \left(\nu, \nu_{\text{DM}}^0, \frac{d\rho_{\text{DM}}}{d\nu}(\nu, \nu_{\text{DM}}^0) \right) \right|^2 = \frac{P_{\text{DM}}(\nu, g_{\text{DM}}, \frac{d\rho_{\text{DM}}}{d\nu}(\nu, \nu_{\text{DM}}^0))}{g_{\text{DM}}^2 B(\nu)^2}. \tag{83}$$

From equation (82), observe that multiplication of this filter by any constant preserves the value of the SNR. In particular, because g_{DM} is a constant, the optimal filter can be scaled to be independent of coupling. We show this explicitly by omitting g_{DM} from the arguments on the left-hand side of (83) and by adding a normalization $1/g_{\text{DM}}^2$ to cancel the g_{DM}^2 factor in P_{DM} , as can be seen from equations (50), (51), (81).

This form for the filter is qualitatively expected. It contains explicit dependence on the shape of the dark-matter energy-density distribution. The filter gives greater weight to the frequency bins that intrinsically contain more of the dark-matter signal (higher $d\rho_{\text{DM}}/d\nu$), and lower weight to the frequency bins where transmission to the amplifier is small (lower $|S_{21}^{(1)}(\nu)|$). For the optimal filter of (83), the SNR is

$$\begin{aligned}
SNR^{\text{opt}} & \left[\nu_{\text{DM}}^0, g_{\text{DM}}, \frac{d\rho_{\text{DM}}}{d\nu}(\nu, \nu_{\text{DM}}^0), \tau \right] \\
&\equiv SNR \left[\nu_{\text{DM}}^0, g_{\text{DM}}, \frac{d\rho_{\text{DM}}}{d\nu}(\nu, \nu_{\text{DM}}^0), \tau, f_{\text{circ}}^{\text{opt}} \left(\nu, \nu_{\text{DM}}^0, \frac{d\rho_{\text{DM}}}{d\nu}(\nu, \nu_{\text{DM}}^0) \right) \right] \\
&= \left(\tau \int d\nu \frac{P_{\text{DM}}(\nu, g_{\text{DM}}, \frac{d\rho_{\text{DM}}}{d\nu}(\nu, \nu_{\text{DM}}^0))^2}{B(\nu)^2} \right)^{1/2}. \tag{84}
\end{aligned}$$

This form suggests another method for understanding the optimal filter of equation (83). Consider a narrow frequency interval $[\nu, \nu + \delta\nu]$. The signal power in this bin is $\approx P_{\text{DM}}(\nu, g_{\text{DM}}, \frac{d\rho_{\text{DM}}}{d\nu}(\nu, \nu_{\text{DM}}^0)) \delta\nu$ and the noise power $\approx B(\nu) \delta\nu$. Thus, using eq. (41), the SNR from only this bin is

$$SNR_{\text{bin}} \left[\nu_{\text{DM}}^0, g_{\text{DM}}, \frac{d\rho_{\text{DM}}}{d\nu}(\nu, \nu_{\text{DM}}^0), \tau \right] = \frac{P_{\text{DM}}(\nu, g_{\text{DM}}, \frac{d\rho_{\text{DM}}}{d\nu}(\nu, \nu_{\text{DM}}^0))}{B(\nu)} \sqrt{\delta\nu \cdot \tau}. \tag{85}$$

Comparison of (84) and (85) reveals that the optimal filter adds in quadrature the SNRs from all frequency bins in which there is dark-matter signal power.

We now use the results for the SNR from a single circuit/circuit instance to determine the SNR from multiple circuits. It is important to understand how to combine information from different measurements, such as integrations at different resonance frequencies or, more generally, integrations with multiple circuit configurations, including multiple modes. Optimizing this combination is critical to optimizing and understanding the sensitivity of a search for dark matter.

2. SNR for multiple circuit configurations: combining data

We will index the various circuit configurations with an index i . A quantity with the subscript or superscript i will relate to the i th circuit (for example, the i th resonance frequency setting of a single-pole resonator circuit). We wish to test, with data from this set of circuits, whether the dark-matter rest mass is $m_{\text{DM}} = \frac{h\nu_{\text{DM}}^0}{c^2}$. Suppose that for the i th circuit, we integrate for time τ_i and that this time is much longer than $t_{\text{circ},i}^*(\nu_{\text{DM}}^0)$.

For each circuit configuration, from the averaged output of the convolution filter, we obtain a signal power given by equation (80) and a noise power given by equation (79). We wait much longer than $t_{\text{circ},i}^*(\nu_{\text{DM}}^0)$, so the timestream from each circuit represents an approximately statistically independent sample of the dark-matter signal. Therefore, the appropriate combination of data for the total SNR at a dark-matter search frequency is

$$\sum_i w_i d_i, \quad (86)$$

where d_i is defined as in equation (69) and represents the time-averaged output power from i th circuit. $\{w_i\}$ are weights to the data that will be optimized.

The total SNR is

$$\begin{aligned} \text{SNR}_{\text{tot}} & \left[\nu_{\text{DM}}^0, g_{\text{DM},i}, \frac{d\rho_{\text{DM}}}{d\nu}(\nu, \nu_{\text{DM}}^0), \{\tau_i\}, \left\{ f_{\text{circ},i} \left(\nu, \nu_{\text{DM}}^0, \frac{d\rho_{\text{DM}}}{d\nu}(\nu, \nu_{\text{DM}}^0) \right) \right\}, \{w_i\} \right] \\ & = \frac{\sum_i w_i d_{\text{DM},i} \left(\nu_{\text{DM}}^0, g_{\text{DM},i}, \frac{d\rho_{\text{DM}}}{d\nu}(\nu, \nu_{\text{DM}}^0), f_{\text{circ},i} \left(\nu, \nu_{\text{DM}}^0, \frac{d\rho_{\text{DM}}}{d\nu}(\nu, \nu_{\text{DM}}^0) \right) \right)}{\left(\sum_i w_i^2 \sigma_{d_i} \left(\tau_i, f_{\text{circ},i} \left(\nu, \nu_{\text{DM}}^0, \frac{d\rho_{\text{DM}}}{d\nu}(\nu, \nu_{\text{DM}}^0) \right) \right)^2 \right)^{1/2}}. \end{aligned} \quad (87)$$

The quantity $d_{\text{DM},i}$ in the numerator is as given in (80), and the quantity σ_{d_i} in the denominator is as given in (79); the subscript i indicates that the quantities relate to the i th

circuit. We have also allowed the dark-matter coupling between field and detector, g_{DM}^i , to vary among circuits. This could be the result of using different detector volumes $V_{\text{PU},i}$ or possessing different geometrical factors $c_{\text{PU},i}$ in each configuration—see eq. (52) and (53). For any choice of weighting parameters $\{w_i\}$,

$$\begin{aligned} SNR_{\text{tot}} & \left[\nu_{\text{DM}}^0, \{g_{\text{DM},i}\}, \frac{d\rho_{\text{DM}}}{d\nu}(\nu, \nu_{\text{DM}}^0), \{\tau_i\}, \left\{ f_{\text{circ},i} \left(\nu, \nu_{\text{DM}}^0, \frac{d\rho_{\text{DM}}}{d\nu}(\nu, \nu_{\text{DM}}^0) \right) \right\}, \{w_i\} \right] \\ & \leq \left(\sum_i \frac{d_{\text{DM},i} \left(\nu_{\text{DM}}^0, g_{\text{DM},i}, \frac{d\rho_{\text{DM}}}{d\nu}(\nu, \nu_{\text{DM}}^0), f_{\text{circ},i} \left(\nu, \nu_{\text{DM}}^0, \frac{d\rho_{\text{DM}}}{d\nu}(\nu, \nu_{\text{DM}}^0) \right) \right)^2}{\sigma_{d_i} \left(f_{\text{circ},i} \left(\nu, \nu_{\text{DM}}^0, \frac{d\rho_{\text{DM}}}{d\nu}(\nu, \nu_{\text{DM}}^0) \right) \right)^2} \right)^{1/2}. \end{aligned} \quad (88)$$

The highest SNR is achieved if

$$w_i = \kappa \frac{d_{\text{DM},i} \left(\nu_{\text{DM}}^0, \{g_{\text{DM},i}\}, \frac{d\rho_{\text{DM}}}{d\nu}(\nu, \nu_{\text{DM}}^0), f_{\text{circ},i} \left(\nu, \nu_{\text{DM}}^0, \frac{d\rho_{\text{DM}}}{d\nu}(\nu, \nu_{\text{DM}}^0) \right) \right)}{\sigma_{d_i} \left(\tau_i, f_{\text{circ},i} \left(\nu, \nu_{\text{DM}}^0, \frac{d\rho_{\text{DM}}}{d\nu}(\nu, \nu_{\text{DM}}^0) \right) \right)^2}, \quad (89)$$

where κ is arbitrary. It follows from (82) that the SNR for circuit is the square root of the summand in (88). Thus, when SNR_{tot} is maximized with respect to the weights, the total SNR is the quadrature sum of the SNRs from all circuits. From (83), the SNR for each circuit i is maximized when the filter f is chosen to be

$$\left| f_{\text{circ},i}^{\text{opt}} \left(\nu, \nu_{\text{DM}}^0, \frac{d\rho_{\text{DM}}}{d\nu}(\nu, \nu_{\text{DM}}^0) \right) \right|^2 = \frac{P_{\text{DM},i} \left(\nu, g_{\text{DM},i}, \frac{d\rho_{\text{DM}}}{d\nu}(\nu, \nu_{\text{DM}}^0) \right)}{g_{\text{DM},i}^2 B_i(\nu)^2}. \quad (90)$$

In this case, the sum in (88) is

$$\left(\sum_i \tau_i \int d\nu \frac{P_{\text{DM}} \left(\nu, g_{\text{DM},i}, \frac{d\rho_{\text{DM}}}{d\nu}(\nu, \nu_{\text{DM}}^0) \right)^2}{B_i(\nu)^2} \right)^{1/2}. \quad (91)$$

Additionally, eqs. (79) and (80) give the relation

$$\begin{aligned} & d_{\text{DM},i} \left(\nu_{\text{DM}}^0, g_{\text{DM},i}, \frac{d\rho_{\text{DM}}}{d\nu}(\nu, \nu_{\text{DM}}^0), f_{\text{circ},i}^{\text{opt}} \left(\nu, \nu_{\text{DM}}^0, \frac{d\rho_{\text{DM}}}{d\nu}(\nu, \nu_{\text{DM}}^0) \right) \right) \\ & = g_{\text{DM},i}^2 \tau_i \sigma_d \left(\tau_i, f_{\text{circ},i}^{\text{opt}} \left(\nu, \nu_{\text{DM}}^0, \frac{d\rho_{\text{DM}}}{d\nu}(\nu, \nu_{\text{DM}}^0) \right) \right)^2. \end{aligned} \quad (92)$$

Therefore, weights $w_i = g_{\text{DM},i}^2 \tau_i$ correspond to $\kappa = 1$ in (89). The relation (88) is then satisfied with equality for the optimal filter of (90). The maximized SNR over all configurations is given by

$$SNR_{\text{tot}}^{\text{opt}} \left[\nu_{\text{DM}}^0, \{g_{\text{DM},i}\}, \frac{d\rho_{\text{DM}}}{d\nu}(\nu, \nu_{\text{DM}}^0), \{\tau_i\} \right] = \left(\sum_i \tau_i \int d\nu \frac{P_{\text{DM},i} \left(\nu, g_{\text{DM},i}, \frac{d\rho_{\text{DM}}}{d\nu}(\nu, \nu_{\text{DM}}^0) \right)^2}{B_i(\nu)^2} \right)^{1/2}. \quad (93)$$

We emphasize that this result applies not only to scan steps of a tunable resonator, but also for combining data from multiple modes, from more general configuration changes, or for datastreams from entirely different instruments, subject to conditions discussed previously that the amplitude and (in the case of vectors) direction of the dark-matter field is presumed to be the same.

3. SNR of search with a quantum-limited amplifier

In this section, we use the results of sections IV C 1 and IV C 2 to calculate the SNR of the special case of a circuit read out by an amplifier operating at the standard quantum limit. The standard quantum limit provides a fundamental noise floor for a search with a phase-insensitive amplifier, so these results are critical for the scan optimization in the next section.

We assume the ideal case that the imprecision and backaction noise modes of the amplifier are uncorrelated, so that

$$C_{12}(\nu) = C_{21}(\nu)^* = 0. \quad (94)$$

This is often achieved in practical setups by inserting a circulator, with one port terminated by a cold matched load (e.g. a $50\ \Omega$ resistor matched to a $50\ \Omega$ transmission lines and held at temperature $kT \ll h\nu$), between the impedance matching network and amplifier input. For a two-port amplifier, the native backaction is absorbed by the matched load. In this case, the noise injected into the detector (circuit (1) in Fig. 6) from the matched load effectively plays the role of the backaction noise mode $c_2^{(2)}(\nu)$ in (57). For a one-port amplifier, such as a resonant Josephson parametric amplifier [30], a circulator is used to embed the device in a two-port environment. Again, the backaction noise mode is effectively provided by the matched resistor. The circulator at the amplifier input also provides reverse isolation, protecting the resonator from any interference that propagates from the follow-on readout chain toward the detector. See Ref. [28] for further discussion.

In Appendix D, we show that for a quantum-limited amplifier, the noise waves of equations (57) and (61) possess autocorrelations [21, 28]

$$C_{11}(\nu) = \frac{h\nu}{2} \quad (95)$$

$$C_{22}(\nu) = \frac{h\nu}{2} (|G(\nu)| - 1). \quad (96)$$

Combining equations (59) and (94)-(96) then yields the following expression for $B(\nu)$:

$$\begin{aligned} B(\nu) &= |G(\nu)| |S_{21}^{(1)}(\nu)|^2 h\nu(n(\nu) + 1/2) + |G(\nu)| |S_{22}^{(1)}(\nu)|^2 \frac{h\nu}{2} + \frac{h\nu}{2} (|G(\nu)| - 1) \\ &\approx h\nu |G(\nu)| \left(|S_{21}^{(1)}(\nu)|^2 n(\nu) + 1 \right), \end{aligned} \quad (97)$$

where, since $S^{(1)}$ represents a lossless, linear, passive circuit, we have used the power conservation relation

$$|S_{21}^{(1)}(\nu)|^2 + |S_{22}^{(1)}(\nu)|^2 = 1, \quad (98)$$

as well as the high-gain approximation $|G(\nu)| \gg 1$. $B(\nu)$ is readily interpreted as the mean noise power per unit bandwidth at the output of the amplifier. Here, $|S_{21}^{(1)}(\nu)|^2 n(\nu)$ represents the thermal noise power transmitted from the signal source. The “+1” term in the approximate form of Eqn. (97) represents the quantum noise in the standard quantum limit (SQL). This noise incorporates 1/2 photon per unit bandwidth from the amplifier’s added output noise (imprecision noise). The other 1/2 photon is split between the amplifier backaction and the zero-point energy in the signal source. The relative contributions are determined by the fraction of the zero-point energy transmitted through the matching network (with amplitude $|S_{21}^{(1)}|^2$) and the fraction of the backaction power reflected off of the impedance filter (with amplitude $|S_{22}^{(1)}|^2$). The two are related by Eqn. (98), summing to the 1/2 photon contribution in the SQL.

From (97), we may also recognize that, for a quantum-limited amplifier, the amplifier noise impedance is equal to its input impedance. When the source impedance is set equal to the input impedance, the transmission $|S_{21}|$ is unity, and the amplifier backaction does not contribute to the total noise. The total amplifier noise consists only of the imprecision noise, represented by the third term in the first line of equation (97). This results in a quantum-limited noise temperature of $kT_N(\nu) = h\nu/2$. When the transmission is less than unity, the amplifier backaction, represented by the second term in (97), contributes to the total noise power. This implies that we would need to increase $n(\nu)$ by more than 1/2 in order for the increase in noise from the source resistor to equal the amplifier noise. In this case, $kT_N(\nu) > h\nu/2$. The noise impedance may also be derived directly from the techniques in Ref. [29].⁷

⁷In fact, even for an amplifier that misses the quantum limit, the practical necessities of perfect input and output match and of a circulator at the amplifier input imply that the noise impedance equals the input impedance.

We can define

$$N_{\text{tot}}(\nu, S_{21}^{(1)}(\nu), n(\nu)) \equiv \frac{|S_{21}^{(1)}(\nu)|^2 n(\nu) + 1}{|S_{21}^{(1)}(\nu)|^2} \quad (99)$$

as the total noise-equivalent number (for a phase-insensitive amplifier operating at the quantum limit), which is a unitless measure of all noise sources. N_{tot} represents the total system noise at frequency ν referred to the signal source. From (81), (84), and (97), we may evaluate the SNR for the optimally filtered signal with a quantum-limited readout amplifier. For a measurement of duration τ from a single circuit configuration, the SNR is

$$SNR^{\text{opt}} \left[\nu_{\text{DM}}^0, g_{\text{DM}}, \frac{d\rho_{\text{DM}}}{d\nu}(\nu, \nu_{\text{DM}}^0), \tau \right] = 2\pi^2 \quad (100)$$

$$\times \left(\tau \int_{\nu_{\text{DM}}^0}^{\nu_{\text{DM}}^0 + \Delta\nu_{\text{DM}}^c(\nu_{\text{DM}}^0)} d\nu \left(\frac{\nu L_{\text{PU}}}{R(\nu)} \frac{E_{\text{DM}}(\nu, \nu_{\text{DM}}^0, g_{\text{DM}}, \frac{d\rho_{\text{DM}}}{d\nu}(\nu, \nu_{\text{DM}}^0))}{h} \frac{1}{N_{\text{tot}}(\nu, S_{21}^{(1)}(\nu), n(\nu))} \right)^2 \right)^{1/2}.$$

Thus, the total SNR for the measurement is determined from the convolution of the optimal filter (which adds the SNR from all narrow frequency bins in quadrature) with the presumed spectrum of the dark-matter signal and the inverse of the total noise-equivalent number. It is evident from equation (100) that N_{tot} contains all information and parameters about the impedance-matching network as they pertain to search sensitivity. The total noise-equivalent number must therefore play a principal role in determining the optimal matching network between signal source and amplifier, as is described in the first part of Section V.

For simplicity, we define ψ as the inverse of the total noise-equivalent number:

$$\psi(\nu, S_{21}^{(1)}(\nu), n(\nu)) \equiv N_{\text{tot}}(\nu, S_{21}^{(1)}(\nu), n(\nu))^{-1} = \frac{|S_{21}^{(1)}(\nu)|^2}{|S_{21}^{(1)}(\nu)|^2 n(\nu) + 1}, \quad (101)$$

and parametrize the arguments of the SNR in terms of ψ :

$$SNR^{\text{opt}} \left[\nu_{\text{DM}}^0, g_{\text{DM}}, \frac{d\rho_{\text{DM}}}{d\nu}(\nu, \nu_{\text{DM}}^0), \tau \right] \rightarrow SNR^{\text{opt}} \left[\nu_{\text{DM}}^0, g_{\text{DM}}, \frac{d\rho_{\text{DM}}}{d\nu}(\nu, \nu_{\text{DM}}^0), \psi(\nu, S_{21}^{(1)}(\nu), n(\nu)), \tau \right]. \quad (102)$$

We now consider implications of the SNR analysis (specifically equations (100) and (102)) for a search using resonators. This discussion guides the formation of value functions for the search optimization in Section V.

Consider placement of two resonators of the same Q: one resonator at frequency $\nu_{r1} = \nu_{\text{DM}}^0$ and the other at a frequency ν_{r2} close to ν_{DM}^0 (i.e. $|\nu_{\text{DM}}^0 - \nu_{r2}| \ll \nu_{r2}$), but still several resonator bandwidths away. The transmission is described by the Lorentzian in equation

(48). If, at each frequency ν of the integral in eq. (100), the transmitted thermal noise power is much larger than the quantum noise, $|S_{21}^{(1)}(\nu)|^2 n(\nu) \equiv |S_{21}^{(1)}(\nu, \nu_r)|^2 n(\nu) \gg 1$, so the SNR is approximately the same for both circuits. The conclusion is that, if the transmitted thermal noise is larger than the quantum noise, then an off-resonance circuit gives the same sensitivity to dark matter as an on-resonance circuit. Equivalently, one may observe that a single resonator will be sensitive, without degradation from quantum noise, *not only to the dark-matter search frequencies within the resonator bandwidth, but also to frequencies past the resonator rolloff.*

The physics of this process is displayed in Fig. 7. The narrowband resonator transmission (black), $|S_{21}^{(1)}(\nu, \nu_r)|^2$, which determines the dark-matter signal power at the input of the amplifier, possesses the same shape as the thermal noise (green) because the thermal noise is filtered by the same matching network. As such, the SNR will remain constant (as effectively determined by the ratio of the two shapes), as a function of dark-matter frequency detuning from resonance, as long as the thermal noise is greater than the quantum noise (dark red line). The regime over which this is the case is termed the “sensitivity bandwidth” (dashed blue lines) and can be considerably larger than the resonator bandwidth (dashed purple lines) when the thermal occupation is much larger than unity, $n(\nu_r) \gg 1$.

This observation can again be explained from Fig. 1 in the introduction. If the amplifier noise is sub-dominant, then the filter characteristics of the impedance-matching network between the source and the readout, and in particular, the placement of the resonance frequency, do not affect SNR. The SNR is completely determined from the two parts of the signal source, the signal from the inductor and the noise from the resistor. The off-resonance contribution to the SNR was not considered in previous analyses, such as [16]; as we will find, consideration of this effect adds substantially to the sensitivity of a search, especially at lower frequency.

Therefore, for a search over a wide band, any optimization function for evaluating a matching network must consider not only the possibility of dark-matter signal on resonance, but also the information available over the entire search band. We must develop a measure of integrated sensitivity. For the case of a phase-preserving amplifier operating at the quantum limit, this sensitivity will be limited by the spectrum of ψ , the inverse of the total noise-equivalent number for the standard quantum limit, which contains all information about the impedance-matching network.

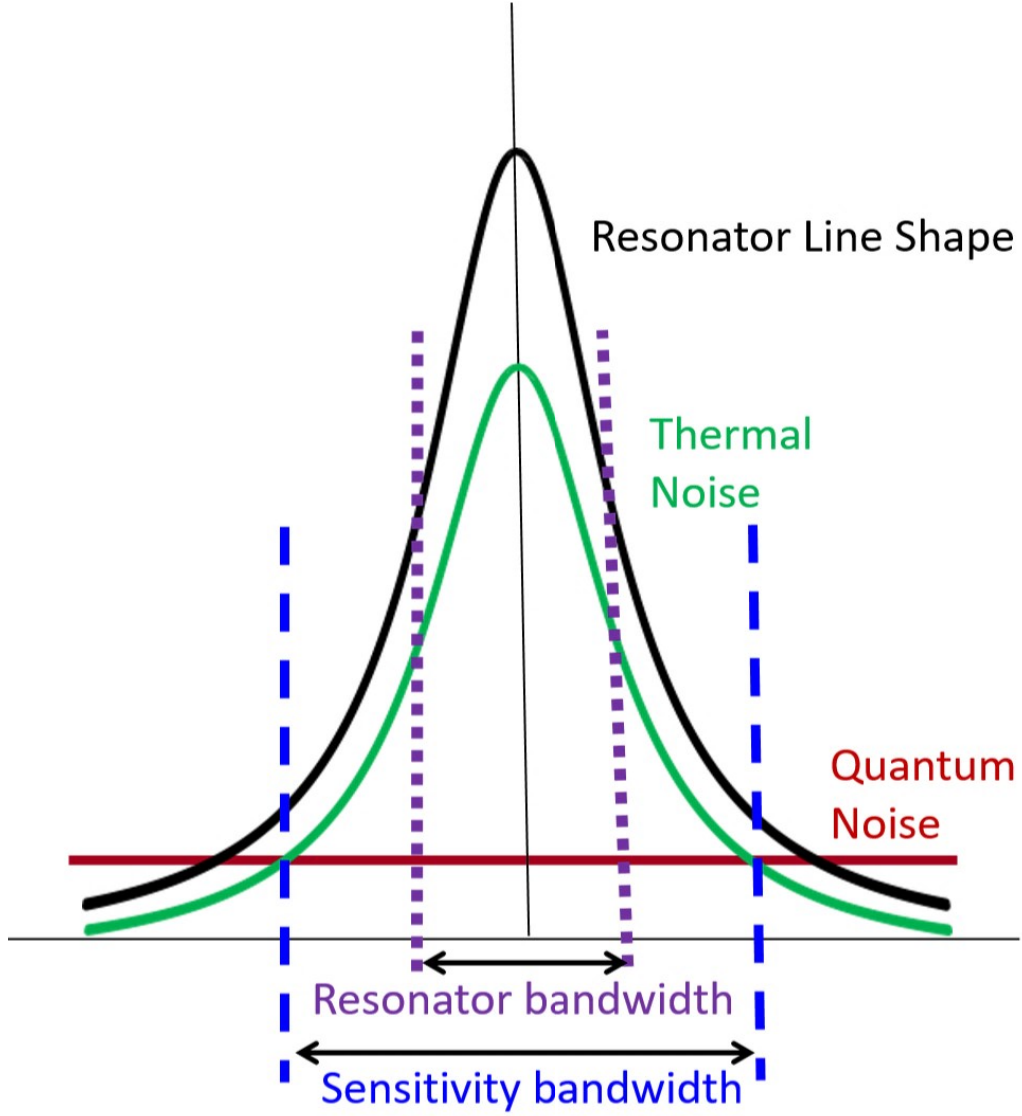


FIG. 7. Relative noise contributions in a resonator circuit. The x-axis is frequency (arbitrary units), while the y-axis is power referred to the input of the amplifier (arbitrary units). Thermal noise is in green, quantum noise is in dark red, and the resonator line shape $|S_{21}^{(1)}(\nu, \nu_r)|^2$ is in black. The resonator bandwidth is bounded by the dashed purple lines. The resonator is sensitive to dark matter, without degradation from quantum noise, over the sensitivity bandwidth, bounded by the dashed blue lines.

V. SEARCH OPTIMIZATION

Having derived the SNR for the scattering-mode detection scheme, we consider the optimization of the search. We assume that the search probes dark matter between frequencies ν_l and ν_h . As summarized in the introduction, the optimization consists of two parts:

1. First, we optimize the matching network for a single circuit configuration (the second element in the receiver circuit of Fig. 1). This optimization applies to any matching network, resonant or not. We introduce a value function for evaluating a given matching network. This function determines the sensitivity integrated across the search band, including sensitivity outside the resonator bandwidth. We also develop a framework for incorporating priors. These priors can take the form of favored or well motivated regimes (e.g. QCD axion bands), as well as limits and constraints set by previous probes. The value function corresponds to the weighted expected value of the square of the SNR.

We define in detail a “log uniform” search. The log-uniform search assumes that dark matter is uniformly likely, on a logarithmic scale, to be anywhere in the search band. Under this assumption, and limiting our attention to the results for a quantum-limited amplifier in Section IV C 3, we maximize the value function for a single-moded reactive detector. In performing the optimization, we hold fixed the characteristics of the signal source, e.g. the pickup inductance L_{PU} , the pickup coupled volume V_{PU} , and the resistance $R(\nu)$. The maximization is subject to the Bode-Fano criterion [31, 32], which constrains the match between a complex impedance (the signal source) and a real impedance (the amplifier input). We find that the matching network is parametrized by the resonance frequency ν_r as well as the coupling coefficient $\xi = Q_{\text{int}}/Q_{\text{cpl}}$ [30]. Holding the resonance frequency and internal quality factor fixed, we maximize the value function with respect to ξ (which is equivalent to maximizing with respect to Q_{cpl} , which may be varied by changing the coupling capacitance in our circuit model). Our result will be readily interpreted in the context of noise matching and backaction, introduced in Section I. We find that the optimized resonator matching network is close to the limit dictated by the Bode-Fano constraint. This establishes a one-pole resonator as a near-ideal technique for single-moded dark-matter detection. (As explored in Section V A 5, the claim comes with some caveats associated with

the limitations of the Bode-Fano criterion and the use of multiple receiver circuits.) Because a resonator is a near-ideal matching network for a log-uniform search, as well as most other conceivable priors, we focus hereafter on scanning resonant searches.

We also briefly consider the optimization for validating a candidate signal that has been found in a previous search. This result, though different from the log-uniform search, is also closely related to the concept of noise matching.

2. As stated before, an optimized resonant search requires tuning the resonance frequency across the search band. We assume that the total experiment time is fixed, i.e.

$$\sum_i \tau_i = T_{\text{tot}} \quad (103)$$

for some time T_{tot} , where the sum is over all circuit configurations/resonance frequencies. In this second part, we determine and optimize a value function for the distribution of time across scan steps. For a log-uniform search, this corresponds to maximizing the area of the exclusion region in a log-log plot of mass ν_{DM}^0 vs. coupling g_{DM} . To perform this maximization, we again consider a quantum-limited readout and assume a sufficiently dense scan, where each dark-matter frequency is probed by multiple resonance-frequency steps. We build upon the result of the first step optimization by assuming every resonator can be tuned to the optimal value of the coupling coefficient ξ . We also qualitatively discuss other possible time-allocation value functions, such as those appropriate for QCD-axion dark-matter searches.

The analogous optimization for flux-to-voltage amplifiers is carried out in Appendix F 3. For a quantum-limited flux-to-voltage amplifier, with no correlations between imprecision and backaction, we find that the optimal resonant scan—in terms of both matching network and time allocation—is the same as that found here for scattering-mode amplifiers.

A. Optimization of Matching Network

We first formulate a universal value function for evaluating the merits of a matching network. This value function should be “universal” in the sense that it should apply not only to resonant circuits, but also more generally to any receiver. The circuit is assumed to be tunable during the search (e.g. a tunable resonance frequency). The optimized matching

network will maximize the chance of finding dark matter over a broad bandwidth at each tuning step. Qualitatively, we will maximize the frequency range over which the thermal noise dominates the amplifier noise, while also not degrading detector sensitivity (quantified by the value of ψ , the inverse of the noise-equivalent number).

Prior information about the dark-matter signal will affect the search strategy. For example, there may exist constraints on the phase space from astrophysical or cosmological considerations, well motivated mass regions that we wish to probe to lower coupling, or candidate signals in previous searches that we wish to validate or exclude; we will return to the third possibility at the end of this section as an example of how the optimal impedance matching may change as a result of these priors. This information must also be accounted for in any universal value function. A priori we do not know the mass/frequency of the dark-matter signal, so we will define a probability distribution $P(\nu_{\text{DM}}^0)$ for finding dark matter of mass $m_{\text{DM}} = \frac{h\nu_{\text{DM}}^0}{c^2}$. Similarly, a priori we do not know the effective coupling of dark matter to the detection circuit, so we will define a conditional probability distribution $P(g_{\text{DM}}|\nu_{\text{DM}}^0)$. This distribution describes the probability that the coupling defined below equation (51) is g_{DM} given that the dark-matter frequency is ν_{DM}^0 . Additionally, we do not know the dark-matter frequency distribution $\frac{d\rho_{\text{DM}}}{d\nu}$. We assume that, for each possible frequency ν_{DM}^0 , there is a set of possible dark-matter distribution models:

$$\left\{ \left(\frac{d\rho_{\text{DM}}}{d\nu} \right)_1 (\nu, \nu_{\text{DM}}^0), \left(\frac{d\rho_{\text{DM}}}{d\nu} \right)_2 (\nu, \nu_{\text{DM}}^0), \left(\frac{d\rho_{\text{DM}}}{d\nu} \right)_3 (\nu, \nu_{\text{DM}}^0), \dots \right\}. \quad (104)$$

For example, one possible model is the standard halo model, explored in the appendix. The conditional probability associated with each model (i.e. the probability that model $\left(\frac{d\rho_{\text{DM}}}{d\nu} \right)_j$ is representative of the true dark-matter distribution) is denoted as $P \left(\left(\frac{d\rho_{\text{DM}}}{d\nu} \right)_j (\nu, \nu_{\text{DM}}^0) | \nu_{\text{DM}}^0 \right)$. Probability functions are defined to optimize a search.

Under these considerations, the generic value function for optimization of the matching network is the expected value of the square of the SNR.⁸ Explicitly, since the sensitivity, as it pertains to the matching network, is determined by the S-matrix—and specifically, the

⁸We have assumed implicitly that the probability distribution over dark-matter models is not conditional on the coupling g_{DM} . In the event that one wishes to devise a search with such a condition, the modification in our value function would be to make such a dependence explicit, e.g. $P \left(\left(\frac{d\rho_{\text{DM}}}{d\nu} \right)_j (\nu, \nu_{\text{DM}}^0) \middle| \nu_{\text{DM}}^0 \right) \rightarrow P \left(\left(\frac{d\rho_{\text{DM}}}{d\nu} \right)_j (\nu, \nu_{\text{DM}}^0, g_{\text{DM}}) \middle| g_{\text{DM}}, \nu_{\text{DM}}^0 \right)$.

transmission $S_{21}^{(1)}(\nu)$ —the value functional is

$$\begin{aligned}
F[S_{21}^{(1)}(\nu), n(\nu)] &\equiv \mathbf{E} \left[\text{SNR}^{\text{opt}} \left[\nu_{\text{DM}}^0, g_{\text{DM}}, \frac{d\rho_{\text{DM}}}{d\nu}(\nu, \nu_{\text{DM}}^0), \psi(\nu, S_{21}^{(1)}(\nu), n(\nu)), \tau \right]^2 \right] \\
&= \int d\nu_{\text{DM}}^0 \int dg_{\text{DM}} \sum_j \text{SNR}^{\text{opt}} \left[\nu_{\text{DM}}^0, g_{\text{DM}}, \frac{d\rho_{\text{DM}}}{d\nu}(\nu, \nu_{\text{DM}}^0), \psi(\nu, S_{21}^{(1)}(\nu), n(\nu)), \tau \right]^2 \\
&\quad \times P \left(\left(\frac{d\rho_{\text{DM}}}{d\nu} \right)_j (\nu, \nu_{\text{DM}}^0) \middle| \nu_{\text{DM}}^0 \right) P(g_{\text{DM}} | \nu_{\text{DM}}^0) P(\nu_{\text{DM}}^0).
\end{aligned} \tag{105}$$

In the top line of this equation (see also (100)), we have implicitly assumed, by parametrizing SNR with ψ , that the matching network is lossless and read out by a quantum-limited amplifier. The value function is readily extended to situations in which the network possesses loss and in which a quantum-limited amplifier is not used—see, for example, Appendix F 4. (One simply replaces the SNR formula for the lossless network read out by a quantum-limited amplifier with the appropriate expression.) Nevertheless, since the quantum limit represents a fundamental noise floor with a phase-insensitive amplifier, we will fully work out that case, while laying the foundation of a more complex optimization with different noise parameters. Strictly, the value functional depends on the thermal occupation number function $n(\nu)$. However, as this is determined by the temperature, rather than the network properties, we will, from here on, omit it from the explicit representation as an argument of F . Physically, $F[S_{21}^{(1)}(\nu)]$ measures the detector sensitivity to dark matter, integrated over a wide search range and weighted by probability densities relating to its mass, its coupling to electromagnetism, and the distribution across frequency space (determined by the velocity). Note that we have chosen the square of SNR, instead of simply SNR, in the definition of our value functional, since the SNR contributions from all circuit configurations add in quadrature.

The optimal matching network maximizes the value functional. Clearly, $F[S_{21}^{(1)}(\nu)]$ is user defined, and sometimes qualitative. In that case, we may only make some qualitative statements about these probability distributions. The joint probability distribution of mass and coupling, given by $P(g_{\text{DM}} | \nu_{\text{DM}}^0) P(\nu_{\text{DM}}^0)$, may have negligible weight at parts of the phase space that have been excluded, either by indirect astrophysical probes or by direct detection experiments. Additionally, for the axion, we may weight the joint distribution higher at mass-coupling ranges corresponding to the QCD axion. For the hidden photon, we may weight the distribution higher at mass-coupling ranges corresponding to an inflationary pro-

duction mechanism [15], which produces an order unity fraction of the observed dark-matter density. We may choose to weight the distribution over dark-matter frequency very high at the frequencies of candidate signals found in previous searches. In the context of such signals, discussed at the end of this section, we will see the utility of having a generic, probabilistic scan function (105). This function enables the direct comparison of different search scenarios for impedance/noise matching optimization; in other words, we may treat these optimizations on equal footing, rather than arriving at results from potentially disparate value functions. The distribution of dark matter across frequency space, given a particular rest mass, is also unknown. For virialized dark matter, we know that the distribution has approximate width $\Delta\nu_{\text{DM}}/\nu_{\text{DM}}^0 \sim 10^{-6}$, but we do not know the precise value of the signal bandwidth or the particular fine structure. In fact, as shown by Ref. [46], the narrowband distribution may contain even narrower peaks, representing dark matter that has fallen into the galactic gravitational potential well relatively recently, and therefore, has not yet virialized. These features may constitute a significant percentage of the dark-matter energy density.

1. Value functional for matching network optimization in a log-uniform search

We will compute the value function under the following assumptions. These assumptions are for a “log uniform” search—an uninformative prior for the properties of the dark matter. In large regions of unexplored axion/hidden photon phase space, this is the most appropriate assumption.

1. The probability distribution over dark-matter search frequency is log uniform:

$$P(\nu_{\text{DM}}^0) \propto \frac{1}{\nu_{\text{DM}}^0}. \quad (106)$$

A log-uniform prior is appropriate for a search in which we are ignorant about the scale of the mass and coupling of the dark matter. A log-uniform distribution is a prior that qualitatively matches exclusion plots, which are usually logarithmic, and it is also more natural than a linear-uniform distribution because the bandwidth of the dark-matter signal is proportional to the frequency ν_{DM}^0 .

2. It is a fairly common assumption that the distribution over dark-matter velocity—and therefore, the distribution over speed—has no explicit dependence on mass or coupling.

[47–49] The standard halo model, as demonstrated in Appendix C, is one such model. Then, the distribution over frequency $\frac{d\rho_{\text{DM}}}{d\nu}(\nu, \nu_{\text{DM}}^0)$ will depend not separately on the two arguments, but on the parameter $u = (\nu - \nu_{\text{DM}}^0)/\nu_{\text{DM}}^0 = v^2/2c^2$, where v is the speed corresponding to frequency ν . (See equation (A4).) We may then re-parameterize the energy-density distribution over frequency as

$$\left(\frac{d\rho_{\text{DM}}}{d\nu}\right)(\nu, \nu_{\text{DM}}^0) = \frac{1}{\nu_{\text{DM}}^0} \frac{d\rho_{\text{DM}}}{du}(u). \quad (107)$$

We assume a single such distribution. In other words, the probability is unity for that distribution and zero for all others, and for each mass, $d\rho_{\text{DM}}/du$ is the same. It is evident from equation (100) that the limit on sensitivity, set by the coupling $g_{\text{DM},\text{min}}$ for which the total SNR is unity (see Section IV C), will depend on the particular dark-matter distribution. However, as we will show, the optimal matching and time allocation does not depend on the distribution for either the log-uniform or candidate searches. We define a constant

$$\beta \equiv \max_{\nu_1 \leq \nu_{\text{DM}}^0 \leq \nu_h} \frac{\Delta\nu_{\text{DM}}^c(\nu_{\text{DM}}^0)}{\nu_{\text{DM}}^0}. \quad (108)$$

By construction, $\beta \ll 1$. Additionally, note that these assumptions regarding the distribution naturally lead to a value of $\Delta\nu_{\text{DM}}^c(\nu_{\text{DM}}^0)/\nu_{\text{DM}}^0$ that can be taken to be constant across the search band (although, for the impedance-matching optimization, we will not make this restriction).

3. We assume that the dwell time τ is much longer than $t_{\text{circ}}^*(\nu_{\text{DM}}^0)$ for all dark-matter frequencies within the search band. Under this assumption, steady-state is reached upon excitation of a dark-matter voltage signal and (100) applies. This allows an apples-to-apples comparison of all possible impedance-matching circuits (see eq. (63)).

We note that, in practice, this assumption may not hold. For instance, if probing with a narrowband resonator with resonance frequency near the high end of the search range, the dark-matter coherence time at the low end of the search range may be much longer than the resonator ring-up time. This is especially true when performing a search over orders of magnitude in mass. It is inefficient to wait such long times because as we will learn in Section V A 3, the sensitivity bandwidth is also narrowband and the resonator will not provide high-SNR information at frequencies far detuned from

resonance. It also leaves the experiment more vulnerable to spurious electromagnetic interference. Practical limitations will restrict the range of dark-matter frequencies at which we retrieve data from a particular resonance frequency. The follow-on room-temperature electronics will include analog filters, passing data only in a narrowband around the resonance frequency. This is necessary to reject out-of-band noise that can saturate amplifiers. Moreover, far away from the resonance frequency, constructing the optimal filter with sufficiently low noise level becomes challenging. We stress that our assumption about the dwell time is simply to provide a comparison of all possible matching networks, resonant or otherwise, rather than a reflection of these practical circumstances.

4. Within the range of integration over search frequency, the probability distribution over g_{DM} is approximately independent of dark-matter mass.

Under these assumptions, from (51) and (100), we find that, for the log-uniform search, the value functional reduces to

$$\begin{aligned}
F_{\text{neu}}[S_{21}^{(1)}(\nu)] &= \gamma_0 \int_{\nu_l}^{\nu_h} d\nu_{\text{DM}}^0 \int_0^\beta du \left(\frac{(1+u)L_{\text{PU}}}{R(\nu_{\text{DM}}^0(1+u))} \frac{1}{h} \frac{d\rho_{\text{DM}}}{du}(u) \right. \\
&\quad \left. \psi(\nu_{\text{DM}}^0(1+u), S_{21}^{(1)}(\nu_{\text{DM}}^0(1+u)), n(\nu_{\text{DM}}^0(1+u))) \right)^2 \\
&= \gamma_0 \int_0^\beta du \left(\frac{\sqrt{1+u}}{h} \frac{d\rho_{\text{DM}}}{du}(u) \right)^2 \int_{\nu_l(1+u)}^{\nu_h(1+u)} d\bar{\nu} \left(\frac{L_{\text{PU}}}{R(\bar{\nu})} \psi(\bar{\nu}, S_{21}^{(1)}(\bar{\nu}), n(\bar{\nu})) \right)^2,
\end{aligned} \tag{109}$$

where γ_0 is a constant, independent of the matching network. In the second line, we have exchanged the order of integration and have made the change of variable $\bar{\nu} = \nu_{\text{DM}}^0(1+u)$. In any practical search, during the data-taking period, there will not be a sharp cutoff to the search range; for example, if a resonator is placed close to ν_h , it will collect data not only on the hypothesis that $\nu_{\text{DM}}^0 = \nu_h$ but also on the hypothesis that $\nu_{\text{DM}}^0 = \nu_h(1+\delta)$, where $\delta \ll 1$. By this reasoning, we may omit the $(1+u)$ factors in the limits of the integral over $\bar{\nu}$. In fact, as we will see in the maximization with the Bode-Fano constraint, doing so induces a negligible fractional error of order at most $\beta \ll 1$. This decouples the integrals over u and $\bar{\nu}$ and yields

$$F_{\text{neu}}[S_{21}^{(1)}(\nu)] = \gamma_1 \int_{\nu_l}^{\nu_h} d\bar{\nu} \left(\frac{L_{\text{PU}}}{R(\bar{\nu})} \psi(\bar{\nu}, S_{21}^{(1)}(\bar{\nu}), n(\bar{\nu})) \right)^2, \tag{110}$$

where γ_1 is a constant containing the integral over u .

2. Matching network optimization for log-uniform search: the Bode-Fano constraint

Let us assume that the loss is frequency-independent, $R = R(\bar{\nu})$. Scaling out the constants of equation (110), namely $\gamma_1(L_{\text{PU}}/R)^2$, we finally arrive at

$$\begin{aligned}\bar{F}_{\text{neu}}[S_{21}^{(1)}(\nu)] &= \int_{\nu_l}^{\nu_h} d\bar{\nu} \left(\psi(\bar{\nu}, S_{21}^{(1)}(\bar{\nu}), n(\bar{\nu})) \right)^2 \\ &= \int_{\nu_l}^{\nu_h} d\bar{\nu} N_{\text{tot}}(\bar{\nu}, S_{21}^{(1)}(\bar{\nu}), n(\bar{\nu}))^{-2} = \int_{\nu_l}^{\nu_h} d\bar{\nu} \left(\frac{|S_{21}^{(1)}(\bar{\nu})|^2}{|S_{21}^{(1)}(\bar{\nu})|^2 n(\bar{\nu}) + 1} \right)^2,\end{aligned}\quad (111)$$

which we will refer to as the scaled, log-uniform-search value functional. By maximizing this functional in particular, we will determine the best matching network. This value functional is similar to the Wiener-filtered energy resolution in a calorimeter [35], which is the integral of the inverse-squared noise-equivalent power (instead of the integral of inverse-squared noise-equivalent number).

The signal source contains a complex impedance, with resistance R and pickup inductance L_{PU} , and the amplifier input impedance is real. Let us assume that the matching network is linear, passive, lossless and reciprocal. The Bode-Fano criterion [31, 32, 39] then applies:

$$\int_{\nu_l}^{\nu_h} d\bar{\nu} \ln \left(\frac{1}{|S_{22}^{(1)}(\bar{\nu})|} \right) \leq \frac{R}{2L_{\text{PU}}}.\quad (112)$$

We will discuss relaxation of the loss and reciprocity assumptions in Section V A 5.

For the lossless network, equation (98) yields

$$\int_{\nu_l}^{\nu_h} d\bar{\nu} \ln \left(\frac{1}{1 - |S_{21}^{(1)}(\bar{\nu})|^2} \right) \leq \frac{R}{L_{\text{PU}}}.\quad (113)$$

We now derive the constraint that the Bode-Fano criterion imposes on the scaled, log-uniform-search value functional (equation 111). This will allow us to understand the limit placed by Bode-Fano on the matching network, and to evaluate how close a single-pole resonator is to this limit. The derivation of this inequality will require the definition and manipulation of an auxiliary function h .

We define the auxiliary function of two variables

$$h(y, s) := \ln \left(\frac{1}{1 - y} \right) - s \left(\frac{y}{yn(\nu_h) + 1} \right)^2\quad (114)$$

on the domain $(y, s) \in [0, 1] \times [0, \infty)$. This function has the following properties:

- $h(0, s) = 0$ for all s .
- $\lim_{y \rightarrow 1^-} h(y, s) = \infty$ for all s .
- There exists a unique value of s , termed s^* , such that $h(y, s^*)$ has precisely two zeros and is nonnegative for all y , $0 \leq y \leq 1$. One of these zeros is located at $y_0 > 0$. The zero is also a minimum of $h(y, s^*)$, so from h and its first derivative we find

$$\ln \left(\frac{1}{1 - y_0} \right) - s^* \left(\frac{y_0}{y_0 n(\nu_h) + 1} \right)^2 = 0, \quad (115)$$

and

$$\frac{1}{1 - y_0} - 2s^* \frac{y_0}{(y_0 n(\nu_h) + 1)^3} = 0. \quad (116)$$

We may solve for s^* in terms of y_0 , which gives

$$s^* = \left(\frac{y_0 n(\nu_h) + 1}{y_0} \right)^2 \ln \left(\frac{1}{1 - y_0} \right). \quad (117)$$

We also find an equation for y_0 :

$$\ln \left(\frac{1}{1 - y_0} \right) = \frac{y_0}{1 - y_0} \frac{y_0 n(\nu_h) + 1}{2}. \quad (118)$$

Since $0 \leq |S_{21}^{(1)}(\nu)|^2 \leq 1$, we may substitute $|S_{21}^{(1)}(\nu)|^2$ for y in $h(y, s^*)$. Then, we find for any frequency $\bar{\nu}$, $\nu_l \leq \bar{\nu} \leq \nu_h$,

$$\ln \left(\frac{1}{1 - |S_{21}^{(1)}(\bar{\nu})|^2} \right) \geq s^* \left(\frac{|S_{21}^{(1)}(\bar{\nu})|^2}{|S_{21}^{(1)}(\bar{\nu})|^2 n(\nu_h) + 1} \right)^2. \quad (119)$$

Integrating both sides and using $n(\nu) \geq n(\nu_h)$, we arrive at

$$\begin{aligned} \bar{F}_{\text{neu}}[S_{21}^{(1)}(\nu)] &= \int_{\nu_l}^{\nu_h} d\bar{\nu} \left(\frac{|S_{21}^{(1)}(\bar{\nu})|^2}{|S_{21}^{(1)}(\bar{\nu})|^2 n(\bar{\nu}) + 1} \right)^2 \\ &\leq \int_{\nu_l}^{\nu_h} d\bar{\nu} \left(\frac{|S_{21}^{(1)}(\bar{\nu})|^2}{|S_{21}^{(1)}(\bar{\nu})|^2 n(\nu_h) + 1} \right)^2 \\ &\leq \frac{1}{s^*} \int_{\nu_l}^{\nu_h} d\bar{\nu} \ln \left(\frac{1}{1 - |S_{21}^{(1)}(\bar{\nu})|^2} \right) \\ &\leq \left(\frac{y_0}{y_0 n(\nu_h) + 1} \right)^2 \left(\ln \left(\frac{1}{1 - y_0} \right) \right)^{-1} \frac{R}{L_{\text{PU}}}, \end{aligned} \quad (120)$$

where in the last inequality, we have used (117). The value y_0 satisfies (118), so it depends on $n(\nu_h)$. We omit explicit dependence for conciseness where convenient.

Is it possible to have equality, or approximate equality, in (120)? To satisfy with equality, we must have the following:

- From the third inequality of (120), the matching circuit must satisfy the Bode-Fano constraint (112) with equality. From [32], we find that equality is satisfied for top-hat transmission profiles.
- From the second inequality, $h(|S_{21}^{(1)}(\bar{\nu})|^2, s^*) = 0$ for all frequencies $\bar{\nu}$. This means the transmission profile only takes on two values: $|S_{21}^{(1)}(\bar{\nu})|^2 = 0$ or $|S_{21}^{(1)}(\bar{\nu})|^2 = y_0(n(\nu_h))$.
- From the first inequality, we must have $\bar{\nu} \approx \nu_h$ for all frequencies where $|S_{21}^{(1)}(\bar{\nu})|^2 \neq 0$.

Together, these imply that equality is achieved by a narrowband top-hat transmission profile centered near ν_h . The height of the top-hat transmission is

$$|S_{21}^{(1)}|_{\text{BF,hat}}^2 = y_0(n(\nu_h)), \quad (121)$$

and the width is, from (112),

$$\Delta\nu_{\text{BF,hat}} = \frac{R}{L_{\text{PU}}} \left(\ln \left(\frac{1}{1 - y_0(n(\nu_h))} \right) \right)^{-1}. \quad (122)$$

The top-hat can be considered narrowband if $\Delta\nu_{\text{BF,hat}} \ll \nu_h$, which will be the case for a sufficiently low-loss signal source.

We analyze two limits of expressions (120), (121), and (122): low thermal occupation number $n(\nu_h) \ll 1$ and high thermal occupation number $n(\nu_h) \gg 1$.

In the $n(\nu_h) \ll 1$ limit, we find

$$|S_{21}^{(1)}|_{\text{BF,hat}}^2 \approx 0.7, \quad \Delta\nu_{\text{BF,hat}} \approx 0.8 \frac{R}{L_{\text{PU}}}, \quad (123)$$

and

$$\bar{F}_{\text{neu}}[S_{21}^{(1)}(\nu)] \lesssim 0.4 \frac{R}{L_{\text{PU}}}. \quad (124)$$

In the $n(\nu_h) \gg 1$ limit, we find

$$|S_{21}^{(1)}|_{\text{BF,hat}}^2 \approx \frac{1}{n(\nu_h)}, \quad \Delta\nu_{\text{BF,hat}} \approx n(\nu_h) \frac{R}{L_{\text{PU}}}, \quad (125)$$

and

$$\bar{F}_{\text{neu}}[S_{21}^{(1)}(\nu)] \lesssim \frac{1}{4n(\nu_h)} \frac{R}{L_{\text{PU}}}. \quad (126)$$

Of particular interest in these limits is the Bode-Fano bound, summarized here:

$$\bar{F}_{\text{neu}}[S_{21}^{(1)}(\nu)] \lesssim \begin{cases} 0.4 \frac{R}{L_{\text{PU}}}, & n(\nu_h) \ll 1 \\ \frac{1}{4n(\nu_h)} \frac{R}{L_{\text{PU}}}, & n(\nu_h) \gg 1 \end{cases} \quad (127)$$

which achieves equality with the top-hat profiles discussed above.

We note that a constraint similar to (112) exists for RC circuits. Therefore, if one chose to couple to the observable electric field produced by the dark matter, an inequality similar to (120) would result. A construction of the top-hat transmission may be performed using Chebyshev filters. As one increases the number of LC poles in the filter, the transmission profile approaches a top-hat. For more information, see [32]. Because these circuits are multi-pole and would need to be tunable to search for a wide range of dark matter, they would be difficult to implement in an experiment. It is therefore important to ask how well a single-pole resonator compares to the Bode-Fano optimal top-hat, described by (127), and whether this simply tunable implementation is close enough to optimal to be used in practical circuits.

3. Matching network optimization for log-uniform search with single-pole resonator

Here, we will optimize the matching network under the assumption that the transmission profile represents a single-pole resonator. The log-uniform-search value functional that we start with is (109). Thus, unlike the Bode-Fano bound, our optimization of the single-pole resonator will not require the assumption of frequency-independent resistance. The optimization occurs in three steps. First, we identify the specific parameters (more specific than the entire transmission profile $S_{21}^{(1)}(\nu)$, which is already substantially constrained by restriction to a single-pole resonator) that govern matching between the resonator and the amplifier input. For the purpose of further analysis in Section V A 4, we will relate these parameters back to Fig. 7 and the concept of sensitivity bandwidth that led to our value functional. Second, fixing the resonance frequency ν_r and internal quality factor, we maximize the value functional with respect to the matching parameters. Third, setting the loss to be frequency-independent, varying the resonance frequency, and building on the results of the second step, we compare the optimized single-pole resonator to the Bode-Fano bound of (120).

a. Resonator Matching Parameters

Let us hold the signal source properties L_{PU} and $R(\nu)$ fixed. The matching network (the capacitance C and the coupling capacitance C_c in Fig. 5) and, therefore, the scattering parameters, are then determined by the resonance frequency ν_r and the coupling coefficient

[30]. The coupling coefficient is defined by

$$\xi \equiv \frac{Q_{\text{int}}}{Q_{\text{cpl}}}. \quad (128)$$

ξ describes the coupling of the resonator to the output transmission line. For $\xi > 1$, the resonator is overcoupled and losses through the transmission line dominate. For $\xi < 1$, the resonator is undercoupled and losses intrinsic to the resonator ($R(\nu_r)$) dominate. For $\xi = 1$, the resonator is critically coupled, and the loss is the same in both channels. The overall quality factor is

$$Q = \frac{Q_{\text{int}}}{1 + \xi}. \quad (129)$$

From equations (37) and (38), ξ can be rewritten as

$$\xi = \frac{(2\pi\nu_r L_{\text{PU}})^2 (2\pi\nu_r C_c)^2 Z_0}{R(\nu_r)}. \quad (130)$$

Recognizing $R(\nu_r)/((2\pi\nu_r L_{\text{PU}})^2 (2\pi\nu_r C_c)^2)$ as the impedance of the resonator at the resonance frequency, as seen from the transmission line, we observe that ξ is also the ratio of the amplifier noise impedance (equal to input impedance) to the resonator impedance. We will thus call ξ the resonator matching parameter. Additionally, note that the matching parameter can be adjusted in our circuit model by varying the capacitance coupling the resonator to the output transmission line.

We rewrite the transmission profile and the inverse of the noise-equivalent number, ψ in terms of the resonator matching parameter ξ . The resonator transmission (48) may be written as

$$|S_{21}^{(1)}(\nu, \nu_r, Q_{\text{int}}, \xi)|^2 = \frac{4\xi}{(1 + \xi)^2 + 4(Q_{\text{int}})^2 \left(\frac{\nu}{\nu_r} - 1\right)^2}, \quad (131)$$

where we have made the approximation $|\nu - \nu_r| \ll \nu_r$. Eq. (101) then becomes

$$\psi(\nu, \nu_r, n(\nu), Q_{\text{int}}, \xi) = \frac{4\xi}{4\xi n(\nu) + (1 + \xi)^2 + 4(Q_{\text{int}})^2 \left(\frac{\nu}{\nu_r} - 1\right)^2}. \quad (132)$$

Note that we have changed the parametrization of ψ from (101). Instead of using $S_{21}^{(1)}(\nu)$ as the argument, we have inserted the variables ν_r , Q_{int} , and ξ . This is simply because, for the resonator, we are specifically able to point out the variables of significance to the inverse of the noise-equivalent number; they are these three parameters.

Recall from Section IV that we assume the total and internal Qs are both much greater 1, so $\xi \ll Q_{\text{int}}$. As a consistency check, we will show that the optimum value of the resonator

matching parameter satisfies this inequality. We also assume, that for all resonant scan steps in our search band, $n(\nu_r) \ll Q_{\text{int}}$ —that is, the on-resonance thermal occupation number is much less than the internal quality factor. At dilution refrigerator temperatures of 10 mK and for internal quality factors on the order of one million, this is an accurate approximation down to a resonance frequency of ~ 1 kHz.

Under these assumptions, (132) shows that $\psi_r(\nu, \nu_r, n(\nu), Q_{\text{int}}, \xi)$ is strongly peaked at $\nu = \nu_r$. In particular, for frequencies ν , $|\nu - \nu_r| \ll \nu_r$,

$$\begin{aligned} \psi(\nu, \nu_r, n(\nu), Q_{\text{int}}, \xi) &\approx \psi(\nu, \nu_r, n(\nu_r), Q_{\text{int}}, \xi) \\ &= \frac{4\xi}{4\xi n(\nu_r) + (1 + \xi)^2} \left(1 + \frac{4(Q_{\text{int}})^2}{4\xi n(\nu_r) + (1 + \xi)^2} \left(\frac{\nu}{\nu_r} - 1 \right)^2 \right)^{-1}. \end{aligned} \quad (133)$$

ψ thus behaves as a Lorentzian centered at ν_r with a maximum value of

$$\psi_{\text{max}}(\nu_r, n(\nu_r), \xi) = \frac{4\xi}{4\xi n(\nu_r) + (1 + \xi)^2}, \quad (134)$$

and a quality factor of

$$Q_s(\nu_r, n(\nu_r), Q_{\text{int}}, \xi) = \frac{Q_{\text{int}}}{(4\xi n(\nu_r) + (1 + \xi)^2)^{1/2}}. \quad (135)$$

Since $n(\nu_r), \xi \ll Q_{\text{int}}$, we have $Q_s(\nu_r, n(\nu_r), Q_{\text{int}}, \xi) \gg 1$. We will refer to $Q_s(\nu_r, n(\nu_r), Q_{\text{int}}, \xi)$ as the sensitivity quality factor and $\nu_r/Q_s(\nu_r, n(\nu_r), Q_{\text{int}}, \xi)$ as the sensitivity bandwidth. From equation (131), for dark-matter search frequencies within the sensitivity bandwidth,

$$|\nu_{\text{DM}}^0 - \nu_r| \leq \frac{\nu_r}{2Q_s(\nu_r, n(\nu_r), Q_{\text{int}}, \xi)}, \quad (136)$$

we obtain

$$|S_{21}^{(1)}(\nu, \nu_r, Q_{\text{int}}, \xi)|^2 n(\nu) \geq 1, \quad (137)$$

so the thermal noise transmitted to the amplifier is greater than or equal to the quantum noise. It is over this range of frequencies that the resonator is sensitive to dark matter without degradation from the quantum noise. A smaller value of Q_s implies a larger sensitivity bandwidth. Comparing with (129), we find that the sensitivity quality factor must always be smaller than the overall quality factor. This sensitivity bandwidth is displayed pictorially in Fig. 7.

It is also useful to make the change of variable $x = 2Q_{\text{int}} \left(\frac{\nu - \nu_r}{\nu_r} \right)$. x represents the detuning from the resonance frequency as a fraction of the linewidth of the uncoupled resonator. Eq.

(133) becomes

$$\begin{aligned}\psi(x, \nu_r, n(\nu_r), \xi) &= \frac{4\xi}{4\xi n(\nu_r) + (1 + \xi)^2} \left(1 + \frac{1}{4\xi n(\nu_r) + (1 + \xi)^2} x^2 \right)^{-1} \\ &= \psi_{\max}(\nu_r, n(\nu_r), \xi) \left(1 + \frac{Q_s(\nu_r, n(\nu_r), \xi)^2}{Q_{\text{int}}^2} x^2 \right)^{-1}.\end{aligned}\quad (138)$$

As we see, ψ is dependent on resonator matching parameter ξ . Therefore, it is precisely the parameter we should use to optimize the impedance filter for fixed resonance frequency.

b. Optimization at fixed resonator frequency

Suppose we fix the resonance frequency ν_r somewhere in the search band, $\nu_l \leq \nu_r \leq \nu_h$. Since we are already fixing the pickup inductance and the frequency-dependent loss, this also fixes the internal quality factor Q_{int} . The parameter ξ now completely determines the impedance properties of the single-pole resonator. We will therefore optimize the value function (110) with respect to ξ . With resonance frequency, pickup inductance, and source loss fixed, this is equivalent to maximizing with respect to the transmission profile $S_{21}^{(1)}(\nu)$.

Since ψ is a sharply-peaked Lorentzian of quality factor much greater than unity and the loss is assumed to be relatively slowly varying with frequency, we may approximate the resistance to take on its on-resonance value everywhere in the integration range: $R(\bar{\nu}) \approx R(\nu_r)$. Additionally, changing variables $x = 2Q_{\text{int}} \frac{\bar{\nu} - \nu_r}{\nu_r}$, we find

$$F_{\text{neu}}[\nu_r, \xi] = \gamma_1 \left(\frac{L_{\text{PU}}}{R(\nu_r)} \right)^2 \frac{\nu_r}{2Q_{\text{int}}} \int_{-\infty}^{\infty} dx \, \psi(x, \nu_r, n(\nu_r), \xi)^2. \quad (139)$$

We have extended the limits of integration to $-\infty$ to ∞ because the search band will contain multiple sensitivity bandwidths on each side of ν_r (as discussed below eq. (109), the search band cutoffs are “soft” and can be adjusted slightly for resonant frequencies on either edge). Performing the integral using (138) yields

$$F_{\text{neu}}[\nu_r, \xi] = \gamma_1 \left(\frac{L_{\text{PU}}}{R(\nu_r)} \right)^2 \frac{4\pi\nu_r}{Q_{\text{int}}} \frac{\xi^2}{(4\xi n(\nu_r) + (1 + \xi)^2)^{3/2}}. \quad (140)$$

Maximizing with respect to ξ ,

$$\xi^{\text{opt}}(\nu_r, n(\nu_r)) = \frac{1}{2} \left(2n(\nu_r) + 1 + \sqrt{(2n(\nu_r) + 1)^2 + 8} \right). \quad (141)$$

In the high $n(\nu_r) \ll 1$ and low $n(\nu_r) \gg 1$ occupation limits, this expression reduces to

$$\xi^{\text{opt}}(\nu_r, n(\nu_r)) \approx \begin{cases} 2 & \text{if } n(\nu_r) \ll 1 \\ 2n(\nu_r) & \text{if } n(\nu_r) \gg 1 \end{cases} \quad (142)$$

As a consistency check, note that, because $n(\nu_r) \ll Q_{\text{int}}$, our assumption of $\xi \ll Q_{\text{int}}$ is satisfied by the optimum. Where convenient, we will omit the arguments of ξ^{opt} .

c. Comparison of Bode-Fano optimal matching circuit and single-pole resonator

We now compare the Bode-Fano optimal matching circuit (the top-hat described in Section V A 2). We find the resonance frequency and the matching parameter ξ that maximize the scaled, log-uniform-search value functional (111) for integrated sensitivity across $\nu_l \leq \nu \leq \nu_h$. In the previous section, we asked, given a resonance frequency, how do we optimize the matching parameter ξ for integrated sensitivity. Here, we ask which resonance frequency we choose to best approach the Bode-Fano bound. We expect that the resonance frequency should be close to the upper bound of the search range, $\nu_r \approx \nu_h$, because the thermal occupation number decreases with frequency, decreasing the noise-equivalent number and increasing ψ .

We relax the assumption of fixed resonance frequency and observe that whatever the resonance frequency is, the optimal matching parameter is given by (141). We take the loss $R(\nu) = R$ to be frequency-independent. The scaled, log-uniform-search value functional of equation (111) now reads

$$\bar{F}_{\text{neu}}[\nu_r, \xi^{\text{opt}}(\nu_r, n(\nu_r))] \approx \frac{2(\xi^{\text{opt}}(\nu_r, n(\nu_r)))^2}{(4\xi^{\text{opt}}(\nu_r, n(\nu_r))n(\nu_r) + (1 + \xi^{\text{opt}}(\nu_r, n(\nu_r)))^2)^{3/2}} \frac{R}{L_{\text{PU}}}, \quad (143)$$

where we have, similar to ψ , replaced the transmission profile with the relevant matching network parameters in the argument of \bar{F} . We have derived the above equation simply by eliminating the $\gamma_1(L_{\text{PU}}/R)^2$ term in (140), as we did in deriving (111). The first fraction is an increasing function of ν , so the value function is optimized by taking $\nu_r = \nu_h$. In summary, the resonant circuit that best approaches the Bode-Fano bound in (120) is one at the top of the search range, for which the value of the optimization functional is

$$\begin{aligned} \bar{F}_{\text{neu}}[\nu_h, \xi^{\text{opt}}(\nu_h, n(\nu_h))] &= \frac{2(\xi^{\text{opt}}(\nu_h, n(\nu_h)))^2}{(4\xi^{\text{opt}}(\nu_h, n(\nu_h))n(\nu_h) + (1 + \xi^{\text{opt}}(\nu_h, n(\nu_h)))^2)^{3/2}} \frac{R}{L_{\text{PU}}} \\ &\approx \begin{cases} \frac{8}{27} \frac{R}{L_{\text{PU}}} & \text{if } n(\nu_h) \ll 1 \\ \frac{1}{3\sqrt{3}} \frac{1}{n(\nu_h)} \frac{R}{L_{\text{PU}}} & \text{if } n(\nu_h) \gg 1 \end{cases} \end{aligned} \quad (144)$$

We now discuss important features of the results for resonators—in particular, the optimum matching parameter (141) and the result (144) comparing the best resonator to the Bode-Fano bound.

4. Discussion of single-pole resonator matching optimization for log-uniform search

Interestingly, for the log-uniform search, noise matching to the amplifier on resonance, corresponding to $\xi = 1$ and $|S_{21}^{(1)}(\nu_r, \nu_r, Q_{\text{int}}, \xi)| = 1$, is not the optimum for detector sensitivity. This may seem counterintuitive. We are not transmitting maximum power from the resonator at the optimum and the optimal match is a noise mismatch!

To understand this result, we focus on the limit $n(\nu) \gg 1$. The argument for the limit $n(\nu) \ll 1$ is similar, but the difference in value function (between optimal matching and noise matching) is small, approximately 20%. From (139), the quantity of interest is the integral of the square of the inverse noise-equivalent number, $\psi(x, \nu_r, n(\nu_r), \xi)^2$, over detuning. As ψ is Lorentzian, the integral can be approximated parametrically as the maximum value of the integrand multiplied by the linewidth. From (138),

$$\int_{-\infty}^{\infty} dx \psi(x, \nu_r, n(\nu_r), \xi)^2 \sim \psi_{\text{max}}(\nu_r, n(\nu_r), \xi)^2 \frac{Q_{\text{int}}}{Q_s(\nu_r, n(\nu_r), Q_{\text{int}}, \xi)}. \quad (145)$$

Using eqs. (134) and (135), for the noise matched case $\xi = 1$, the maximum value of ψ is

$$\psi_{\text{max}}(\nu_r, n(\nu_r), \xi = 1) \approx \frac{1}{n(\nu_r)}, \quad (146)$$

and the sensitivity quality factor is

$$Q_s(\nu_r, n(\nu_r), Q_{\text{int}}, \xi = 1) \approx \frac{Q_{\text{int}}}{2\sqrt{n(\nu_r)}}. \quad (147)$$

In contrast, for the optimally matched case $\xi = \xi^{\text{opt}}$, the maximum value of ψ is

$$\psi_{\text{max}}(\nu_r, n(\nu_r), \xi = \xi^{\text{opt}}) \approx \frac{2}{3n(\nu_r)}. \quad (148)$$

This corresponds to an SNR that is a factor of 2/3 worse than the noise-matched case for a signal on resonance. The sensitivity quality factor is

$$Q_s(\nu_r, n(\nu_r), Q_{\text{int}}, \xi = \xi^{\text{opt}}) \approx \frac{Q_{\text{int}}}{2\sqrt{3n(\nu_r)}}. \quad (149)$$

The sensitivity quality factor is smaller than that in the optimally matched case by a factor of $\sqrt{3n(\nu_r)}$.

Now we see what has happened. In return for a small, order unity sacrifice in on-resonance SNR, we have gained parametrically in the frequency range over which the resonator is not degraded by quantum noise. The bandwidth is $\sim \sqrt{n(\nu_r)}$ larger in the optimally matched

case than the noise matched case. Therefore, our value function should be $\sim \sqrt{n(\nu_r)}$ larger. Indeed, equation (140) gives, in the thermal limit,

$$\frac{F_{\text{neu}}[\nu_r, \xi^{\text{opt}}]}{F_{\text{neu}}[\nu_r, \xi = 1]} \approx \left(\frac{16}{27} n(\nu_r) \right)^{1/2}. \quad (150)$$

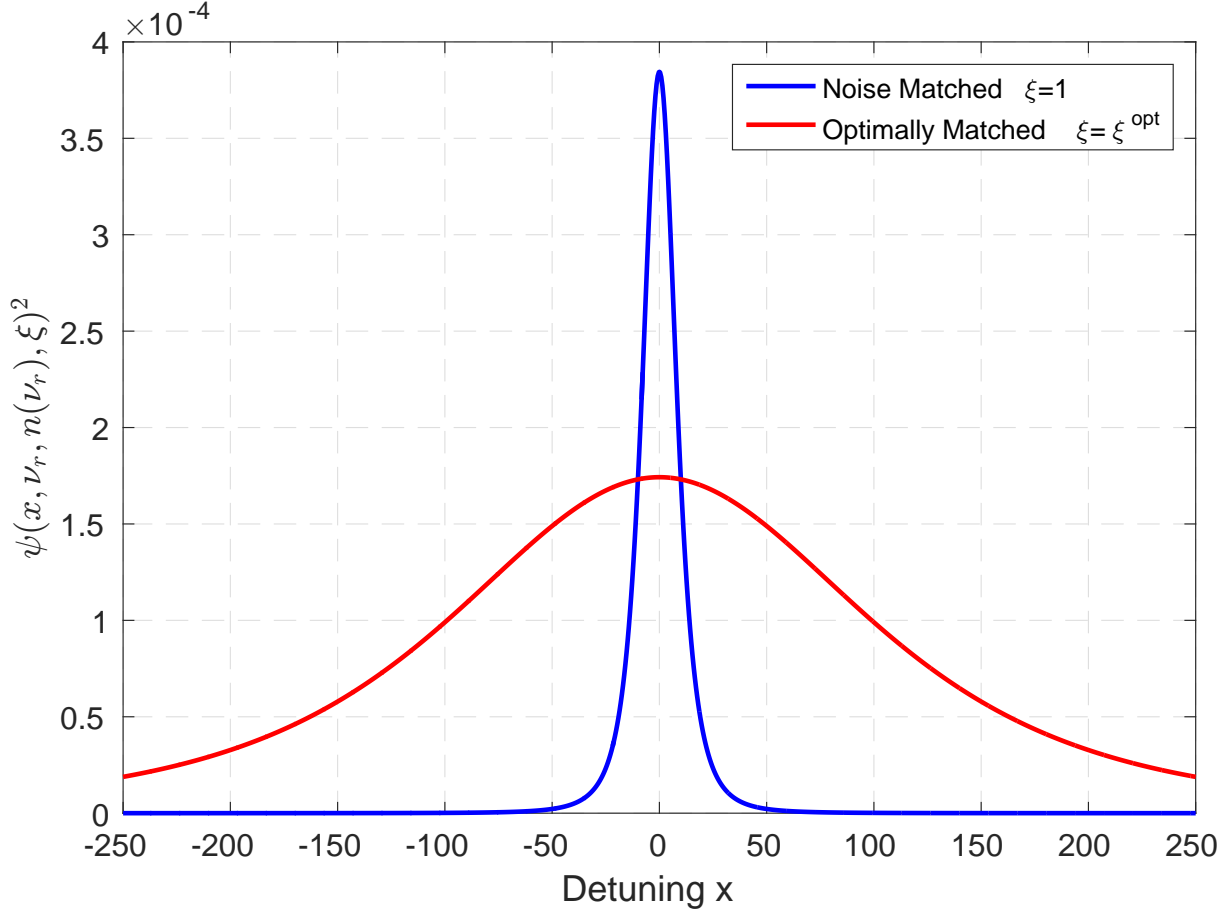


FIG. 8. $\psi(x, \nu_r, n(\nu_r), \xi)^2$ vs. the detuning from resonance $x = 2Q_{\text{int}} \left(\frac{\nu - \nu_r}{\nu_r} \right)$ for noise matching (blue) and optimal (red) matching, as determined by equation (141). We use $n(\nu_r) = 50$ for the on-resonance thermal occupation number.

In Fig. 8, we pictorially demonstrate the advantage obtained with optimal matching, as given by equation (141). Here, we plot the value of $\psi(x, \nu_r, n(\nu_r), \xi)^2$ vs the detuning from resonance $x = 2Q_{\text{int}} \left(\frac{\nu - \nu_r}{\nu_r} \right)$ for the noise-matched and optimally matched resonators, using the on-resonance thermal occupation number $n(\nu_r) = 50$. The maximum value of ψ^2 , which gives the square of the on-resonance inverse noise number, is smaller in the optimally matched case by a factor of $\approx 4/9$. In the noise-matched case, ψ^2 falls to half of its maximum

value at $|x| \approx 9$. In contrast, in the optimally matched case, ψ^2 has much larger width, falling to half of its maximum at $|x| \approx 112$. Therefore, the area under the curve, i.e. the integral of ψ^2 , which measures integrated detector sensitivity and which directly relates to the value of $F_{\text{neu}}[\nu_r, \xi]$, is larger in the optimally-matched resonator than in the noise-matched resonator.

It is useful to connect the result (141) back to the discussion of amplifier noise in the introduction. After all, it was the analysis of the noise in Section IV C 3 and Fig. 7 that ultimately led to these results. We consider each contribution to the total noise number of eq. (99). From equations (48), (49), (97),

$$N_{\text{tot}}(\nu, \nu_r, n(\nu_r), Q_{\text{int}}, \xi) = n(\nu_r) + \frac{1}{2} + \frac{1}{|S_{21}^{(1)}(\nu, \nu_r, Q_{\text{int}}, \xi)|^2} \frac{1}{2} + \frac{|S_{22}^{(1)}(\nu, \nu_r, Q_{\text{int}}, \xi)|^2}{|S_{21}^{(1)}(\nu, \nu_r, Q_{\text{int}}, \xi)|^2} \frac{1}{2}, \quad (151)$$

where we have approximated the thermal noise number as constant $n(\nu) \approx n(\nu_r)$ because we are interested in frequencies close to resonance. Rewriting this equation in terms of detuning x , for $|\nu - \nu_r| \ll \nu_r$,

$$N_{\text{tot}}(x, \nu_r, n(\nu_r), \xi) \equiv n(\nu_r) + \frac{1}{2} + \left(\frac{(1 + \xi)^2}{4\xi} + \frac{x^2}{4\xi} \right) \frac{1}{2} + \left(\frac{(1 - \xi)^2}{4\xi} + \frac{x^2}{4\xi} \right) \frac{1}{2}. \quad (152)$$

On the right-hand side of (152), the four terms, from left to right, represent thermal noise, zero-point fluctuation noise, amplifier imprecision noise, and amplifier backaction noise. We may readily read off the added noise number of the amplifier at detuning x

$$N_A(x, \xi) = \left(\frac{(1 + \xi)^2}{4\xi} + \frac{x^2}{4\xi} \right) \frac{1}{2} + \left(\frac{(1 - \xi)^2}{4\xi} + \frac{x^2}{4\xi} \right) \frac{1}{2} = \frac{1 + \xi^2}{4\xi} + \frac{x^2}{4\xi}, \quad (153)$$

which shows, as discussed previously, that quantum-limited noise temperature is only achieved when on-resonance and when noise-matched ($\xi = 1$). In (152), at detunings for which the sum of the first two terms is greater than the sum of the last two terms, the sensitivity is not degraded by amplifier noise. For what follows, we again assume the high occupation-number limit.

From equation (145), to determine the integrated sensitivity (quantified by the integral of ψ^2) and the optimal value of the matching parameter ξ , we must consider the sensitivity bandwidth as well as the on-resonance SNR. In the language of total noise-equivalent number, this is equivalent to determining the bandwidth over which thermal noise is larger than amplifier noise and determining the on-resonance, $x = 0$ noise number. We thus consider: (i) the change in on-resonance, $x = 0$ noise number as ξ varies from its noise matched value

$\xi = 1$ and (ii) the change in noise number as the frequency is detuned from resonance for fixed matching parameter ξ .

It is evident from (152) and (153) that the imprecision and backaction contributions to on-resonance noise number are minimized at $\xi = 1$. *Importantly, the variation of ξ from its noise-matched value is associated with the appearance of backaction on the resonator.* Additionally, the imprecision and backaction noise are each quadratic in detuning and increase away from resonance. As ξ is changed from unity, the on-resonance amplifier noise increases, and the detuning is effectively rescaled $x/2 \rightarrow x/2\sqrt{\xi}$.

For $\xi < 1$, the rescaling squeezes the profile of $N_{\text{tot}}(x, \nu_r, n(\nu_r), \xi)$ vs x , relative to the profile that we would find if $x^2/4\xi$ in (152) was replaced by its $\xi = 1$ value, $x^2/4$. As a result, there is a smaller bandwidth over which thermal noise dominates amplifier noise. Combined with the increased on-resonance noise number, this implies that the integrated sensitivity must be strictly worse for $\xi < 1$ than for $\xi = 1$. Any value of ξ less than unity therefore cannot be the optimum of $F[\nu_r, \xi]$.

For $\xi > 1$, the rescaling stretches the profile. In other words, there is a tradeoff between the on-resonance amplifier noise—and therefore, on-resonance SNR—and the bandwidth over which amplifier noise is sub-dominant, i.e. the bandwidth over which the resonator possesses appreciable sensitivity to dark matter. This observation is consistent with Fig. 8. We do not expect significant degradation as long as the on-resonance amplifier noise is less than or comparable to the thermal noise:

$$\left(\frac{(1 + \xi)^2}{4\xi} + \frac{(1 - \xi)^2}{4\xi} \right) \frac{1}{2} \lesssim n(\nu_r), \quad (154)$$

which is equivalent to

$$1 + (\xi)^2 \lesssim 4\xi n(\nu_r). \quad (155)$$

In combination with the stretching of the profile as ξ increases, (155) suggests that the optimal value of ξ varies parametrically as

$$\xi^{\text{opt}} \sim n(\nu_r), \quad (156)$$

which is consistent with equation (141). At this coupling, the on-resonance imprecision and backaction noise are comparable to the thermal noise.

We plot each of the terms contributing to $N_{\text{tot}}(x, \nu_r, n(\nu_r), \xi)$ in Fig. 9, using the same parameters as Fig. 8, for three different values of ξ : $\xi = 1/\xi^{\text{opt}}$, $\xi = 1$, $\xi = \xi^{\text{opt}}$. We

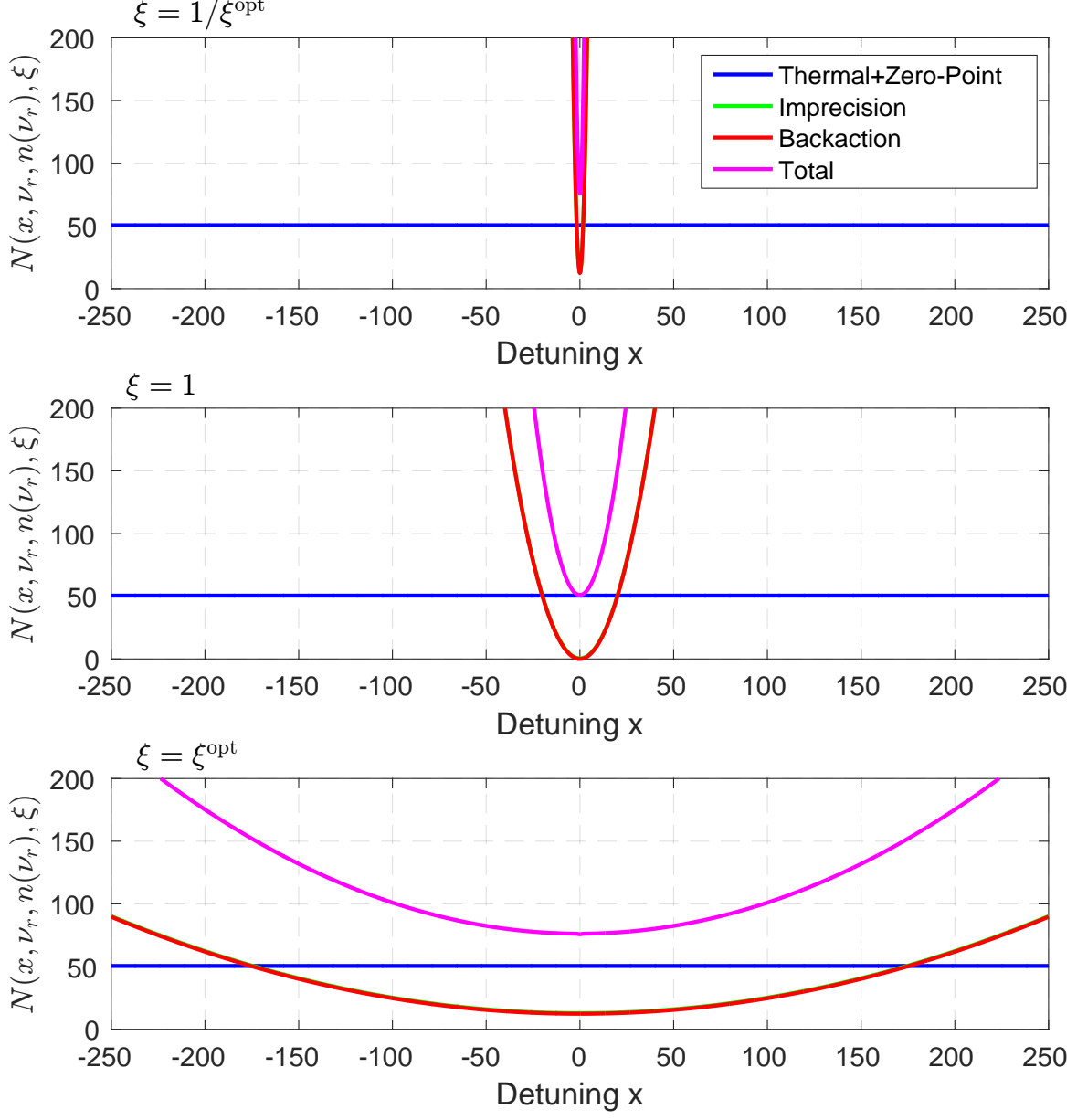


FIG. 9. The noise terms of equation (152) plotted for three different values of ξ : the inverse of optimal matching $\xi = 1/\xi^{\text{opt}}$ (top panel), noise matching $\xi = 1$ (middle panel), and optimal matching $\xi = \xi^{\text{opt}}$. Thermal and zero-point noise is in blue, imprecision noise is in green, and backaction noise is in red. The sum of these three curves, which represents the total noise number $N_{\text{tot}}(x, \nu_r, n(\nu_r), \xi)$, is plotted in magenta. As in Fig. 8, we use the thermal occupation number $n(\nu_r) = 50$. The imprecision curve is not visible because it overlaps with the backaction curve.

group together the thermal and zero-point fluctuation noise (blue curve). The imprecision curve (green) is not visible because of the overlap with the backaction (red). The sum of these three curves gives the total noise number (magenta). As indicated in (152), the on-resonance noise number is invariant under the transformation $\xi \rightarrow 1/\xi$, so the total noise number should not change between the cases $\xi = 1/\xi^{\text{opt}}$ (top panel) and $\xi = \xi^{\text{opt}}$ (bottom panel). This is observed in Fig. 9, where the on-resonance noise number is approximately 75, which is 50% worse than the noise matched case $\xi^i = 1$ (middle panel). This is consistent with equation (148) and corresponds to an on-resonance SNR which is 2/3 worse for the optimally-matched case than for the noise-matched case. As ξ increases, we observe the stretching of the amplifier noise profile, which in turn, stretches the profile of noise number. (The total noise number is offset vertically from the amplifier noise by the thermal noise, which is approximately constant for frequencies close to resonance $|\nu - \nu_r| \ll \nu_r$.) As a result, whereas the thermal noise is larger than amplifier noise for detunings $|x| < 2$ for $\xi = 1/\xi^{\text{opt}}$ and $|x| < 20$ for $\xi = 1$, it is the dominant noise source over a much larger bandwidth for $\xi = \xi^{\text{opt}}$; the thermal noise is the largest noise source for detunings $|x| < 175$. We see that the optimally matched resonator compensates for a small, order unity penalty in on-resonance noise number with a parametrically larger sensitivity bandwidth, yielding the maximum integrated sensitivity.

Additionally, the added noise number of the amplifier on resonance for the optimal match is

$$N_A(x = 0, \xi^{\text{opt}}) \approx \frac{1}{2}n(\nu_r), \quad (157)$$

where we have used the high-temperature value of (142). The added noise number is nowhere near the quantum limited value of 1/2, but rather, is comparable to the thermal noise number.

In summary, the optimal match for a search with a single-pole resonator read out by a quantum-limited amplifier is a noise mismatch on resonance, which is accompanied by large backaction on the resonator and amplifier noise number comparable to the thermal occupation number. A similar result applies to flux-to-voltage amplifiers, as discussed in the appendix.

Finally, we place the optimized single-pole resonator in the context of the Bode-Fano bound on single-moded inductive detectors (120). Comparing (144) and this bound, we find that the optimized resonator is approximately 75% of the fundamental limit, regardless of

the value of the thermal occupation number $n(\nu_h)$. *For any search range, the optimized single-pole resonator is close to the bound on integrated sensitivity given by the Bode-Fano constraint.* In combination with its superiority over purely broadband resistive and broadband reactive searches, demonstrated in Section II and Appendix G, this observation establishes the resonator as a near-ideal method for searching for dark matter over a wide bandwidth. Utilizing optimal matching is important as it provides a parametric $\sim \sqrt{n(\nu_r)}$ boost to the value of the value function. A similar Bode-Fano criterion exists for complex impedances (signal sources) with capacitors. Therefore, when capacitively coupling to electric fields induced by the dark matter (which one may do when the Compton wavelength of the dark matter is comparable to the detector size), the single-pole resonator will also be close to the Bode-Fano optimum.

Because the single-pole resonator is practical to implement, and is close to the Bode-Fano limit, we will focus on optimization and fundamental limits of a search with a tunable resonator. But first we digress to place the Bode-Fano constraint in broader context.

5. Evading the Bode-Fano Constraint

The Bode-Fano constraint is derived subject to particular (stated) assumptions. Relaxation of these assumptions can in principle make it possible to outperform the constraint.

In deriving the bound in eq. (120), we assume that the matching network is linear, passive, lossless, and reciprocal. These are key assumptions in the proof of the Bode-Fano criterion, as derived in [32]. Active and nonlinear schemes may be used to outperform our derived constraint. The limitations of the Bode-Fano criterion in this respect are documented in ref. [50]. We will explore these schemes, including active feedback, in future work.

First, we establish that the Bode-Fano constraint holds if the assumption of a lossless network is relaxed. It is not surprising that a lossy network does not outperform a lossless network. Broadband matching criteria allowing for network loss have been derived in a manner similar to the Bode-Fano criterion. Ref. [51] gives, for a reciprocal circuit,

$$\int_{\nu_l}^{\nu_h} d\bar{\nu} \ln \left(\frac{1}{1 - |S_{21}^{(1)}(\bar{\nu})|^2} \right) \leq \frac{R}{L_{\text{PU}}}. \quad (158)$$

For a lossless network, this expression reduces to the classic bound of eq. (112). We assume that any network loss is at temperature T and therefore, at the same temperature as the

loss R in the signal source. The total noise-equivalent number is not that given by (99), but instead, the more general expression

$$N_{\text{tot}}^{\text{lossy}}(\nu, S^{(1)}(\nu), n(\nu)) = \frac{(1 - |S_{22}^{(1)}(\nu)|^2)n(\nu) + 1}{|S_{21}^{(1)}(\nu)|^2}, \quad (159)$$

which may be derived using the techniques in Ref. [21]. $|S_{21}^{(1)}(\nu)|^2 + |S_{22}^{(1)}(\nu)|^2 < 1$ for a lossy network, so the noise-equivalent number is naturally greater when the matching network possesses loss. The analogue of the scaled, log-uniform-search value functional is the integral of the inverse-squared of equation (159):

$$\bar{F}_{\text{neu}}^{\text{lossy}}[S_{21}^{(1)}(\nu)] = \int_{\nu_l}^{\nu_h} d\bar{\nu} N_{\text{tot}}^{\text{lossy}}(\bar{\nu}, S^{(1)}(\bar{\nu}), n(\bar{\nu}))^{-2} = \int_{\nu_l}^{\nu_h} d\bar{\nu} \left(\frac{|S_{21}^{(1)}(\bar{\nu})|^2}{(1 - |S_{22}^{(1)}(\bar{\nu})|^2)n(\bar{\nu}) + 1} \right)^2. \quad (160)$$

Note that

$$\bar{F}_{\text{neu}}^{\text{lossy}}[S_{21}^{(1)}(\nu)] \leq \int_{\nu_l}^{\nu_h} d\bar{\nu} \left(\frac{|S_{21}^{(1)}(\bar{\nu})|^2}{|S_{21}^{(1)}(\bar{\nu})|^2 n(\bar{\nu}) + 1} \right)^2, \quad (161)$$

where equality is achieved when the network is lossless. We may proceed as in Section V A 2 to obtain a bound identical to (120). The bound can only be achieved with equality when the conditions laid out below eq. (120) are satisfied and when the matching network is lossless. For a reciprocal circuit, optimized integrated sensitivity thus requires no network loss. This leaves us with just the three assumptions of linear, passive, and reciprocal networks.

It should be remembered that a search can be accelerated by using multiple receiver circuits, and combining their information with the mathematical techniques described in previous sections. One must be careful to determine what one is holding fixed when comparing different implementations to determine an optimal experiment.

For example, one may consider dividing a fixed experimental volume into smaller sub-volumes that are scanned at different frequencies with approximately non-overlapping frequency response. The different sub-volumes can thus be frequency-division multiplexed and read out with a single amplifier. However, one can show that, if the size of the setup is less than a coherence length in all dimensions, at all frequencies being probed, that this multiplexing approach suffers a disadvantage. We compare a tunable one-pole resonator of volume V_{PU} to an N -element multiplexer, each element possessing volume V_{PU}/N . With the multiplexer, one is able to integrate at each search frequency $\sim N$ times longer than the single, larger resonator, but the energy coupled is at least $\sim N$ times smaller. We assume

that the noise power is identical for the large resonator and each resonator in the multiplexed setup. Then, the SNR at every frequency in the search range is reduced (relative to the large resonator) by at least $\sim N/\sqrt{N} = \sqrt{N}$. The coherence allows the SNR to increase at least linearly in volume, which leads to the advantage for the larger, single-pole resonator. Alternatively, instead of frequency division multiplexing sub-volumes operated at non-overlapping frequencies, one may consider building multiple identical resonators in sub-volumes tuned simultaneously to the same frequency (as opposed to the use of different frequencies in the multiplexed setup). Adding the output timestreams coherently then gives the same SNR as one would find with the single resonator. So there is no advantage over a single larger resonator.

One can generalize the question to consider multiple, spatially separated receiver circuits read out by the same amplifier. If the frequency bands overlap, we expect that there are strong constraints on sensitivity from generalized broadband matching criteria, such as those in the aforementioned reference [51]. One must also consider fundamental limitations on signal combining. For instance, it is a well-known theorem that no power combiner can be matched, reciprocal, and lossless [39]. The general optimization of multi-port receivers will be explored in further work. The analysis framework of Section IV is readily extended to calculate the sensitivity of these receivers. Instead of considering a 2×2 scattering matrix of one receiver port and one readout port, we could consider a $(N + 1) \times (N + 1)$ scattering matrix for N receiver ports and one readout port. One could even examine the case of multiple readout ports (e.g. multiple amplifiers) using a $(N + M) \times (N + M)$ scattering matrix. It also should be remembered that the receivers will interact, which could provide practical challenges in calibration.

Another possible multiple-receiver technique is to use receiver modes that possess overlapping volume. A multi-moded circuit falls into this category. The development of such circuits—in particular, multi-mode resonators—is an active area of inquiry in the axion detection community [52]. Multi-mode circuits naturally reduce the scan time in a light-field dark-matter search. Like the multi-port receivers of the previous paragraph, we can extend Section IV to investigate multi-mode circuits. We would write a scattering matrix for each mode, or a multi-port scattering matrix similar to that discussed above, with each receiver port representing a different mode; the latter may be required to more appropriately model mode interactions. At each search frequency, we could then consider sensitivity from

coherently-added or incoherently-added mode responses, depending on the details of the mode interactions.

In summary, the Bode-Fano limit can in principle be evaded by relaxing the assumption of a linear, passive, reciprocal system, using for example an active matching circuit. Furthermore, the optimization framework developed here can be extended to a generalized multiple receiver approach (including spatially isolated receivers and multiple spatial modes within the same volume) by extending to scattering matrices with larger dimensions and making optimal use of coherent and incoherent information. Strictly speaking, however, the optimized multiple receiver approach does not evade the Bode-Fano limit, but rather will be limited by a generalized broadband matching criteria.

6. Optimization of matching network for candidate signal

We return to the value function of equation (105) and consider the situation in which there is a candidate signal to validate. Is it still optimal to noise mismatch, in accordance with equation (141)? Suppose that the frequency of the signal is ν_{DM}^{0*} . Assume the resonator is centered at frequency ν_{DM}^{0*} with $Q_s(\nu_r, n(\nu_r), Q_{\text{int}}, \xi) \lesssim 10^6$ so that the signal is maximally resonantly enhanced and so that the dark-matter signal, of inverse width $\nu_{\text{DM}}^{0*}/\Delta\nu_{\text{DM}} \sim 10^6$, is within the sensitivity bandwidth. This condition may be enforced by setting the internal quality factor to $Q_{\text{int}} \lesssim 10^6$. In such a situation, we would, rather than assuming a log-uniform frequency probability distribution, adopt a prior that weights the probability high at this frequency. Keeping the other three assumptions introduced for the log-uniform search, this weighting would reduce the value function (105) to

$$F_{\text{cand}}(\xi) \approx \int dg_{\text{DM}} SNR^{\text{opt}} \left[\nu_{\text{DM}}^{0*}, g_{\text{DM}}, \left(\frac{d\rho_{\text{DM}}}{d\nu} \right) (\nu, \nu_{\text{DM}}^{0*}), \psi(\nu, \nu_r, n(\nu_r), Q_{\text{int}}, \xi), \tau \right]^2 P(g_{\text{DM}} | \nu_{\text{DM}}^{0*}). \quad (162)$$

For example, we could set the distribution to a delta function

$$P(\nu_{\text{DM}}^0) = \delta(\nu_{\text{DM}}^0 - \nu_{\text{DM}}^{0*}). \quad (163)$$

Using (100) and (133),

$$F_{\text{cand}}(\xi) \approx \gamma_2 \psi(\nu_{\text{DM}}^{0*} = \nu_r, \nu_r, n(\nu_r), Q_{\text{int}}, \xi)^2 = \gamma_2 \left(\frac{4\xi}{4\xi n(\nu_r) + (1 + \xi)^2} \right)^2, \quad (164)$$

where γ_2 is a constant. This expression is maximized when $\xi = 1$. Thus, when probing a fixed frequency, the resonator should be noise matched on-resonance to the transmission-line amplifier, such that the signal power is fully transmitted. That we should noise match is expected because for a fixed frequency probe, obtaining maximum sensitivity (maximum inverse noise number) at that frequency is important; obtaining maximum *integrated* sensitivity, as we did for the log-uniform search, is not a factor. *In summary, the optimization of the impedance-matching network differs for a wideband, scanning search and a search with the prior of a candidate signal. It is optimal to be noise-mismatched on resonance, as per (141), in the former case, and noise matched in the latter case.*

7. Comparison to other calculations

As a final remark for Section V A, we compare our calculations to similar results.

It was first observed by Krauss, Moody, and Wilczek in [53] that the resonator coupling coefficient (matching parameter) that maximizes integrated sensitivity is different from that which maximizes on-resonance SNR. However, the authors did not consider two aspects that are analyzed in this work.

First, it is clear that one must consider the spectral shape of the thermal noise, which is filtered through the matching network. If one does not, then $|S_{21}^{(1)}(\nu)|^2 n(\nu)$ simply becomes $n(\nu)$ in the denominator of (101). In this case, the thermal noise factor can be pulled out of the value functional (110) for a resonant detector, which yields the same optimization as that found for $n(\nu) \ll 1$: $\xi^{\text{opt}} \approx 2$. This is precisely what was found in Ref. [53].

A similar conclusion regarding integrated sensitivity was found in [24] for quantum squeezing. In this approach, the quantum limit is evaded by injecting a squeezed state in the resonator. The optimized coupling coefficient is $\xi \sim G_S$, where G_S is the squeezer gain. The authors explain the effect in terms of sensitivity outside of the resonator bandwidth (relative to internal quality factor), as we have done here. However, squeezer gains are often of order 10, while at low frequencies, the thermal occupation number in a 10 mK dilution refrigerator is much larger than that. For experiments using near-quantum-limited SQUID amplifiers, this implies a much larger sensitivity bandwidth as a fraction of resonator bandwidth, referred to the internal quality factor. This point will be revisited in Section VI, where we discuss the linear relationship between sensitivity bandwidth and scan time. The

optimization of quantum squeezing in the context of the framework developed in this paper will be explored in Part II.

We used the Bode-Fano criterion to show that the optimized single-pole resonator is close to the fundamental limit on matching networks for single-moded reactive detection. To our knowledge, this result is new and demonstrates the efficiency of cavity searches.

B. Optimization of Time Distribution

We have seen from the Bode-Fano analysis that a narrowband matching network is more sensitive than a broadband search. It is necessary to tune the narrowband matching circuit to different central frequencies to search over a large mass range. We now determine the optimal time distribution of a scanned system. We consider a single-pole resonator, which is almost as efficient as a tophat, but is much more practical in a tuned experiment.

The potential for a significant off-resonance contribution to the SNR shows the importance of considering SNR contributions from multiple resonant scan steps. Let $\{\nu_r^i\}$ represent the set of resonator scan frequencies; in the language of Section IV C 2, ν_r^i is the resonance frequency of the i th circuit configuration in the scan. The SNR for dark matter at frequency ν_{DM}^0 from the i th circuit is

$$\begin{aligned}
SNR^{\text{opt}} & \left[\nu_{\text{DM}}^0, g_{\text{DM}}, \left(\frac{d\rho_{\text{DM}}}{d\nu} \right) (\nu, \nu_{\text{DM}}^0), \psi(\nu, \nu_r^i, n(\nu), Q_{\text{int}}^i, \xi^i), \tau_i \right]^2 \\
& = (2\pi^2)^2 \tau_i \int_{\nu_{\text{DM}}^0}^{\nu_{\text{DM}}^0 + \Delta\nu_{\text{DM}}^c} d\nu \left(\frac{\nu L_{\text{PU}}}{R(\nu)} \frac{E_{\text{DM}}(\nu, \nu_{\text{DM}}^0, g_{\text{DM}}, \frac{d\rho_{\text{DM}}}{d\nu}(\nu, \nu_{\text{DM}}^0))}{h} \psi(\nu, \nu_r^i, n(\nu), Q_{\text{int}}^i, \xi^i) \right)^2 \\
& \approx (4\pi Q_{\text{int}}^i)^2 \tau_i \int_{\nu_{\text{DM}}^0}^{\nu_{\text{DM}}^0 + \Delta\nu_{\text{DM}}^c} d\nu \left(\frac{\nu}{\nu_r^i} \frac{g_{\text{DM}}^2 V_{\text{PU}}}{h} \frac{d\rho_{\text{DM}}}{d\nu}(\nu, \nu_{\text{DM}}^0) \frac{\xi^i}{4\xi^i n(\nu) + (1 + \xi^i)^2 + 4(Q_{\text{int}}^i)^2 \left(\frac{\nu}{\nu_r^i} - 1 \right)^2} \right)^2,
\end{aligned} \tag{165}$$

where ψ is as defined in (101), with the specific resonator parameters $\nu_r^i, Q_{\text{int}}^i, \xi^i$ in place of the entire transmission profile $S_{21}^{(1)}(\nu)$. We have allowed the quality factor to vary with resonance frequency, but have fixed the volume of the pickup element and the geometric factor c_{PU} , so that g_{DM} is not related to circuit configuration (e.g. subscript i is not necessary). This is an appropriate assumption for a tunable resonator, either in the form of free-space cavity or a lumped LC with a fixed pickup inductor and varying capacitance; we do not expect the detector volume or the overlap with the drive field pattern to change substantially (or at all)

during a scan. In the third line we assume that $|\nu_{\text{DM}}^0 - \nu_r^i| \ll \nu_r^i$; the resonator will only have sensitivity to dark matter within its sensitivity bandwidth, which we have found is a narrow bandwidth at optimal matching. For the narrowband dark-matter signal, this implies that $|\nu - \nu_r^i| \ll \nu_r^i$ for the entire integration range over ν and we approximate $R(\nu) \approx R(\nu_r^i)$ (see the resonator matching optimization in Section V A 1). Additionally, implicit in our SNR expression is that the dwell τ_i is much longer than $t_{\text{circ},i}^*(\nu_{\text{DM}}^0)$, defined in (66). For a resonator, the characteristic pole time is just the resonator ring-up time $\sim Q^i/\nu_r^i$. Because we restrict to resonators, we will define the timescale specifically as

$$t_{\text{circ},i}^*(\nu_{\text{DM}}^0) \rightarrow t^*(\nu_{\text{DM}}^0, \nu_r^i) \equiv \max(10^6/\nu_{\text{DM}}^0, Q_{\text{int}}^i/(\nu_r^i(1 + \xi^i))). \quad (166)$$

The time depends on the resonator parameters Q_{int}^i and ξ^i , but these will be fixed in the optimization.

We demonstrated in Section IV C 2 that the total SNR from all scan steps is the quadrature sum of the SNR from individual scan steps, which yields the total SNR:

$$\begin{aligned} SNR_{\text{tot}}^{\text{opt}} & \left[\nu_{\text{DM}}^0, g_{\text{DM}}, \left(\frac{d\rho_{\text{DM}}}{d\nu} \right) (\nu, \nu_{\text{DM}}^0), \{\psi(\nu, \nu_r^i, n(\nu), Q_{\text{int}}^i, \xi^i)\}, \{\tau_i\} \right]^2 \\ & = \sum_i SNR^{\text{opt}} \left[\nu_{\text{DM}}^0, g_{\text{DM}}, \left(\frac{d\rho_{\text{DM}}}{d\nu} \right) (\nu, \nu_{\text{DM}}^0), \psi(\nu, \nu_r^i, n(\nu), Q_{\text{int}}^i, \xi^i), \tau_i \right]^2. \end{aligned} \quad (167)$$

We know from the previous section how to optimize the matching network given a resonance frequency. However, how do we choose the time allocation at each resonance frequency? More specifically, given fixed total integration time T_{tot} , and a search band $\nu_l \leq \nu_{\text{DM}}^0 \leq \nu_h$, what is the optimal scan strategy? What is the optimal distribution of resonator frequencies and dwell times?

Of course, the answer to this question depends on how one defines “optimal.” A natural definition, as discussed previously, is to choose the scan strategy that maximizes the area excluded in a log-log plot of mass vs dark-matter coupling g_{DM} : a log-uniform distribution in both variables. That is, we determine the scan steps $\{\nu_r^i\}$ and dwell times $\{\tau_i\}$ such that

$$A[\{\nu_r^i\}, \{\tau_i\}] \equiv - \int_{\nu_l}^{\nu_h} \frac{d\nu_{\text{DM}}^0}{\nu_{\text{DM}}^0} \ln g_{\text{DM},\text{min}}(\nu_{\text{DM}}^0, \{\nu_r^i\}, \{\tau_i\}) \quad (168)$$

is maximized. $g_{\text{DM},\text{min}}(\nu_{\text{DM}}^0, \{\nu_r^i\}, \{\tau_i\})$ is the minimum coupling to which our experiment is sensitive, defined by the coupling value for which

$$SNR_{\text{tot}}^{\text{opt}} \left[\nu_{\text{DM}}^0, g_{\text{DM}}, \left(\frac{d\rho_{\text{DM}}}{d\nu} \right) (\nu, \nu_{\text{DM}}^0), \{\psi(\nu, \nu_r^i, n(\nu), Q_{\text{int}}^i, \xi^i)\}, \{\tau_i\} \right]^2 \quad (169)$$

of eq. (167) is unity. Since $g_{\text{DM},\min}$ is proportional to the ε for hidden photons and $g_{a\gamma\gamma}$ for axions, our optimization function maximizes the exclusion area in a log-log plot of mass vs $\varepsilon / g_{a\gamma\gamma}$. This value function thus optimizes a search with a log-uniform prior. We discuss other possible value functions at the close of this section.

Define

$$\begin{aligned} \varphi & \left(\nu_{\text{DM}}^0, \nu_r^i, \frac{d\rho_{\text{DM}}}{d\nu}(\nu, \nu_{\text{DM}}^0), Q_{\text{int}}^i, \xi^i \right) \\ & \equiv g_{\text{DM}}^{-4} \tau_i^{-1} \text{SNR}^{\text{opt}} \left[\nu_{\text{DM}}^0, g_{\text{DM}}, \left(\frac{d\rho_{\text{DM}}}{d\nu} \right) (\nu, \nu_{\text{DM}}^0), \psi(\nu, \nu_r^i, n(\nu), Q_{\text{int}}^i, \xi^i), \tau_i \right]^2, \end{aligned} \quad (170)$$

which is independent of g_{DM} (see equation (165)). $\varphi(\nu_{\text{DM}}^0, \nu_r^i, \frac{d\rho_{\text{DM}}}{d\nu}(\nu, \nu_{\text{DM}}^0), Q_{\text{int}}^i, \xi^i)$ represents the square of the SNR contribution from the resonator at ν_r^i per unit time per unit g_{DM}^4 when $\tau_i \gg t^*(\nu_{\text{DM}}^0, \nu_r^i)$. It is therefore an important quantity for time allocation optimization. We have made explicit the dependence of φ on the resonator parameters Q_{int}^i and ξ^i . These two parameters will be discussed in the assumptions for the optimization. For each search frequency ν_{DM}^0 , we only consider scan steps for which the dwell time is much longer than $t^*(\nu_{\text{DM}}^0, \nu_r^i)$; otherwise, our SNR treatment from Section IV is not valid and equation (170) cannot be interpreted as stated. We then obtain, from (167),

$$\ln g_{\text{DM},\min}[\nu_{\text{DM}}^0, \{\nu_r^i\}, \{\tau_i\}] = -\frac{1}{4} \ln \left(\sum_{i_k(\nu_{\text{DM}}^0)} \tau_{i_k(\nu_{\text{DM}}^0)} \varphi \left(\nu_{\text{DM}}^0, \nu_r^{i_k(\nu_{\text{DM}}^0)}, \frac{d\rho_{\text{DM}}}{d\nu}(\nu, \nu_{\text{DM}}^0), Q_{\text{int}}^{i_k(\nu_{\text{DM}}^0)}, \xi^{i_k(\nu_{\text{DM}}^0)} \right) \right), \quad (171)$$

and

$$A[\{\nu_r^i\}, \{\tau_i\}] = \frac{1}{4} \int_{\nu_l}^{\nu_h} \frac{d\nu_{\text{DM}}^0}{\nu_{\text{DM}}^0} \ln \left(\sum_{i_k(\nu_{\text{DM}}^0)} \tau_{i_k(\nu_{\text{DM}}^0)} \varphi \left(\nu_{\text{DM}}^0, \nu_r^{i_k(\nu_{\text{DM}}^0)}, \frac{d\rho_{\text{DM}}}{d\nu}(\nu, \nu_{\text{DM}}^0), Q_{\text{int}}^{i_k(\nu_{\text{DM}}^0)}, \xi^{i_k(\nu_{\text{DM}}^0)} \right) \right), \quad (172)$$

where $\{i_k(\nu_{\text{DM}}^0)\}$ is the index set for the subsequence of scan steps satisfying

$$\tau_{i_k(\nu_{\text{DM}}^0)} \gg t^*(\nu_{\text{DM}}^0, \nu_r^{i_k(\nu_{\text{DM}}^0)}). \quad (173)$$

Equation (172) would, in general, have to be evaluated and optimized numerically. However, in practice, the scan will take steps much smaller than a sensitivity bandwidth over the entire range. Thus, multiple scan frequencies ring up the signal at any particular dark-matter search frequency without degradation. Such a scan pattern ensures that there are no gaps in coverage of the search band. We will refer to this class of scans as “dense” scans. For

dense scans, we may discuss the scan strategy not in terms of discrete steps, but rather in terms of an approximately continuous object. As we will demonstrate, the transformation from a discrete to a continuous scan enables us to solve for the optimal scan strategy.

We will adopt the assumptions from the optimization of the impedance-matching network for a log-uniform search, as carried out in Section V A. We make five additional assumptions regarding the scan:

1. The internal Q , pickup volume, and temperature are fixed during the search. That is, they are independent of resonance frequency.
2. For each scan step, the matching parameter ξ^i is set to its optimal value $\xi^i = \xi^{\text{opt}}(\nu_r^i, n(\nu_r^i))$. We omit the dependence on thermal occupation number for brevity in this section; it will be implied.
3. For each circuit configuration, τ_i is much longer than $t^*(\nu_r^i, \nu_r^i)$. This implies that, within any narrow band around resonance, the dwell time is much longer than $t^*(\nu_{\text{DM}}^0, \nu_r^i)$ and $\varphi(\nu_{\text{DM}}^0, \nu_r^i, \frac{d\rho_{\text{DM}}}{d\nu}(\nu, \nu_{\text{DM}}^0), Q_{\text{int}}, \xi^{\text{opt}}(\nu_r^i))$, given by (170), applies.
4. Suppose that the scan step sequence $\{\nu_r^i\}$ is in ascending order, $\nu_r^1 \leq \nu_r^2 \leq \dots$. We assume that the set of scan steps that provide information on the hypothesis of dark matter at ν_{DM}^0 form an integer interval of indices. In other words, if resonators at $\nu_r^{i_1}$ and $\nu_r^{i_2}$ collect information on dark matter at ν_{DM}^0 and $i_1 < i_2$, then, for any i_m , $i_1 \leq i_m \leq i_2$, $\nu_r^{i_m}$ also collects information on ν_{DM}^0 . This is a sensible assumption, given that we expect all resonant frequencies “close” to the search frequency to give high SNR information.

We denote by $\nu_{r,l}(\nu_{\text{DM}}^0)$ the lowest resonance frequency which collects SNR data on ν_{DM}^0 and by $\nu_{r,h}(\nu_{\text{DM}}^0)$ the highest resonance frequency. In any practical search, we will be able to probe over a wide bandwidth. In particular, we will be able to cover a range around ν_{DM}^0 that contains several sensitivity bandwidths $\nu_{\text{DM}}^0/Q_s(\nu_{\text{DM}}^0, n(\nu_{\text{DM}}^0), Q_{\text{int}}, \xi^{\text{opt}}(\nu_{\text{DM}}^0))$, as well as several dark-matter cutoff bandwidths $\beta\nu_{\text{DM}}^0$. Therefore, we may assume that $\nu_{r,l}(\nu_{\text{DM}}^0)$ and $\nu_{r,h}(\nu_{\text{DM}}^0)$ satisfy

$$\frac{\nu_{\text{DM}}^0}{Q_s(\nu_{\text{DM}}^0, n(\nu_{\text{DM}}^0), Q_{\text{int}}, \xi_{\text{opt}}(\nu_{\text{DM}}^0))}, \beta\nu_{\text{DM}}^0 \ll |\nu_{r,l}(\nu_{\text{DM}}^0) - \nu_{\text{DM}}^0|, |\nu_{r,h}(\nu_{\text{DM}}^0) - \nu_{\text{DM}}^0| \ll \nu_{\text{DM}}^0. \quad (174)$$

We thus rewrite eq. (172) as

$$A[\{\nu_r^i\}, \{\tau_i\}] = \frac{1}{4} \int_{\nu_l}^{\nu_h} \frac{d\nu_{\text{DM}}^0}{\nu_{\text{DM}}^0} \ln \left(\sum_{i: \nu_{r,l}(\nu_{\text{DM}}^0) \leq \nu_r^i \leq \nu_{r,h}(\nu_{\text{DM}}^0)} \tau_i \varphi \left(\nu_{\text{DM}}^0, \nu_r^i, \frac{d\rho_{\text{DM}}}{d\nu}(\nu, \nu_{\text{DM}}^0), Q_{\text{int}}, (\xi^i)^{\text{opt}} \right) \right) \quad (175)$$

We note that, though we make the restriction (174), the values of $\nu_{r,l}(\nu_{\text{DM}}^0)$ and $\nu_{r,h}(\nu_{\text{DM}}^0)$ can be chosen flexibly.

5. The total experiment time T_{tot} is long enough that we may take small steps:

$$\frac{\Delta \nu_r^i}{\nu_r^i} = \frac{\nu_r^{i+1} - \nu_r^i}{\nu_r^i} \ll \frac{1}{Q_s(\nu_r^i, n(\nu_r^i), Q_{\text{int}}, \xi^{\text{opt}}(\nu_r^i))} = \frac{((1 + \xi^{\text{opt}}(\nu_r^i))^2 + 4(\xi^{\text{opt}}(\nu_r^i)n(\nu_r^i))^{1/2})}{Q_{\text{int}}} \quad (176)$$

We refer to this assumption as the “dense scan” assumption. It can be met under the condition that

$$T_{\text{tot}} \gg \int_{\nu_l}^{\nu_h} \frac{d\nu_r}{\nu_r} t^*(\nu_r, \nu_r) \frac{Q_{\text{int}}}{((1 + \xi^{\text{opt}}(\nu_r))^2 + 4\xi^{\text{opt}}(\nu_r)n(\nu_r))^{1/2}}, \quad (177)$$

where, from (166), we have $t^*(\nu_r, \nu_r) = \max(10^6/\nu_r, Q_{\text{int}}/(\nu_r(1 + \xi^{\text{opt}}(\nu_r))))$. For reference, for internal quality factors on the order of one million, $\nu_l = 1$ kHz, and $\nu_h = 100$ MHz, the integral in (177) evaluates to several hours.

As discussed above, the dense scan assumption implies that, for each dark-matter frequency, there are multiple resonant frequencies that will ring up the signal with maximum SNR—that is, without degradation from quantum noise. For such dense a scan, we may turn the sum in equation (175) into an integral. A useful proxy for dwell time τ_i is a positive, differentiable scan density function $\tau(\nu_r)$. Here, $\tau(\nu_r)$ is defined such that the time to scan a frequency band of width $d\nu_r$ centered at frequency ν_r is $\tau(\nu_r) \frac{d\nu_r}{\nu_r}$. By choosing a scan density function $\tau(\nu_r)$ and steps $\{\nu_r^i\}$, we choose dwell times:

$$\tau_i = \tau(\nu_r^i) \frac{\nu_r^{i+1} - \nu_r^i}{\nu_r^i}. \quad (178)$$

One may note that turning a sum into a integral usually means that we are taking the limit of infinitesimally small frequency steps: $\Delta \nu_r^i = \nu_r^{i+1} - \nu_r^i \rightarrow 0$. This may seem odd given that, physically, this would mean, for a fixed scan time T_{tot} , that the dwell time τ_i at each step would also go to zero; this would imply that we are not dwelling longer than

the resonator ring-up/dark-matter-coherence times. When not dwelling for a coherence time, the SNR formulae presented above are no longer valid, and therefore, it would seem that our argument is not self-consistent. However, as long as the physical frequency scan steps (each with dwell time longer than the coherence times) are sufficiently small, then mathematically, the sum may be approximated as an integral. We thus distinguish between the physical requirement that the dwell time be longer than the ring-up/coherence times for each resonant scan step and the mathematical approximation of turning the sum of (171) into an integral for a dense scan.

From (175), we then obtain

$$A[\tau(\nu_r)] = \frac{1}{4} \int_{\nu_l}^{\nu_h} \frac{d\nu_{\text{DM}}^0}{\nu_{\text{DM}}^0} \ln \left(\int_{\nu_{r,l}(\nu_{\text{DM}}^0)}^{\nu_{r,h}(\nu_{\text{DM}}^0)} \frac{d\nu_r}{\nu_r} \tau(\nu_r) \varphi \left(\nu_{\text{DM}}^0, \nu_r, \frac{d\rho_{\text{DM}}}{d\nu}(\nu, \nu_{\text{DM}}^0), Q_{\text{int}}, \xi^{\text{opt}}(\nu_r) \right) \right), \quad (179)$$

where $\nu_{r,l}(\nu_{\text{DM}}^0)$ and $\nu_{r,h}(\nu_{\text{DM}}^0)$ satisfy (174), but are chosen flexibly.

In general, the interval $[\nu_{r,l}(\nu_{\text{DM}}^0), \nu_{r,h}(\nu_{\text{DM}}^0)]$ will contain several sensitivity bandwidths $\nu_{\text{DM}}^0/Q_s(\nu_{\text{DM}}^0, n(\nu_{\text{DM}}^0), Q_{\text{int}}, \xi^{\text{opt}}(\nu_{\text{DM}}^0))$ and several dark-matter cutoff bandwidths $\beta\nu_{\text{DM}}^0$. We can take the scan density function $\tau(\nu_r)$ to vary slowly on the scale of a dark-matter cutoff bandwidth, because any pair of resonators separated by less than this bandwidth will probe the same dark-matter signal. Additionally, we can take the scan density function $\tau(\nu_r)$ to vary slowly on the scale of a sensitivity bandwidth. Consider two resonators in a dense scan within the sensitivity bandwidth. Suppose we allocate equal time (equal $\tau(\nu_r)$ to both) at the steps. If we allocated more time to one resonance frequency than at the other, represented by a higher value of $\tau(\nu_r)$ at the former frequency, then the value functional $A[\tau(\nu_r)]$ would not change appreciably from the equal time situation. Both resonators are ringing up the dark-matter signal without degradation from quantum noise and hence, contribute approximately equally to the sensitivity on coupling. We thus assume

$$\left| \frac{d\tau}{d\nu_r}(\nu_{\text{DM}}^0) \right| \ll \frac{\tau(\nu_{\text{DM}}^0)}{\nu_{r,h}(\nu_{\text{DM}}^0) - \nu_{r,l}(\nu_{\text{DM}}^0)}. \quad (180)$$

Equation (179) can then be approximated as

$$A[\tau(\nu_r)] = \frac{1}{4} \int_{\nu_l}^{\nu_h} \frac{d\nu_{\text{DM}}^0}{\nu_{\text{DM}}^0} \ln \left(\tau(\nu_{\text{DM}}^0) \int_{\nu_{r,l}(\nu_{\text{DM}}^0)}^{\nu_{r,h}(\nu_{\text{DM}}^0)} \frac{d\nu_r}{\nu_r} \varphi \left(\nu_{\text{DM}}^0, \nu_r, \frac{d\rho_{\text{DM}}}{d\nu}(\nu, \nu_{\text{DM}}^0), Q_{\text{int}}, \xi_{\text{opt}}(\nu_r) \right) \right). \quad (181)$$

Maximizing the functional $A[\tau(\nu_r)]$ with respect to the constraint of fixed search time

$$T_{\text{tot}} = \int_{\nu_l}^{\nu_h} \frac{d\nu_r}{\nu_r} \tau(\nu_r) \quad (182)$$

is now straightforward. The solution is that $t(\nu)$ should be constant:

$$\tau_{\text{opt}}(\nu) = \frac{T_{\text{tot}}}{\ln(\nu_h/\nu_l)}. \quad (183)$$

As such, the optimum scan will distribute time logarithmically among bins. The time spent at a resonance frequency should be proportional to the size of the frequency step $\Delta\nu_r$, or equivalently, the width of the bin. It is not better, from the standpoint of maximizing the area of the log-log exclusion curve, to spend more time in one decade of frequency than another.

A constant scan density function is expected. In the log-space of coupling g_{DM} , one does not gain faster as a function of time at some set of search frequencies over another set. The single-step SNR increases with time as $t^{1/4}$ regardless of frequency, as long as the dwell time is much longer than the dark-matter/resonator coherence times.

Note that though we solved for the optimal scan density function, we said nothing about the frequencies $\{\nu_r^i\}$ at which we should step. For a sufficiently dense scan, the particular frequencies are inconsequential. It is easy to see that we could double the number of steps, halving the dwell time, and assuming that we still wait longer than the coherence time and resonator ring-up time, the value of the functional $A[\{\nu_r^i\}, \{\tau_i\}]$ will change negligibly.

The time allocation of equation (183) is appropriate when we know nothing regarding the dark-matter mass/coupling. However, one could consider scan strategies and time distributions that take into account strongly favored regimes. For example, for axion dark matter, the QCD band is a coupling regime that is well-motivated theoretically by the strong CP problem [5]. If one wished to search for axion dark matter that also solves the strong CP problem, then one would integrate down to the QCD band at each frequency, rather than following the scan strategy function (183).

1. Aspects of a Practical Scan Strategy

Multiple aspects of a practical scan must be observed in interpreting our result for time allocation optimization.

For instance, in assumption 4 above, we assume that all resonant frequencies “close” to the search frequency give high SNR information. However, it is possible in a practical scan, that there is a resonance frequency close to the search frequency that gives low SNR. The existence of mechanical resonances is inevitable in any practical system. When tuned to a particular resonance frequency of the detector, it is possible that we may excite one of these mechanical resonances. If the coupling between electrical and mechanical modes produces a sideband at the dark-matter search frequency, there will be large excess noise at the search frequency. Such data would need to be considered on a case-by-case basis and may result in discarding the data from the total dataset. For our optimization, we will assume that these parasitics can be avoided, either by appropriate choice of resonance frequency or carefully designed mechanical damping.

Furthermore, no scan is entirely continuous, as assumed above. At each step, one will need to wait for the system to settle. If one is tuning the resonator with a dielectric structure—as is the case in DM Radio, ADMX, and HAYSTAC—, moving the dielectric inevitably causes vibrations. One must wait for these vibrations to damp to a negligible amplitude before acquiring low-noise data. The settling time may be dependent on resonance frequency, and a more detailed time optimization would be required to take this effect into account. In addition, after some number of scan steps, when the frequency has changed enough that the thermal occupation number is appreciably different, the noise impedance of the amplifier will need to be optimized. This optimization can be conducted, e.g., by tuning a variable transformer based on Josephson junctions, or by tuning the bias parameters of some amplifiers.

Additionally, searches over many octaves require significant hardware changes over the scan because of the limited frequency range of any tuning system. Such a hardware change could entail changing the pickup inductor (e.g. adding turns to the coil to lower the range of resonance frequencies achieved by a capacitively-tuned resonator) or switching cavities. These changes might occur, perhaps, every decade in frequency. In addition, the amplifier would need to be swapped with an amplifier with different coupling strength to enable a larger tuning range in noise impedance. These changes of course cannot be made while acquiring search data.

It is straightforward to include the lost integration time due to settling, cryogenic cycling, and apparatus modification in the optimization analysis above, if these costs are quantita-

tively known. However, these time costs are sufficiently ad hoc that they should probably be implemented on a case-by-case basis. We note that the idealized optimization here still provides a baseline for planning scans that can be modified due to practical constraints.

VI. FUNDAMENTAL LIMIT: RESONANT DETECTOR READ OUT BY A QUANTUM-LIMITED AMPLIFIER

Now that we have optimized the scan strategy, we may calculate the fundamental sensitivity of a resonant detector followed on by a quantum-limited amplifier.

Assuming a sufficiently dense scan lasting at least several hours, and assuming fixed internal Q and pickup volume, equations (165) and (167) give, with optimized matching network (141) and time allocation (183),

$$\begin{aligned}
SNR^{\text{opt}} \left[\nu_{\text{DM}}^0, g_{\text{DM}}, \frac{d\rho_{\text{DM}}}{d\nu}(\nu, \nu_{\text{DM}}^0) \right]^2 &= (4\pi Q_{\text{int}})^2 \frac{T_{\text{tot}}}{\ln(\nu_h/\nu_l)} \int \frac{d\nu_r}{\nu_r} \\
&\times \int_{\nu_{\text{DM}}^0}^{\nu_{\text{DM}}^0 + \Delta\nu_{\text{DM}}^c} d\nu \left(\frac{\nu}{\nu_r} \frac{g_{\text{DM}}^2 V_{\text{PU}} \frac{d\rho_{\text{DM}}}{d\nu}(\nu, \nu_{\text{DM}}^0)}{h} \frac{\xi^{\text{opt}}(\nu_r)}{4\xi^{\text{opt}}(\nu_r)n(\nu) + (1 + \xi^{\text{opt}}(\nu_r))^2 + 4(Q_{\text{int}})^2 \left(\frac{\nu}{\nu_r} - 1\right)^2} \right)^2 \\
&\approx 4\pi^3 Q_{\text{int}} \frac{T_{\text{tot}}}{\ln(\nu_h/\nu_l)} \frac{\xi^{\text{opt}}(\nu_{\text{DM}}^0)^2}{(4\xi^{\text{opt}}(\nu_{\text{DM}}^0)n(\nu_{\text{DM}}^0) + (1 + \xi^{\text{opt}}(\nu_{\text{DM}}^0))^2)^{3/2}} \int_{\nu_{\text{DM}}^0}^{\nu_{\text{DM}}^0 + \Delta\nu_{\text{DM}}^c} d\nu \left(\frac{g_{\text{DM}}^2 V_{\text{PU}} \frac{d\rho_{\text{DM}}}{d\nu}(\nu, \nu_{\text{DM}}^0)}{h} \right)^2,
\end{aligned} \tag{184}$$

where the first integral is over the range of data-taking frequencies flexibly-defined in the assumptions of Section VB. It may be evaluated in a manner similar to the Lorentzian integral over $\bar{\nu}$ in equations (139) and (140). Additionally, note that $\xi^{\text{opt}}(\nu_{\text{DM}}^0)$ is implicitly dependent on the thermal occupation number $n(\nu_{\text{DM}}^0)$. The limit on sensitivity is determined by the coupling g_{DM} for which the SNR is unity. Therefore, the detector is sensitive to couplings

$$\begin{aligned}
g_{\text{DM}} &\geq \left(Q_{\text{int}} \frac{\nu_{\text{DM}}^0 T_{\text{tot}}}{\ln(\nu_h/\nu_l)} \frac{4\pi^3 \xi^{\text{opt}}(\nu_{\text{DM}}^0)^2}{(4\xi^{\text{opt}}(\nu_{\text{DM}}^0)n(\nu_{\text{DM}}^0) + (1 + \xi^{\text{opt}}(\nu_{\text{DM}}^0))^2)^{3/2}} \left(\frac{\rho_{\text{DM}} V_{\text{PU}}}{h\nu_{\text{DM}}^0} \right)^2 \right)^{-1/4} \\
&\quad \left(\int_{\nu_{\text{DM}}^0}^{\nu_{\text{DM}}^0 + \Delta\nu_{\text{DM}}^c} \frac{d\nu}{\nu_{\text{DM}}^0} \left(\frac{\nu_{\text{DM}}^0}{\rho_{\text{DM}}} \frac{d\rho_{\text{DM}}}{d\nu}(\nu, \nu_{\text{DM}}^0) \right)^2 \right)^{-1/4}.
\end{aligned} \tag{185}$$

For a top-hat dark-matter spectrum of width $\Delta\nu_{\text{DM}} = \nu_{\text{DM}}^0/Q_{\text{DM}}$, where $Q_{\text{DM}} = 10^6$ is the

characteristic quality factor for the dark-matter bandwidth, this can be further simplified to

$$g_{\text{DM}} \geq \left(Q_{\text{DM}} Q_{\text{int}} \frac{\nu_{\text{DM}}^0 T_{\text{tot}}}{\ln(\nu_h/\nu_l)} \frac{4\pi^3 \xi_{\text{opt}}(\nu_{\text{DM}}^0)^2}{(4\xi_{\text{opt}}(\nu_{\text{DM}}^0)n(\nu_{\text{DM}}^0) + (1 + \xi_{\text{opt}}(\nu_{\text{DM}}^0))^2)^{3/2}} \right)^{-1/4} \left(\frac{\rho_{\text{DM}} V_{\text{PU}}}{h\nu_{\text{DM}}^0} \right)^{-1/2}. \quad (186)$$

We may also evaluate the limit for the standard halo model using the results in the appendix.

The result is

$$g_{\text{DM}} \geq \left((4.4 \times 10^5) Q_{\text{int}} \frac{\nu_{\text{DM}}^0 T_{\text{tot}}}{\ln(\nu_h/\nu_l)} \frac{4\pi^3 \xi_{\text{opt}}(\nu_{\text{DM}}^0)^2}{(4\xi_{\text{opt}}(\nu_{\text{DM}}^0)n(\nu_{\text{DM}}^0) + (1 + \xi_{\text{opt}}(\nu_{\text{DM}}^0))^2)^{3/2}} \right)^{-1/4} \left(\frac{\rho_{\text{DM}} V_{\text{PU}}}{h\nu_{\text{DM}}^0} \right)^{-1/2}. \quad (187)$$

Using the expressions under equation (51), we may evaluate the sensitivity to hidden photon mixing angle ε and axion-photon coupling $g_{a\gamma\gamma}$. We will not calculate these explicitly here. As alluded to in Section IIIB and discussed in detail in appendix F 3, these sensitivity formulae are also valid for quantum-limited flux-to-voltage amplifiers.

The ξ -dependent fraction represents the optimization of the matching network in the presence of thermal noise, given quantum-limited amplifier performance. One important feature of this sensitivity expression is the dependence on internal quality factor. The sensitivity to dark matter grows as $Q_{\text{int}}^{-1/4}$, independent of whether the overall Q satisfies $Q < Q_{\text{DM}}$ or $Q > Q_{\text{DM}}$.⁹ This parametric dependence differs from previous sensitivity estimates given in [11] and [16]. We now explain this difference. It will be useful to reference the results in Section IV and equation (41), reexpressed here in terms of the system noise temperature T_S [17]:

$$SNR \approx \frac{P_{\text{sig}}}{kT_S \Delta\nu} \sqrt{\Delta\nu \cdot t}. \quad (188)$$

As there are two system bandwidths here—namely, the resonator bandwidth and the dark-matter-signal bandwidth—one must carefully choose the value of $\Delta\nu$. The proper choice is provided by our insights in Section IV C 1. We should use the bandwidth of the optimally filtered signal, which is obtained from the integrand of (80) with $f = f^{\text{opt}}$. For dark matter at rest mass frequency ν_{DM}^0 and the resonator centered at ν_r^i , the bandwidth is approximately the minimum of the dark-matter bandwidth and sensitivity bandwidth

$$\Delta\nu_{\text{DM}}^{\text{opt}}(\nu_{\text{DM}}^0, \nu_r^i) \approx \min(\nu_{\text{DM}}^0/Q_{\text{DM}}, \nu_{\text{DM}}^0/Q_s). \quad (189)$$

⁹ Due to the optimization of matching, which fixes ξ^i to its optimal value, Q_{int}^i , Q^i , and Q_s are all proportional to each other. Thus, a scaling of sensitivity as $Q_{\text{int}}^{-1/4}$ implies a scaling as $Q^{-1/4}$ and $Q_s^{-1/4}$. See equations (129) and (135) for scattering-mode amplifiers, as well as the treatments of flux-to-voltage amplifiers in Appendices E and F 3.

We have switched to the variable Q_{DM} , rather than the specific value of 10^6 in the above expression in order to show that the effects discussed below are actually independent of what value we set for the dark-matter bandwidth.

The seminal work of references [10] and [11] presents a sensitivity scaling for resonant axion searches which scales as $Q^{-1/4}$ for $Q \leq Q_{\text{DM}}$ and is independent of Q for $Q \geq Q_{\text{DM}}$. In other words, there is no gain in sensitivity when the resonator bandwidth is smaller than the dark-matter-signal bandwidth. However, our calculation of sensitivity scales as $Q^{-1/4}$ in both regimes. *We benefit from using a resonator whose bandwidth is smaller than that of the dark-matter signal.*

To understand this sensitivity result, we first observe that the most appropriate delineation of regimes is not one which compares the resonator bandwidth and the dark-matter-signal bandwidth. Rather, it is the one which compares the *sensitivity* bandwidth and the dark-matter-signal bandwidth. For the scattering-mode amplifiers discussed in sections IV and V, this distinction may seem superfluous because Q and Q_s differ by a factor of order unity. (See eqs. (129) and (135) with $\xi^i = \xi^{\text{opt}}(\nu_r^i)$, determined in (141).) However, for the quantum-limited flux-to-voltage amplifiers discussed in Appendix E, the low damping from the amplifier input results in the overall Q and internal Q being approximately the same; as a result, at low frequencies where $n(\nu_r) \gg 1$, Q is much larger than Q_s . In such a situation, it is clear that, with a $Q \gg 10^6$ resonator centered at $\nu_r = \nu_{\text{DM}}^0$, we will have maximal sensitivity, without degradation from imprecision noise, to the entire dark-matter signal simultaneously as long as $Q_s \leq Q_{\text{DM}}$. We thus consider two cases: (i) the resonator is sensitive to the whole dark-matter signal, $Q_s \leq Q_{\text{DM}}$ and (ii) the resonator is only sensitive to part of the dark-matter signal, $Q_s \geq Q_{\text{DM}}$. We determine the scaling with Q_s in both cases using equation (188). It will be important to recall that Q_s is proportional to the cavity quality factor Q . We fix the system noise temperature and will assume that the scan step size is

$$\Delta\nu_r/\nu_r = 1/(NQ_s), \quad (190)$$

where $N \gg 1$ is a constant. We use the scan density function (183). The amplifier used in the setup need not be quantum-limited; we simply require a concrete scan pattern to assist in the explanation.

1. Case (i): $Q_s \leq Q_{\text{DM}}$

Consider a tunable resonator of sensitivity quality factor less than the dark-matter quality factor. Suppose we use the resonator to scan over the dark-matter band $\nu_{\text{DM}}^0 \leq \nu \leq \nu_{\text{DM}}^0 + \nu_{\text{DM}}^0/Q_{\text{DM}}$. We consider the signal power at a single scan step. The dark-matter energy that can drive the circuit at maximum sensitivity (without degradation from amplifier noise) is independent of Q_s because the entire dark-matter signal fits within the sensitivity bandwidth. The ratio of the resonator energy E_r to the drive energy varies as Q^2 , and the power into the readout varies as E_r/Q , so the signal power varies as Q_s .

We next consider the noise power in the receiver, denoted by P_n . The bandwidth of the optimally filtered signal is the dark-matter bandwidth and the noise temperature is fixed, so the total noise power is independent of Q_s .

Consider the number of independent samples of the noise power obtained from the data at the single scan step. This is indicated by the factor $\sqrt{\Delta\nu \cdot t}$ in (188) and is representative of averaging fluctuations in the noise power to increase measurement SNR. $\Delta\nu$, as we have discussed, is independent of Q_s . The amount of integration time at this step is proportional to $1/Q_s$, so that the number of samples is proportional to $Q_s^{-1/2}$.

If we were to step at one part in Q_s , then we would be sensitive to the dark-matter signal over ~ 1 step. If we step at one part in NQ_s , then we are sensitive to the dark-matter signal over N steps, independent of Q_s .

Putting these contributions all together, with separate scan step SNRs adding in quadrature, we find that the total SNR is proportional to $Q_s \times Q_s^{-1/2} = Q_s^{1/2}$. Therefore, the minimum coupling to which one is sensitive is proportional to $Q_s^{-1/4} \propto Q_{\text{int}}^{-1/4} \propto Q^{-1/4}$.

Our comparison is similar to that of resistive absorbers and half-wave cavities in Section II. The power received by the readout linearly with Q , while we take a $Q^{-1/2}$ “penalty” for resonant scanning, resulting in an SNR that is proportional to $Q^{1/2}$.

2. Case (ii): $Q_s \geq Q_{\text{DM}}$

Now, consider a tunable resonator of sensitivity quality factor larger than the dark-matter quality factor. Suppose that it scans over the dark-matter signal band.

The energy of the dark matter driving the circuit at maximal sensitivity now decreases as $1/Q_s$ because only part of the signal sits within the sensitivity bandwidth. Proceeding then as in Case (i), the signal power from a measurement at a single scan step is independent of Q_s . This is consistent with estimates in [11] and [17].

The appropriate optimal-filter bandwidth for evaluating the noise power of the single-scan-step measurement is the sensitivity bandwidth. Therefore, the noise power decreases as $1/Q_s$.

The number of independent samples of noise power at the scan step also decreases as $1/Q_s$ because the bandwidth decreases as $1/Q_s$ and the integration time decreases as $1/Q_s$. Combining the three contributions, we find that the SNR at a single scan step is proportional to $Q_s \times 1/Q_s \propto 1$. That is, it is independent of the sensitivity Q . So far, we are still consistent with previous works.

However, there is one contribution that we are yet to consider, which was not considered in previous works. The contribution is that from *the scan*. If we were to step at 1 part in Q_s , we would be sensitive to dark matter over more than one scan step! We would be sensitive over $\sim Q_s/Q_{\text{DM}}$ scan steps. At a step size of 1 part in NQ_s , we will be sensitive over $\sim NQ_s/Q_{\text{DM}}$ steps. Adding SNR contributions in quadrature then tells us that the total SNR at the dark-matter signal band varies as $Q_s^{1/2}$, giving a sensitivity scaling of $Q_s^{-1/4} \propto Q_{\text{int}}^{-1/4} \propto Q^{-1/4}$.

We have demonstrated that the sensitivity to dark matter increases with quality factor even when the sensitivity quality factor exceeds the dark-matter quality factor. *In particular, an experiment benefits fundamentally from a quality factor above one million.*

One caveat is that there must be a limit to this scaling due to power conservation. This is precisely the concept that is explored in ref. [23] and highlighted in Sections II and III A. There, we found that at extremely high cavity quality factors, the apparatus backacts on the dark-matter source. These quality factors are impractical, so we may ignore them for any realizable experiment.

Of course, there are practical aspects that must be taken into consideration. Obtaining an internal Q larger than 10^6 is a difficult task, especially for axion searches in which the large magnetic field makes the use of superconducting materials challenging. Depending on the frequency and the Q , integrating for a resonator ring-up time (which is critical to

obtaining the enhanced sensitivity with increased Q) may be impractical. Also, because of the possibility of dark-matter clumping, the dark-matter signal may disappear or may be substantially reduced in the middle of the longer integration (see Appendix B). However, this could also happen at quality factors lower than one million. We illustrate here that there is no known, fundamental property of the dark-matter field that prevents one from obtaining higher sensitivity at quality factors above Q_{DM} for a resonant scanning search. The coherence time of the dark matter and the intrinsic bandwidth of the dark-matter signal do not fundamentally set an “optimal Q ” for detection.

In the case of hidden-photon dark matter, in evaluating the limits for $Q < Q_{\text{DM}} = 10^6$, the authors of reference [16] find that the sensitivity to g_{DM} varies as $Q^{-1/2}$. Here we find that it varies more weakly with quality factor—as $Q^{-1/4}$. The authors use a bandwidth for the noise power of $\Delta\nu \sim \nu_{\text{DM}}^0/Q$, rather than a smaller bandwidth of $\sim \nu_{\text{DM}}^0/Q_{\text{DM}}$. Using the larger bandwidth is not appropriate. The bandwidth of the optimal filter is at most the bandwidth of the dark-matter signal. Using more filter bandwidth than the optimal results in greater noise power, while keeping the signal power the same. This implies that reference [16] overestimates the uncertainty in noise power, $\sigma_P = kT_S \Delta\nu / \sqrt{\Delta\nu \cdot t}$, by a factor of $\sqrt{Q_{\text{DM}}/Q}$. In turn, the authors underestimate the SNR by a factor of $\sqrt{Q_{\text{DM}}/Q}$. As the SNR is proportional to g_{DM}^2 , this resolves the discrepancy in Q -dependence between the previous estimate for hidden photon sensitivity and the one contained here. Observe that the use of the incorrect bandwidth does not affect the sensitivity limits claimed in [16], as the authors take $Q = Q_{\text{DM}}$.

In summary, for a scanning search to probe a wide range of dark-matter masses, it is beneficial to obtain as high a quality factor as possible, as long as the dwell time at each resonance frequency is longer than the dark-matter coherence time at the resonance frequency, as well as the resonator ring-up time. The minimum coupling to which the resonator is sensitive scales with quality factor as $Q^{-1/4}$.

One may note that we could use Bode-Fano optimal circuits, as described in Section V A 2, instead of resonators for the best search. However, these are narrowband and would also need to be scanned. The optimal scan-density function (183) would still represent the best time allocation, except instead of resonant frequencies, the argument would represent the center frequency of the top-hat. The total squared SNR at the dark-matter search frequency would be $\sim 1/3$ better than that for a resonator. The limit on dark-matter coupling

would only be several percent better. *The quantum-limited scan with a resonator is nearly optimal relative to all single-moded detectors in the scattering mode.*

a. Implications for Scan Rate In A Low-Frequency Tunable Resonator Search

Some previous work, such as ref. [16], computed the sensitivity of a tunable resonator search only considering the information within the resonator bandwidth. As we have shown, at low frequencies $h\nu_{\text{DM}}^0 \ll kT$, such a consideration is not appropriate and does not reflect an optimal scan strategy. Sensitivity, undegraded by amplifier noise, is available far outside of the resonator bandwidth. As the final part of this section, we consider the enhancement in scan rate available at low frequencies from exploiting the entire sensitivity bandwidth.

In terms of sensitivity bandwidth, for a resonator at frequency ν_r , we are able to scan $\sim n(\nu_r)$ (uncoupled) resonator bandwidths simultaneously. As we move across the range, we scan every dark-matter search frequency with multiple resonators, each giving an independent measurement of the dark-matter signal. The total SNR at each frequency then increases, relative to the resonator-bandwidth-only search, by $\sim \sqrt{n(\nu_{\text{DM}}^0)}$. The limit on dark-matter-to-photon couplings, quantified by the minimum ε or $g_{a\gamma\gamma}$ to which an experiment is sensitive, is deeper by a factor of $\sim n(\nu_{\text{DM}}^0)^{1/4}$. For a ~ 1 kHz resonator at ~ 10 mK read out with a quantum-limited amplifier, this corresponds to a limit that is better by approximately 1.25 orders of magnitude.

Alternatively, we may consider the scan time required to reach a particular limit on coupling. The scan time is linearly proportional to the sensitivity bandwidth, so the integration is faster by a factor of $\sim n(\nu_{\text{DM}}^0)$. For the ~ 1 kHz resonator above, the scan rate is enhanced by five orders of magnitude. *The optimal scan strategy allows a reduction in integration times by a few orders of magnitude at frequencies $h\nu_{\text{DM}}^0 \ll kT$.*

Ref. [54] fully works out the fundamental limit of a search with a phase-insensitive amplifier in DM Radio, an existing effort to detect axion and hidden-photon dark matter. This example illustrates the application of this framework to a practical implementation.

VII. CONCLUSIONS

In this work, we provided broad insights into the electromagnetic detection of axion and hidden-photon dark matter, setting a standard quantum limit on the sensitivity of a measurement with a single-moded detector.

We began with a generic description of coupling to the dark-matter-induced electromagnetic fields, categorizing the three parts of a receiver: the signal source, the matching network, and the readout.

We first showed that a resonant circuit possesses superior sensitivity to a broadband resistive sheet in the search for axion or hidden-photon dark matter. We then explained, in terms of the circuit model in ref. [23], why the optimal detector must be driven by an equivalent circuit reactance and why the dark-matter drive signal can be treated as stiff. Using a representation of the dark-matter source as an effective, stiff current density, we compared capacitively-coupled and inductively-coupled detectors. We demonstrated that, in the quasi-static, sub-wavelength limit, the latter is superior. In the limit that the detector size approaches a Compton wavelength, the two are comparable. We thus justified our focus on inductively-coupled detectors.

Having justified the optimal coupling element in the signal source, we then optimized the matching network and the readout. We found that when thermal noise dominates amplifier noise, high-SNR information is available away from the resonator bandwidth. This motivated the notion of integrated sensitivity for a search (resonant or otherwise) over wide bandwidth for axion and hidden photon dark matter.

Building on this notion, we introduced the search optimization. Quantum-limited amplifiers are ideal for maximizing integrated sensitivity, so we assumed such amplification. In the first part of this optimization, we optimized the matching network. This optimization applies not only for resonators, but for any reactively coupled circuit. We introduced the notion of a log-uniform search, where one tries to maximize the integrated, inverse-squared noise-equivalent number. In the scattering mode, the Bode-Fano criterion constrains the match between a complex LR source and a real amplifier input impedance. We used the Bode-Fano criterion to set a bound on the log-uniform search value function for single-moded reactive detectors. We then optimized a single-pole resonator using the same value function, maximizing with respect to coupling coefficient/matching parameter. We found

that, while a single-pole resonator does not satisfy the bound with equality (equality being satisfied by a multi-pole resonator), it is within 75% of the bound. In combination with the insights from the circuit model of ref. [23], we thus established that the resonator is the near-ideal single-moded detector for dark matter. We found that the optimized resonator at any given frequency is not noise-matched to the amplifier and explained the result in terms of measurement backaction; a similar result was found for flux-to-voltage amplifiers in the appendix.

In the second part of the optimization, we focused on resonators, given our insights with the Bode-Fano bound. We optimized the time allocation in the scan. To do so, we realized that any practical scan will be sufficiently dense as to be “continuous.” We introduced the concept of a scan density functional and showed that the optimal scan for a log-uniform search spends equal time in each decade of frequency.

We used our results to derive a limit on the performance of tunable resonant dark-matter detectors. The limit that would be established by the Bode-Fano optimal circuit, a top-hat, is not significantly better (a few percent in terms of dark-matter coupling strength to photons). We showed that the sensitivity continues to increase even for quality factors above one million, the characteristic quality factor associated with the virialized dark-matter-signal bandwidth. The result was interpreted in terms of the scan strategy and sensitivity to dark matter at a single rest mass frequency over multiple scan steps. Finally, we showed that use of the optimized scan strategy can reduce required scan times, to reach a particular limit on dark-matter-to-photon coupling, by a few orders of magnitude.

Given our broad optimization statements, one may ask how to measure more sensitively than the standard quantum limit set herein for electromagnetic detection of dark-matter axions and hidden photons. First, without evading the standard quantum limit, we may build nonlinear or active detection schemes, as opposed to the linear, passive detectors analyzed in this work. Such devices naturally come with additional calibration challenges. We may build multi-moded or multi-port receivers, as described in Section V A 5. Doing so requires fine control of parasitics and fabrication processing. These schemes will be explored in future work. We will pay particular attention to the application of broadband matching criteria (similar to the Bode-Fano criterion) to constrain the performance of multi-port receivers.

Another option is to evade the standard quantum limit for phase-insensitive amplifi-

cation, discussed in Section IV. For example, one could use squeezing and entanglement approaches, backaction-evading measurements, or photon counting. Over the last decade, owing to rapid progress in the quantum measurement community, such techniques have been realized and may be used in practical high-precision measurements. Experimental work in this direction has already begun [24]. In Part II of this work, we will analyze approaches for evading the quantum limit in the context of this generalized optimization framework.

Acknowledgments

This research is funded by the Heising-Simons Foundation, SLAC Laboratory Directed Research and Development, and the Kavli Institute for Particle Astrophysics and Cosmology. We thank Hsiao-Mei Cho, Carl Dawson, Michel Devoret, Stephen Kuenstner, Dale Li, Konrad Lehnert, Harvey Moseley, Lyman Page, Arran Phipps, Surjeet Rajendran, Asimina Arvanitaki, Jamie Titus, Tony Tyson, Betty Young, and Jonas Zmuidzinas for useful discussions.

Appendix A: The Electromagnetic Properties of the Axion and Hidden-Photon Dark-Matter Signal

In this appendix, we discuss the electromagnetic properties of axion and hidden-photon dark matter that need to be understood in order to optimize a search. As discussed in [10, 16, 19], the local dark-matter energy density of $\sim 0.3 \text{ GeV}/\text{cm}^3$ implies a high number density of greater than $\sim 10^{12}$ per cubic centimeter for dark matter mass below 1 meV. Thus, in this low mass range, axion and hidden-photon dark-matter may be treated as a classical field. This stands in contrast to heavier dark-matter candidates, such as WIMPs, which are better described, for purposes of experimental searches, as particles. The distinction is critical to understanding the fundamental theme behind light-field dark-matter detection. Rather than searching for particle scattering off of a fixed target, we look for the collective excitations that the axion/hidden-photon field may induce in a detector.

In the first part of this section, we discuss the spatial and temporal coherence properties of the axion and hidden-photon dark-matter fields. We cover a parametric calculation of the expected signal size in a detection circuit, assuming these fields make up all (or nearly all) of the dark matter, in the second part. The reader may wish to refer to Appendix A of [23] for a primer on axion and hidden-photon electrodynamics.

1. Coherence Properties of the Dark-Matter Field

As with any other classical field, the dark-matter field possesses temporal and spatial coherence. The coherence properties are intimately related to the nonzero dark-matter velocity. They will imprint themselves on the electromagnetic observables, and in particular, on detector signals. This will be evident later when we calculate the signal size. To understand the coherence properties, we Fourier transform the free axion and hidden-photon fields:

$$a(\vec{x}, t) = \int d^3\vec{k} a(\vec{k}, \nu_{\text{DM}}^0) \exp(2\pi i \nu(k)t - i\vec{k} \cdot \vec{x}) + c.c. \quad (\text{A1})$$

$$A'_{m,\mu}(\vec{x}, t) = \int d^3\vec{k} A'_{m,\mu}(\vec{k}, \nu_{\text{DM}}^0) \exp(2\pi i \nu(k)t - i\vec{k} \cdot \vec{x}) + c.c. \quad (\text{A2})$$

$\nu(k)$ is given by the dispersion relation

$$(2\pi\nu(k))^2 = (2\pi\nu_{\text{DM}}^0)^2 + (\vec{k}c)^2, \quad (\text{A3})$$

where \vec{k} is the wavevector of the dark-matter component and may be related to its velocity \vec{v} by $\vec{k} = m_{\text{DM}}\vec{v}/\hbar$. $k = |\vec{k}|$ is the wavenumber. In the nonrelativistic limit, the dispersion relation can be rewritten as

$$h\nu(k) = h\nu_{\text{DM}}^0 + \frac{1}{2}m_{\text{DM}}\vec{v}^2. \quad (\text{A4})$$

Expansions (A1) and (A2) do not account for slow variations in the Fourier amplitudes that may occur due to interactions, e.g. electromagnetic or gravitational. We discuss such variations in the context of detection in Appendix B. The lower bound on this expansion is zero velocity (and wavenumber), corresponding to frequency ν_{DM}^0 . The upper bound is not explicitly stated here, but is determined by the highest dark-matter velocities. Virialization endows dark matter with a $\sim 10^{-3}c$ speed in the galactic rest frame, and the speed of the Earth (and therefore, the detector) in this rest frame is also $\sim 10^{-3}c$. This determines the width of the integration in k -space to be $\Delta k \sim 10^{-3}m_{\text{DM}}c/\hbar$. The width in frequency space is $\Delta\nu_{\text{DM}} \sim 10^{-6}\nu_{\text{DM}}^0$. We now rewrite these expansions as

$$a(\vec{x}, t) = \exp(2\pi i\nu_{\text{DM}}^0 t) \int d^3\vec{k} a(\vec{k}, \nu_{\text{DM}}^0) \exp(2\pi i(\nu(k) - \nu_{\text{DM}}^0)t - i\vec{k} \cdot \vec{x}) + c.c. \quad (\text{A5})$$

$$A'_{m,\mu}(\vec{x}, t) = \exp(2\pi i\nu_{\text{DM}}^0 t) \int d^3\vec{k} A'_\mu(\vec{k}, \nu_{\text{DM}}^0) \exp(2\pi i(\nu(k) - \nu_{\text{DM}}^0)t - i\vec{k} \cdot \vec{x}) + c.c. \quad (\text{A6})$$

The integral expression now contains both slow time-varying components and slow spatial components. The characteristic length scale for the spatial variation is

$$\lambda_{\text{coh}} \sim \frac{2\pi}{\Delta k} \sim 10^3 \frac{h}{m_{\text{DM}}c^2} \approx 1240 \text{ km} \frac{1 \text{ neV}}{m_{\text{DM}}c^2}, \quad (\text{A7})$$

which describes the coherence length of the dark-matter field. Over this length scale, the axion and hidden-photon fields can be treated as spatially uniform. That is, the field will have approximately the same amplitude and phase everywhere within the coherence length at all times. For the hidden photon, the field will also have the same direction.

Suppose we are sitting at a fixed position \vec{x}_0 and observing the field over a time interval $[t_0, t_0 + \delta t]$. According to (A5) and (A6), the dark matter behaves as a field whose phase experiences fast oscillations on the time scale $(\nu_{\text{DM}}^0)^{-1}$ and is modulated on a slower time scale $\sim (\Delta\nu_{\text{DM}})^{-1}$. The slow modulation, represented by the integral term, is a result of the nonzero velocity and the consequent spectral spread of the dark-matter frequency components. On timescales $(\nu_{\text{DM}}^0)^{-1} \ll \delta t \ll (\Delta\nu_{\text{DM}})^{-1}$, the integral can be treated as a constant, so that the fields behave as a phase-coherent, monochromatic wave at frequency ν_{DM}^0 . On

timescales $\delta t \gtrsim (\Delta\nu_{\text{DM}})^{-1}$, the spectral spread becomes observable. The waveform has decohered, and the various frequency components become distinguishable. The coherence time of the field is therefore

$$t_{\text{coh}} \sim \frac{1}{\Delta\nu_{\text{DM}}} \sim \frac{10^6}{m_{\text{DM}}c^2/h} \approx 4 \text{ sec} \frac{1 \text{ neV}}{m_{\text{DM}}c^2}. \quad (\text{A8})$$

The temporal and spatial coherence properties of light-field dark-matter provide key discrimination mechanisms for determining whether a detection of dark matter has been made. One of the major technical challenges in any coherent detection experiment is mitigation of electromagnetic interference. It is inevitable, regardless of the quality of the shielding and grounding, that spurious pickup from the environment will occur, given sufficiently long integration times. If a signal is detected, we may autocorrelate the timestream to determine whether the signal possesses the appropriate coherence time needed to be dark matter. Furthermore, if a signal is detected, a second experiment will be built to validate the signal as dark matter or reject it as a false signal. If that second experiment is located well within the coherence length (A7) corresponding to the signal frequency, then the output timestreams should be highly correlated, with the signals carrying the same amplitude and phase in the two experiments (and in the case of the hidden photon, implying the same direction).

2. Signal Size

To calculate the signal size, we rely on the representation of the axion and hidden photon as effective electromagnetic current densities. As shown in [23], these are

$$\vec{J}_a^{\text{eff}}(\vec{x}, t) = -\frac{\kappa_a}{\mu_0 c} \left(\vec{B}_b(\vec{x}, t) \partial_t a(\vec{x}, t) - \vec{E}_b(\vec{x}, t) \times \vec{\nabla} a(\vec{x}, t) \right), \quad (\text{A9})$$

where \vec{E}_b, \vec{B}_b are the background electric and magnetic fields required for axion-to-photon conversion and

$$\vec{J}_{HP}^{\text{eff}}(\vec{x}, t) = -\varepsilon\epsilon_0 \left(\frac{m_{\text{DM}}c^2}{\hbar} \right)^2 \vec{A}'_i(\vec{x}, t), \quad (\text{A10})$$

where $\vec{A}'_i(\vec{x}, t)$ is the interaction-basis hidden-photon three-vector potential (omitting the scalar component). The distinction between mass basis and interaction basis is denoted in the subscripts for the potential (“ m ” vs. “ i ”). Dark-matter fields also produce an effective charge density, but the effects of the charge density are suppressed by the virial velocity

$v/c \sim 10^{-3}$. Even if one were to parasitically couple to the charge density, the excitation of the circuit would be negligible, compared to the excitation from the current.

For the axion effective current, for background fields of equal energy density, a background electric field will give rise to a current density—and thus, an oscillating electromagnetic field—that is smaller than that from a background magnetic field by a factor of $v/c \sim 10^{-3}$. We can thus consider only background magnetic fields. In practice, DC magnetic fields produced in the lab can be orders of magnitude larger than their AC counterparts. We will thus use a background field of the form:

$$\vec{E}_b = 0, \vec{B}_b = B_0 \hat{B}_0, \quad (\text{A11})$$

where we have assumed the DC magnetic field to be uniform. In Section II, the magnetic field points in the z -direction, i.e. $\hat{B}_0 = \hat{z}$. For the calculation that follows, we permit the uniform field to be finite in extent. The axion-induced effective, electromagnetic current density is then

$$\vec{J}_a^{\text{eff}}(\vec{x}, t) = -\frac{\kappa_a}{\mu_0 c} B_0 \partial_t a(\vec{x}, t) \hat{B}_0, \quad (\text{A12})$$

where the equality holds for the region in which the field is applied. Outside of this region, there is no axion current density.

For the hidden-photon current density, we may replace the interaction-basis hidden-photon vector potential with the mass-basis vector potential. The error is negligible in the stiff-field limit. See Appendix A of [23] for more information on the basis transformation. The hidden-photon effective current density is then

$$\vec{J}_{HP}^{\text{eff}}(\vec{x}, t) = -\varepsilon \epsilon_0 \left(\frac{m_{\text{DM}} c^2}{\hbar} \right)^2 \vec{A}'_m(\vec{x}, t). \quad (\text{A13})$$

We derive the signal size—in particular, the equation (51)—based on the dark-matter-induced magnetic field. The magnetic field is coupled into an inductor and creates a voltage in the detection circuit. This mode of detection, in contrast with electric field coupling, is motivated in Section III. Detailed calculations for particular experimental setups can be found in Refs. [11, 16]. Here, we give a simple parametric argument to help guide the reader. Our scaling agrees with that in the aforementioned references. We assume that the size of the experimental setup is much smaller than the coherence length (A7) in all dimensions, so that we may take the dark-matter fields to be spatially uniform. The assumption is usually appropriate for dark-matter rest-mass frequencies below 300 GHz,

where the coherence length is ~ 1 meter. For higher frequencies, one may need to consider corrections due to spatial variation of the field. We may then drop the position dependence from the dark-matter fields (A1) and (A2) and write the Fourier transforms of the $a(x, t)$ and $\vec{A}'_m(x, t)$ fields as

$$a(x, t) \rightarrow a(t) = \int_{\nu_{\text{DM}}^0}^{\nu_{\text{DM}}^0 + \Delta\nu_{\text{DM}}^c(\nu_{\text{DM}}^0)} d\nu \, a(\nu, \nu_{\text{DM}}^0) \exp(+2\pi i \nu t) + c.c. \quad (\text{A14})$$

$$\vec{A}'_m(x, t) \rightarrow \vec{A}'_m(t) = \int_{\nu_{\text{DM}}^0}^{\nu_{\text{DM}}^0 + \Delta\nu_{\text{DM}}^c(\nu_{\text{DM}}^0)} d\nu \, \vec{A}'_m(\nu, \nu_{\text{DM}}^0) \exp(+2\pi i \nu t) + c.c. \quad (\text{A15})$$

where we are using the cutoff bandwidth defined in equation (39).

We use delta-function normalizations for our Fourier transforms so that the units for $a(\nu, \nu_{\text{DM}}^0)$ are $\text{V}/\sqrt{\text{Hz}}$ and the units for $\vec{A}'_i(\nu, \nu_{\text{DM}}^0)$ are $\text{V} \cdot \text{s}/(\text{m} \cdot \sqrt{\text{Hz}})$. Following [53], the Fourier amplitudes from (A18) and (A19) are related to the dark-matter energy density distribution over frequency $d\rho_{\text{DM}}/d\nu$ by

$$\frac{\epsilon_0}{2} \left(\frac{m_{\text{DM}} c}{\hbar} \right)^2 |a(\nu, \nu_{\text{DM}}^0)|^2 \approx \frac{d\rho_{\text{DM}}}{d\nu}(\nu, \nu_{\text{DM}}^0) \quad (\text{A16})$$

$$\frac{1}{2\mu_0} \left(\frac{m_{\text{DM}} c}{\hbar} \right)^2 |\vec{A}'_m(\nu, \nu_{\text{DM}}^0)|^2 \approx \frac{d\rho_{\text{DM}}}{d\nu}(\nu, \nu_{\text{DM}}^0) \quad (\text{A17})$$

Implicit in these relationships is the approximation that the axion and hidden-photon fields are stiff electromagnetic sources—that the dark-matter density is essentially unperturbed by the interaction with a detector.

The Fourier components of the current are related to the axion and hidden-photon Fourier components by

$$\vec{J}_a(\nu, \nu_{\text{DM}}^0) = -i(2\pi\nu) \frac{\kappa_a}{\mu_0 c} B_0 a(\nu, \nu_{\text{DM}}^0) \hat{B}_0 \approx -i \frac{m_{\text{DM}} c}{\hbar} \frac{\kappa_a B_0}{\mu_0} a(\nu, \nu_{\text{DM}}^0) \hat{B}_0 \quad (\text{A18})$$

$$\vec{J}_{HP}(\nu, \nu_{\text{DM}}^0) = -\varepsilon \frac{1}{\mu_0} \left(\frac{m_{\text{DM}} c}{\hbar} \right)^2 \vec{A}'_m(\nu, \nu_{\text{DM}}^0) \quad (\text{A19})$$

At frequencies where the Compton wavelength of the dark-matter signal, λ_{DM}^0 , is much larger than the size of experimental apparatus that can be constructed, a lumped-element inductor, such as that in the SQUID setup of (3), is used. In this situation, the electromagnetic fields produced by the dark-matter current density can be treated as quasi-static. The magnetic field strength can be estimated using Biot-Savart:

$$B(\nu, \nu_{\text{DM}}^0) \sim \mu_0 J(\nu, \nu_{\text{DM}}^0) V_{\text{PU}}^{1/3}, \quad (\text{A20})$$

where V_{PU} is the volume of the coupling inductor. $V_{\text{PU}}^{1/3}$ is the characteristic size of the detector. $J(\nu, \nu_{\text{DM}}^0)$ is the magnitude of the current density Fourier component at frequency ν assuming a dark-matter rest-mass frequency of ν_{DM}^0 . The size of the electric field is suppressed by $\sim V_{\text{PU}}^{1/3}/\lambda_{\text{DM}}^0$. For the axion, if the spatial extent of the DC magnetic field is much smaller or much larger than the size of the detector, then we may need to replace $V_{\text{PU}}^{1/3}$ by the characteristic length scale of the magnetic field. However, the two spatial scales are comparable in practice, so the parametrization in eq. (A20) is appropriate.¹⁰

When the Compton wavelength of the dark-matter signal, is comparable to the size of the experimental apparatus that may be built, a free-space or dielectric cavity is typically used to couple to the dark-matter signal. In this case, the dark-matter drive fields can no longer be treated as quasi-static. The electric and magnetic field strengths are

$$B(\nu, \nu_{\text{DM}}^0) \sim \mu_0 J(\nu, \nu_{\text{DM}}^0) \lambda_{\text{DM}}^0 \quad (\text{A21})$$

$$E(\nu, \nu_{\text{DM}}^0) \sim \frac{\mu_0 J(\nu, \nu_{\text{DM}}^0) \lambda_{\text{DM}}^0}{c} \quad (\text{A22})$$

Essentially, the wavelength has replaced the pickup volume factor $V_{\text{PU}}^{1/3}$. This substitution is appropriate because in a typical cavity, the linear dimension is comparable to the wavelength. For magnetic coupling, we speak not of coupling to a lumped inductor, but rather the equivalent inductance of the mode. This is denoted as L_{PU} , as shown in Figs. 3, 5. Because the energy in the electric and magnetic fields is comparable, one could decide to couple capacitively rather than inductively. There is no fundamental advantage one way or the other.

The energy of the detector excitation is described by the spectral density

$$E(\nu, \nu_{\text{DM}}^0) = c_{\text{PU}}^2 \frac{1}{2\mu_0} |B(\nu, \nu_{\text{DM}}^0)|^2 V_{\text{PU}} \quad (\text{A23})$$

c_{PU}^2 is a geometrical factor relating to the aspect ratio of the inductor and the alignment of the inductor (e.g. as determined by the central axis of a lumped solenoid or the mode pattern of an antenna or cavity) with the drive fields.

¹⁰Such a distinction regarding spatial extents may be relevant when the DC field is spatially separated from the pickup inductor. For any experiment, there will be a fixed total volume. If, within this volume, the magnetic field extent is much smaller than the pickup size, then we sacrifice induced AC magnetic field strength. If the field extent is much larger, then the pickup volume is necessarily small and we sacrifice coupled energy. A straightforward optimization of this tradeoff yields that the two length scales should be comparable.

Combining (A16), (A17), (A18), (A19), (A20), (A21), and (A23) now yields (51). The result is reproduced here for convenience:

$$E_{\text{DM}} \left(\nu, g_{\text{DM}}, \frac{d\rho_{\text{DM}}}{d\nu}(\nu, \nu_{\text{DM}}^0) \right) = g_{\text{DM}}^2 V_{\text{PU}} \frac{d\rho_{\text{DM}}}{d\nu}(\nu, \nu_{\text{DM}}^0), \quad (\text{A24})$$

The value of $g_{\text{DM}} = g_{\text{DM}}(\nu_{\text{DM}}^0)$ is

$$g_{\text{DM}} = \begin{cases} \kappa_a c B_0 c_{\text{PU}} V_{\text{PU}}^{1/3}, & \text{axions} \\ \varepsilon c_{\text{PU}} V_{\text{PU}}^{1/3} / \lambda_{\text{DM}}^0, & \text{hidden photons} \end{cases} \quad (\text{A25})$$

at frequencies for which the Compton wavelength is much larger than the characteristic size of the detector. When the wavelength is comparable to the size of the detector,

$$g_{\text{DM}} = \begin{cases} \kappa_a c B_0 c_{\text{PU}} \lambda_{\text{DM}}^0, & \text{axions} \\ \varepsilon c_{\text{PU}}, & \text{hidden photons} \end{cases} \quad (\text{A26})$$

where we absorb purely numerical factors into c_{PU} .

Appendix B: Amplitude, Direction, and Distribution Variation in the Dark-Matter Field

1. Amplitude Variation

The local dark matter is likely to have some substructure. This substructure can affect the optimal scan strategy for a resonant experiment, as we discuss in this appendix.

Substructure can be created just through the gravitational interactions of dark matter as is seen in N-body simulations. This applies to any dark-matter particle so long as its de Broglie wavelength, $h(mv)^{-1}$, is small (much less than the length scale on which we are interested in substructure). Over much of the frequency range of interest to axion and hidden-photon detectors the de Broglie wavelength is indeed small and substructure can be relevant to direct detection experiments.

Additionally, more dramatic substructure may have been created by the original dark-matter production mechanism. For example, the most natural production mechanism for light vector dark matter is quantum fluctuations of the vector field during inflation [15]. This mechanism naturally produces a power spectrum with a peak at intermediate length scales

(which depends on the Hubble scale of inflation and the mass of the vector). Such a vector will have substructure on a range of scales which turn out to be relevant for direct detection experiments. These clumps can be many orders of magnitude more dense than the average local dark-matter density. Since the Hubble scale of inflation is currently unknown, even given this production mechanism we cannot know the length scale for these clumps. Thus in this section we will consider the optimal scan strategy if the substructure length scale is unknown. Of course if we did know the clump size, we would use the optimal strategy for that size.

To see that dark-matter substructure can affect the optimal scan strategy, consider the case that an order one fraction of dark matter is in clumps of significant overdensity compared to the average. Consider the example that the earth (or the direct detection experiment) passes through a clump every 10^5 s and spends 10 s inside each clump. Then the optimal strategy would be to scan the entire frequency range every 10 s and continually repeat this scan to use up the entire experimental integration time. If we are inside a clump, we desire to scan all frequencies while we are inside that clump in order to maximize the chance of hitting the dark-matter frequency while we are in the region of overdensity. A caveat to this scan strategy is that it is (likely) still optimal to spend time at each frequency equal to the dark-matter coherence time (or the resonator ring-up time, if that is longer), and the maximum practical scan speed is likely to be limited by constraints on the experimental apparatus. Depending on the actual time spent inside a clump and the frequency range being considered, it may not be possible to cover the entire range during that time and still integrate to the coherence time at each frequency. In this case it would be optimal to cover only part of the range.

Since we do not know the expected substructure length scale, the actual optimal scan strategy is simply to scan as fast as possible over all frequencies while still spending a coherence time at each frequency, and then continually repeat that scan. This optimal scan strategy assumes that we do not lose any time while changing frequencies. In a practical implementation, there will be settling time while changing from one frequency to another. The length of this settling time compared to the other time scales affects the optimal scan strategy. Furthermore, it may be necessary to change coil sets every \sim decade in frequency, or have multiple copies of the experiment at different frequency ranges.

2. Direction Variation

For axion searches, the direction of the effective current density—and therefore, the direction of resultant oscillating magnetic fields—is set by the direction of the applied DC magnetic field. We may always align our resonant detector to couple optimally to the axion-induced magnetic fields; for example, if the DC magnetic field direction is set so that any axion-induced magnetic field lies in the \hat{z} direction, then we may build a resonant LC circuit whose inductor couples to magnetic fields in the \hat{z} direction.

In contrast, for the hidden photon, which is a vector particle, the direction of the effective current density cannot be defined by the experimentalist. It is unknown. During the course of a scan, the direction of the hidden-photon field may change. It is natural that a single resonant detector will only have sensitivity to dark-matter current density fields that have a component along the axis of the detector [16], and as such, will not detect a signal along either of the two orthogonal axes. It thus follows that an optimal search for the hidden photon will involve a minimum of three identical resonant detectors, pointing in mutually orthogonal directions. This ensures that, regardless of the direction of the hidden-photon field, at all times, we will couple to a minimum of one-third of the energy to which a perfectly aligned detector would couple.

For practical purposes, one may benefit from having two sets of three mutually orthogonal detectors, with the sets spaced by less than a coherence length and misaligned in space. For example, if one set of three is aligned to sense hidden-photon currents in the \hat{x} , \hat{y} , and \hat{z} directions, then the other set of three could be aligned in the $\hat{x} + \hat{y} + \hat{z}$, $\hat{x} - 2\hat{y} + \hat{z}$, and $\hat{x} - \hat{z}$ directions. If a signal is detected in both sets of three detectors at the same frequency, then one may determine the hidden-photon direction that would be required to explain the signal in each set. Because the sets are spaced by less than a coherence length, the direction inferred from each set must be the same. This provides a strong discrimination technique for any potential signal.

3. Distribution Variation

It is expected that the distribution of dark matter with frequency/velocity will vary during the search. In fact, owing to the Earth’s orbit around the Sun and the Sun’s motion

in the galactic rest frame, we expect some form of annual modulation in the dark-matter signal. In this section, we describe this annual modulation and how it may be used as another discrimination mechanism for candidate signals.

Annual modulation was first described in the context of WIMP direct detection [48, 55]. In the galactic rest frame, the Sun is moving at a speed of $v_S \approx 220$ km/s. In the rest frame of the Sun, this produces a “wind” of dark matter. When the Earth is orbiting against the wind, the flux of dark matter through the detector is highest, leading to an enhanced event rate. When the Earth is orbiting in the same direction as the wind, the flux of dark matter is lowest, leading to a reduced event rate. Thus, there is an annual modulation in the detection event rate.

Because ultralight dark matter is better described as a field, rather than a particle, it is not necessarily appropriate to discuss event rate. Rather, there is annual modulation in the bandwidth of the signal. We may write the orbital speed of the Earth in the rest frame of the dark-matter population (where the average velocity is zero) as [48, 56]

$$v_d(t) = v_S + v_O \cos \gamma \cos(\omega_O(t - t_0)), \quad (\text{B1})$$

where $\omega_O = 2\pi/\text{year}$ is the orbital frequency, $v_O \approx 29.8$ km/s is the orbital speed of the Earth around the Sun, and $\cos \gamma \sim 0.51$ is a numerical factor arising from the relative orientations of the orbital plane and the velocity of the Sun. t_0 represents the time when the velocity $v_d(t)$ is maximal (Earth’s orbital velocity aligns maximally with the Sun’s motion) and is the time at which the flux of dark matter would be largest.

In the dark-matter rest frame, the maximum speed of the dark-matter is set approximately by galactic escape velocity. In the Milky Way, this escape velocity is $v_{\text{esc}} = 544$ km/sec. Then, in the rest frame of the detector, the maximum speed is $\sim v_{\text{esc}} + v_d(t)$. From equation (A4), this corresponds to a dark-matter-signal bandwidth of

$$\frac{\Delta\nu_{\text{DM}}}{\nu_{\text{DM}}^0} \sim \frac{1}{2} \frac{(v_{\text{esc}} + v_d(t))^2}{c^2}. \quad (\text{B2})$$

We thus expect a $\sim 7.6\%$ peak-to-peak variation in signal bandwidth. At time $t = t_0$, the bandwidth of the distribution is largest, owing to the largest detector velocity in the galactic frame and the consequent largest maximum speed $\sim v_{\text{esc}} + v_d(t_0)$ for dark-matter particles in the detector frame. The width is smallest 1/2 year later, owing to the smallest maximum speed.

If we detect a signal in a receiver, we may monitor it over the course of one year. If the signal does indeed represent dark matter, we should observe an approximately sinusoidal variation in bandwidth.

Appendix C: The Standard Halo Model

As discussed in [49, 53], the standard halo model (SHM) describes the velocity distribution of virialized dark matter. Under this model, it is assumed that the dark matter follows a isothermal, isotropic phase-space distribution, yielding, in the galactic rest frame (in which the dark matter average velocity is zero), a Maxwellian velocity distribution cut off at the galactic escape velocity v_{esc} :

$$Q(\vec{v}) = \frac{K}{\sigma_v^3} \exp\left(-\frac{\vec{v}^2}{2\sigma_v^2}\right) \quad (\text{C1})$$

for $|\vec{v}| \leq v_{\text{esc}}$ and $Q(\vec{v}) = 0$ for $|\vec{v}| > v_{\text{esc}}$. For the Milky Way, the velocity dispersion is $\sigma_v = \sqrt{3/2}v_c$, $v_c = 220$ km/s being the circular speed. K is a normalization constant defined such that

$$\int Q(\vec{v}) d^3\vec{v} = 1. \quad (\text{C2})$$

Let \vec{v}_d be the velocity of the detector in the galactic rest frame. We calculate the mass density distribution $\frac{d\rho_{\text{DM}}}{d\nu}$, which determines the signal power density. (See equations (51) and (81).) The dark-matter distribution over relative velocity is

$$\bar{Q}(\vec{v}_r) = \frac{K}{\sigma_v^3} \exp\left(-\frac{(\vec{v}_r + \vec{v}_d)^2}{2\sigma_v^2}\right) \quad (\text{C3})$$

for $|\vec{v}_r + \vec{v}_d| \leq v_{\text{esc}}$ and $\bar{Q}(\vec{v}_r) = 0$ for $|\vec{v}_r + \vec{v}_d| > v_{\text{esc}}$. Letting θ be the polar angle between the relative velocity and the detector velocity, and integrating over azimuthal and polar angles yields the distribution $q(v_r)$ over speed $v_r = |\vec{v}_r|$:

$$1 = \int \bar{Q}(\vec{v}_r) d^3\vec{v}_r = 2\pi \frac{K}{v_d \sigma_v} \left(\int_0^{v_{\text{esc}}-v_d} dv_r v_r \left(\exp\left(-\frac{(v_r - v_d)^2}{2\sigma_v^2}\right) - \exp\left(-\frac{(v_r + v_d)^2}{2\sigma_v^2}\right) \right) + \int_{v_{\text{esc}}-v_d}^{v_{\text{esc}}+v_d} dv_r v_r \left(\exp\left(-\frac{(v_r - v_d)^2}{2\sigma_v^2}\right) - \exp\left(-\frac{v_{\text{esc}}^2}{2\sigma_v^2}\right) \right) \right) \quad (\text{C4})$$

so

$$q(v_r) = \frac{2\pi K}{v_d \sigma_v} \times \begin{cases} v_r \left(\exp\left(-\frac{(v_r - v_d)^2}{2\sigma_v^2}\right) - \exp\left(-\frac{(v_r + v_d)^2}{2\sigma_v^2}\right) \right) & v_r < v_-(v_d) \\ v_r \left(\exp\left(-\frac{(v_r - v_d)^2}{2\sigma_v^2}\right) - \exp\left(-\frac{v_{\text{esc}}^2}{2\sigma_v^2}\right) \right) & v_-(v_d) \leq v_r \leq v_+(v_d) \\ 0 & v_r > v_+(v_d) \end{cases} \quad (\text{C5})$$

where $v_{\pm}(v_d) = v_{\text{esc}} \pm v_d$. From (A4),

$$v_r = c \sqrt{\frac{2(\nu - \nu_{\text{DM}}^0)}{\nu_{\text{DM}}^0}}. \quad (\text{C6})$$

The mass distribution over frequency is therefore given by

$$\frac{d\rho_{\text{DM}}}{d\nu}(\nu, \nu_{\text{DM}}^0) = \rho_{\text{DM}} q(v_r) \frac{dv_r}{d\nu} = \rho_{\text{DM}} q \left(c \sqrt{\frac{2(\nu - \nu_{\text{DM}}^0)}{\nu_{\text{DM}}^0}} \right) \frac{c}{\sqrt{2\nu_{\text{DM}}^0(\nu - \nu_{\text{DM}}^0)}}, \quad (\text{C7})$$

where ρ_{DM} is the local dark-matter density, measured to be $\sim 0.3 \text{ GeV/cm}^3$.

Finally, we evaluate the integral

$$\int_{\nu_{\text{DM}}^0}^{\nu_{\text{DM}}^0 + \Delta\nu_{\text{DM}}^c} \frac{d\nu}{\nu_{\text{DM}}^0} \left(\frac{\nu_{\text{DM}}^0}{\rho_{\text{DM}}} \frac{d\rho_{\text{DM}}}{d\nu}(\nu, \nu_{\text{DM}}^0) \right)^2 \quad (\text{C8})$$

relevant to the detector sensitivity of equation (185). Taking the detector velocity to be its maximum value $v_d(t) = v_d(t_0)$, this integral evaluates to ¹¹

$$\int_{\nu_{\text{DM}}^0}^{\nu_{\text{DM}}^0 + \Delta\nu_{\text{DM}}^c} \frac{d\nu}{\nu_{\text{DM}}^0} \left(\frac{\nu_{\text{DM}}^0}{\rho_{\text{DM}}} \frac{d\rho_{\text{DM}}}{d\nu}(\nu, \nu_{\text{DM}}^0) \right)^2 \approx 4.4 \times 10^5. \quad (\text{C9})$$

Appendix D: Noise Correlations for Quantum-Limited, Phase-Insensitive Amplifiers in the Scattering Mode Representation

Here, we derive the noise correlations (94)-(96) for a quantum-limited, phase-insensitive amplifier in the scattering mode representation. For more information on these correlations, as they pertain to our work, see [21] and [25]. We assume, as we did in the main text, that the amplifier possesses high gain $|G(\nu)| \gg 1$, perfect input and output match, and reverse isolation. The two-port amplifier scattering matrix is then

$$S_{\text{amp}} = \begin{bmatrix} 0 & 0 \\ \sqrt{G(\nu)} & 0 \end{bmatrix} \quad (\text{D1})$$

Because this matrix is non-unitary, the amplifier circuit must add noise. We denote the noise modes classically as $c_1^{(2)}(\nu)$ and $c_2^{(2)}(\nu)$ in the main text.

¹¹If we assume a dark-matter density that stays constant throughout the year, then the value of this integral will vary annually. We will see an annual modulation in the value of the integral, ranging from 4.4×10^5 to 4.8×10^5 . The modulation corresponds to a $\sim 3.6\%$ variation in SNR. However, it is possible that such a small effect will not be observable in an experiment due to variations in system noise or variations in density.

To derive the noise correlations for a quantum-limited amplifier, we promote the amplitudes in equation (57) to operators, e.g. $a_1^{(2)}(\nu) \rightarrow \sqrt{\hbar\nu}a_1^\dagger(\nu)$. The prefactor $\sqrt{\hbar\nu}$ relates to the energy of a single photon at frequency ν and keeps the units consistent. Thus, we may write the scattering relation:

$$\begin{bmatrix} b_1^\dagger(\nu) \\ b_2^\dagger(\nu) \end{bmatrix} = \begin{bmatrix} 0 & 0 \\ \sqrt{G(\nu)} & 0 \end{bmatrix} \begin{bmatrix} a_1^\dagger(\nu) \\ a_2^\dagger(\nu) \end{bmatrix} + \begin{bmatrix} c_1^\dagger(\nu) \\ c_2^\dagger(\nu) \end{bmatrix}. \quad (\text{D2})$$

and similarly for the operators $a_{1,2}(\nu)$, $b_{1,2}(\nu)$, $c_{1,2}(\nu)$, with $G(\nu)$ replaced by $G(\nu)^*$. Because the input ($a_{1,2}^\dagger(\nu)$) and output operators ($b_{1,2}^\dagger(\nu)$) of the amplifier represent signals consisting of photons, they must obey the canonical bosonic commutation relations:

$$[a_1(\nu), a_1^\dagger(\nu')] = \delta(\nu - \nu'), \quad (\text{D3})$$

and similarly for $a_2^\dagger(\nu)$, $b_{1,2}^\dagger(\nu)$. Plugging the commutation relations into equation (D2), we obtain

$$[c_1(\nu), c_1^\dagger(\nu')] = \delta(\nu - \nu') \quad (\text{D4})$$

and

$$[c_2(\nu), c_2^\dagger(\nu')] = (1 - |G(\nu)|)\delta(\nu - \nu'). \quad (\text{D5})$$

As promised, the commutator for the imprecision noise mode $c_2(\nu)$ is nonzero as long as $|G(\nu)| > 1$; if the amplifier gains the input signal, the noise mode must be nontrivial.

The symmetrized quantum noise correlator obeys

$$\langle \{c_1^\dagger(\nu), c_1(\nu')\} \rangle \geq | \langle [c_1(\nu), c_1^\dagger(\nu')] \rangle |, \quad (\text{D6})$$

and similarly for $c_2^\dagger(\nu)$. Here, $\langle \rangle$ represents an expectation value, and $\{, \}$ represents the anti-commutator. The inequality becomes an equality when $c_1^\dagger(\nu)$ and $c_2^\dagger(\nu)$ each represent a single degree of freedom in its vacuum state:

$$c_1(\nu) = g(\nu) \quad (\text{D7})$$

$$c_2(\nu) = \sqrt{|G(\nu)| - 1}h^\dagger(\nu), \quad (\text{D8})$$

where $g(\nu)$ and $h^\dagger(\nu)$ obey the canonical bosonic commutation relations. These conditions represent the quantum limit for a phase-insensitive amplifier operated in scattering mode. [25],[28]

The classical noise correlators may be related to the symmetrized quantum noise correlators via [21]

$$\langle c_{1,2}^{(2)}(\nu)(c_{1,2}^{(2)}(\nu'))^* \rangle = \frac{h\nu}{2} \langle \{c_{1,2}^\dagger(\nu), c_{1,2}(\nu')\} \rangle. \quad (\text{D9})$$

Assume that the imprecision and backaction noise modes are uncorrelated. As discussed in the main text, this is typical in many experimental realizations of quantum-limited scattering-mode amplifiers [30]. Combining equations (D4)-(D9) then yields equations (94)-(96).

Appendix E: Flux-to-Voltage Amplifiers

In the main text, we discussed the optimization of impedance/noise matching and time allocation in an impedance-controlled system best described with a scattering mode representation. In that system, the input impedance of the amplifier is matched to the input transmission line. (See Fig. 5.) The noise impedance and input impedance of the amplifier are identical and real-valued. Such a description is appropriate for a free-space cavity read out with an impedance matched amplifier in scattering mode, as is used in ADMX and HAYSTAC.

In this appendix, we discuss flux-to-voltage amplifiers. Such amplifiers are used in the DM Radio, Axion LC, and ABRACADABRA searches. The most common example of a flux-to-voltage amplifier is a dc SQUID. The current in the input coil of a dc SQUID couples flux into the device, resulting in an amplified voltage on its output. The dc SQUID typically possesses a noise impedance far greater than its input impedance [57, 58]. In a sense, it is the low-impedance dual of a standard voltage op-amp: a low-impedance current amplifier reading out a relatively high impedance source. Moreover, owing to correlations between the imprecision noise mode and the backaction noise mode, the noise impedance tends to be complex-valued.

Numerous sophisticated models for noise in dc SQUIDs have been developed [41], but these models typically only apply to specific architectures in specific regimes. Moreover, the last few decades has seen the advent of numerous Josephson-junction-based flux-to-voltage amplifiers which are not described by these preexisting models. One example, discussed in Refs. [16, 42], is a dissipationless rf SQUID coupled to a lithographed microwave resonator. The microwave resonator is coupled to a feedline and interrogated with a \sim GHz probe

tone. The SQUID acts as a flux-variable inductor. When a flux is applied to the SQUID loop, the inductance of the SQUID changes, causing the resonance frequency of the coupled microwave circuit to change. The change in resonance frequency is read out as a phase shift in the probe tone. This phase shift may be modeled as an equivalent microwave-frequency voltage source in series with the SQUID loop, which is converted to a low-frequency, near-DC voltage source at a follow-on homodyne mixer. Owing to the use of unshunted junctions, these dissipationless rf SQUIDs enable a higher quality factor in the dark-matter detector than is possible with a dc SQUID.

As such, rather than adopting a pre-existing model for a particular architecture, in this appendix, we develop a broad framework for understanding imprecision and backaction noise in idealized flux-to-voltage amplifiers. We first discuss these noise modes classically and define noise temperature. We then use a linear response approach, adapted from ref. [28], to place a standard quantum limit on the performance of these amplifiers. The next appendix will be dedicated to optimization of the matching network using the quantum limit. We will derive a Bode-Fano constraint analogous to the scattering-mode constraint of Section V A 2. We will show that, again, the single-pole resonator is close to the Bode-Fano limit and discuss the optimization of impedance matching/noise matching in the context of a tunable resonator search using a quantum-limited flux-to-voltage amplifier. There, we will also discuss changes in the optimization that arise from correlations in the imprecision and backaction noise modes and from minimum noise temperature in excess of the quantum limit.

1. Classical Description of Noise in Flux-to-Voltage Amplifiers

A circuit model for the flux-to-voltage amplifier is shown in Fig. 10a. The source of voltage $V_s(\nu)$ and impedance $Z'_s(\nu)$ drives current $I_s(\nu)$ through the amplifier input coil of inductance L_{IN} . In response to the flux $\Phi_a(\nu) = MI_s(\nu)$ applied to the amplifier loop, the amplifier, presenting input impedance $Z_{\text{in}}(\nu)$ to the source, produces circulating screening currents $J(\nu)$. The circulating current, in turn, produces a voltage $V_{\text{out}}(\nu)$ in the output circuit.¹² This voltage drives currents across the series combination of the amplifier output

¹²In a dissipationless rf SQUID coupled to a microwave resonator, the voltage is the open-circuit voltage produced at the output of a homodyne mixer, which reads out the phase change of the probe tone.¹³

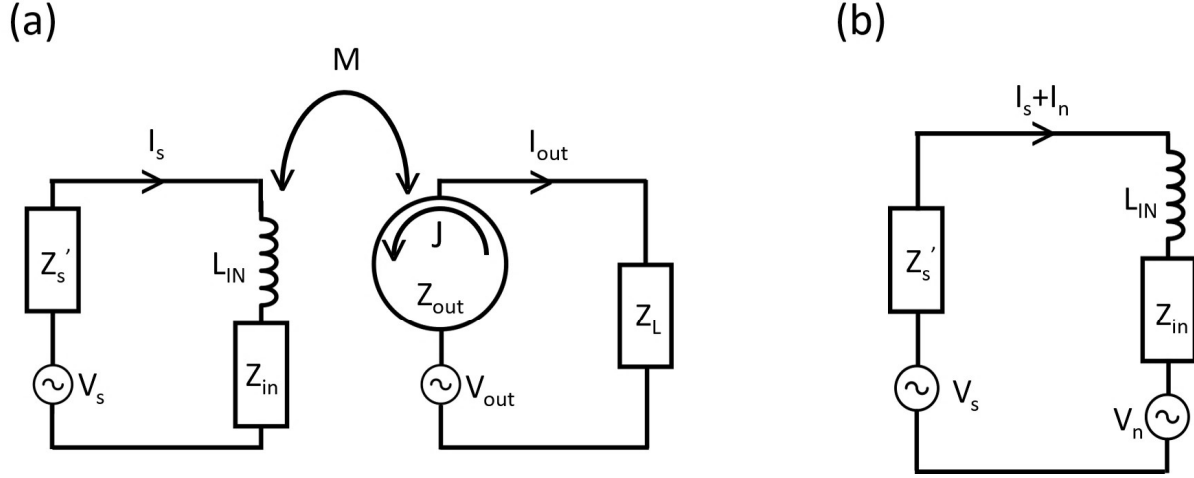


FIG. 10. Flux-to-voltage amplifier circuit model. (a) Circuit model including input circuit, amplifier, and output circuit. (b) Equivalent circuit model showing the effect of noise sources in the amplifier on the input circuit. All noises and impedances are permitted to be frequency-dependent, but we have suppressed the dependence for brevity.

impedance $Z_{out}(\nu)$ and the load impedance $Z_L(\nu)$. The load impedance is typically the input of a second-stage amplifier. We will assume that the gain of the flux-to-voltage amplifier is large enough that the noise from the later amplification stages is negligible.

There are two noise sources in the amplifier. First, there are intrinsic fluctuations in the output voltage. Through the flux-to-voltage transfer function, the output voltage fluctuation can be referred as a fluctuation in the current through the input circuit. This noise current is denoted as $I_n(\nu)$ in Fig. 10b and represents the imprecision noise of the amplifier. Second, there are fluctuations in the circulating current. This circulating current, via Faraday's Law, produces a noise voltage in the input current. This noise voltage is denoted as $V_n(\nu)$ in Fig. 10b and represents the backaction noise of the amplifier. It will drive additional noise currents through the input coil, resulting in additional noise at the output of the amplifier. The total noise current in the input circuit is thus

$$I_{n,tot}(\nu) = I_n(\nu) + \frac{V_n(\nu)}{Z'_s(\nu) + 2\pi i\nu L_{IN} + Z_{in}(\nu)}. \quad (E1)$$

We now define the noise temperature of the flux-to-voltage amplifier. We define the following single-sided, classical noise spectral densities:

$$\langle V_n(\nu) V_n^*(\nu') \rangle \equiv \mathcal{S}_{VV}^{FV}(\nu) \delta(\nu - \nu') \quad (E2)$$

$$\langle I_n(\nu) I_n^*(\nu') \rangle \equiv \mathcal{S}_{II}^{FV}(\nu) \delta(\nu - \nu') \quad (\text{E3})$$

$$\langle I_n(\nu) V_n^*(\nu') \rangle \equiv \mathcal{S}_{IV}^{FV}(\nu) \delta(\nu - \nu') \quad (\text{E4})$$

We assume that these noise spectral densities are intrinsic to the amplifier and have no dependence on the input circuit. Such is typical for an amplifier with adequate linearity to be used in a practical measurement. We define the total source impedance as

$$Z_s(\nu) \equiv Z'_s(\nu) + 2\pi i \nu L_{IN}. \quad (\text{E5})$$

This is effectively the source impedance as seen by the flux-to-voltage amplifier. From this point, we will refer to this quantity as “the source impedance.” The total impedance of the input circuit, as seen by any voltage source in the input circuit is,

$$Z_T(\nu) \equiv Z_s(\nu) + Z_{in}(\nu). \quad (\text{E6})$$

The one-sided, classical noise spectral density for the total noise current is

$$\mathcal{S}_{II,\text{tot}}^{FV}(\nu) = \mathcal{S}_{II}^{FV}(\nu) + \frac{\mathcal{S}_{VV}^{FV}(\nu)}{|Z_T(\nu)|^2} + 2\text{Re} \left(\frac{\mathcal{S}_{IV}^{FV}(\nu)}{Z_T^*(\nu)} \right). \quad (\text{E7})$$

We define the noise temperature $T_N(\nu)$ by

$$\frac{4kT_N(\nu)\text{Re}(Z_T(\nu))}{|Z_T(\nu)|^2} \equiv \mathcal{S}_{II,\text{tot}}^{FV}(\nu). \quad (\text{E8})$$

Qualitatively, suppose the real part of the total impedance is represented a physical, equilibrium resistor at temperature $kT_0 \gg h\nu$. The noise temperature is the amount that we would have to increase the physical temperature of the resistor to increase the Johnson current noise spectral density by an amount $\mathcal{S}_{II,\text{tot}}(\nu)$. Writing $Z_T(\nu) = |Z_T(\nu)|e^{i\phi(\nu)}$,

$$kT_N(\nu) = \frac{1}{4 \cos \phi(\nu)} \left(\frac{\mathcal{S}_{VV}^{FV}(\nu)}{|Z_T(\nu)|} + \mathcal{S}_{II}^{FV}(\nu)|Z_T(\nu)| + 2\text{Re}(\mathcal{S}_{IV}^{FV}(\nu)e^{i\phi(\nu)}) \right). \quad (\text{E9})$$

Minimizing with respect to $Z_T(\nu)$, we obtain a bound on the noise temperature

$$kT_N(\nu) \geq \frac{1}{2} \left(\sqrt{\mathcal{S}_{VV}^{FV}(\nu)\mathcal{S}_{II}^{FV}(\nu) - (\text{Im } \mathcal{S}_{IV}^{FV}(\nu))^2} + \text{Re } \mathcal{S}_{IV}^{FV}(\nu) \right), \quad (\text{E10})$$

where the minimum is achieved for the noise impedance $Z_N(\nu) = |Z_N(\nu)|e^{i\phi_N(\nu)}$, given by

$$|Z_N(\nu)| = \sqrt{\mathcal{S}_{VV}^{FV}(\nu)/\mathcal{S}_{II}^{FV}(\nu)} \quad (\text{E11})$$

$$\sin \phi_N(\nu) = \text{Im } \mathcal{S}_{IV}^{FV}(\nu) / \sqrt{\mathcal{S}_{VV}^{FV}(\nu)\mathcal{S}_{II}^{FV}(\nu)} \quad (\text{E12})$$

Note that if the noise spectral densities appearing on the right-hand side of equations (E11) and (E12) are dependent on the input circuit, it may not be possible to reach the minimum noise temperature (E10). We avoid this scenario, as it is usually not representative of a linear amplifier.

2. Standard Quantum Limit on Noise in a Flux-to-Voltage Amplifier

To describe the standard quantum limit on noise in a flux-to-voltage amplifier, previously described classically, we utilize the linear response approach of refs. [28, 59]. As discussed in [28], the scattering description of quantum limits, which appears in ref. [25] and which is the subject of appendix D, does not directly apply to flux-to-voltage amplifiers. The linear response approach enables us to express the quantum limits and the amplifier performance in terms of the noise spectral densities (E2)-(E4). For details regarding this approach and the distinction between flux-to-voltage amplifiers and scattering mode amplifiers, see [28], in which a related linear response analysis is carried out for high-impedance voltage op-amps.

In a linear response approach, the interaction between the amplifier and its input and output circuits is treated perturbatively, and first-order perturbation theory is used to develop a description of the amplifier. Within this framework, we characterize the amplifier's input and output impedance and power gain in terms of response coefficients that describe how system currents and voltages are affected by the interaction. These response coefficients depend on the intrinsic properties of the amplifier, i.e. they are parameters of the uncoupled amplifier. The same response coefficients are then used in expression of the quantum limit.

We first define Hamiltonians for the interaction of the input circuit with the amplifier and for the interaction of the amplifier with the output circuit. This requires us to promote the voltages and currents in Fig. 10 to Hermitian operators. The input Hamiltonian describes a flux from the input circuit which couples to the circulating currents of the amplifier [44]:

$$H_{\text{int}} = M \hat{I}_s \hat{J}, \quad (\text{E13})$$

where \hat{I}_s is the interaction-picture operator for the current in the input circuit, and \hat{J} is the operator for the circulating current. The output Hamiltonian describes a current in the output circuit due to the voltage signal from the amplifier:

$$H'_{\text{int}} = \hat{Q}_{\text{out}} \hat{V}_{\text{out}}, \quad (\text{E14})$$

where $\hat{I}_{\text{out}} = -\frac{d\hat{Q}_{\text{out}}}{dt}$ is the current flowing in the output circuit, and \hat{V}_{out} is the operator for voltage at the amplifier output. We assume that the coupling between the input circuit and the amplifier is sufficiently weak such that the voltage response is linear in the input current.

We characterize the amplifier input and output impedances and power gain in terms of the amplifier operators \hat{J} and \hat{V}_{out} . This characterization will prove useful in later discussions of amplifier noise. For what follows, we assume that when the amplifier is uncoupled from the input and output circuits, the expectation value of the circulating current in the flux-to-voltage amplifier loop and the output voltage vanish. If the expectation values are nonzero, we subtract them from the operators (i.e. subtract the product of the expectation and the identity operator) and proceed as below. Assuming that the interaction Hamiltonians are turned on adiabatically at time $t = -\infty$, the expectation value of the circulating current in the flux-to-voltage amplifier due to the input signal $\hat{I}_s(t)$ is given by the Kubo formula

$$\langle \hat{J}(t) \rangle = M \int_{-\infty}^{\infty} dt' \chi_{JJ}(t-t') \langle \hat{I}_s(t') \rangle, \quad (\text{E15})$$

where the $J - J$ susceptibility is defined by

$$\chi_{JJ}(t) \equiv -\frac{i}{\hbar} \theta(t) \langle [\hat{J}(t), \hat{J}(0)] \rangle_0, \quad (\text{E16})$$

and $\theta(t)$ is the Heaviside function. The subscript zero indicates expectation value of the commutator is taken with respect to the density matrix of the uncoupled amplifier. Fourier transforming the currents and the $J - J$ susceptibility

$$\chi_{JJ}(\nu) = -\frac{i}{\hbar} \int_0^{\infty} dt \langle [\hat{J}(t), \hat{J}(0)] \rangle_0 e^{2\pi i \nu t} \quad (\text{E17})$$

yields

$$\langle \hat{J}(\nu) \rangle = M \chi_{JJ}(\nu) \langle \hat{I}_s(\nu) \rangle. \quad (\text{E18})$$

The circulating current induces a voltage $\hat{V}(\nu) = 2\pi i \nu M \hat{J}(\nu)$ in the input circuit, so we obtain an input impedance of

$$Z_{\text{in}}(\nu) = 2\pi i \nu M^2 \chi_{JJ}(\nu) \quad (\text{E19})$$

The real part of the input impedance determines the damping of the input circuit due to the coupling to the amplifier. Similarly, we may relate the output voltage to the output current via the $V_{\text{out}} - V_{\text{out}}$ susceptibility.

$$\langle \hat{V}_{\text{out}}(t) \rangle = \int_{-\infty}^{\infty} dt' \chi_{V_{\text{out}} V_{\text{out}}}(t-t') \langle \hat{Q}_{\text{out}}(t') \rangle \quad (\text{E20})$$

$$\chi_{V_{\text{out}} V_{\text{out}}}(t) \equiv -\frac{i}{\hbar} \theta(t) \langle [\hat{V}_{\text{out}}(t), \hat{V}_{\text{out}}(0)] \rangle_0 \quad (\text{E21})$$

Fourier transforming, we find

$$Z_{\text{out}} = \frac{i\chi_{V_{\text{out}}V_{\text{out}}}(\nu)}{2\pi\nu}. \quad (\text{E22})$$

We define a power-gain $G_P(\nu)$ in the frequency domain, which is the ratio of the power delivered to the load impedance Z_L to the power drawn by the amplifier input, maximized over the load impedance. To compute the power gain, we first note that the output voltage response to an input current signal is

$$\langle \hat{V}_{\text{out}}(t) \rangle = M \int_{-\infty}^{\infty} dt' \chi_{V_{\text{out}}J}(t-t') \langle \hat{I}_s(t') \rangle, \quad (\text{E23})$$

where the $V_{\text{out}} - J$ susceptibility is defined by

$$\chi_{V_{\text{out}}J}(t) \equiv -\frac{i}{\hbar} \theta(t) \langle [\hat{V}_{\text{out}}(t), \hat{J}(0)] \rangle_0. \quad (\text{E24})$$

Identifying $\hat{\Phi}_a = M\hat{I}_s$ as the flux applied to the flux-to-voltage amplifier input, we may identify the Fourier component $\chi_{V_{\text{out}}J}(\nu)$ as the more familiar flux-to-voltage transfer function:

$$\chi_{V_{\text{out}}J}(\nu) \leftrightarrow V_{\Phi}(\nu) = \frac{V_{\text{out}}(\nu)}{\Phi_a(\nu)}. \quad (\text{E25})$$

The maximum power delivered to the load is achieved for $Z_L = Z_{\text{out}}^*$, so we obtain a power gain

$$G_P(\nu) = \frac{M^2 |\chi_{V_{\text{out}}J}(\nu)|^2}{4\text{Re}(Z_{\text{in}}(\nu))\text{Re}(Z_{\text{out}}(\nu))} = \frac{|\chi_{V_{\text{out}}J}(\nu)|^2}{4\text{Im}(\chi_{JJ}(\nu))\text{Im}(\chi_{VV}(\nu))}. \quad (\text{E26})$$

When the power gain is greater than unity, both quadratures of the signal are amplified (the amplifier discussed here being phase-insensitive) and Heisenberg's uncertainty principle dictates that a minimum amount of noise must be added.

We are now ready to set the standard quantum limit on the added noise of the idealized flux-to-voltage amplifier. We assume that the amplifier possesses no reverse gain; a signal coupled into the amplifier through the output voltage does not produce input flux. Furthermore, we assume that the in-phase correlations of the current imprecision noise and voltage backaction noise vanishes, $\text{Re } \mathcal{S}_V^{FV}(\nu) = 0$. (Such an assumption is compatible with some dc SQUID models. See, for example, [60].) Since both quadratures of the signal are amplified equally, Heisenberg's uncertainty principle places a constraint on the symmetrized quantum noise spectral densities of the flux-to-voltage amplifier circulating current and the output voltage. Identifying the symmetrized quantum spectral densities with the one-sided

classical noise spectral densities (i.e. $\hat{F} = \hat{J}$, $\hat{I} = \hat{V}_{\text{out}}$, and $\bar{S}_{JJ} \rightarrow \mathcal{S}_{JJ}/2$ in equation (4.11) of [28]), the constraint can be written as

$$\mathcal{S}_{V_{\text{out}}V_{\text{out}}}(\nu)\mathcal{S}_{JJ}(\nu) - |\mathcal{S}_{V_{\text{out}}J}(\nu)|^2 \geq |\hbar\chi_{V_{\text{out}}J}(\nu)|^2 \left(1 + \Xi\left(\frac{\mathcal{S}_{V_{\text{out}}J}(\nu)}{\hbar\chi_{V_{\text{out}}J}(\nu)}\right)\right), \quad (\text{E27})$$

where $\Xi(z)$ is a complex function defined as

$$\Xi(z) = \frac{|1 + z^2| - (1 + |z|^2)}{2}. \quad (\text{E28})$$

We may relate the output voltage and flux-to-voltage amplifier circulating currents to the current and induced voltage in the input coil:

$$I(\nu) = \frac{1}{M\chi_{V_{\text{out}}J}(\nu)}V_{\text{out}}(\nu) \quad (\text{E29})$$

$$V(\nu) = 2\pi i\nu MJ(\nu) \quad (\text{E30})$$

so

$$\mathcal{S}_{VV}^{FV}(\nu)\mathcal{S}_{II}^{FV}(\nu) - |\mathcal{S}_{IV}^{FV}(\nu)|^2 \geq |h\nu|^2 \left(1 + \Xi\left(\frac{i\mathcal{S}_{IV}^{FV}(\nu)}{h\nu}\right)\right). \quad (\text{E31})$$

Since we assume that $\text{Re } \mathcal{S}_{IV}^{FV} = 0$, Ξ vanishes. From (E10) and (E31), we now obtain the quantum limit on the noise temperature of a flux-to-voltage amplifier:

$$kT_N(\nu) \geq \frac{1}{2}\sqrt{\mathcal{S}_{VV}^{FV}(\nu)\mathcal{S}_{II}^{FV}(\nu) - (\text{Im } \mathcal{S}_{IV}^{FV}(\nu))^2} \geq \frac{h\nu}{2}. \quad (\text{E32})$$

The quantum limit on the added noise of the amplifier is equal to the zero-point fluctuation noise of the equivalent source resistance $\text{Re } Z_T(\nu)$. The quantum limit on noise temperature is achieved when:

1. The quantum noise constraint (E31) for noise spectral densities \mathcal{S}_{VV}^{FV} , \mathcal{S}_{II}^{FV} , and \mathcal{S}_{IV}^{FV} is satisfied (i.e. equality is obtained).
2. The impedance $Z_T(\nu)$, which is the sum of source and input impedances, is the noise impedance $Z_N(\nu)$ determined by the spectral densities.

Before moving on to the optimization of resonant searches using these amplifiers, we discuss a few properties of a quantum-limited flux-to-voltage amplifier. First, when the quantum noise constraint (E27) is satisfied and the power gain is much larger than unity, one may show that $\mathcal{S}_{V_{\text{out}}J}(\nu)$ is in phase with $\chi_{VJ}(\nu)$. (See Appendix I.3 of [28].) This implies that $\text{Re } \mathcal{S}_{IV}(\nu) = 0$, which is consistent with our original assumptions. This is expected

because the presence of such in-phase noise correlations constitutes wasted information and thus, would prevent an amplifier from reaching the quantum limit. Second, combining equations (E11) and (E19), we find

$$\left| \frac{\text{Re } Z_{in}(\nu)}{Z_N(\nu)} \right| = \left| \sqrt{\frac{\mathcal{S}_{VV}(\nu)}{\mathcal{S}_{JJ}(\nu)}} \frac{\text{Im } \chi_{JJ}(\nu)}{\chi_{VJ}(\nu)} \right| = \frac{1}{2\sqrt{G_P(\nu)}} \sqrt{\frac{\mathcal{S}_{VV}(\nu)}{\mathcal{S}_{JJ}(\nu)} \frac{\text{Im } \chi_{JJ}(\nu)}{\text{Im } \chi_{VV}(\nu)}} = \frac{1}{2\sqrt{G_P(\nu)}} \ll 1, \quad (\text{E33})$$

where, in the last equality, we have used the proportionality condition (I13)-(I15) from [28]. Assuming that the noise impedance is real (no correlations between imprecision and backaction noise modes), eq. (E33) demonstrates that, when the input circuit impedance $Z_T(\nu)$ is tuned to the noise impedance, the damping resulting from coupling to the amplifier is much less than the internal damping of the input circuit. Then, $Z_T(\nu) \approx Z_s(\nu) + \text{Im } Z_{in}(\nu)$. In the next section, we will actually require the stronger condition that $G_P(\nu) \gg \xi^{\text{opt}}(\nu, n(\nu))^2/4$, where ξ is defined in (141). The purpose of eq. (E33) is to show that sufficiently high power gain is consistent with negligible damping from the amplifier input impedance. Without such a property, additional complexities emerge in the scan optimization.

Appendix F: Scan Optimization for Tunable Resonator Searches with Flux-to-Voltage Amplifiers

With the results on quantum limits in hand, we now discuss the optimization of searches with flux-to-voltage amplifiers. Our treatment mirrors that in Sections IV and V of the main text.

First, we present a brief SNR analysis for a readout with a flux-to-voltage amplifier, which is analogous to the scattering-mode SNR analysis in Section IV. Then, we establish a Bode-Fano constraint on integrated sensitivity in a log-uniform search read out by a quantum-limited amplifier. The constraint is analogous to that in Section V A 2.

We then turn our attention to the optimization of single-pole resonant dark matter searches with flux-to-voltage amplifiers. We discuss two examples. In the first example, to compare our results to those in the main text, we consider a quantum-limited flux-to-voltage amplifier with uncorrelated imprecision and backaction noise. Such an amplifier is analogous to the scattering-mode amplifier described by equations (94)-(96). We show that, like the scattering-mode case, a single-pole resonator is close to the Bode-Fano limit. In the

second example, we relax the assumption of a minimum noise temperature equal to one-half photon and the assumption of uncorrelated imprecision and backaction noise.

1. Signal-To-Noise Ratio of Search With Flux-To-Voltage Amplifier

Here, we evaluate the SNR of a search with a flux-to-voltage amplifier. We assume that the damping resulting from coupling to the amplifier is negligible, which is consistent with eq. (E33).

We evaluate the sensitivity, not in terms of a scattering parameters, but rather, in terms of the impedance seen by the amplifier. This quantity is denoted as $Z_T(\nu)$ in eq. (E6), and is displayed schematically, with the LR signal source, in Fig. 11. We have lumped the imaginary part of the amplifier input impedance into the impedance $Z_T(\nu)$. We assume that the matching network between the signal source and amplifier is lossless and contains only linear, passive, and reciprocal elements.

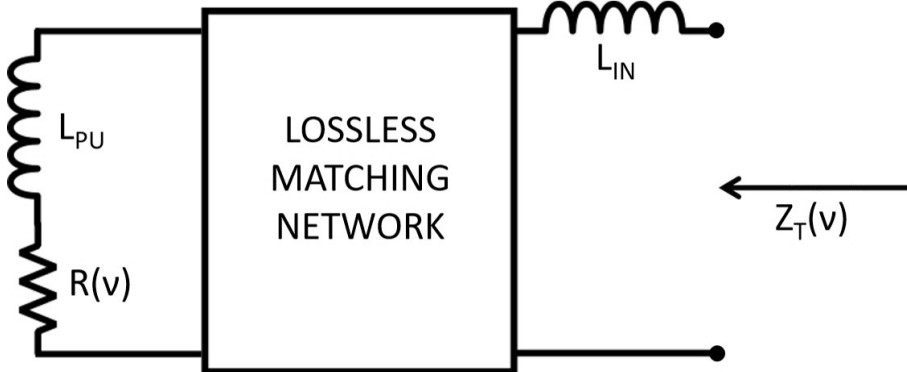


FIG. 11. Impedance seen by the flux-to-voltage amplifier.

The SNR is determined by the voltage measured at the output of the amplifier, which may be referred to a current through the input inductor L_{IN} . This is analogous to the determination of the SNR by analyzing the timestream of the wave at the output of the scattering-mode amplifier.

Referencing Figs. 3 and 10, as well as our discussion in the introduction, there are two voltage sources in the signal source that drive currents in the amplifier input coil. First, the dark-matter signal coupling to the inductor produces a drive voltage $V_{DM}(\nu, g_{DM}, \frac{d\rho_{DM}}{d\nu}(\nu, \nu_{DM}^0))$, defined in equation (50), across the inductor. Second, the loss in our circuit produces an

equivalent noise voltage $V_{FD}(\nu)$ across the resistor $R(\nu)$, as dictated by the fluctuation-dissipation theorem. The noise spectral density is given by

$$\langle V_{FD}(\nu)V_{FD}(\nu') \rangle = \mathcal{S}_{V_{FD}V_{FD}}(\nu)\delta(\nu - \nu') \quad (\text{F1})$$

where

$$\mathcal{S}_{V_{FD}V_{FD}}(\nu) = 4h\nu R(\nu)(n(\nu) + 1/2) \quad (\text{F2})$$

In order to determine the SNR, we must transform these series voltages in the signal source to voltages between the terminals at the right-hand side of Fig. 11. For the thermal/zero-point noise, the transformed noise voltage $V_{FD}^t(\nu)$ possesses power spectral density

$$\langle V_{FD}^t(\nu)V_{FD}^t(\nu') \rangle = \mathcal{S}_{V_{FD}^tV_{FD}^t}(\nu)\delta(\nu - \nu') \quad (\text{F3})$$

where

$$\mathcal{S}_{V_{FD}^tV_{FD}^t}(\nu) = 4h\nu Re(Z_T(\nu))(n(\nu) + 1/2) \quad (\text{F4})$$

The dark-matter signal voltage spectral density must transform similarly because impedance transformations do not change signal-to-thermal noise. We denote the transformed Fourier voltages as $V_{DM}^t(\nu, g_{DM}, \frac{d\rho_{DM}}{d\nu}(\nu, \nu_{DM}^0))$. They obey

$$\left| V_{DM}^t \left(\nu, g_{DM}, \frac{d\rho_{DM}}{d\nu}(\nu, \nu_{DM}^0) \right) \right|^2 = \frac{Re(Z_T(\nu))}{R(\nu)} \left| V_{DM} \left(\nu, g_{DM}, \frac{d\rho_{DM}}{d\nu}(\nu, \nu_{DM}^0) \right) \right|^2 \quad (\text{F5})$$

The flux-to-voltage amplifier produces an equivalent current imprecision noise and voltage backaction noise, denoted by $I_n(\nu)$ and $V_n(\nu)$ in equation (E1), with noise spectral densities given by equations (E2)-(E4). The total equivalent current fed into the amplifier is then

$$I(\nu) = \frac{V_{DM}^t(\nu, g_{DM}, \frac{d\rho_{DM}}{d\nu}(\nu, \nu_{DM}^0)) + V_{FD}^t(\nu) + V_n(\nu)}{Z_T(\nu)} + I_n(\nu) \quad (\text{F6})$$

Note that, if the thermal noise dominates the flux-to-voltage amplifier noise, the SNR will be independent of value of the impedance $Z_T(\nu)$. In the case of a resonant impedance, this will give rise to sensitivity at frequencies outside of the resonator bandwidth.

Using the same optimal-filtering approach as in the main text, and replacing the amplifier output $b(\nu)$ with the input current $I(\nu)$ (which can be referred from the flux-to-voltage amplifier output voltage), we find that the SNR of a measurement of integration time τ much longer than the dark-matter coherence time and input-circuit pole time (t_{pole} , introduced

above (66)) is

$$SNR \left[\nu_{\text{DM}}^0, g_{\text{DM}}, \frac{d\rho_{\text{DM}}}{d\nu}(\nu, \nu_{\text{DM}}^0), \tau, f_{\text{circ}} \left(\nu, \nu_{\text{DM}}^0, \frac{d\rho_{\text{DM}}}{d\nu}(\nu, \nu_{\text{DM}}^0) \right) \right] \quad (\text{F7})$$

$$= \frac{\int d\nu |f_{\text{circ}}(\nu, \nu_{\text{DM}}^0, \frac{d\rho_{\text{DM}}}{d\nu}(\nu, \nu_{\text{DM}}^0))|^2 |V_{\text{DM}}^t(\nu, g_{\text{DM}}, \frac{d\rho_{\text{DM}}}{d\nu}(\nu, \nu_{\text{DM}}^0))|^2 / |Z_T(\nu)|^2}{(\tau^{-1} \int d\nu |f_{\text{circ}}(\nu, \nu_{\text{DM}}^0, \frac{d\rho_{\text{DM}}}{d\nu}(\nu, \nu_{\text{DM}}^0))|^4 \mathcal{S}_{II}^{\text{tot}}(\nu)^2)^{1/2}}$$

where $\mathcal{S}_{II}^{\text{tot}}(\nu)$ is the total noise spectral density

$$\mathcal{S}_{II}^{\text{tot}}(\nu) = \frac{\mathcal{S}_{V_{FD}^t V_{FD}^t}(\nu) + \mathcal{S}_{V_V^{FV}}(\nu)}{|Z_T(\nu)|^2} + \mathcal{S}_{II}^{FV}(\nu) + 2\text{Re} \left(\frac{\mathcal{S}_{IV}^{FV}(\nu)}{Z_T^*(\nu)} \right) \quad (\text{F8})$$

The filter which maximizes SNR is the Wiener filter

$$\left| f_{\text{circ}}^{\text{opt}} \left(\nu, \nu_{\text{DM}}^0, \frac{d\rho_{\text{DM}}}{d\nu}(\nu, \nu_{\text{DM}}^0) \right) \right|^2 = \frac{|V_{\text{DM}}^t(\nu, g_{\text{DM}}, \frac{d\rho_{\text{DM}}}{d\nu}(\nu, \nu_{\text{DM}}^0))|^2}{|Z_T(\nu)|^2 \mathcal{S}_{II}^{\text{tot}}(\nu)^2} \quad (\text{F9})$$

for which the SNR is

$$SNR^{\text{opt}} \left[\nu_{\text{DM}}^0, g_{\text{DM}}, \frac{d\rho_{\text{DM}}}{d\nu}(\nu, \nu_{\text{DM}}^0), \tau \right] \quad (\text{F10})$$

$$\equiv SNR^{\text{opt}} \left[\nu_{\text{DM}}^0, g_{\text{DM}}, \frac{d\rho_{\text{DM}}}{d\nu}(\nu, \nu_{\text{DM}}^0), \tau, f_{\text{circ}}^{\text{opt}} \left(\nu, \nu_{\text{DM}}^0, \frac{d\rho_{\text{DM}}}{d\nu}(\nu, \nu_{\text{DM}}^0) \right) \right]$$

$$= \left(\tau \int d\nu \frac{|V_{\text{DM}}^t(\nu, g_{\text{DM}}, \frac{d\rho_{\text{DM}}}{d\nu}(\nu, \nu_{\text{DM}}^0))|^4}{|Z_T(\nu)|^4 \mathcal{S}_{II}^{\text{tot}}(\nu)^2} \right)^{1/2}$$

In a scan, in which multiple circuit configurations are used, each with a different impedance $Z_T(\nu)$, one may calculate the total SNR by adding the single-configuration SNRs in quadrature. Such a technique is useful in particular when considering a scanned single-pole resonator, such as that in Fig. 3.

2. Bode-Fano constraint on integrated sensitivity

Having an expression for the SNR in a search with a flux-to-voltage amplifier, we establish a Bode-Fano constraint analogous to the scattering-mode treatment of Section V A 2.

We assume that the flux-to-voltage amplifier is quantum-limited and possesses a real-valued noise impedance Z_N that does not change appreciably within the sensitivity bandwidth. The real-valued, frequency-independent noise impedance mirrors that in the scattering mode case, where the noise impedance is equal to the real-valued, frequency-independent input impedance. A real-valued noise impedance implies from equation (E12) that the imprecision and backaction noise are uncorrelated. We will revisit the assumptions regarding

noise impedance at the end of this section. We express the voltage backaction and current imprecision noise spectral densities as

$$S_{VV}^{FV}(\nu) = h\nu Z_N \quad (\text{F11})$$

$$S_{II}^{FV}(\nu) = \frac{h\nu}{Z_N} \quad (\text{F12})$$

Combining the amplifier noise spectral densities with equations (50), (F4), (F5) yields

$$SNR^{\text{opt}} \left[\nu_{\text{DM}}^0, g_{\text{DM}}, \frac{d\rho_{\text{DM}}}{d\nu}(\nu, \nu_{\text{DM}}^0), \tau \right] = 2\pi^2 \quad (\text{F13})$$

$$\times \left(\tau \int_{\nu_{\text{DM}}^0}^{\nu_{\text{DM}}^0 + \Delta\nu_{\text{DM}}^c(\nu_{\text{DM}}^0)} d\nu \left(\frac{\nu L_{\text{PU}}}{R(\nu)} \frac{E_{\text{DM}}(\nu, \nu_{\text{DM}}^0, g_{\text{DM}}, \frac{d\rho_{\text{DM}}}{d\nu}(\nu, \nu_{\text{DM}}^0))}{h} \frac{1}{N_{\text{tot}}^{FV}(\nu, Z_T(\nu), n(\nu))} \right)^2 \right)^{1/2}.$$

where

$$N_{\text{tot}}^{FV}(\nu, Z_T(\nu), n(\nu)) = \frac{\text{Re}(Z_T(\nu))(n(\nu) + \frac{1}{2}) + \frac{1}{4} \left(\frac{|Z_T(\nu)|^2}{Z_N} + Z_N \right)}{\text{Re}(Z_T(\nu))} \quad (\text{F14})$$

plays the role of noise-equivalent number, similar to eq. (99). Define

$$\zeta(Z_T(\nu)) = 1 - \left| \frac{Z_T(\nu) - Z_N}{Z_T(\nu) + Z_N} \right|^2 \quad (\text{F15})$$

$\zeta(Z_T(\nu))$ describes the match, at frequency ν , between the impedance seen by the flux-to-voltage amplifier and the noise impedance. ζ takes on values between zero and one; when it is equal to one, the input circuit is noise-matched to the amplifier. One may note the similarity between transmission in the scattering system of the main text and the definition of ζ . As we will see, ζ plays the role of $|S_{21}^1(\nu)|^2$ in the evaluation of SNR and the determination of the Bode-Fano limit. In terms of ζ , the noise equivalent number of equation (F14) may be rewritten as

$$N_{\text{tot}}^{FV}(\nu, Z_T(\nu), n(\nu)) = \frac{\zeta(Z_T(\nu))n(\nu) + 1}{\zeta(Z_T(\nu))} \quad (\text{F16})$$

which is identical in form to (99) with $|S_{21}^1(\nu)|^2$ replaced by $\zeta(Z_T(\nu))$.

Following Section V A 1, we may define a scaled log-uniform-search value functional, which is the frequency-integrated inverse squared of noise-equivalent number. Assuming a frequency-independent signal source resistance, $R = R(\nu)$, the functional is

$$\bar{F}_{\text{neu}}^{FV}[\zeta(Z_T(\nu))] = \int_{\nu_l}^{\nu_h} d\nu \left(\frac{\zeta(Z_T(\nu))}{\zeta(Z_T(\nu))n(\nu) + 1} \right)^2 \quad (\text{F17})$$

where $\nu_l \leq \nu \leq \nu_h$ is the search band. The Bode-Fano criterion constrains the match between the impedance $Z_T(\nu)$ and the real noise impedance Z_N :

$$\int_{\nu_l}^{\nu_h} \ln \frac{1}{\left| \frac{Z_T(\nu) - Z_N}{Z_T(\nu) + Z_N} \right|} \leq \frac{R}{2L_{PU}} \quad (\text{F18})$$

which implies

$$\int_{\nu_l}^{\nu_h} \ln \frac{1}{1 - \zeta(Z_T(\nu))} \leq \frac{R}{L_{PU}} \quad (\text{F19})$$

Substituting ζ for $|S_{21}^{(1)}(\nu)|^2$ in Sec. V A 2, we may proceed identically and establish an identical limit on the value functional. The result is summarized here, for convenience:

$$\bar{F}_{\text{neu}}^{FV}[\zeta(Z_T(\nu))] \lesssim \begin{cases} 0.4 \frac{R}{L_{PU}}, & n(\nu_h) \ll 1 \\ \frac{1}{4n(\nu_h)} \frac{R}{L_{PU}}, & n(\nu_h) \gg 1 \end{cases} \quad (\text{F20})$$

Equality is achieved when $\zeta(Z_T(\nu))$ is a top-hat with respect to frequency. In other words, outside of a narrow band, the input circuit is maximally mismatched to the amplifier noise impedance. Such a top hat may be constructed using multi-pole LC Chebyshev filters. Note that the Bode-Fano limit is independent of the noise impedance. We will find that the single-pole resonator, with optimized noise impedance, is close to the fundamental Bode-Fano limit.

Having set the Bode-Fano limit, we revisit an assumption made at the beginning of the section: that the noise impedance is real-valued and frequency-independent. A common feature of quantum-limited readouts operating in the op-amp mode (op-amp mode being the mode in which flux-to-voltage amplifiers operate [28]), is uncorrelated backaction and imprecision noise. For instance, in quantum-limited cavity detectors used for mechanical displacement sensing possess, the radiation pressure fluctuations responsible for backaction and the shot noise in the light output from the cavity (e.g. the imprecision noise) are uncorrelated[61]. As demonstrated in Appendix E, for uncorrelated backaction and imprecision noise, the noise impedance of the amplifier is real-valued.

A flux-to-voltage amplifier, such as a dc SQUID, tends to possess a noise impedance that increases linearly with frequency [57]. In other words, the noise impedance is not frequency-independent. However, we expect that the frequency-dependence has little effect on the limit on integrated sensitivity. If the Bode-Fano limit (F20) pointed toward the optimal circuit possessing a broadband noise match, then the frequency-dependence of noise impedance

would be important. However, the Bode-Fano limit (F20) points to a narrowband match. In a narrow band, the noise impedance can be approximated as constant. We thus conclude that, even with a frequency-dependent real-valued noise impedance, the single-pole resonator is close to ideal for single-moded dark matter detection.

We now turn our attention to the optimization of single-pole resonant searches. Suppose that the input circuit is resonant. The impedance seen by a voltage source is the sum of circuit and amplifier input impedances:

$$Z_T(\nu) = R(\nu) + 2\pi i\nu(L_{\text{IN}} + L_{\text{PU}}) + \frac{1}{2\pi i\nu C}. \quad (\text{F21})$$

For a quantum-limited flux-to-voltage amplifier, the intrinsic damping of the input circuit is much greater than the damping due to the amplifier (equation (E33)) so that the resistance R is solely the intrinsic resistance (dielectric losses, etc). As such, from this point, we will ignore the amplifier-dependent damping. We have lumped the imaginary part of the input impedance into the reactive part of the circuit impedance L_{IN} .¹⁴ Letting $L = L_{\text{IN}} + L_{\text{PU}}$ represent the total inductance, the resonance frequency of this circuit is $\nu_r = 1/2\pi\sqrt{LC}$ and the quality factor is $Q(\nu_r) = 2\pi\nu_r L/R(\nu_r)$. We have denoted the quality factor as a function of resonance frequency because in general, the loss may vary as we tune the resonator. For quantum-limited flux-to-voltage amplifiers, unlike quantum-limited scattering mode amplifier, the internal quality factor and overall quality factor are the same. This is due to the fundamentally different damping properties of the quantum-limited amplifiers, as dictated by the input impedance. For frequencies $|\nu - \nu_r| \ll \nu_r$, we may then write the impedance as

$$Z_T(\nu, \nu_r) \approx R(\nu_r) \left(1 + 2iQ(\nu_r) \frac{\nu - \nu_r}{\nu_r} \right). \quad (\text{F22})$$

A scan is comprised of measurements conducted at a set of resonance frequencies ν_r^i . We allow the quality factor $Q^i = Q(\nu_r^i)$ to vary with resonance frequency. In accordance with equation (166), we assume that the dwell time τ_i at frequency ν_r^i is much longer than $t^*(\nu_{\text{DM}}^0, \nu_r^i)$ at all frequencies ν_{DM}^0 for which F22 is a good approximation. Equation (F10) gives the SNR for a measurement at a single resonance frequency. As in the main text, the

¹⁴We have implicitly assumed here that the magnitude of the imaginary part of the input impedance is small enough that it acts to reduce or increase the input coil inductance. A small reduction is commonplace; it represents the screening of the input inductance by the input loop in a practical flux-to-voltage amplifier. One usually does not need to consider a situation where the imaginary part of the input impedance is larger than the input coil impedance in magnitude.

total SNR, integrated over the scan, is obtained from adding in quadrature the SNRs for each resonance frequency.

3. Quantum-Limited Flux-to-Voltage Amplifiers with Uncorrelated Imprecision and Backaction Noise

We assume that the noise impedance of the amplifier can be changed or tuned at each scan step, so that the noise spectral densities of the amplifier depend both on frequency and resonance frequency: $S_{VV}^{FV}(\nu) \rightarrow S_{VV}^{FV}(\nu, \nu_r^i)$ and similarly for the current noise. From equation (E12), for uncorrelated voltage and current noise, the noise impedance must be real. Furthermore,

$$\mathcal{S}_{VV}^{FV}(\nu, \nu_r^i) = h\nu Z_N(\nu, \nu_r^i), \quad (\text{F23})$$

and

$$\mathcal{S}_{II}^{FV}(\nu, \nu_r^i) = \frac{h\nu}{Z_N(\nu, \nu_r^i)}. \quad (\text{F24})$$

We define

$$\xi_{FV}^i \equiv \frac{Z_N(\nu = \nu_r^i, \nu_r^i)}{R(\nu_r^i)} \quad (\text{F25})$$

as the ratio of the on-resonance noise impedance to resonator resistance at frequency ν_r^i . For $\xi_{FV}^i < 1$, the total flux-to-voltage amplifier input loop current noise is dominated on-resonance by the imprecision noise, while for $\xi_{FV}^i > 1$, the total flux-to-voltage amplifier input current noise is dominated by the voltage back-action from input loop circulating currents. At $\xi_{FV}^i = 1$, the readout is noise-matched; the two noise sources contribute equally to the total flux-to-voltage amplifier noise. Equation (F25) is the analogue of equation (128).

Combining spectral densities (F23) and (F24) with equations (50), (51), (F2), (F8), (F10), (F22) yields the SNR for a single resonance frequency

$$\begin{aligned} SNR^{\text{opt}} \left[\nu_{\text{DM}}^0, g_{\text{DM}}, \frac{d\rho_{\text{DM}}}{d\nu}(\nu, \nu_{\text{DM}}^0), \nu_r^i, \xi_{FV}^i, \tau_i \right]^2 &= (4\pi Q^i)^2 \tau_i \\ &\times \int_{\nu_{\text{DM}}^0}^{\nu_{\text{DM}}^0 + \Delta\nu_{\text{DM}}^c} d\nu \left(\frac{\nu}{\nu_r^i} \frac{2L_{\text{PU}}}{L} \frac{g_{\text{DM}}^2 V_{\text{PU}}}{h} \frac{\frac{d\rho_{\text{DM}}}{d\nu}(\nu, \nu_{\text{DM}}^0)}{4\xi_{FV}^i n(\nu) + (1 + \xi_{FV}^i)^2 + 4(Q^i)^2 \left(\frac{\nu}{\nu_r^i} - 1 \right)^2} \frac{\xi_{FV}^i}{\xi_{FV}^i} \right)^2 \end{aligned} \quad (\text{F26})$$

and the SNR for the scan:

$$\begin{aligned}
SNR_{\text{tot}}^{\text{opt}} & \left[\nu_{\text{DM}}^0, g_{\text{DM}}, \frac{d\rho_{\text{DM}}}{d\nu}(\nu, \nu_{\text{DM}}^0), \{\nu_r^i\}, \{\xi_{FV}^i\}, \{\tau_i\} \right]^2 \\
& \equiv \sum_i SNR^{\text{opt}} \left[\nu_{\text{DM}}^0, g_{\text{DM}}, \frac{d\rho_{\text{DM}}}{d\nu}(\nu, \nu_{\text{DM}}^0), \nu_r^i, \xi_{FV}^i, \tau_i \right]^2. \tag{F27}
\end{aligned}$$

In equation (F26), we have assumed that the dark-matter frequency is sufficiently close to the resonance frequency and the noise impedance is sufficiently slowly varying, so that it may be taken as a constant over the integration range: $Z_N(\nu, \nu_r^i) \approx Z_N(\nu_r^i, \nu_r^i)$. In particular, we will require that this be a good approximation within a few sensitivity bandwidths of the resonance, as defined by the Q-factor (135). We restrict our attention to $Q_s(\nu_r^i, n(\nu_r^i), Q^i, \xi_{FV}^i) \gg 1$.

Our optimization procedure consists of two parts:

1. For each scan frequency ν_r^i , we maximize the expectation value of the square of the SNR with respect to ξ_{FV}^i . In performing this optimization, we hold the internal resistance fixed, so we are effectively optimizing with respect to noise impedance. The value function for this optimization is $F[\nu_r^i, \xi_{FV}^i]$, as defined in (105); we have replaced the scattering transmission $S_{21}^{(1)}(\nu)$ with the resonator matching parameters ν_r^i, ξ_{FV}^i of the flux-to-voltage detection circuit. This function measures the resonator sensitivity to dark matter, integrated over a wide search range, and weighted by probability densities associated with dark-matter properties. In this step of the optimization, we ask, for a particular resonator design, with a particular quality factor (i.e. resistance), what is the optimal noise impedance for the amplifier. Is it optimal to be noise-matched?
2. Assume that the total experiment time is fixed, i.e. $\sum_i \tau_i = T_{\text{tot}}$. We find the distribution of time over scan steps that maximizes the area of the exclusion region in a log-log plot of mass ν_{DM}^0 vs coupling g_{DM} . The value function for this optimization is the integral $A[\{\nu_r^i\}, \{\tau_i\}]$ of (168). We make the same assumptions as those given in Section V B.

In a typical experiment, we match the pickup and input inductances to maximize flux transfer. Then, comparing equation (F26) with equation (165), we note that the two are identical if we replace Q^i with Q_{int}^i and ξ^i with ξ_{FV}^i . The first identification is simply a reflection of our treatment of the flux-to-voltage amplifier. In the scattering mode picture,

the input impedance of the amplifier strongly damps the resonator, so that the internal Q and the overall Q are not the same. In fact, when the thermal occupation number of the resonator is much greater than unity, the optimum value of ξ^i is such that overall Q is much less than the internal Q . In contrast, our treatment of the quantum-limited flux-to-voltage amplifier has shown that the damping from the amplifier is much less than the intrinsic damping of the resonator; the internal Q and overall Q are approximately the same in this case. The second identification reflects that both parameters are the ratio of noise impedance to internal resonator resistance. The similarity in the SNR expressions should not be surprising. In both cases, a resonant circuit is being read out by a quantum-limited amplifier, which means that the minimum noise added by the amplifier is equivalent to the zero-point noise in the system. (See equation (97).) Note that the sensitivity limits from the flux-to-voltage amplifier will be identical to those shown in equations (186) and (187).

Recognizing the similarity in SNR expressions, we may make the following statements about an optimized search with a flux-to-voltage amplifier, which are identical to their scattering mode counterparts:

1. The optimum value of ξ_{FV}^i in the log-uniform search is

$$\xi^{\text{opt}}(\nu_r^i, n(\nu_r^i)) = \frac{1}{2} \left(2n(\nu_r^i) + 1 + \sqrt{(2n(\nu_r^i) + 1)^2 + 8} \right). \quad (\text{F28})$$

2. The optimum scan strategy is described by the density function

$$\tau_{\text{opt}}(\nu) = \frac{T_{\text{tot}}}{\ln(\nu_h/\nu_l)}. \quad (\text{F29})$$

The particular placement of resonant frequencies is not consequential, for the scan is sufficiently dense.

The second of these observations follows the same reasoning as the scattering case. The first implies that, in a resonant scan across a large frequency regime, it is optimal not to be noise-matched, but rather, dominated by back-action! We explore this further, focusing on the thermal limit $n(\nu) \gg 1$.

For a circuit with resonance frequency ν_r^i and quality factor Q^i , the total current noise from the resistor and the quantum-limited flux-to-voltage amplifier is described by the spectral density

$$\mathcal{S}_{II}^{\text{tot}}(\nu, \nu_r^i, \xi_{FV}^i) \approx \frac{h\nu_r^i}{R(\nu_r^i)} \left(\frac{1}{\xi_{FV}^i} + \frac{\xi_{FV}^i + 2(2n(\nu_r^i) + 1)}{1 + 4(Q^i)^2 ((\nu - \nu_r^i)/\nu_r^i)^2} \right) \quad (\text{F30})$$

for frequencies sufficiently close to resonance, $|\nu - \nu_r^i| \ll \nu_r^i$. Here, we have used equations (F8), (F2), (F23),(F24), along with the approximation $R(\nu) \approx R(\nu_r^i)$. The first term represents the current imprecision noise, the second represents the voltage backaction, and the third represents the noise from the resistor. If the second and third terms dominate the first, the SNR is independent of the detuning from resonance. This gives rise to significant sensitivity outside of the resonator bandwidth, as we observed in the main text. Indeed, the resonator will provide maximal sensitivity, without degradation from the imprecision noise, for detunings satisfying

$$\frac{\xi_{FV}^i + 2(2n(\nu_r^i) + 1)}{1 + 4(Q^i)^2 ((\nu - \nu_r^i)/\nu_r^i)^2} \gtrsim \frac{1}{\xi_{FV}^i} \implies |\nu - \nu_r^i| \lesssim \frac{\nu_r^i}{2Q_s(\nu_r^i, n(\nu_r^i), Q^i, \xi_{FV}^i)}, \quad (\text{F31})$$

where $Q_s(\nu_r^i, n(\nu_r^i), Q^i, \xi_{FV}^i)$ is defined in (135). By assumption, $Q_s(\nu_r^i, n(\nu_r^i), Q^i, \xi_{FV}^i) \gg 1$. The assumption was validated in Section V A 3.

Suppose the readout is noise-matched to the input circuit on resonance. The on-resonance current noise power spectral density is

$$\mathcal{S}_{II}^{\text{tot}}(\nu = \nu_r^i, \nu_r^i, \xi_{FV}^i = 1) \approx \frac{4h\nu_r^i}{R} n(\nu_r^i). \quad (\text{F32})$$

$Q_s(\nu_r^i, n(\nu_r^i), Q^i, \xi_{FV}^i = 1) \approx Q^i/(2\sqrt{n(\nu_r^i)})$, so the sensitivity of the resonator to dark matter is degraded by a factor of 2 for all frequencies

$$|\nu - \nu_r^i| \lesssim \frac{\nu_r^i}{Q^i} \sqrt{n(\nu_r^i)}. \quad (\text{F33})$$

Now suppose the readout is noise-mismatched so that $\xi_V^i = \xi^{\text{opt}}(\nu_r^i, n(\nu_r^i))$ and the voltage noise backaction dominates. $\xi_{FV}^i \approx 2n(\nu_r^i) \gg 1$, so the current noise power spectral density on resonance is

$$\mathcal{S}_{II}^{\text{tot}}(\nu = \nu_r^i, \nu_r^i, \xi_{FV}^i = \xi^{\text{opt}}(\nu_r^i, n(\nu_r^i))) \approx \frac{6h\nu_r^i}{R} n(\nu_r^i). \quad (\text{F34})$$

From $Q_s(\nu_r^i, n(\nu_r^i), Q^i, \xi_{FV}^i = 1) \approx Q^i/(2\sqrt{3}n(\nu_r^i))$, so the resonance has maximal sensitivity to all detunings

$$|\nu - \nu_r^i| \lesssim \frac{\nu_r^i}{Q^i} n(\nu_r^i) \sqrt{3}. \quad (\text{F35})$$

In return for a modest penalty in on-resonance SNR, the optimal coupling to the amplifier achieves a parametrically larger frequency range over which the resonator has near-maximal sensitivity to dark matter. The bandwidth is $\sim \sqrt{n(\nu_r^i)}$ larger in the optimal, noise-mismatched case than the noise-matched case. Thus, the sensitivity integrated over the search band, as represented by the log-uniform search value function, is $\sim \sqrt{n(\nu_r^i)}$ larger.

A pictorial representation of this result, displaying the relative contributions of current imprecision noise, voltage backaction noise, and thermal/zero-point noise of the resonator, is shown in Fig. 12. We plot each noise term on the right-hand side of equation (F30), normalized to the current noise spectral density scale $h\nu_r^i/R(\nu_r^i)$, as a function of detuning $x = 2Q^i \frac{\nu - \nu_r^i}{\nu_r^i}$, assuming a thermal occupation number of $n(\nu_r^i) = 50$. We consider both the noise-matched and optimally-matched scenarios.

In the noise-matched case (top panel of Fig. 12), the imprecision noise and backaction noise are sub-dominant to the thermal noise on resonance by a factor of $\sim 1/4n(\nu_r^i)$. In the optimally noise-mismatched case (bottom panel of Fig. 12), we have a larger $\sim 2n(\nu_r^i)$ voltage back-action contribution relative to the noise-matched amplifier. The backaction noise on resonance is $\sim 1/2$ of the thermal noise, resulting in a 50% SNR penalty. However, for the quantum-limited flux-to-voltage amplifier with no current-voltage correlations, the current-noise and voltage-noise back-action are inversely proportional, as per equation (E32). This means the intrinsic current noise is reduced by a factor of $\sim 1/2n(\nu_r^i)$ compared to the noise-matched case, resulting in sensitivity further away from the resonance frequency. In the case shown in the figure, the imprecision noise accounts for less than one-half of the total noise at detunings $|x| < 14$ when the readout is noise-matched. This corresponds to the bandwidth in which the SNR is not degraded by the imprecision noise and represents the “useful” bandwidth of the resonator. When the readout is optimally mismatched, the imprecision noise is less than one-half of the total at detunings $|x| < 173$. The penalty in on-resonance SNR is order unity, while the number of bandwidths at which we have “useful” sensitivity is parametrically $\sim \sqrt{n(\nu_r^i)}$ much larger. In the thermal limit, the second effect is much larger, so it is beneficial to be noise-mismatched, with noise impedance a factor of $\sim 2n(\nu_r^i)$ larger than the on-resonance resistance. This is analogous to the scattering mode picture in the main text, where the backaction is increased to an order-unity fraction of the thermal noise in order to provide sensitivity over a larger frequency range. See Fig. 9.

We may compare the single-pole resonator with optimized noise impedance to the Bode-Fano limit of eq. (F20). Evaluating the log-uniform search value functional (F17) for a resonator at frequency ν_r with amplifier coupling $\xi^{\text{opt}}(\nu_r, n(\nu_r))$ (i.e. with frequency-independent, real-valued noise impedance given by the value of $R\xi^{\text{opt}}(\nu_r, n(\nu_r))$) yields

$$\bar{F}[\nu_r, \xi^{\text{opt}}(\nu_r, n(\nu_r))] \approx \frac{2(\xi^{\text{opt}}(\nu_r, n(\nu_r)))^2}{(4\xi^{\text{opt}}(\nu_r, n(\nu_r))n(\nu_r) + (1 + \xi^{\text{opt}}(\nu_r, n(\nu_r)))^2)^{3/2}} \frac{R}{L_{\text{PU}} + L_{\text{IN}}} \quad (\text{F36})$$

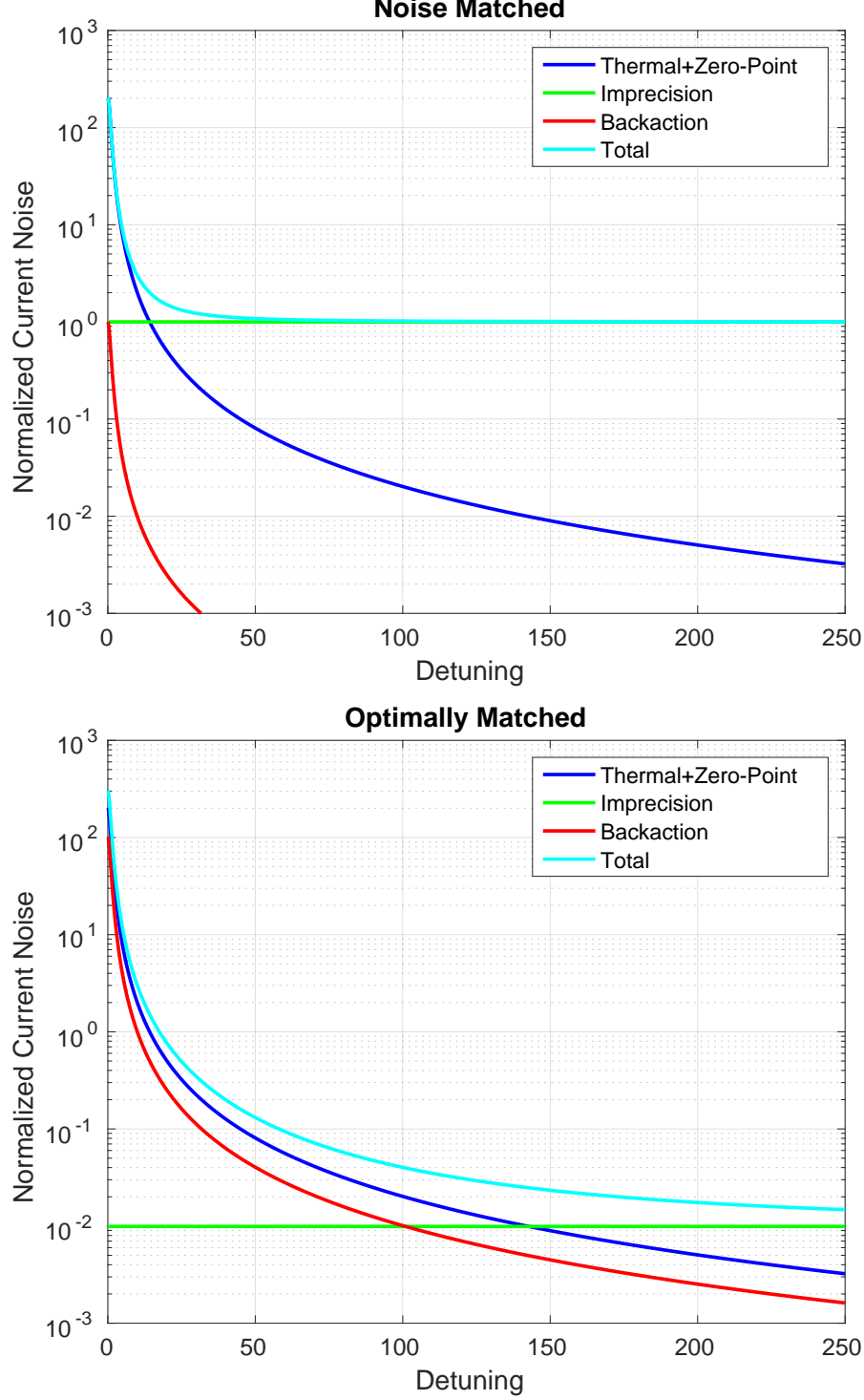


FIG. 12. The noise terms of equation (F30) plotted for the noise matched (top) and optimally matched (bottom) networks. The x-axis is the detuning from resonance $x = 2Q^i \frac{\nu - \nu_r^i}{\nu_r^i}$, while the y-axis is a normalized noise spectral density $S_{II}/(h\nu_r^i/R(\nu_r^i))$. The y-axis has been plotted on a logarithmic scale. We restrict to positive detunings as the spectrum is symmetric about $x = 0$. Thermal and zero-point noise are lumped together in blue, imprecision noise is in green, and backaction noise is in red. The total noise is in cyan.

The first fraction is an increasing function of ν , so the value functional is optimized by taking $\nu_r = \nu_h$. The resonant circuit that best approaches the Bode-Fano bound in (F20) is one at the top of the search range, for which the value of the optimization function is

$$\begin{aligned} \bar{F}_{\text{neu}}[\nu_h, \xi^{\text{opt}}(\nu_h, n(\nu_h))] &= \frac{2(\xi^{\text{opt}}(\nu_h, n(\nu_h)))^2}{(4\xi^{\text{opt}}(\nu_h, n(\nu_h))n(\nu_h) + (1 + \xi^{\text{opt}}(\nu_h, n(\nu_h)))^2)^{3/2}} \frac{R}{L_{\text{PU}} + L_{\text{IN}}} \\ &\approx \begin{cases} \frac{8}{27} \frac{R}{L_{\text{PU}} + L_{\text{IN}}} & \text{if } n(\nu_h) \ll 1 \\ \frac{1}{3\sqrt{3}} \frac{1}{n(\nu_h)} \frac{R}{L_{\text{PU}} + L_{\text{IN}}} & \text{if } n(\nu_h) \gg 1 \end{cases} \end{aligned} \quad (\text{F37})$$

If input and pickup inductances are matched, comparison of eqs. (F20) and (F37) demonstrates that the optimized single-pole resonator is approximately $\sim 37.5\%$ of the Bode-Fano limit. However, fundamentally, we may take the input inductance to be much smaller than the pickup inductance (although not be equal to zero, so that we may still feed flux into the amplifier). Then, the optimized single-pole resonator is approximately $\sim 75\%$ of the Bode-Fano limit; the result is identical to the scattering-mode analysis of the main text. *We find that in a log-uniform search with quantum-limited flux-to-voltage amplification, the single-pole resonator is a near-ideal single-moded dark matter detector.*

As a final remark, we ask: What if we decide to sit at a single resonance frequency, rather than scanning? This is what one would do if a signal was found, and a longer integration was needed to validate the signal. In that case, the resonator would sit at the frequency of the candidate signal and the value function reduces to the analog of (164), proportional to

$$\frac{\xi_{FV}^i}{4\xi_{FV}^i n(\nu_r^i) + (1 + \xi_{FV}^i)^2}, \quad (\text{F38})$$

which is maximized when noise-matched $\xi_{FV}^i = 1$. Therefore, the optimal noise impedance differs between a resonant scan and an integration at a single frequency. The fundamental difference lies in the fact that, in the former, one is concerned about sensitivity integrated over a wide bandwidth, whereas in the latter, one is concerned about obtaining the largest possible sensitivity at a single frequency.

4. Optimization for Imperfect Flux-to-Voltage Amplifiers

Here, we relax two of the assumptions made in appendix F 3. We permit the amplifier to possess a minimum noise temperature greater than the quantum limit of equation (E31). We also permit correlations between the current noise and voltage noise, $\mathcal{S}_{IV}^{FV}(\nu, \nu_r) \neq 0$.

However, to compare our results with the previous section, we will later set the real part of the correlation to zero. We will also assume, in keeping with appendices E 2 and F 3, that we may ignore the damping from the input impedance of the amplifier and that the damping is dominated by intrinsic sources.

The SNR for a dark-matter signal at frequency ν_{DM}^0 from a resonance at ν_r^i (i fixed) is, for $|\nu_{\text{DM}}^0 - \nu_r^i| \ll \nu_r^i$,

$$\begin{aligned} \text{SNR} & \left[\nu_{\text{DM}}^0, g_{\text{DM}}, \frac{d\rho_{\text{DM}}}{d\nu}(\nu, \nu_{\text{DM}}^0), \nu_r^i, \mathcal{S}_{VV}^{FV}(\nu, \nu_r^i), \mathcal{S}_{II}^{FV}(\nu, \nu_r^i), \mathcal{S}_{IV}^{FV}(\nu, \nu_r^i) \right]^2 \\ & = (4\pi Q^i)^2 \left(\frac{2L_{\text{PU}}}{L} \right)^2 \tau_i \int_{\nu_{\text{DM}}^0}^{\nu_{\text{DM}}^0 + \Delta\nu_{\text{DM}}} d\nu \left(\frac{\nu}{\nu_r^i} \frac{g_{\text{DM}}^2 V_{\text{PU}} \frac{d\rho_{\text{DM}}(\nu, \nu_{\text{DM}}^0)}{d\nu}}{h} \right)^2 \times \\ & \left(\frac{h\nu}{4h\nu(n(\nu) + 1/2) + \frac{\mathcal{S}_{VV}^{FV}(\nu, \nu_r^i)}{R(\nu)} + \mathcal{S}_{II}^{FV}(\nu, \nu_r^i)R(\nu) \left(1 + 4(Q^i)^2 \left(\frac{\nu - \nu_r^i}{\nu_r^i} \right)^2 \right) + 2\text{Re}(\mathcal{S}_{IV}^{FV}(\nu, \nu_r^i)(1 + 2iQ^i \frac{\nu - \nu_r^i}{\nu_r^i}))} \right)^2 \end{aligned} \quad (\text{F39})$$

We will assume matched pickup and input inductances. The SNR of a search, consisting of scan frequencies $\{\nu_r^i\}$, is given by adding the single-resonance-frequency SNRs in quadrature:

$$\begin{aligned} \text{SNR}_{\text{tot}} & \left[\nu_{\text{DM}}^0, g_{\text{DM}}, \frac{d\rho_{\text{DM}}}{d\nu}(\nu, \nu_{\text{DM}}^0), \{\nu_r^i\}, \{\mathcal{S}_{VV}^{FV}(\nu, \nu_r^i)\}, \{\mathcal{S}_{II}^{FV}(\nu, \nu_r^i)\}, \{\mathcal{S}_{IV}^{FV}(\nu, \nu_r^i)\} \right]^2 \\ & = \sum_i \text{SNR} \left[\nu_{\text{DM}}^0, g_{\text{DM}}, \frac{d\rho_{\text{DM}}}{d\nu}(\nu, \nu_{\text{DM}}^0), \nu_r^i, \mathcal{S}_{VV}^{FV}(\nu, \nu_r^i), \mathcal{S}_{II}^{FV}(\nu, \nu_r^i), \mathcal{S}_{IV}^{FV}(\nu, \nu_r^i) \right]^2. \end{aligned} \quad (\text{F40})$$

The four terms in the denominator of (F39) represent the various noise sources in the system. The first term is the thermal and zero-point noise of the resonator. The second and third terms are the backaction and imprecision noise of the amplifier, respectively. The last term is the noise due to correlations between the backaction and imprecision noise. The amplifier noise spectral densities are functions both of the frequency and of the resonance frequency, as we assume that the amplifier can be re-optimized at each scan frequency. If detuning-dependent (i.e. dependent on $\nu - \nu_r^i$) terms are smaller than the other terms in the denominator, then the SNR is not degraded by the resonator rolloff. At these detunings, the signal rolls off, but the noise does as well, keeping the SNR the same. Similar to the treatment in the main text and the previous section, the frequencies over which this occurs are the frequencies over which the resonator is maximally sensitive. An optimization entails maximizing this range of search frequencies without significantly degrading the SNR.

Assume that at each resonance frequency, all noise spectral densities can be taken to be

constants over frequencies $|\nu - \nu_r^i| \ll \nu_r^i$, e.g.

$$\mathcal{S}_{VV}^{FV}(\nu, \nu_r^i) \approx \mathcal{S}_{VV}^{FV}(\nu_r^i, \nu_r^i) \quad (\text{F41})$$

$$\mathcal{S}_{VV}^{FV}(\nu_r^i, \nu) \approx \mathcal{S}_{VV}^{FV}(\nu_r^i, \nu_r^i) \quad (\text{F42})$$

and similarly for \mathcal{S}_{II}^{FV} and \mathcal{S}_{IV}^{FV} . The precise range over which we need this approximation to hold for self-consistency will be discussed below. Let

$$\alpha_1(\nu_r) = \frac{\mathcal{S}_{II}^{FV}(\nu_r, \nu_r) R(\nu_r)}{h\nu_r} \quad (\text{F43})$$

$$\alpha_2(\nu_r) = \frac{\text{Im } \mathcal{S}_{IV}^{FV}(\nu_r, \nu_r)}{h\nu_r} \quad (\text{F44})$$

$$\alpha_3(\nu_r) = 4(n(\nu_r) + 1/2) + \frac{\mathcal{S}_{VV}^{FV}(\nu_r, \nu_r)}{h\nu_r R(\nu_r)} + \frac{\mathcal{S}_{II}^{FV}(\nu_r, \nu_r) R(\nu_r)}{h\nu_r} + 2 \frac{\text{Re } \mathcal{S}_{IV}^{FV}(\nu_r, \nu_r)}{h\nu_r} \quad (\text{F45})$$

As in previous appendices, define $x = 2Q \frac{\nu - \nu_r^i}{\nu_r^i}$, as the detuning from the resonance frequency as a fraction of the resonator bandwidth. The fraction in the last line of equation (F39), which represents the SNR as a function of detuning, then reads

$$\begin{aligned} \bar{\mathcal{F}}(x, \alpha_1(\nu_r^i), \alpha_2(\nu_r^i), \alpha_3(\nu_r^i)) &\approx \frac{1}{\alpha_1(\nu_r^i)x^2 - 2\alpha_2(\nu_r^i)x + \alpha_3(\nu_r^i)} \\ &= \alpha_1(\nu_r^i)^{-1} \left(\left(x - \frac{\alpha_2(\nu_r^i)}{\alpha_1(\nu_r^i)} \right)^2 + \frac{\alpha_1(\nu_r^i)\alpha_3(\nu_r^i) - \alpha_2(\nu_r^i)^2}{\alpha_1(\nu_r^i)^2} \right)^{-1}. \end{aligned} \quad (\text{F46})$$

The SNR is not degraded by the resonator rolloff, and the resonator is maximally sensitive to the dark-matter signal at detuning x , as long as

$$\left| x - \frac{\alpha_2(\nu_r^i)}{\alpha_1(\nu_r^i)} \right| \lesssim \sqrt{\frac{\alpha_1(\nu_r^i)\alpha_3(\nu_r^i) - \alpha_2(\nu_r^i)^2}{\alpha_1(\nu_r^i)^2}}. \quad (\text{F47})$$

Equation (F47) gives the number of bandwidths over which the resonator is maximally sensitive to the dark-matter signal. In the language of the main text, the sensitivity Q , describing the bandwidth of maximal sensitivity is,

$$Q_s(\nu_r^i, Q^i, \alpha_1(\nu_r^i), \alpha_2(\nu_r^i), \alpha_3(\nu_r^i)) = Q^i \left(\frac{\alpha_1(\nu_r^i)\alpha_3(\nu_r^i) - \alpha_2(\nu_r^i)^2}{\alpha_1(\nu_r^i)^2} \right)^{-1/2}. \quad (\text{F48})$$

We require that the dark-matter frequencies that lie within a few sensitivity bandwidths of the resonance satisfy the approximation of a constant noise spectral density in (F41)-(F42).

We will assume, as we did in the main text, that

$$Q_s(\nu_r^i, Q^i, \alpha_1(\nu_r^i), \alpha_2(\nu_r^i), \alpha_3(\nu_r^i)) \gg 1, \quad (\text{F49})$$

and that the frequency range of equation (F47) is not comparable in scale to the resonance frequency itself. Implicit in this calculation is the assumption that $\alpha_1(\nu_r^i)\alpha_3(\nu_r^i) - \alpha_2(\nu_r^i)^2 > 0$. If $\text{Re } \mathcal{S}_{IV}^{FV}(\nu_r^i, \nu_r^i) \geq 0$, this is readily satisfied because $\mathcal{S}_{VV}(\nu_r^i, \nu_r^i)\mathcal{S}_{II}(\nu_r^i, \nu_r^i) - |\mathcal{S}_{IV}(\nu_r^i, \nu_r^i)|^2 > 0$ (see eq. (E31)).

We see from equation (F46) that the presence of out-of-phase current-voltage correlations, represented by $\text{Im } S_{IV}$, has introduced an asymmetry in the resonator sensitivity to dark matter. If $\text{Im } S_{IV}^{FV}(\nu_r^i, \nu_r^i) > 0$, then for detunings $x > 0$, the correlation reduces the noise, relative to the detuning $-x$, and results in a larger range of positive detunings where the SNR is not degraded, relative to the range of negative detunings. If $\text{Im } S_{IV}^{FV}(\nu_r^i, \nu_r^i) < 0$, the opposite happens, and there is a larger range of negative detunings at which the SNR is not degraded.

We optimize the resonator readout and noise matching at each resonance frequency for a log-uniform search. We maximize the expectation value of the square of the SNR. The value function evaluates to, in analogy with equation (139),

$$F(\alpha_{1,2,3}(\nu_r^i)) \approx \gamma_0^{FV} \int_0^\beta du \left(\frac{\sqrt{1+u}}{h} \frac{d\rho_{\text{DM}}(u)}{du} \right)^2 \quad (\text{F50})$$

$$\times \int_{\nu_l(1+u)}^{\nu_h(1+u)} d\bar{\nu} \left(\frac{1}{4(Q^i)^2 \alpha_1(\nu_r^i) \left(\frac{\bar{\nu}}{\nu_r^i} - 1 \right)^2 - 4Q^i \alpha_2(\nu_r^i) \left(\frac{\bar{\nu}}{\nu_r^i} - 1 \right) + \alpha_3(\nu_r^i)} \right)^2,$$

where γ_0^{FV} is a constant. Note that, instead of optimizing with respect to a single noise matching parameter ξ_{FV}^i , we are optimizing with respect to three parameters, $\alpha_{1,2,3}(\nu_r^i)$, owing to the two additional degrees of freedom—noise temperature and correlations. The value function will need to be optimized with respect to all noise matching parameters. Far away from resonance, the approximation (F22) breaks down; strictly speaking, the integrand of the $\bar{\nu}$ is then not an appropriate representation for the SNR. However, at these frequencies far detuned from resonance, there is negligible sensitivity, and the contribution to the integral is nearly zero. As such, it is an appropriate approximation, for the purpose of evaluating the integral, to use this integrand expression at all frequencies. The integrand is sharply peaked near $\bar{\nu} \approx \nu_r^i$, so using the change of variables $x = 2Q^i(\bar{\nu} - \nu_r^i)/\nu_r^i$ and extending the limits of integration to $\pm\infty$ (similar to (140)), we find

$$F(\alpha_{1,2,3}(\nu_r^i)) \approx \gamma_1^{FV} \frac{\alpha_1(\nu_r^i)}{(\alpha_1(\nu_r^i)\alpha_3(\nu_r^i) - \alpha_2(\nu_r^i)^2)^{3/2}}, \quad (\text{F51})$$

where γ_1^{FV} is a constant, containing the integral over u . The expression

$$\bar{\mathcal{G}}(\alpha_{1,2,3}(\nu_r^i)) = \frac{\alpha_1(\nu_r^i)}{(\alpha_1(\nu_r^i)\alpha_3(\nu_r^i) - \alpha_2(\nu_r^i)^2)^{3/2}} \quad (\text{F52})$$

represents the effect of thermal, zero-point, and amplifier noise integrated over the search band. In analogy with the optimization over ξ performed for resonator readout with quantum-limited scattering-mode and flux-to-voltage amplifiers (see Section V A 3 and Appendix F 3), it is critical to maximize the value of this quantity. We optimize $\bar{\mathcal{G}}$ with respect to the three noise matching parameters $\alpha_{1,2,3}(\nu_r^i)$, assuming fixed temperature and fixed minimum noise temperature.

Assume that $\text{Re } S_{IV} = 0$, so that we may compare our results to the previous section and utilize the quantum limits derived in Appendix E 2. This assumption is also in keeping with SQUID models, such as that in [60]. Let $kT_N^{\min}(\nu_r^i)$ be the minimum noise temperature for the amplifier corresponding to resonance frequency ν_r^i

$$kT_N^{\min}(\nu_r^i) = \frac{1}{2} \sqrt{\mathcal{S}_{VV}^{FV}(\nu_r^i, \nu_r^i) \mathcal{S}_{II}^{FV}(\nu_r^i, \nu_r^i) - (\text{Im } \mathcal{S}_{IV}^{FV}(\nu_r^i, \nu_r^i))^2}. \quad (\text{F53})$$

Let

$$\eta(\nu_r^i) = \frac{2kT_N^{\min}(\nu_r^i)}{h\nu_r^i} \geq 1. \quad (\text{F54})$$

Then, (F52) can be rewritten as

$$\bar{\mathcal{G}}(\alpha_1(\nu_r^i), \eta(\nu_r^i)) = \frac{\alpha_1(\nu_r^i)}{(\alpha_1(\nu_r^i)^2 + 2(2n(\nu_r^i) + 1)\alpha_1(\nu_r^i) + \eta(\nu_r^i)^2)^{3/2}}. \quad (\text{F55})$$

With noise temperature fixed, the maximum of \mathcal{G} over $\alpha_1(\nu_r^i)$ occurs at

$$\alpha_1^{\text{opt}}(\nu_r^i) = \frac{2\eta(\nu_r^i)^2}{2n(\nu_r^i) + 1 + \sqrt{(2n(\nu_r^i) + 1)^2 + 8\eta(\nu_r^i)^2}}, \quad (\text{F56})$$

which corresponds to an current noise spectral density of

$$\mathcal{S}_{II}(\nu_r^i, \nu_r^i) = \frac{h\nu_r^i \alpha_1^{\text{opt}}(\nu_r^i)}{R(\nu_r^i)}. \quad (\text{F57})$$

Note that at $\eta = 1$, corresponding to a quantum-limited readout, $\alpha_1^{\text{opt}}(\nu_r^i) = \xi^{\text{opt}}(\nu_r^i, n(\nu_r^i))^{-1}$, and we recover the results of the previous section. We find that the optimal amplifier, given fixed noise temperature, is not unique. There are infinitely many solutions for amplifier noise spectral densities $\mathcal{S}_{VV}^{FV}, \mathcal{S}_{IV}^{FV}$ that satisfy equation (F53), given the constraint (F57) on \mathcal{S}_{II}^{FV} . The conditions for the optimum only precisely constrain the current noise. In particular,

for fixed noise temperature (e.g. quantum-limited noise temperature), a readout with out-of-phase correlations between current imprecision noise and voltage backaction noise can perform (in terms of maximizing the value function $F(\alpha_{1,2,3}(\nu_r^i))$) as well as a readout with uncorrelated noise sources. This is of practical importance because these noise sources are often the result of the same physical fluctuations (e.g. Johnson noise from resistive shunts in a dc SQUID) and therefore, are usually correlated.

We may have guessed that correlations do not prevent us from obtaining the optimum from analysis of equation (F46). This equation, indicative of the SNR as a function of frequency detuning from resonance, may be rewritten in terms of the noise temperature parameter $\eta(\nu_r^i)$,

$$\bar{\mathcal{F}}(x, \alpha_1(\nu_r^i), \alpha_2(\nu_r^i), \eta(\nu_r^i)) = \alpha_1(\nu_r^i)^{-1} \left(\left(x - \frac{\alpha_2(\nu_r^i)}{\alpha_1(\nu_r^i)} \right)^2 + \frac{\alpha_1(\nu_r^i)^2 + 2(2n(\nu_r^i) + 1)\alpha_1(\nu_r^i) + \eta(\nu_r^i)^2}{\alpha_1(\nu_r^i)^2} \right)^{-1}. \quad (\text{F58})$$

The second fraction in the outer parentheses represents the number of bandwidths over which the resonator has maximal sensitivity to dark matter; it is the value of Q_s/Q^i . This term depends only on the value of α_1 and η . The maximum value of $\bar{\mathcal{F}}$ with respect to detuning, which is a metric of the maximum sensitivity of the resonator, also depends only α_1 . As our value function $F(\alpha_{1,2,3}(\nu_r^i))$ is roughly proportional to the maximum of $\bar{\mathcal{F}}^2$ multiplied by the frequency range of maximum sensitivity, it follows that our value function, and the value of $\bar{\mathcal{G}}$ only depends on these parameters. This is precisely what we see in (F55). The only relevant effect of correlations between imprecision and backaction noise is to shift the frequency at which $\bar{\mathcal{F}}$ is maximized, i.e. introduce an asymmetry in resonator sensitivity at positive and negative detunings.

One may also understand this result by looking at the total noise spectral density referred to a voltage excitation in the resonator:

$$\frac{\mathcal{S}_{VV}^{\text{ref,tot}}(x, \nu_r^i)}{h\nu_r^i R(\nu_r^i)} \approx 4(n(\nu_r^i) + 1/2) + \frac{\alpha_2(\nu_r^i)^2 + \eta(\nu_r^i)^2}{\alpha_1(\nu_r^i)} - 2x\alpha_2(\nu_r^i) + \alpha_1(\nu_r^i)(1 + x^2). \quad (\text{F59})$$

The first term represents the thermal/zero-point noise from the resonator, the second term represents the voltage-backaction-noise spectral density of the amplifier, the third term represents the correlation between voltage-noise backaction and current imprecision noise, and fourth term represents the current-imprecision-noise spectral density of the amplifier.

We plot each of these terms for $\eta(\nu_r^i) = 10$, $n(\nu_r^i) = 100$, $\alpha_1(\nu_r^i) = \alpha_1^{\text{opt}}(\nu_r^i)$, as specified

by equation (F56), for three different values of $\alpha_2(\nu_r^i)$, $\alpha_2(\nu_r^i) = -20, 0, +20$. See Figs. 13 and 14. Even though the backaction and correlated-noise terms have different values for the three situations, the minimum level of $S_{VV}^{\text{ref,tot}}(x, \nu_r^i)$ is the same ($\approx 604 h \nu_r^i R(\nu_r^i)$). The number of bandwidths over which the total noise is less than a factor of 2 above its minimum is indicated by points below the dashed horizontal line in Fig. 13. This represents the number of bandwidths of maximal sensitivity and is the same for each of the three cases (≈ 70 bandwidths). Indeed, Fig. 14 shows that the total noise curves are simply translations of one another, as dictated by the sign and magnitude of the correlated noise.

The signal-to-noise of the scan at a single dark-matter frequency of interest can be evaluated by approximating a continuum of resonator frequencies and using the scan density function (183) found in the main text, $t_{\text{opt}}(\nu_r) = \frac{T_{\text{tot}}}{\ln(\nu_h/\nu_l)}$. Assuming fixed Q across resonant frequencies and matched pickup and input inductances, we find, using methods similar to those already presented and the optimum readout defined by equations (F53)-(F56),

$$SNR^2(\nu_{\text{DM}}^0) \approx 4\pi^3 Q \frac{T_{\text{tot}}}{\ln(\nu_h/\nu_l)} \bar{\mathcal{G}}(\nu_{\text{DM}}^0, \alpha_1^{\text{opt}}(\nu_{\text{DM}}^0), \eta(\nu_{\text{DM}}^0)) \int_{\nu_{\text{DM}}^0}^{\nu_{\text{DM}}^0 + \Delta\nu_{\text{DM}}^c} d\nu \left(\frac{g_{\text{DM}}^2 V_{\text{PU}} \frac{d\rho_{\text{DM}}(\nu, \nu_{\text{DM}}^0)}{d\nu}}{h} \right)^2 \quad (\text{F60})$$

From this equation, sensitivity limits on g_{DM} and therefore, sensitivity limits on ε and $g_{a\gamma\gamma}$ may be readily obtained.

Appendix G: Comparison of Resonant and Broadband Searches with Flux-to-Voltage Amplifiers

A broadband, non-resonant search using flux-to-voltage amplifiers has been proposed as an alternative to a tunable resonant search. In [22], the sensitivity of a broadband search is compared to a tunable resonant search, with the conclusion that the broadband search is more sensitive at frequencies below 100 kHz. In this appendix, we develop an apples-to-apples comparison between broadband and resonant searches in our generalized optimization framework, and show that, in contrast to the conclusion in [22], a tunable resonant search has better integrated scan sensitivity at any frequency where an electromagnetic resonator can be practically constructed ($\gtrsim 100$ Hz).

We first discuss amplifier noise and noise impedance in a broadband search. We then lay out assumptions for carrying out an apples-to-apples comparison of an optimized single-pole

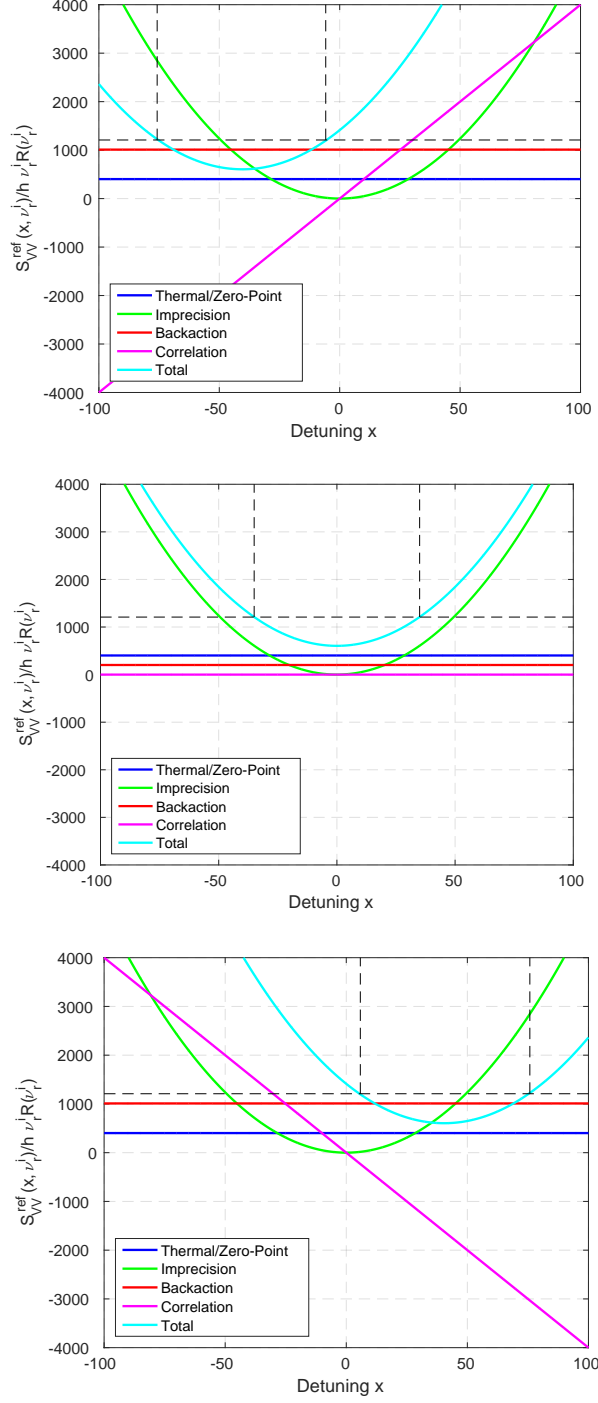


FIG. 13. The various contributions to the noise, referred to an excitation voltage in the input circuit, as a function of detuning $x = 2Q^i \frac{\nu - \nu_r^i}{\nu_r^i}$ from resonance frequency. $\eta(\nu_r^i) = 10$, $n(\nu_r^i) = 100$, $\alpha_1(\nu_r^i) = \alpha_1^{\text{opt}}(\nu_r^i)$. The top, middle, and bottom figures all represent different values of $\alpha_2(\nu_r^i)$: $\alpha_2(\nu_r^i) = -20, 0, +20$, respectively. The region of the total noise curve below the horizontal dashed line represents the detunings at which the noise is less than a factor of 2 from its minimum value. This region sets the bandwidth of maximal sensitivity (set by Q_{eff}).

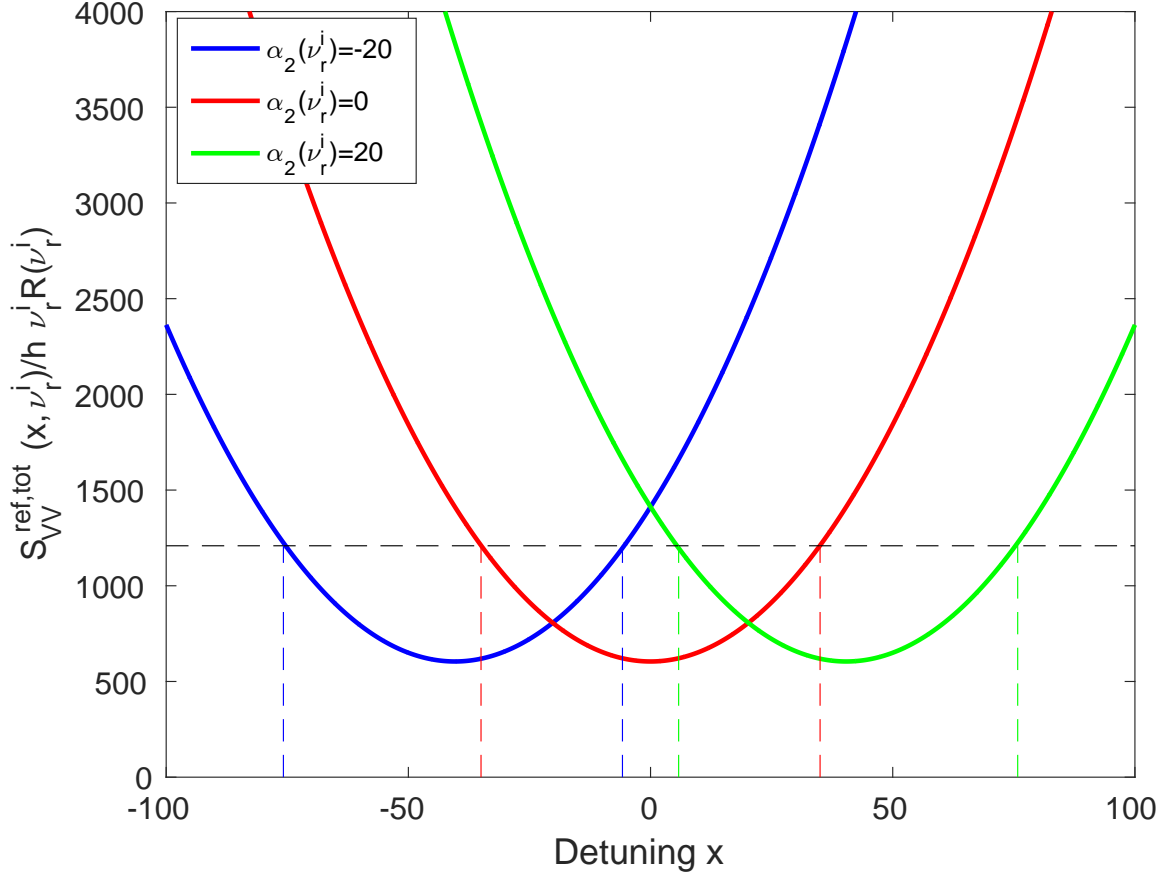


FIG. 14. Total noise of equation (F59) as a function of resonator detuning for $\alpha_2(\nu_r^i) = -20, 0, +20$. The region of the total noise curve below the horizontal dashed line, and bounded by the colored vertical line, represents the detunings at which the noise is less than a factor of 2 from its minimum value.

tunable resonant search and a broadband search with the same integration time. We discuss the topic of optimized time allocation (scan strategy) in a resonant search, which does not apply to broadband. We calculate the SNR of each experiment at each search frequency, and then determine the ratio of SNRs for two scans: a wide scan and a low-frequency scan. Finally, we conclude that the tunable resonant search is superior to the broadband search at all frequencies at which a resonator can be built ($\gtrsim 100$ Hz).

Circuit diagrams are shown for both types of searches in Fig. 15. The two fundamental sources of noise in the detection scheme are thermal/zero-point noise from the resistor and amplifier noise.

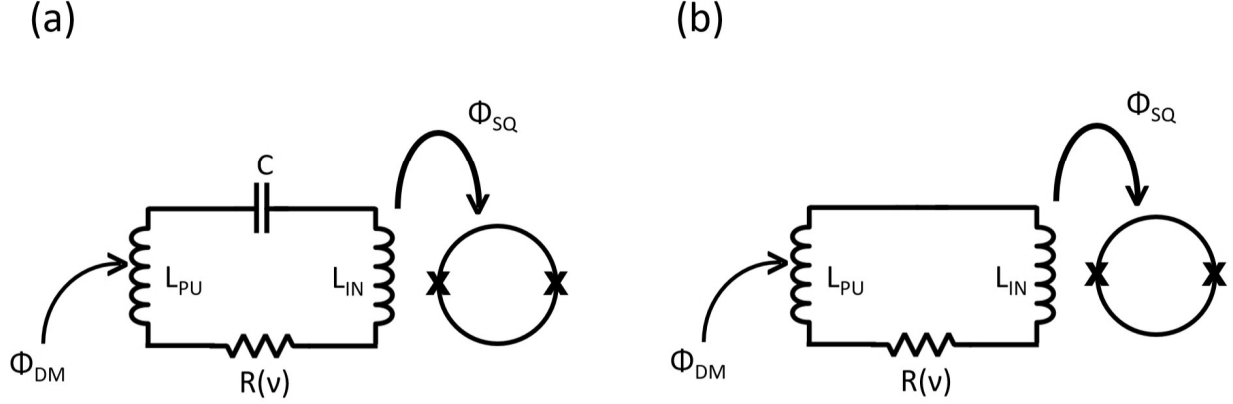


FIG. 15. (a) Resonant dark matter search (shown at a particular resonance frequency). (b) Broadband dark matter search. The oscillating dark matter signal causes a flux in the inductor, which in turn causes currents to flow in the circuit. These currents are then read out as a flux in the flux-to-voltage amplifier, shown here schematically as a dc SQUID. The values of the pickup inductor L_{PU} and input inductor L_{IN} are assumed to be the same in the two experiments for an apples-to-apples comparison of the coupled experimental volumes. However, it should be noted that the number of wiring turns around each coupled inductance L_{PU} and L_{IN} can be changed without invalidating this apples-to-apples comparison, as this constitutes a broadband impedance transformation, and not a change in coupled volume.

An apples-to-apples comparison of single-pole resonant and broadband sensitivities requires a careful treatment of the amplifier noise spectral densities and noise impedance. In our previous calculations, we assumed that the noise impedance and amplifier noise spectral densities are, to good approximation, constant in a narrow bandwidth centered about the resonance frequency: the region in which the SNR is constant with respect to detuning from resonance, which can be many resonance linewidths. This is the “useful” bandwidth for detection. Beyond this bandwidth, the SNR is degraded by the amplifier imprecision noise and therefore, the region outside of the “useful” bandwidth provides a negligible contribution to the overall sensitivity. In a resonant search, the resonance frequency is scanned, and the sensitivity of the search in different frequency bands can be chosen by time allocation. However, in a broadband search, there is no scanning and one uses the information over all bandwidth (up to ~ 100 MHz, where parasitic capacitances not shown in Fig. 15 degrade the coupling to the amplifier). Over most of this bandwidth, the SNR is greatly degraded

by amplifier noise. But instead of discarding this information, it is integrated over the full time of the experiment. To some degree, the degradation of SNR from amplifier noise is mitigated by long experimental time.

In a broadband search, practically speaking, the noise spectral densities and noise impedance of the flux-to-voltage amplifier, which is operated without retuning in the broadband search, vary significantly over the entire frequency range. In order to enable a comparison of broadband and resonant searches, we must make an assumption about the frequency-dependent noise impedance of the flux-to-voltage amplifier used in the broadband search. One natural choice for a flux-to-voltage amplifier for a broadband search is a dc SQUID. Because of correlations between imprecision noise and backaction noise in a dc SQUID, the noise impedance tends to have a complex value. We ignore this non-ideal property for the purposes of this comparison, assume that the noise impedance of the amplifier is real, and make use of the fact that flux-to-voltage amplifiers tend to possess a noise impedance that increases linearly with frequency [57]. A simple and natural model for this noise impedance is thus that it is real-valued and increases linearly with frequency:

$$Z_N(\nu) = 2\pi\nu L_N \quad (\text{G1})$$

where L_N is a characteristic inductance. As we have done in the previous appendix, we will assume that the damping from the amplifier input impedance is negligible.

It is important to understand this assumption in the context of the resonator optimization in Appendix F 3 in order to ensure that we are establishing an apples-to-apples comparison of tunable resonant and broadband sensitivity. In the resonator optimization, we assumed approximately constant noise impedance in the sensitivity bandwidth at each resonant scan step. However, the noise impedance of (G1) is not constant with frequency, but rather, linear with frequency. We may reconcile the two sets of assumptions by observing that the sensitivity bandwidth is narrow (much smaller than the resonance frequency), and therefore, though the noise impedance is frequency-dependent, we may substitute ν_r for ν for the purposes of sensitivity optimization and calculation. In other words, the noise impedance can be approximated as constant during one scan step in the resonant search.

In the resonant search, after enough scan steps have been taken that the thermal occupation number changes significantly, the noise impedance of the amplifier is reoptimized. This optimization can be conducted, e.g., by tuning a variable transformer based on Josephson

junctions, or by tuning the bias parameters of some flux-to-voltage amplifiers. At some frequency interval, perhaps a decade in frequency, the amplifier would need to be swapped with an amplifier with different coupling strength to enable a larger change in noise impedance, in conjunction with the swap of the coil set to enable tuning to the next decade of frequency. Optimizing this noise impedance is equivalent to optimizing L_N . We also note that changing the coil set does not invalidate the apples-to-apples comparison as long as the coupled volume remains the same — we are just changing the number of turns, which is a broadband impedance transformation.

For the broadband experiment, we also need to optimize L_N . In this case, we only choose a single value of L_N because we do not scan and change circuit and readout parameters. Because we need to choose a single value for a wideband search, it would then seem that we would require a value function that weights the importance of different search frequencies. However, we will find that the value of L_N that maximizes the SNR at each search frequency is independent of the frequency, and therefore, such a value function is not required. This observation suggests that an amplifier exhibiting this noise impedance scaling is an appropriate choice for a broadband search.

We now establish the assumptions under which we will compare the optimized tunable resonator search to the optimized broadband search.

We assume that the two experiments use the same pickup volume, which ensures that the two experiments couple to the same amount of dark-matter signal energy, denoted E_{DM} in eq. (51). However, the two experiments may have different numbers of wiring turns around the detector volume, as long as the coupled volume is the same. We further assume that the pickup and input inductances are matched. The resonator is tuned by a variable lossless capacitor (e.g. a vacuum gap parallel-plate capacitor for which the electrode overlap area or the separation distance may be changed), represented by C in the figure. The broadband circuit can be realized by removing the capacitor and shorting the leads together. In this manner, we may assume that the loss in both circuits is the same; the loss is quantified by the inductor quality, which is the ratio of its reactance to its resistance $2\pi\nu_{\text{DM}}^0(L_{\text{PU}} + L_{\text{IN}})/R(\nu)$. We emphasize that we do not require the values of the pickup inductance and resistance to be the same in the broadband and resonant searches. It is evident from the first fraction inside the integrand equation (F13) and from our analysis below that inductor quality is the relevant parameter for the signal source's effect on SNR.

We assume that the tunable resonator is high Q, which implies $R(\nu_{\text{DM}}^0) \ll 2\pi\nu_{\text{DM}}^0(L_{\text{PU}} + L_{\text{IN}})$ at all dark matter frequencies in both searches.

We assume that both searches possess optimized noise impedance, as described above. The impedance optimization for the tunable resonator was carried out in Appendix F 3. The optimization for the broadband search, in which the value of L_N in eq. (G1) is chosen to maximize SNR, and will be carried out below.

We set the lower limit for this mathematical comparison at $\nu_l = 1$ kHz. Below 1 kHz, some of the approximations in our narrowband analysis begin to break down. However, we emphasize that the results of this analysis apply down to the lowest frequency at which a resonator can be practically built, $\nu_l \sim 100$ Hz. Below ~ 100 Hz, building a resonant circuit is challenging due to the physically large components required and resultant parasitic inductances and capacitances. As for the upper limit, we will consider two different scans. In the first scan, a wide band scan, we set the upper limit for the comparison at $\nu_h = 100$ MHz. Above this frequency, uncontrolled impedances (for instance, stray inductances/capacitances) in the nominally lumped-element input circuit will degrade system performance in both the broadband and resonant experiment. We also consider a low-frequency scan, where $\nu_h = 10$ kHz.

We assume that the total search time T_{tot} is long enough that we may dwell at each resonance frequency longer than the resonator ring-up/dark matter coherence time. For the resonant scan time allocation, we assume the log-uniform search optimization represented by eq. (183).

Intuition suggests that the assertion that broadband has higher sensitivity below 100 kHz[22] may not be accurate. For a fixed resonance frequency, at frequencies high above resonance, the capacitor shorts out and the RLC circuit is identical in filter characteristics to the broadband circuit. However, near resonance, the thermal noise, presented as a voltage noise in series with the resistance, is rung up. If this thermal noise dominates the amplifier noise, as is commonplace in SQUID readout of MHz resonant circuits [62], the SNR is not degraded by the readout. In a broadband search, the thermal noise is rolled off by the L/R pole of the input circuit and is generically lower than the amplifier noise; the sensitivity is then degraded by readout. Near resonance, one then expects the SNR of the resonant detector to be better than the broadband detector, and well above the resonance, they should be the same. If the resonator were not scanned at all, but fixed at a single frequency, one

should expect the SNR to be better than or equal to the broadband search at the resonance frequency and above. If we then scan the resonator frequency, one might expect better SNR than broadband at all frequencies at which a resonator can be built. A rigorous analysis is somewhat more complicated, but comes to the same conclusion.

We may gain further insight from our Bode-Fano constraint in Appendix F 2. The optimized scan sensitivity, as constrained by the Bode-Fano limit, is achieved with a narrowband noise match (a top-hat spectrum when we consider $\zeta(Z_T(\nu))$ as a function of frequency), and the single-pole resonator is close to this limit. If a broadband search were better than a resonant search, then we would expect the Bode-Fano limit to point toward a wideband match, with ζ taking on nonzero values over a broad bandwidth of frequencies. However, this is not the case.

One may analyze the integrated scan sensitivity of both broadband and resonant searches under any set of priors. As an example, we assume the prior of a log-uniform search, in which no knowledge is assumed about the likely properties of dark matter. To do the comparison, we evaluate the SNR for each search over the specified frequency range. The SNR for the optimized resonant search was derived in Appendix F 3 and is given in eq. (184) for the log-uniform search time allocation of Section V B. We will denote the square of this SNR as $SNR_R^2(\nu_{\text{DM}}^0)$, where the subscript ‘R’ denotes a resonant search. It thus suffices to derive below only the optimized SNR for the broadband search.

From equations (F10), (F13), and (F14), the signal-to-noise ratio for the broadband search at search frequency ν_{DM}^0 is given by

$$SNR_B \left[\nu_{\text{DM}}^0, g_{\text{DM}}, \frac{d\rho_{\text{DM}}}{d\nu}(\nu, \nu_{\text{DM}}^0), \tau \right]^2 = (2\pi^2)^2 T_{\text{tot}} \quad (\text{G2})$$

$$\times \int_{\nu_{\text{DM}}^0}^{\nu_{\text{DM}}^0 + \Delta\nu_{\text{DM}}^c} d\nu \left(\frac{\nu L_{\text{PU}}}{R(\nu)} \frac{E_{\text{DM}}(\nu, \nu_{\text{DM}}^0, g_{\text{DM}}, \frac{d\rho_{\text{DM}}}{d\nu}(\nu, \nu_{\text{DM}}^0))}{h} \frac{1}{N_B^{FV}(\nu, Z_B(\nu), Z_N(\nu), n(\nu))} \right)^2$$

where

$$Z_B(\nu) = R(\nu) + 2\pi i \nu (L_{\text{PU}} + L_{\text{IN}}) \quad (\text{G3})$$

is the source impedance seen by the amplifier, and we have absorbed the imaginary part of the amplifier input impedance into the total inductance. We have substituted T_{tot} for τ because at each search frequency, we integrate for the total experiment time. The subscript

‘B’ denotes that the SNR is for the broadband search.

$$N_B^{FV}(\nu, Z_B(\nu), Z_N(\nu), n(\nu)) = \frac{\text{Re}(Z_B(\nu))(n(\nu) + \frac{1}{2}) + \frac{1}{4} \left(\frac{|Z_B(\nu)|^2}{Z_N(\nu)} + Z_N(\nu) \right)}{\text{Re}(Z_B(\nu))} \quad (\text{G4})$$

is the noise-equivalent number. Since we have assumed low-loss, $R(\nu) \ll 2\pi\nu(L_{\text{PU}} + L_{\text{IN}})$, we may approximate, using (G1),

$$N_B^{FV}(\nu, Z_B(\nu), Z_N(\nu), n(\nu)) \approx n(\nu) + \frac{1}{2} + \frac{1}{4} \frac{2\pi\nu \left(\frac{(L_{\text{PU}} + L_{\text{IN}})^2}{L_N} + L_N \right)}{R(\nu)}. \quad (\text{G5})$$

The noise equivalent number is minimized and the SNR is maximized when the characteristic inductance for the noise impedance is the sum of the input and pickup inductances: $L_N = L_{\text{PU}} + L_{\text{IN}}$. The optimal value of the noise equivalent number is then

$$N_B^{\text{opt}}(\nu, Z_B(\nu), n(\nu)) = n(\nu) + \frac{1}{2} + \frac{1}{2} \frac{2\pi\nu(L_{\text{PU}} + L_{\text{IN}})}{R(\nu)} \quad (\text{G6})$$

The first term on the right-hand side represents the thermal noise, the second the zero-point fluctuation noise, and the third the amplifier noise. We identify $2\pi\nu(L_{\text{PU}} + L_{\text{IN}})/R(\nu)$ as the quality factor of a resonator (i.e. the inductor quality) at center frequency ν . For the purposes of the sensitivity comparison, we will set the quality factor to be a frequency-independent value $Q \gg 1$. Combining eqs. (51), (G2), and (G6) yields the SNR expression

$$\text{SNR}_B(\nu_{\text{DM}}^0)^2 \approx \frac{\pi^2}{4} T_{\text{tot}} \left(\frac{Q}{n(\nu_{\text{DM}}^0) + \frac{1}{2}Q} \right)^2 \int_{\nu_{\text{DM}}^0}^{\nu_{\text{DM}}^0 + \Delta\nu_{\text{DM}}^c} d\nu \left(\frac{g_{\text{DM}}^2 V_{\text{PU}} \frac{d\rho_{\text{DM}}}{d\nu}(\nu, \nu_{\text{DM}}^0)}{h} \right)^2 \quad (\text{G7})$$

where we have assumed matched pickup and input inductances.

We are now ready to quantitatively compare the sensitivity of the two searches. The ratio of the SNR for broadband and resonant searches is, from (184),

$$\Gamma(\nu_{\text{DM}}^0) \equiv \frac{\text{SNR}_R^2(\nu_{\text{DM}}^0)}{\text{SNR}_B^2(\nu_{\text{DM}}^0)} = \frac{16\pi}{\ln(\nu_{\text{h}}/\nu_{\text{l}})} \frac{\xi^{\text{opt}}(n(\nu_{\text{DM}}^0))^2}{(4\xi^{\text{opt}}(n(\nu_{\text{DM}}^0))n(\nu_{\text{DM}}^0) + (1 + \xi^{\text{opt}}(n(\nu_{\text{DM}}^0)))^2)^{3/2}} \frac{(n(\nu_{\text{DM}}^0) + \frac{1}{2}Q)^2}{Q} \quad (\text{G8})$$

We now focus on particular limits relevant to the frequency range in question. Assume that both experiments are conducted at a temperature of 10 mK. Then, in the frequency range of 1 kHz to 100 MHz, the high thermal-occupation limit $n(\nu_{\text{DM}}^0) \gg 1$ applies. In this regime, $\xi_{\text{opt}} \approx 2n(\nu_{\text{DM}}^0)$, so we find

$$\Gamma(\nu_{\text{DM}}^0) \approx \frac{2\pi}{\ln(\nu_{\text{h}}/\nu_{\text{l}})} \frac{4}{3\sqrt{3}} \frac{(n(\nu_{\text{DM}}^0) + \frac{1}{2}Q)^2}{n(\nu_{\text{DM}}^0)Q} \quad (\text{G9})$$

We calculated the resonator sensitivity under the assumption that the sensitivity quality factor is much larger than unity, which is appropriate at 10 mK for internal Qs on the order of one million down to resonance frequencies of approximately ~ 1 kHz. This condition implies that $Q \gg n(\nu_{\text{DM}}^0)$, so we find

$$\Gamma(\nu_{\text{DM}}^0) \approx \frac{2\pi}{3\sqrt{3}\ln(\nu_h/\nu_l)} \frac{Q}{n(\nu_{\text{DM}}^0)} \gg 1 \quad (\text{G10})$$

The numerical prefactor in the approximation step is approximately 0.1 for the wide band scan ($\nu_h = 100$ MHz) and 0.5 for the low-frequency scan ($\nu_h = 10$ kHz). We thus find that the resonator sensitivity is superior to the sensitivity of the broadband search.

To demonstrate the advantage of the resonant search more explicitly, we may consider the ratio of minimum couplings to which each search is sensitive,

$$\frac{g_{\text{DM,min}}^R}{g_{\text{DM,min}}^B} = \Gamma(\nu_{\text{DM}}^0)^{-1/4} \quad (\text{G11})$$

A value less than unity implies that the resonant search is superior. For the wide band scan, the ratio is plotted for the optimized log-uniform resonant search, with the optimized time allocation of eq. (183), in Fig. 16 as the blue curve. We have assumed a quality factor of one million.

In contrast to the limits shown in [22], the resonant search with Q of 10^6 is considerably better than the broadband search at all frequencies above 1 kHz. The ratio is lower than one at all frequencies, dropping below 0.1 in coupling at the highest frequencies. This corresponds to a scan rate (reflecting the time to reach a particular coupling) that is more than four orders of magnitude higher.

We have cut off the analysis at 1 kHz not because coils at lower frequencies cannot be made, but because the approximations used in the analysis break down. At these low frequencies, the thermal occupation number is comparable to, or larger, than the resonator quality factor, and the approximations used to derive the curve in the figure break down at such low frequencies, which manifests in the curving of the lines at lower frequencies. Nonetheless, one may qualitatively extrapolate the sensitivity comparison to lower frequencies, and it may seem that, extrapolating to frequencies below 1 kHz, a broadband approach may be fundamentally more suitable. However, this conclusion is not accurate. This is because the time allocation for the scanned search was selected by assuming the prior of a log-uniform search. In terms of integrated scan sensitivity over the whole frequency range,

if one search is conducted, the resonant search is much more sensitive. If there were reason to expect that dark matter is more likely at the lower frequencies, a different prior would be used, and one finds that the integrated scan sensitivity for the resonant search is superior to broadband for any priors (at frequencies above which a resonator can be built).

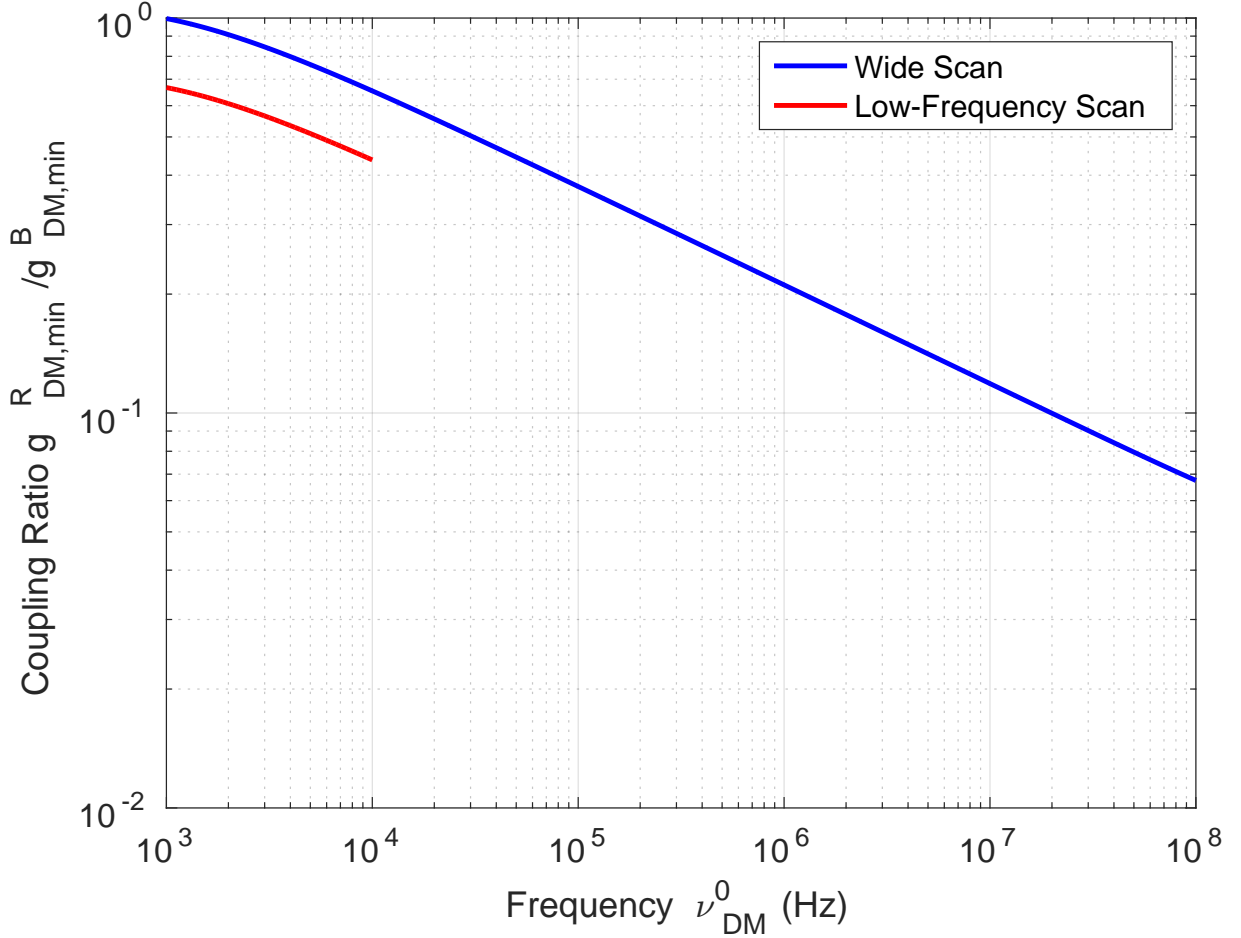


FIG. 16. Resonant vs broadband sensitivity. $\frac{g_{\text{DM,min}}^R}{g_{\text{DM,min}}^B}$ vs frequency for a quality factor of 10^6 and temperature of 10 mK. The comparison for a wide scan between 1 kHz and 100 MHz is shown in blue, while that for a low-frequency scan between 1 kHz and 10 kHz is shown in red. The small curvature at the lowest frequencies in both curves is the result of increasing error in the approximations used to evaluate resonant sensitivity. This error reflects the sensitivity quality factor approaching unity.

This observation begs the question of conducting two separate experiments. If two experiments were conducted for the same integration time, might one expect that, selecting a resonant experiment for one, and a broadband experiment for the other, that the lower

frequency sensitivity might be improved? However, asking this question is assuming a prior that weights low frequency information as particularly interesting. Assuming that prior, we find that two resonant scans can always be designed to outperform a resonant scan and a broadband scan at all frequencies where a resonator can be practically built. One scan will spend more integration time at lower frequency. For example, we may consider a second, low-frequency scan covering only the 1 kHz-10 kHz band. The ratio of minimum detectable couplings is shown in red. Again, the ratio is smaller than unity, and it is evident that the low-frequency resonant scan will outperform the broadband scan at lower frequencies. The scan rate is roughly an order of magnitude higher for resonant than for broadband at 1 kHz. The optimal choice for two experiments is thus two resonant scans, rather than a resonant scan and a broadband scan, at all frequencies above which a resonator can be built.

The data shown in figure 16 is plotted with $Q = 10^6$. The advantage of a resonant search is diminished as the Q is reduced. One may ask if an experiment only achieves a lower $Q \approx 50,000$, whether a broadband search would have a fundamental advantage at lower frequencies. In other words, at low $Q \approx 50,000$, and using priors emphasizing low frequencies, might the broadband search have an advantage in integrated scan sensitivity? The analysis presented here shows that, as long as the Q is high enough that the approximations used in the resonant derivation are correct, the integrated scan sensitivity is better for a resonant search for any set of priors, including priors emphasizing lower frequencies. At $Q \approx 50,000$, our approximations break down at ≈ 10 kHz, but we can still state with some confidence that the advantage of a resonant search persists to lower frequencies and Q . This assertion is based on the intuitive argument presented earlier, that for a fixed resonance frequency, at frequencies high above resonance, the capacitor shorts out and the RLC circuit is identical in filter characteristics to the broadband circuit. So in the limit that the resonator is fixed (not scanned) at the lowest frequency, one should expect the SNR to be better than or equal to the broadband search at the resonance frequency and above, even at lower Q . So there exists a scan strategy at which the resonator is equal to, or superior to the broadband experiment at all frequencies equal to, or above the resonant frequency. So the statement holds that a scanned resonator outperforms a broadband experiment at all frequencies at which a resonator can be constructed.

As a final remark in this section, we consider some of the practical advantages for a resonant search. Both resonant and broadband searches will be susceptible to false signals

from electromagnetic interference. In a resonant search, an interfering signal at a given frequency will be quickly detected, and after elimination of the source or modification of the experiment, confirmation that the spurious signal is gone can be quickly achieved. In contrast, in a broadband search, a weak spurious signal can only be detected (and its removal can only be confirmed) after a long integration time. Broadband searches are also more vulnerable to weak, intermittent transient signals, which can be eliminated in resonant experiments by repeated scans. Resonant scans also have more subtle advantages. Because of amplifier nonlinearities, in broadband scans, the many pickup lines that will inevitably couple to the experiment will produce a forest of weak intermodulation products at many points in the bandwidth of the experiment. These very weak products will only be evident after a lengthy integration time. A resonator filters the pickup lines outside of the resonator bandwidth, greatly reducing problems with intermodulation products. Finally, if a weak candidate signal is identified in a broadband search, optimal follow-up will require a resonant measurement at the frequency of interest. A resonant experiment can quickly integrate to a much higher signal-to-noise ratio than a broadband experiment at a given frequency of interest in order to determine spatial, temporal, and directional properties, and measure the candidate signal power spectrum.

-
- [1] P. A. Ade, N. Aghanim, M. Alves, C. Armitage-Caplan, M. Arnaud, M. Ashdown, F. Atrio-Barandela, J. Aumont, H. Aussel, C. Baccigalupi, *et al.*, *Astronomy & Astrophysics* **571**, A1 (2014).
 - [2] R. Agnese *et al.* (SuperCDMS), *Phys. Rev. Lett.* **116**, 071301 (2016), arXiv:1509.02448 [astro-ph.CO].
 - [3] D. Akerib *et al.* (LUX Collaboration), *Phys. Rev. Lett.* **118**, 021303 (2017).
 - [4] E. Aprile, M. Alfonsi, K. Arisaka, F. Arneodo, C. Balan, L. Baudis, B. Bauermeister, A. Behrens, P. Beltrame, K. Bokeloh, *et al.*, *Phys. Rev. Lett.* **109**, 181301 (2012).
 - [5] R. Peccei and H. Quinn, *Phys. Rev. Lett.* **38**, 1440 (1977).
 - [6] R. Peccei and H. Quinn, *Phys. Rev. Lett.* **38**, 1440 (1977).
 - [7] M. Dine and W. Fischler, *Phys. Lett.* **B120**, 137 (1983).
 - [8] J. Preskill, M. Wise, and F. Wilczek, *Phys. Lett.* **B120**, 127 (1983).
 - [9] D. Budker *et al.*, *Phys. Rev.* **X4**, 021030 (2014), arXiv:1306.6089 [hep-ph].
 - [10] P. Sikivie, *Phys. Rev. Lett.* **51**, 1415 (1983).
 - [11] P. Sikivie, *Phys. Rev. D* **32**, 2988 (1985).
 - [12] B. Holdom, *Physics Letters B* **178**, 65 (1986).
 - [13] A. Nelson and J. Scholtz, *Phys. Rev.* **D84**, 103501 (2011), arXiv:1105.2812 [hep-ph].
 - [14] P. Arias, D. Cadamuro, M. Goodsell, J. Jaeckel, J. Redondo, and A. Ringwald, *JCAP* **2012**, 013 (2012).
 - [15] P. Graham, J. Mardon, and S. Rajendran, *Phys. Rev.* **D93**, 103520 (2016), arXiv:1504.02102 [hep-ph].
 - [16] S. Chaudhuri *et al.*, *Phys. Rev.* **D92**, 075012 (2015), arXiv:1411.7382 [hep-ph].
 - [17] S. Asztalos *et al.*, *Physical Review Letters* **104**, 041301 (2010).
 - [18] B. Brubaker *et al.*, arXiv preprint arXiv:1610.02580 (2016), arXiv:1610.02580 [astro-ph.CO].
 - [19] P. Sikivie, N. Sullivan, and D. Tanner, *Phys. Rev. Lett.* **112**, 131301 (2014), arXiv:1310.8545 [hep-ph].
 - [20] M. Silva-Feaver *et al.*, *IEEE Transactions on Applied Superconductivity* **27**, 1 (2017).
 - [21] J. Zmuidzinas, *Applied Optics* **42**, 4989 (2003).
 - [22] Y. Kahn *et al.*, *Physical Review Letters* **117**, 141801 (2016).

- [23] S. Chaudhuri, (in preparation).
- [24] H. Zheng, M. Silveri, R. Brierley, S. Girvin, and K. Lehnert, arXiv preprint arXiv:1607.02529 (2016), arXiv:1607.02529v2 [hep-ph].
- [25] C. M. Caves, Phys. Rev. D **26**, 1817 (1982).
- [26] G. Rybka, arXiv preprint arXiv:1403.6720 (2014), arXiv:1403.6720 [physics.ins-det].
- [27] H. Seton, D. Bussell, J. Hutchison, and D. Lurie, IEEE Transactions on Applied Superconductivity **5**, 3218 (1995).
- [28] A. A. Clerk, M. H. Devoret, S. M. Girvin, F. Marquardt, and R. J. Schoelkopf, Rev. Mod. Phys. **82**, 1155 (2010).
- [29] S. W. Wedge, *Computer-aided design of low noise microwave circuits*, Ph.D. thesis, California Institute of Technology (1991).
- [30] M. Castellanos-Beltran, K. Irwin, G. Hilton, L. Vale, and K. Lehnert, Nature Physics **4**, 929 (2008).
- [31] H. W. Bode, *Network analysis and feedback amplifier design* (van Nostrand, 1945).
- [32] R. M. Fano, Journal of the Franklin Institute **249**, 57 (1950).
- [33] R. H. Dicke, Review of Scientific Instruments **17**, 268 (1946).
- [34] N. Wiener, *Extrapolation, interpolation, and smoothing of stationary time series*, Vol. 7 (MIT press Cambridge, MA, 1949).
- [35] H.-C. Stahl, *Cryogenic particle detection*, Vol. 99 (Springer Science & Business Media, 2005).
- [36] P. Graham *et al.*, Phys. Rev. **D90**, 075017 (2014), arXiv:1407.4806 [hep-ph].
- [37] D. Horns, J. Jaeckel, A. Lindner, J. Redondo, A. Ringwald, *et al.*, Journal of Cosmology and Astroparticle Physics **2013**, 016 (2013).
- [38] P. Sikivie, N. Sullivan, and D. Tanner, Phys. Rev. Lett. **112**, 131301 (2014).
- [39] D. M. Pozar, “Microwave engineering. 4th,” (2012).
- [40] D. A. Hill, *Electromagnetic fields in cavities: deterministic and statistical theories*, Vol. 35 (John Wiley & Sons, 2009).
- [41] J. Clarke and A. I. Braginski, *The SQUID handbook: Applications of SQUIDs and SQUID systems* (John Wiley & Sons, 2006).
- [42] J. Mates *et al.*, Applied Physics Letters **92**, 023514 (2008).
- [43] M. Mück, J. Kycia, and J. Clarke, Applied Physics Letters **78**, 967 (2001).
- [44] B. Yurke and J. S. Denker, Physical Review A **29**, 1419 (1984).

- [45] J. Zmuidzinas, The Astrophysical Journal **813**, 17 (2015).
- [46] P. Sikivie, I. I. Tkachev, and Y. Wang, Physical review letters **75**, 2911 (1995).
- [47] L. Baudis, Physics of the Dark Universe **1**, 94 (2012).
- [48] K. Freese, M. Lisanti, and C. Savage, Reviews of Modern Physics **85**, 1561 (2013).
- [49] L. Rosenberg, in *this SLAC Summer Institute, available at http://www-conf.slac.stanford.edu/ssi/2004/lec_notes/Rosenberg* (2004).
- [50] D. Youla, IEEE Transactions on Circuit Theory **11**, 30 (1964).
- [51] D. Nie and B. M. Hochwald, IEEE Transactions on Circuits and Systems I: Regular Papers **62**, 995 (2015).
- [52] P. W. Graham, I. G. Irastorza, S. K. Lamoreaux, A. Lindner, and K. A. van Bibber, Annual Review of Nuclear and Particle Science **65**, 485 (2015).
- [53] L. Krauss, J. Moody, F. Wilczek, and D. E. Morris, Physical review letters **55**, 1797 (1985).
- [54] DM Radio collaboration (in preparation).
- [55] A. K. Drukier, K. Freese, and D. N. Spergel, Physical Review D **33**, 3495 (1986).
- [56] C. Kelso, D. Hooper, and M. R. Buckley, Physical Review D **85**, 043515 (2012).
- [57] P. Falferi, M. Bonaldi, M. Cerdonio, A. Vinante, and S. Vitale, Applied physics letters **73**, 3589 (1998).
- [58] C. Hilbert and J. Clarke, Journal of low temperature physics **61**, 237 (1985).
- [59] A. Clerk, Physical Review B **70**, 245306 (2004).
- [60] J. Clarke, C. D. Tesche, and R. Giffard, Journal of Low Temperature Physics **37**, 405 (1979).
- [61] M. Aspelmeyer, T. J. Kippenberg, and F. Marquardt, Reviews of Modern Physics **86**, 1391 (2014).
- [62] W. Myers, D. Slichter, M. Hatridge, S. Busch, M. Möble, R. McDermott, A. Trabesinger, and J. Clarke, Journal of Magnetic Resonance **186**, 182 (2007).